Michael Reichert

Hydrodynamic Interactions in Colloidal and Biological Systems

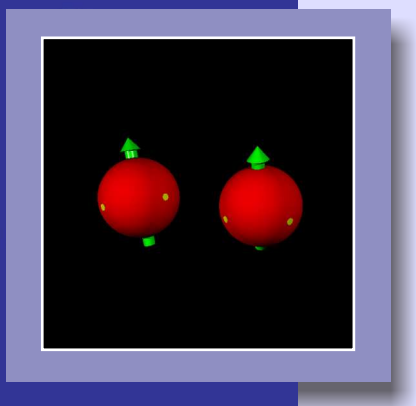

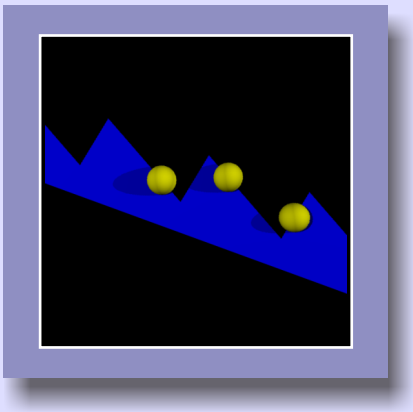

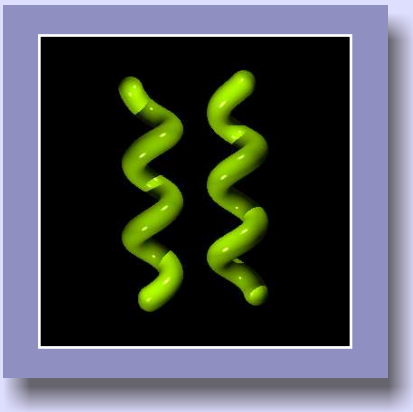

Hydrodynamic Interactions in Colloidal and Biological Systems

Dissertation

zur Erlangung des akademischen Grades
Doktor der Naturwissenschaften (*Dr. rer. nat.*)

an der Universität Konstanz,
Mathematisch-Naturwissenschaftliche Sektion,
Fachbereich Physik,

vorgelegt von

Michael Reichert

Referenten:

PD Dr. Holger Stark
Prof. em. Dr. Rudolf Klein

Tag der mündlichen Prüfung:

14. Juli 2006

Quand tu veux
construire un bateau,
ne commence pas
par rassembler du bois,
couper des planches
et distribuer du travail,
mais réveille
au sein des hommes
le désir de la mer
grande et large.

Antoine de Saint-Exupéry

Contents

1 General introduction 1

1.1 Colloids as model systems . . . 1
1.2 Recent studies on hydrodynamic interactions . . . 2
1.3 Outline of this thesis . . . 4

A Hydrodynamic interactions
Theoretical concepts and simulation methods

2 Stokesian dynamics 9

2.1 Hydrodynamic equations . . . 10
2.1.1 Continuity equation and incompressibility . . . 10
2.1.2 The Navier-Stokes equation . . . 10
2.1.3 The Reynolds number . . . 12
2.1.4 The Stokes equations . . . 12
2.2 Translation and rotation of a single sphere . . . 13
2.2.1 Translation . . . 14
2.2.2 Rotation . . . 14
2.3 Hydrodynamic interactions . . . 15
2.3.1 Theoretical description and definitions . . . 15
2.3.2 On the propagation of hydrodynamic interactions . . . 17
2.4 Mobility matrix for configurations of beads . . . 18
2.4.1 The Oseen tensor . . . 18
2.4.2 Method of reflections: the Rotne-Prager approximation . . . 19
2.4.3 Method of induced forces . . . 22
2.4.4 Lubrication effects . . . 24
2.4.5 Mobilities of a two-sphere system . . . 26
2.4.6 Mobility matrix for rigid clusters . . . 29
2.5 Stokesian-dynamics simulations . . . 30
2.5.1 Equation of motion . . . 30
2.5.2 Numerical integration schemes . . . 31

3 Brownian motion 33

3.1 The Langevin equation . . . 34
3.1.1 From Newton's second law to the Langevin equation . . . 34
3.1.2 Fluctuation-dissipation theorem . . . 35
3.1.3 Brownian displacements and Wiener processes . . . 36

3.1.4 Evolution equation of Langevin dynamics 39
3.1.5 Deterministic vs. diffusive motion 40
3.2 The Smoluchowski equation 41
3.3 Brownian-dynamics simulations 43
3.3.1 Numerical integration schemes 43
3.3.2 The Cholesky decomposition 45
3.3.3 Generation of Gaussian random numbers 46

B Two-point microrheology ■ Hydrodynamic coupling of rotating beads in optical traps

4 Optical tweezers and microrheology 51
4.1 Optical tweezers 51
4.1.1 Trapping of dielectric particles in a laser spot 51
4.1.2 Rotation of birefringent particles in polarized traps 53
4.2 Concepts of microrheology 54
4.2.1 One-point microrheology 54
4.2.2 Two-point microrheology 54
4.3 Experiments measuring hydrodynamic interactions 55

5 Theory of coupled motions of two trapped beads 57
5.1 Tweezer setup and dynamics of trapped particles 57
5.1.1 Forces and translational motion 57
5.1.2 Torques and rotational motion 58
5.2 Relaxational eigenmodes of two trapped spheres 60
5.2.1 Longitudinal modes 61
5.2.2 Transversal modes 62
5.3 Correlated Brownian motion of two trapped spheres 65
5.3.1 Longitudinal fluctuations 67
5.3.2 Transversal fluctuations 69

6 Brownian-dynamics simulations and experiments 75
6.1 Brownian-dynamics simulations 75
6.1.1 Trap forces and torques 75
6.1.2 Correlation functions 76
6.2 Experiments 77

7 Conclusions I 79

C | Drafting of colloids ■
The benefits of hydrodynamic interactions

8 Colloidal particles orbiting in circular optical traps 83
8.1 Optical vortices . . . 83
8.2 Circulating optical tweezer . . . 85

9 Collective drafting dynamics of circling particles 87
9.1 Model system . . . 87
9.2 Stability of regular clusters . . . 88
9.2.1 Dynamics of regular clusters . . . 89
9.2.2 Eigenmodes of perturbed clusters . . . 90
9.3 Nonlinear dynamics and periodic limit cycle . . . 93
9.3.1 Dynamic transition to periodic limit cycle . . . 93
9.3.2 Enhanced particle motion due to drafting effects . . . 94
9.3.3 Harmonic analysis of the limit cycle . . . 95
9.3.4 Clustering in weak radial traps . . . 97

10 Dynamics in a sawtooth potential supported by drafting 99
10.1 Model system . . . 99
10.1.1 Sawtooth-modulated circular trap . . . 99
10.1.2 Electrostatic interaction . . . 102
10.1.3 Brownian-dynamics simulations . . . 102
10.2 Experimental realization and validation of the model . . . 104
10.3 Single-particle dynamics . . . 105
10.4 Cooperative motion of drafting and thermal jumps . . . 107
10.4.1 The “caterpillar” mode . . . 107
10.4.2 Enhanced cluster dynamics . . . 109
10.4.3 On the role of hydrodynamic interactions . . . 111
10.4.4 Influence of sawtooth asymmetry and temperature . . . 115

11 Conclusions II 117

D | Swimming of microorganisms ■
Synchronization of rotating helical flagella

12 Locomotion of microorganisms 121
12.1 Principles of swimming at low Reynolds number . . . 122
12.2 Flagellar propulsion . . . 123

12.2.1 Ciliary beating . . . 124
12.2.2 Phenomenology of propulsion by rotating helical flagella . 125
12.3 Hydrodynamic interactions in flagellar systems . . . 126

13 Synchronized rotation of rigid helical filaments 129

13.1 Model system . . . 129
13.2 Symmetry considerations . . . 133
13.3 Synchronization dynamics . . . 134
13.3.1 Phase synchronization . . . 134
13.3.2 On the role of "flexibility" . . . 137
13.3.3 Robustness against torque differences . . . 139
13.3.4 "Extrapolation" to real flagella . . . 140

14 Synchronization of flexible flagella 143

14.1 Model system . . . 143
14.1.1 The Frenet-Serret equations . . . 143
14.1.2 Helical worm-like chain model . . . 144
14.1.3 Discrete bead-spring model of a flexible helix . . . 146
14.1.4 Equilibrium configuration . . . 149
14.1.5 Elastic forces and torques . . . 150
14.1.6 Motor forces . . . 152
14.1.7 Equations of motion . . . 153
14.2 Synchronization dynamics . . . 156
14.2.1 Dynamics and deformations of rotating helices . . . 156
14.2.2 Phase synchronization . . . 157
14.2.3 Dependence on flexibility . . . 159
14.2.4 Flexible vs. rigid helices . . . 159

15 Conclusions III 163

Bibliography 165

List of publications 179

Zusammenfassung 181

Danksagung 185

1 General introduction

Colloids are widely considered as model systems to elucidate fundamental processes in atomic systems. However, there is one feature truly specific to colloidal suspensions which distinguishes them fundamentally from atomic systems: *hydrodynamic interactions*.

In this introductory chapter, we first give a rough overview of the physics of colloids and their applications as model systems. As a motivation of this work, we then discuss representative examples of colloidal and biological systems where hydrodynamic interactions lead to fascinating collective behavior. Finally, an outline of this thesis is given in Sect. 1.3.

1.1 Colloids as model systems

Colloids are mesoscopic particles that are suspended in a continuous medium and whose size ranges from 10 nm to 1 μm, such as fog (water droplets in air) or milk (fat globules in water). In this regime, the suspended particles are much larger than the solvent molecules, but small enough to exhibit vivid thermal (Brownian) motion, so they rapidly sample the accessible configuration space [60, 80]. Suspensions of more or less compact particles in liquids form the basis of a wide variety of systems of scientific and technological importance, including inks, paints, detergents, and biological cells.

Since the characteristic length scales are close to (or larger than) the wavelength of visible light, many optical techniques such as confocal microscopy [87, 242], total-internal-reflection microscopy [100, 210], and light scattering [56, 139] can be employed to study colloidal suspensions. Real-space trajectories of the suspended particles can be monitored by means of video microscopy [48, 105], which allows for direct comparison with analytical and numerical results and leads to a close and fruitful interplay between theory, computer simulation, and experiment.

Colloidal suspensions have many features in common with atomic systems; in particular, with increasing volume fraction of colloidal particles, fluid, crystalline, and glassy phases are observed [197, 200]. In some sense, colloidal suspensions can be regarded as "analog computers" which allow real-time "calculations" in complex situations such as crystal nucleation and growth [87], particle dynamics near the glass transition [242], interactions of dislocations [69], and many more.

The striking advantage of using colloids as model systems is the fact that their interactions can be tailored as desired [60, 80]. For instance, the screened

electrostatic repulsion of like-charged particles in suspension is an adjustable short-range interaction, while the dipole-dipole interaction of superparamagnetic particles yields long-range forces. Moreover, the magnetic dipole interactions can be tuned from repulsive to attractive (depending on the orientation of the magnetic field that induces the magnetic dipole moments) [82]. Colloidal particles can be controlled and manipulated rather easily by external fields [156], such as electric and magnetic fields or optical traps, so-called optical "tweezers". Therefore, colloids are often referred to as versatile model systems to study fundamental processes in atomic systems and to address novel concepts in the context of statistical physics, such as entropic forces [210], light-induced phase transitions [243], or two-dimensional melting scenarios [68].

However, besides the potential forces described above, which are sort of analogous to the interactions in atomic systems, there are also interactions peculiar to colloids. Particles moving in a viscous fluid induce a flow field that affects other particles in their motion. These long-range interactions, which are mediated by the solvent and which are only present if particles are moving, are called *hydrodynamic interactions* [60, 106, 134]. Typically, the dynamics of colloids takes place at very low Reynolds numbers, where viscous forces dominate over inertial effects. Thus, colloidal dynamics is predominantly governed by hydrodynamic interactions.

The detailed study of hydrodynamic interactions in micron-scale colloidal and biological systems and how they govern their dynamics are the central issue of this thesis.

1.2 Recent studies on hydrodynamic interactions

During the last decades, experimental and theoretical studies mostly investigated macroscopic rheological or transport properties of colloidal suspensions (such as effective viscosities or diffusion coefficients) where hydrodynamic effects enter only as an ensemble average over the complete configuration space [14, 183, 200, 251]. Yet, despite their scientific and technological relevance, our understanding of hydrodynamic interactions is still far from complete. One example is the long-standing debate whether the fluctuations of settling velocities in sedimenting suspensions diverge with increasing container size or not [33, 36, 145, 217, 235].

Recent studies suggest another route, namely to concentrate on colloidal systems comprised of only a few particles in order to systematically investigate the role of hydrodynamic couplings, starting with the free diffusion of an isolated pair [49]. Furthermore, two colloidal beads held at fixed distance by optical tweezers perform thermal fluctuations that are correlated via the surrounding fluid [15, 179].

Due to their long-range nature and many-body character, hydrodynamic interactions trigger a large zoo of interesting and fascinating collective phenomena,

in particular when particles are driven far from equilibrium. For instance, they give rise to periodic or almost periodic motions in time [37, 121, 222] or even transient chaotic dynamics in sedimenting clusters comprised of few spherical particles [84, 120].

Hydrodynamic interactions also lead to pattern formation by self-assembly of rotating colloidal motors [101, 150]. Experiments with magnetized disks floating in a liquid-air interface and rotating under the influence of a rotating external magnetic field reveal spontaneous pattern formation by dynamic self-assembly [101]. Theoretical studies suggest that the hydrodynamic coupling of rotational motions induces repulsive forces between rotating particles [150]. This may generate microvortex assemblies that are reminiscent of a Wigner crystal, with a possible two-dimensional melting transition. Such a scenario might occur in active membranes, i.e., membranes in which biological motors (e.g., ATP-synthase) are embedded.

It was demonstrated by simulations that the aggregation or microphase separation of colloids look qualitatively different depending on whether hydrodynamic interactions are included or not [231, 232]. During the microphase separation of block copolymers, the hydrodynamic flow can help the system to overcome barriers and provide a new and smooth kinetic pathway to equilibrium, whereas without hydrodynamic interactions, the system gets trapped in a metastable state [99]. In a similar way, the collapse of a polymer to a spherical globule occurs more smoothly and homogeneously along the chain owing to the coupling to the surrounding solvent; without hydrodynamic interactions, a rapid formation of local blobs connected by linear chain segments is observed [39, 130]. In this context, the interesting question has arisen whether hydrodynamic interactions affect the early stages in the process of protein folding in aqueous solution. As shape influences the dynamics, hydrodynamic interactions may affect the hierarchical ordering processes [232].

Swimming motions of microorganisms also occur at low Reynolds numbers [199]. Thus, they are subject to hydrodynamic interactions, too. There is both experimental and theoretical evidence that the undulating tails of adjacent spermatozoa, for instance, move in phase due to hydrodynamic coupling [23, 233]. Recent experiments with spermatozoa swimming at a planar surface reveal self-organization into a hexagonal array of dynamic vortices formed by circling cells [204]. In analogy, it has been suggested that hydrodynamic interactions may also play a governing role in the motility of bacterial cells that swim by cranking a bundle of helical flagellar filaments [23]. In fact, the effect of bundling was demonstrated in macroscopic-scale experiments by rotating stiff helical wires in highly viscous silicone oil [131, 163].

As a further biological example, the surfaces of many epithelial cells in the body are covered with cilia beating in synchrony to transport fluid. This phenomenon called metachronism is thought to be mediated by the hydrodynamic coupling of the individual cilia, as several numerical studies indicate [102, 103,

146, 239]. The hydrodynamic flow generated by cilia plays a key role during the morphogenesis of higher organisms. The beating of nodal cilia generates a fluid flow to one side of the cell, which breaks the left-right symmetry of the vertebrate body plan [71, 188, 189, 227].

All these examples strikingly demonstrate that hydrodynamic interactions give rise to many intriguing phenomena that are of relevance in both fundamental and applied sciences, ranging from material sciences to biology.

1.3 Outline of this thesis

We present analytical work and simulation results for several micron-scale colloidal and biological systems whose dynamics is predominantly governed by hydrodynamic interactions. In Part A, we lay a thorough theoretical basis of hydrodynamic interactions and introduce the concepts of Stokesian and Brownian dynamics. Parts B–D present the results of three distinct projects and can thus be read separately. Each part opens with a detailed introduction to the respective topic and closes with a short summary and conclusion of the results.

Part B deals with hydrodynamic interactions in two-point microrheology, a method to explore the viscoelastic behavior of soft materials (such as biological tissue) on the micron scale. We consider the overdamped motion of two birefringent colloidal beads immersed in a Newtonian fluid. The particles are assumed to be trapped by optical tweezers with respect to both their position and orientation. On the basis of a Langevin description of this system, we analyze the thermal fluctuations and obtain a rich spectrum of correlation functions. In particular, we focus on the rotational degrees of freedom and how they couple to translation, thus extending recent investigations restricted to translational correlations [15, 179]. An important feature of our system is the self-coupling of translation and rotation of one particle mediated by the neighboring particle. It thus shows a characteristic time delay that is clearly visible in the appropriate self-correlation function. Finally, we compare our analytical results with correlation functions determined both from Brownian-dynamics simulations that we performed and from available experimental data [172].

In Part C, we study the dynamics of spherical particles circling in a ring-shaped harmonic trap. Hydrodynamic interactions completely determine their characteristic collective behavior. At first, the particles are driven by constant forces. A linear stability analysis for regular clusters of circling particles is performed, and we illustrate the periodic limit cycle to which the system converges. We clarify that drafting of particle doublets is essential to interpret this limit cycle. When we apply a spatially periodic sawtooth potential along the circular trap, in addition to the constant force, we find a novel caterpillar-like motional sequence that is dominated by the long-range hydrodynamic interactions and that promotes the surmounting of potential barriers by the particles. Our numerical

findings are in good agreement with experiments [160]. Such collective effects in sawtooth potentials may also be relevant in thermal ratchets that are commonly used to describe, e.g., biological motors [9, 126, 185].

The issue of Part D is locomotion of microorganisms. As already mentioned, many types of bacteria use several rotating helical flagella to swim. Typically, the flagellar filaments form bundles, which means that their rotations must be synchronized. The central question of our study is whether hydrodynamic interactions are capable of such a synchronization. In a first approach, we consider two stiff helices that are modeled by rigidly connected beads, neglecting any elastic deformations. They are driven by constant and equal torques, and they are fixed in space by anchoring their ends in harmonic traps. For finite anchoring strength, we do indeed observe a synchronization of the helix rotations. However, the speed of phase synchronization decreases with increasing trap stiffness, and in the limit of infinite trap stiffness, the helices do not synchronize. This leads to the conclusion that some kind of flexibility is essential. Thus, as a second step, we refine our model and consider elastic deformations of the helices within the nontrivial theory of helical elastic rods. Again, we observe that the rotations of the two helices are synchronized. In particular, the additional flexibility of the helices further increases the synchronization speed. Besides the phase locking of the helices, we furthermore observe the "onset" of flagellar bundling.

A Hydrodynamic interactions ■ Theoretical concepts and simulation methods

Abstract ■ Hydrodynamic interactions play an important role whenever two or more particles move in a viscous fluid. Due to their long-range nature, they govern the dynamics of colloidal suspensions. In this part, we introduce theoretical approaches to describe hydrodynamic interactions. In particular, we shall concentrate on Stokesian dynamics, based on the concept of mobility matrices, and its numerical implementation for simulations. By adding thermal noise mimicking the coupling of the particles to the solvent as a heat bath, we extend this formalism to Brownian dynamics. We discuss in detail the properties of the resulting stochastic differential equation, known as Langevin equation, and its numerical implementation.

2 Stokesian dynamics

Descriptions of the dynamics of colloids have to include the effect of the solvent that transmits hydrodynamic forces between the suspended particles, the so-called *hydrodynamic interactions*. A rigorous theoretical treatment would have to take into account the details of a molecular description of the fluid and its interactions with the colloidal particles. However, as the latter are much larger than the solvent molecules, the fluid can be considered to be continuous on the length scale of the suspended particles. So, in principle, if the spatial distribution of the particles is given as well as their motions, one has "just" to solve a well-defined boundary-value problem for the Navier-Stokes equation describing the flow field. This computational task, however, is extremely time-consuming. Therefore, different (mathematically equivalent) numerical techniques have been developed in recent years to tackle that problem.

One family of simulation methods are coarse-grained molecular-dynamics techniques, such as dissipative-particle dynamics [115], stochastic-rotation dynamics [119], multiparticle-collision dynamics [168], or the lattice-Boltzmann technique [144]. These concepts determine the flow dynamics by means of "effective" fluid particles (i.e., on a larger scale than the single solvent molecules but still much smaller than the colloidal particles) satisfying the fundamental balance equations of continuum theory. An alternative approach that calculates the flow dynamics from continuum theory but avoids rigid boundaries (thus saving computation time) is the concept of fluid-particle dynamics [231], which treats the colloids as "soft" particles, i.e., as a fluid volume but with a much higher viscosity than the solvent.

While all the aforementioned techniques calculate the flow field explicitly, the concept of *Stokesian dynamics* [31] follows a different path. This molecular-dynamics-like approach solves Newton's equations of motion for the colloidal particles only. Their hydrodynamic coupling through the fluid flow is taken into account by the *mobility matrix* (or its inverse, the friction matrix), which is the central element of the theory and constitutes the relation between the particle velocities and the hydrodynamic friction forces and torques. At low Reynolds number, this relation is linear, and analytic expressions for the mobility matrix as a function of the particle configuration can be obtained by means of perturbation expansions (in the inverse particle distances).

Stokesian dynamics is the concept applied in the present work. In the following, we will introduce the essentials of the theory as well as the numerical simulation methods.

2.1 Hydrodynamic equations

2.1.1 Continuity equation and incompressibility

The mass density $\rho(\boldsymbol{r},t)$ of a fluid, varying in space and time, is related to the flow field $\boldsymbol{u}(\boldsymbol{r},t)$ by the continuity equation [60, 148, 190]

$$\frac{\partial\rho}{\partial t}+\nabla\cdot(\rho\boldsymbol{u})=0\,, \tag{2.1}$$

as matter is neither created nor destroyed. It balances the local change of the fluid density inside an arbitrary volume with the flux of mass (given by the term $\rho\boldsymbol{u}$) through the surface of the volume. For an incompressible fluid, as realized by water to a good approximation, the mass density is constant in space and time, i.e., $\rho(\boldsymbol{r},t)=\rho$. According to the continuity equation (2.1), the flow field must then satisfy the relation

$$\nabla\cdot\boldsymbol{u}=0\,, \tag{2.2}$$

which is referred to as *incompressibility condition*. Incompressibility is assumed throughout this work.

2.1.2 The Navier-Stokes equation

In addition, we need the analogon of Newton's equation of motion for the fluid. The local momentum density of the fluid flow is given by $\rho\boldsymbol{u}$. Hence, for an incompressible fluid, the dynamic force balance (per unit volume) in general reads

$$\rho\,\frac{\mathrm{d}\boldsymbol{u}}{\mathrm{d}t}=\boldsymbol{f}_\mathrm{h}+\boldsymbol{f}\,, \tag{2.3}$$

where $\boldsymbol{f}_\mathrm{h}(\boldsymbol{r},t)$ is the hydrodynamic force density that arises from interactions of neighboring fluid volumes moving relative to each other, and $\boldsymbol{f}(\boldsymbol{r},t)$ represents external forces acting on the fluid. The hydrodynamic forces are formally expressed in terms of the stress tensor $\boldsymbol{\sigma}$. The latter is defined such that the hydrodynamic force acting on an infinitesimally small surface element $\boldsymbol{n}\,\mathrm{d}^2r$ inside the fluid ($\boldsymbol{n}$ is the unit normal) can be written as $\boldsymbol{\sigma}\cdot\boldsymbol{n}\,\mathrm{d}^2r$ [60], where the dot symbol denotes here the product of a matrix with a vector.[1] Hence, the force

[1] In general, the dot symbol denotes the contraction of neighboring indices of tensorial quantities. For two vectors $\boldsymbol{a}$ and $\boldsymbol{b}$, the expression $\boldsymbol{a}\cdot\boldsymbol{b}=\sum_\alpha a_\alpha b_\alpha$ represents the inner product. The dot product of a matrix $\boldsymbol{A}$ and a vector $\boldsymbol{b}$ denotes the contraction to a vector with components $(\boldsymbol{A}\cdot\boldsymbol{b})_\alpha=\sum_\beta A_{\alpha\beta}b_\beta$. Inversely, the dot product of a vector $\boldsymbol{a}$ and a matrix $\boldsymbol{B}$ has to be interpreted as the vector $(\boldsymbol{a}\cdot\boldsymbol{B})_\alpha=\sum_\beta a_\beta B_{\beta\alpha}$. The dot product of two matrices $\boldsymbol{A}$ and $\boldsymbol{B}$ is given by $(\boldsymbol{A}\cdot\boldsymbol{B})_{\alpha\beta}=\sum_\gamma A_{\alpha\gamma}B_{\gamma\beta}$.

acting on an arbitrary volume element V due to interactions with the surrounding fluid is given by

$$\boldsymbol{F}_\mathrm{h} = \oint\limits_{\partial V} \mathrm{d}^2 r\, \boldsymbol{\sigma}\cdot\boldsymbol{n} = \int\limits_V \mathrm{d}^3 r\, \nabla\cdot\boldsymbol{\sigma}\,, \tag{2.4}$$

where we have used Gauss's divergence theorem to transfer the surface integral ($\boldsymbol{n}$ is the *outer* normal of the fluid volume) into a volume integral. The torque acting on V is determined from

$$\boldsymbol{T}_\mathrm{h} = \oint\limits_{\partial V} \mathrm{d}^2 r\, \boldsymbol{r}\times(\boldsymbol{\sigma}\cdot\boldsymbol{n})\,. \tag{2.5}$$

From Eq. (2.4), we identify the force density $\boldsymbol{f}_\mathrm{h} = \nabla\cdot\boldsymbol{\sigma}$ and can thus rewrite Newton's equation (2.3) as [60, 148, 190]

$$\rho\left(\frac{\partial}{\partial t} + \boldsymbol{u}\cdot\nabla\right)\boldsymbol{u} = \nabla\cdot\boldsymbol{\sigma} + \boldsymbol{f}\,, \tag{2.6}$$

where we have introduced the total time derivative $\mathrm{d}/\mathrm{d}t = \partial/\partial t + \boldsymbol{u}\cdot\nabla$ (also called substantive derivative). Note that the acceleration $\mathrm{d}\boldsymbol{u}/\mathrm{d}t$ of a small fluid volume does not only originate from the explicit time dependence of $\boldsymbol{u}(\boldsymbol{r},t)$, but also from the change of the velocity due to the motion of the fluid volume to a different region, represented by the convective term $(\boldsymbol{u}\cdot\nabla)\boldsymbol{u}$.

There are two types of contributions to the stress tensor $\boldsymbol{\sigma}$. A static contribution originates from gradients in the hydrodynamic pressure p. The corresponding force density is $-\nabla p$, which can also be written as $\nabla\cdot(-p\mathbf{1})$, where $\mathbf{1}$ is the unit tensor. Furthermore, there are viscous forces that stem from the relative motion of neighboring fluid elements. If the velocity gradients are not too large, these forces are linear in the first-order derivatives $\nabla\boldsymbol{u}$ and $\nabla\cdot\boldsymbol{u}$, where $\nabla\boldsymbol{u}$ is the tensor gradient with components $(\nabla\boldsymbol{u})_{\alpha\beta} = (\partial/\partial r_\alpha)u_\beta$. For incompressible fluids, $\nabla\cdot\boldsymbol{u} = 0$ [Eq. (2.2)]. Furthermore, assuming an isotropic fluid (composed of "spherical" molecules), the only remaining term is the symmetric combination $\nabla\boldsymbol{u} + (\nabla\boldsymbol{u})^\mathrm{T}$ [60, 148], where the superscript T denotes the transpose of a second-rank tensor. The complete hydrodynamic stress tensor is then given by

$$\boldsymbol{\sigma} = -p\mathbf{1} + \eta\left[\nabla\boldsymbol{u} + (\nabla\boldsymbol{u})^\mathrm{T}\right]\,. \tag{2.7}$$

The prefactor η is the (dynamic) *viscosity*, which is specific to each material. Fluids that can be described by this constitutive equation are called *Newtonian fluids*. Combining Eqs. (2.7) and (2.6), we finally end up with the well-known *Navier-Stokes equation*, which for incompressible fluids reads [60, 148, 190]

$$\rho\left(\frac{\partial}{\partial t} + \boldsymbol{u}\cdot\nabla\right)\boldsymbol{u} = \eta\nabla^2\boldsymbol{u} - \nabla p + \boldsymbol{f}\,. \tag{2.8}$$

2.1.3 The Reynolds number

The various terms in the Navier-Stokes equation (2.8) can be very different in magnitude depending on the hydrodynamic problem being considered. In the present work, we are interested in the flow around small particles that are suspended in the fluid. They have a characteristic linear dimension a (e.g., the particle radius) and move with a typical velocity v. Introducing the rescaled variables $\boldsymbol{r}' = \boldsymbol{r}/a$, $\boldsymbol{u}' = \boldsymbol{u}/v$, and $t' = t/\tau$, we obtain the dimensionless Navier-Stokes equation

$$\frac{\rho a^2}{\eta\tau}\frac{\partial \boldsymbol{u}'}{\partial t'} + \mathrm{Re}\,(\boldsymbol{u}'\cdot\nabla')\boldsymbol{u}' = \nabla'^2\boldsymbol{u}' - \nabla' p' + \boldsymbol{f}', \tag{2.9}$$

where the rescaled pressure and force are $p' = p/(\eta v/a)$ and $\boldsymbol{f}' = \boldsymbol{f}/(\eta v/a^2)$, respectively. The characteristic time scale τ will be specified below. The dimensionless factor Re introduced here is the *Reynolds number*, which is defined as [60, 148]

$$\mathrm{Re} = \frac{\rho v a}{\eta}\,. \tag{2.10}$$

This factor can be interpreted as follows. The viscous forces $\eta\nabla^2\boldsymbol{u}$ (per unit volume) are of order $\eta v/a^2$, while the inertial forces $\rho(\boldsymbol{u}\cdot\nabla)\boldsymbol{u}$ scale as $\rho v^2/a$. Hence, the Reynolds number measures the ratio of inertial to viscous forces. Note that only the ratio η/ρ of the material parameters enters the dimensionless Navier-Stokes equation (2.9). This ratio is also known as the kinematic viscosity, denoted by the symbol ν.

2.1.4 The Stokes equations

The previous discussion shows that the convective term $(\boldsymbol{u}\cdot\nabla)\boldsymbol{u}$ in the Navier-Stokes equation (2.8) can be neglected at low Reynolds numbers ($\mathrm{Re} \ll 1$), and we obtain the linear relation

$$\rho\frac{\partial \boldsymbol{u}}{\partial t} = \nabla^2\boldsymbol{u} - \nabla p + \boldsymbol{f}\,. \tag{2.11}$$

Due to linearity, the flow described by this equation is laminar and does not feature turbulent behavior. Furthermore, the superposition principle is valid. In colloidal systems, the Reynolds number covers typically the range from 10^{-3} (e.g., diffusion of micron-sized particles in water at room temperature) down to 10^{-5} (swimming microorganisms as, e.g., bacteria). In these systems, $\mathrm{Re} \approx 0$ is thus a reasonable approximation.

So far, we have not yet speficied the time scale τ that is relevant for the dynamics to be considered [see Eq. (2.9)]. One inherent time scale in the dynamics of colloids is the time that a particle takes to lose its initial momentum due to

friction with the fluid, denoted by τ_m. The equation of motion for a particle with mass m and friction coefficient ζ, $m\dot{v} + \zeta v = 0$, yields the momentum relaxation time

$$\tau_\mathrm{m} = \frac{m}{\zeta}\,. \tag{2.12}$$

Anticipating that the friction coefficient of a spherical particle with radius a is given by the Stokes value $\zeta = 6\pi\eta a$ (see Sect. 2.2.1), we can rewrite Eq. (2.9) for $\mathrm{Re} \ll 1$ as

$$\frac{9}{2}\,\frac{\rho}{\rho_\mathrm{p}}\,\frac{\tau_\mathrm{m}}{\tau}\,\frac{\partial \boldsymbol{u}'}{\partial t'} = \nabla'^2\boldsymbol{u}' - \nabla' p' + \boldsymbol{f}', \tag{2.13}$$

where $\rho_\mathrm{p} = m/(\frac{4}{3}\pi a^3)$ is the mass density of the suspended particle. For colloids, the momentum relaxation time τ_m ranges from 1 to 100 ns (for particles of size $a \approx 0.1$ to 1 μm with density $\rho_\mathrm{p} \approx \rho_{\mathrm{H_2O}}$ in a solvent with viscosity $\eta \approx \eta_{\mathrm{H_2O}}$). The typical time scales, however, that are relevant in experiments with colloids range from 1 ms to 1 s, hence $\tau \gg \tau_\mathrm{m}$. Furthermore, we can assume $\rho_\mathrm{p} \approx \rho$ in most cases.

Thus, at low Reynolds numbers and on typical colloidal time scales, the momenta of the particles are in equilibrium with the surrounding fluid, and we can completely neglect the inertial terms on the left-hand side of Eq. (2.8). The *overdamped* fluid dynamics is then well described by the stationary[2] *Stokes equations* (also known as *creeping-flow equations*) [60, 106]

$$\eta\nabla^2\boldsymbol{u} - \nabla p + \boldsymbol{f} = \boldsymbol{0}\,, \tag{2.14a}$$

$$\nabla\cdot\boldsymbol{u} = 0\,, \tag{2.14b}$$

where Eq. (2.14b) is just again the condition of incompressibility [Eq. (2.2)]. This is the regime that we exclusively consider in this work.[3]

It is an interesting fact to note that the Stokes equations can be derived from a variational principle where one searches for an extremum of the energy dissipated by the fluid flow [76, 147]. The pressure enters as the Lagrange parameter associated with the constraint of incompressibility.

2.2 Translation and rotation of a single sphere

In this section, we briefly summarize the well-known Stokes problem, i.e., the translational and rotational steady motion of a single sphere in a Newtonian fluid

[2] Note that, although the Stokes equations are stationary, the flow field may nevertheless vary in time due to (i) time-dependent forces $\boldsymbol{f}(\boldsymbol{r}, t)$ or (ii) moving boundaries (such as the surfaces of suspended particles).

[3] The overdamped regime of creeping flow is also known as *Aristotelian* dynamics (in contrary to Newtonian dynamics where inertia plays a role).

(for details of the derivation from the Stokes equations, see, e.g., Refs. [60, 148]). This consideration reveals the long-range nature of flow fields generated by motions of suspended particles, which actually causes the long-range hydrodynamic interactions in colloids.

2.2.1 Translation

Consider a single sphere with radius a translating with velocity $\boldsymbol{v}$ in an unbounded fluid which is at rest at infinity. Assuming stick-boundary conditions on the particle surface, the corresponding solution of the Stokes equations (2.14) for the flow field reads

$$\boldsymbol{u}(\boldsymbol{r},t) = \boldsymbol{A}(\boldsymbol{r}-\boldsymbol{v}t)\cdot\boldsymbol{v}\,, \tag{2.15a}$$

where

$$\boldsymbol{A}(\boldsymbol{r}) = \frac{3}{4}\frac{a}{r}\,(\mathbf{1}+\hat{\boldsymbol{r}}\hat{\boldsymbol{r}}) + \frac{1}{4}\left(\frac{a}{r}\right)^3(\mathbf{1}-3\,\hat{\boldsymbol{r}}\hat{\boldsymbol{r}}) \tag{2.15b}$$

(with the initial condition that the sphere is at $\boldsymbol{r}=\mathbf{0}$ for $t=0$). Here, $r=|\boldsymbol{r}|$ and $\hat{\boldsymbol{r}}=\boldsymbol{r}/r$, and the dyadic product[4] $\hat{\boldsymbol{r}}\hat{\boldsymbol{r}}$ projects onto direction $\hat{\boldsymbol{r}}$. As we are in the overdamped regime, the force $\boldsymbol{F}$ needed to drive the particle at constant velocity $\boldsymbol{v}$ is exactly balanced by the force $\boldsymbol{F}_\mathrm{h}$ that the fluid exerts on the particle. Therefore, using Eq. (2.4) with the stress tensor (2.7) calculated for the flow field (2.15), we finally obtain the Stokes law

$$\boldsymbol{F} = -\boldsymbol{F}_\mathrm{h} = \zeta^\mathrm{t}\boldsymbol{v} \tag{2.16}$$

with

$$\zeta^\mathrm{t} = \frac{1}{\mu^\mathrm{t}} = 6\pi\eta a\,. \tag{2.17}$$

The constants ζ^t and μ^t are, respectively, the single-particle friction and mobility coeffient for a translating sphere.

2.2.2 Rotation

Now, consider a sphere rotating with angular velocity $\boldsymbol{\omega}$. The resulting flow field at position $\boldsymbol{r}$ (the sphere being at $\boldsymbol{r}=\mathbf{0}$) is then

$$\boldsymbol{u}(\boldsymbol{r}) = \left(\frac{a}{r}\right)^3\boldsymbol{\omega}\times\boldsymbol{r}\,. \tag{2.18}$$

[4] The dyadic product of two vectors $\boldsymbol{a}$ and $\boldsymbol{b}$, denoted by $\boldsymbol{ab}$, yields a second-rank tensor with components $(\boldsymbol{ab})_{\alpha\beta} = a_\alpha b_\beta$. Accordingly, the dot product of a dyad with a vector is given by $\boldsymbol{ab}\cdot\boldsymbol{c} = \boldsymbol{a}(\boldsymbol{b}\cdot\boldsymbol{c})$ and $\boldsymbol{a}\cdot\boldsymbol{bc} = (\boldsymbol{a}\cdot\boldsymbol{b})\boldsymbol{c}$.

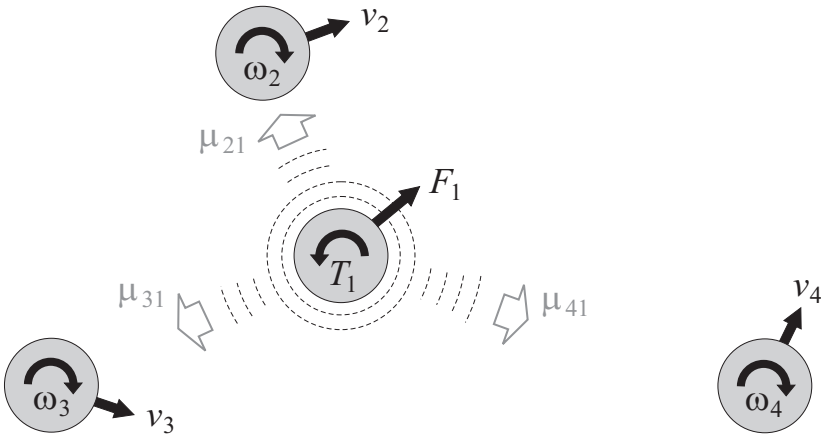

Figure 2.1 ■ Suspended particles moving in a viscous fluid, subject to external forces $\boldsymbol{F}_i$ and torques $\boldsymbol{T}_i$. The translational and rotational motions (with velocities $\boldsymbol{v}_i$ and $\boldsymbol{\omega}_i$, respectively) are all mutually coupled via the surrounding flow field.

Using Eq. (2.5), the torque needed to drive the particle at constant rotational speed $\boldsymbol{\omega}$ is given by

$$\boldsymbol{T} = -\boldsymbol{T}_\mathrm{h} = \zeta^\mathrm{r}\boldsymbol{\omega} \tag{2.19}$$

with

$$\zeta^\mathrm{r} = \frac{1}{\mu^\mathrm{r}} = 8\pi\eta a^3\,. \tag{2.20}$$

2.3 Hydrodynamic interactions

Particles moving in a viscous fluid create a flow field around themselves through which their motions are mutually coupled (Fig. 2.1). Hence, these so-called *hydrodynamic interactions* constitute a complex many-body problem. The results of the previous section show that the perturbations of the fluid due to translations and rotations of suspended particles are of *long range* and so are the resulting interactions between the particles.[5]

2.3.1 Theoretical description and definitions

We consider the motion of N colloidal particles suspended in an unbounded and otherwise quiescent viscous fluid at low Reynolds number. Furthermore, we neglect inertial effects, i.e., we are interested in time scales larger than the momentum relaxation time (see discussion in Sect. 2.1.4). Thus, the interactions can

[5]Comparing the asymptotic behavior of the respective flow fields (2.15) and (2.18), we see that rotational perturbations of the fluid decay faster ($|\boldsymbol{u}(\boldsymbol{r})| \propto 1/r^2$) than translational ones ($|\boldsymbol{u}(\boldsymbol{r})| \propto 1/r$ for $r \gg a$).

be considered to be instantaneous. Due to the linearity of the Stokes equations (2.14), the translational and rotational velocities ($\boldsymbol{v}_i$ and $\boldsymbol{\omega}_i$) depend linearly on all external forces and torques ($\boldsymbol{F}_j$ and $\boldsymbol{T}_j$) acting on the particles (Fig. 2.1) [32, 106]:

$$\boldsymbol{v}_i = \sum_j (\boldsymbol{\mu}_{ij}^{\mathrm{tt}} \cdot \boldsymbol{F}_j + \boldsymbol{\mu}_{ij}^{\mathrm{tr}} \cdot \boldsymbol{T}_j)\,, \tag{2.21a}$$

$$\boldsymbol{\omega}_i = \sum_j (\boldsymbol{\mu}_{ij}^{\mathrm{rt}} \cdot \boldsymbol{F}_j + \boldsymbol{\mu}_{ij}^{\mathrm{rr}} \cdot \boldsymbol{T}_j)\,, \tag{2.21b}$$

where the particle indices i and j run from 1 to N. The essential quantities constituting the coupling of translations and rotations (denoted by superscripts t and r) are the Cartesian 3×3 *mobility tensors* $\boldsymbol{\mu}_{ij}^{\mathrm{tt}}$, $\boldsymbol{\mu}_{ij}^{\mathrm{tr}}$, $\boldsymbol{\mu}_{ij}^{\mathrm{rt}}$, and $\boldsymbol{\mu}_{ij}^{\mathrm{rr}}$. In general, they are functions of the complete spatial configuration of all N particles, i.e., both positions and orientations. For spherical particles, they depend on the positional coordinates $\{\boldsymbol{r}_i\}$ only.

Introducing the generalized $6N$-dimensional velocity vector $\mathbf{v} = [\boldsymbol{v}_1, \ldots, \boldsymbol{v}_N, \boldsymbol{\omega}_1, \ldots, \boldsymbol{\omega}_N]$ and the force vector $\mathbf{f} = [\boldsymbol{F}_1, \ldots, \boldsymbol{F}_N, \boldsymbol{T}_1, \ldots, \boldsymbol{T}_N]$, Eqs. (2.21) can be written in compact form as

$$\mathbf{v} = \mathbf{M} \cdot \mathbf{f} \tag{2.22}$$

with the generalized $6N \times 6N$ mobility matrix

$$\mathbf{M} = \begin{bmatrix} \boldsymbol{\mu}_{11}^{\mathrm{tt}} & \cdots & \boldsymbol{\mu}_{1N}^{\mathrm{tt}} & \boldsymbol{\mu}_{11}^{\mathrm{tr}} & \cdots & \boldsymbol{\mu}_{1N}^{\mathrm{tr}} \\ \vdots & \ddots & \vdots & \vdots & \ddots & \vdots \\ \boldsymbol{\mu}_{N1}^{\mathrm{tt}} & \cdots & \boldsymbol{\mu}_{NN}^{\mathrm{tt}} & \boldsymbol{\mu}_{N1}^{\mathrm{tr}} & \cdots & \boldsymbol{\mu}_{NN}^{\mathrm{tr}} \\ \boldsymbol{\mu}_{11}^{\mathrm{rt}} & \cdots & \boldsymbol{\mu}_{1N}^{\mathrm{rt}} & \boldsymbol{\mu}_{11}^{\mathrm{rr}} & \cdots & \boldsymbol{\mu}_{1N}^{\mathrm{rr}} \\ \vdots & \ddots & \vdots & \vdots & \ddots & \vdots \\ \boldsymbol{\mu}_{N1}^{\mathrm{rt}} & \cdots & \boldsymbol{\mu}_{NN}^{\mathrm{rt}} & \boldsymbol{\mu}_{N1}^{\mathrm{rr}} & \cdots & \boldsymbol{\mu}_{NN}^{\mathrm{rr}} \end{bmatrix}. \tag{2.23}$$

The inversion of this relation yields the generalized friction law

$$\mathbf{f} = -\mathbf{f}_{\mathrm{h}} = \mathbf{Z} \cdot \mathbf{v} \quad \text{with} \quad \mathbf{Z} = \mathbf{M}^{-1}\,, \tag{2.24}$$

where $\mathbf{f}_{\mathrm{h}}$ are the hydrodynamic friction forces and torques, counteracting and compensating the driving forces and torques $\mathbf{f}$. The friction matrix $\mathbf{Z}$ has the same structure as the mobility matrix $\mathbf{M}$ [see Eq. (2.23)] and is composed of the 3×3 friction tensors $\boldsymbol{\zeta}_{ij}^{\mathrm{tt}}$, $\boldsymbol{\zeta}_{ij}^{\mathrm{tr}}$, $\boldsymbol{\zeta}_{ij}^{\mathrm{rt}}$, and $\boldsymbol{\zeta}_{ij}^{\mathrm{rr}}$. According to the reciprocal theorem of Lorentz [106], the mobility tensors obey the symmetry relations

$$(\boldsymbol{\mu}_{ij}^{\mathrm{tt}})^{\mathrm{T}} = \boldsymbol{\mu}_{ji}^{\mathrm{tt}}\,, \quad (\boldsymbol{\mu}_{ij}^{\mathrm{rr}})^{\mathrm{T}} = \boldsymbol{\mu}_{ji}^{\mathrm{rr}}\,, \quad (\boldsymbol{\mu}_{ij}^{\mathrm{tr}})^{\mathrm{T}} = \boldsymbol{\mu}_{ji}^{\mathrm{rt}}\,, \tag{2.25}$$

which means that the entire mobility matrix is symmetric and thus also the friction matrix, i.e.,

$$\mathbf{M} = \mathbf{M}^{\mathrm{T}}\,, \quad \mathbf{Z} = \mathbf{Z}^{\mathrm{T}}\,. \tag{2.26}$$

In the overdamped regime, the power supplied to the particles by the external forces and torques,

$$P = \sum_i (\boldsymbol{F}_i \cdot \boldsymbol{v}_i + \boldsymbol{T}_i \cdot \boldsymbol{\omega}_i) = \mathbf{f} \cdot \mathbf{v} = \mathbf{f} \cdot \mathbf{M} \cdot \mathbf{f} = \mathbf{v} \cdot \mathbf{Z} \cdot \mathbf{v}\,, \tag{2.27a}$$

is completely dissipated into the fluid, and thus

$$P > 0\,. \tag{2.27b}$$

This condition must be obeyed for arbitrary $\mathbf{v}$ and $\mathbf{f}$. Therefore, the matrices $\mathbf{M}$ and $\mathbf{Z}$ are positive definite.

2.3.2 On the propagation of hydrodynamic interactions

A moving particle transfers momentum to a neighboring particle via two mechanisms occuring on different time scales [109]. At first, momentum is rapidly carried away by spherical sound waves arriving at the neighboring particle after a time $\tau_{\mathrm{s}} = r/c$, where c is the speed of sound and r the distance between the particles.[6] Then, a vortex ring develops around the particle, and the vorticity region grows diffusively. The disturbance reaches the neighboring particle after a time of order $\tau_{\mathrm{v}} = r^2/\nu$ [43], where $\nu = \eta/\rho$ is the kinematic viscosity of the fluid.[7]

On time scales significantly shorter than τ_{v}, a hydrodynamic coupling between two particles is already established, i.e., sound waves in fact do play a role, which was also confirmed experimentally [109]. However, the hydrodynamic interactions have not yet fully evolved: Instead of the asymptotic $1/r$ behavior [compare Eq. (2.15); for details, see Sect. 2.4.1], the coupling is "screened" and decays to leading order as $1/r^3$ [43, 109]; for times $t > \tau_{\mathrm{v}}$, the full interactions have developed by vorticity diffusion.

To establish the full hydrodynamic interactions, a typical time scale is $\tau_{\mathrm{v}} \approx 0.1$ ms for a particle distance of $r \approx 10$ μm [109]. Therefore, on the time scales we are interested in, hydrodynamic interactions can be indeed considered to be instantaneous.

[6] Note that for a strictly incompressible fluid, the speed of sound is infinite and thus $\tau_{\mathrm{s}} = 0$.

[7] The type of vorticity propagation can be easily derived by taking the curl $\nabla\times$ of the Navier-Stokes equation (2.8). This yields $(\partial/\partial t)(\nabla \times \boldsymbol{u}) = \nu\nabla^2(\nabla \times \boldsymbol{u})$, which has the form of a diffusion equation for the vorticity $\nabla \times \boldsymbol{u}$ with diffusion coefficient $\nu = \eta/\rho$.

2.4 Mobility matrix for configurations of beads

In the following, we discuss several methods to calculate the mobility matrix. We only consider spherical particles with equal radius a. All the concepts, however, can be easily extended to systems of spheres with different radii. Furthermore, we always assume an unbounded fluid being at rest at infinity and stick-boundary conditions on the particle surfaces.

2.4.1 The Oseen tensor

Consider a point-like particle in the fluid at position $\boldsymbol{r}_1$ subject to a force $\boldsymbol{F}_1$. The force density acting on the fluid is then given by $\boldsymbol{f}(\boldsymbol{r}) = \boldsymbol{F}_1\,\delta(\boldsymbol{r}-\boldsymbol{r}_1)$. Due to the linearity of the Stokes equations (2.14), the flow field at any point $\boldsymbol{r}$ is proportional to the external force. Hence,

$$\boldsymbol{u}(\boldsymbol{r}) = \boldsymbol{G}(\boldsymbol{r}-\boldsymbol{r}_1)\cdot\boldsymbol{F}_1\,, \tag{2.28}$$

where the 3×3 matrix $\boldsymbol{G}$ is called *Oseen tensor*. The velocity field (2.28) is also referred to as *Stokeslet* [134]. As it is the solution for a δ-inhomogeneity, the Oseen tensor is the Green function of the Stokes equations. Thus, the flow field generated by a continuously distributed force density $\boldsymbol{f}(\boldsymbol{r})$ is given by the superposition

$$\boldsymbol{u}(\boldsymbol{r}) = \int \mathrm{d}^3r'\,\boldsymbol{G}(\boldsymbol{r}-\boldsymbol{r}')\cdot\boldsymbol{f}(\boldsymbol{r}')\,. \tag{2.29}$$

Since we assume an infinitely extended fluid, the Oseen tensor must obey translational invariance and therefore can only depend on the relative coordinate $\boldsymbol{r}-\boldsymbol{r}'$. The Stokes equations (2.14) (with the boundary condition that the flow vanishes at infinity) yield [60]

$$\boldsymbol{G}(\boldsymbol{r}) = \frac{1}{8\pi\eta}\,\frac{1}{r}\,(\mathbf{1}+\hat{\boldsymbol{r}}\hat{\boldsymbol{r}})\,. \tag{2.30}$$

Consider now a second point-like particle at position $\boldsymbol{r}_2$, and assume $\boldsymbol{F}_2 = \mathbf{0}$. Then, the velocity of particle 2 is identical to the local fluid flow caused by particle 1, i.e., $\boldsymbol{v}_2 = \boldsymbol{u}(\boldsymbol{r}_2) = \boldsymbol{G}(\boldsymbol{r}_2-\boldsymbol{r}_1)\cdot\boldsymbol{F}_1$. Comparing this with Eq. (2.21a) (for vanishing torques), we obtain for the translational cross-mobility tensor

$$\boldsymbol{\mu}_{ij}^{\mathrm{tt}} = \boldsymbol{G}(\boldsymbol{r}_{ij})\,, \tag{2.31}$$

where $\boldsymbol{r}_{ij} = \boldsymbol{r}_j - \boldsymbol{r}_i$ $(i\neq j)$. As the Oseen tensor assumes point-like particles, Eq. (2.31) can be considered as the first-order term in a far-field expansion[8] for

[8] This is analogous to electrostatics where the potential at distances far from the source corresponds to the field created by a point charge.

the mobilities. This result already shows that hydrodynamic interactions are of very long range[9] since they decay asymptotically as $1/r$. The self-mobilities to this order are given by the constant single-particle Stokes coefficient (2.17) [60]: $\boldsymbol{\mu}_{ii}^{\mathrm{tt}} = \mu^{\mathrm{t}}\mathbf{1}$. Rotation does not play a role for point-like particles and is thus not considered in Oseen approximation.

Note that the Oseen tensor is no longer positive-definite if the particle separation is $\frac{3}{2}a$ or smaller,[10] which is anyway far beyond the range of validity of the asymptotic Oseen approximation. This leads to unphysical behavior of transport properties (such as negative diffusion coefficients, e.g.), which can be removed, however, by taking into account the finite radius of the beads, as discussed in the following.

2.4.2 Method of reflections: the Rotne-Prager approximation

The calculation of the flow field $\boldsymbol{u}(\boldsymbol{r})$ from the Stokes equations (2.14) as a result of the motions of suspended particles is a far too complicated boundary-value problem to be solved analytically in closed form. Instead, one way to calculate the flow and finally the mobility tensors for a given configuration of spheres is the method of reflections [60]. The idea behind this technique is to determine the flow field by iteration, where the flow field is (virtually) "reflected" from the spheres and thus bouncing from particle to particle. This yields a series of corrections to the flow field (in powers of inverse particle distances a/r_{ij}) due to the presence and motion of suspended particles.

The method of reflections is based on the Faxén theorems, which yield the velocities of a particle that is immersed in a flow field $\boldsymbol{u}(\boldsymbol{r})$, satisfying stick-boundary conditions. The Faxén theorem for translation reads [60]

$$\boldsymbol{v}_{\mathrm{p}} = \mu^{\mathrm{t}}\boldsymbol{F}_{\mathrm{p}} + \mathcal{L}_{\mathrm{F}}^{\mathrm{t}}\boldsymbol{u}(\boldsymbol{r})|_{\boldsymbol{r}=\boldsymbol{r}_{\mathrm{p}}} \quad \text{with} \quad \mathcal{L}_{\mathrm{F}}^{\mathrm{t}} = 1 + \frac{1}{6}\,a^2\nabla^2\,, \tag{2.32}$$

where the second term is evaluated at the center of the particle, denoted by $\boldsymbol{r}_{\mathrm{p}}$.[11] Note that without incident flow field ($\boldsymbol{u} = \mathbf{0}$), we recover the Stokes friction law for translation (2.16) with the driving force $\boldsymbol{F}_{\mathrm{p}}$. For rotational motion, the Faxén

[9] Note that the long range arises from low-Reynolds-number flow, neglecting the convective term in the Navier-Stokes equation. At very large distances, however, this term must be taken into account. This actually yields a natural cutoff in the effective range of hydrodynamic interactions, which is estimated as $r/a \approx \mathrm{Re}^{-1}$ [58].

[10] Determining the eigenvalues of the mobility matrix in Oseen approximation, we obtain the condition $r_{ij} > \frac{3}{2}a$ if we require all eigenvalues to be positive. Hence, the mobility matrix is not positive-definite only when the particles already overlap.

[11] Note that the Faxén theorems are exact relations although they are derived by Taylor expansion of the flow field about the particle center $\boldsymbol{r}_{\mathrm{p}}$. This is due to the fact that $\boldsymbol{u}(\boldsymbol{r})$ is a biharmonic function, i.e., $\nabla^2\nabla^2\boldsymbol{u} = \mathbf{0}$, which follows from the Stokes equations (2.14). Therefore (and due to rotational symmetry), all derivatives of higher order than ∇^2 vanish at $\boldsymbol{r} = \boldsymbol{r}_{\mathrm{p}}$.

theorem reads [60]

$$\boldsymbol{\omega}_\mathrm{p} = \mu^\mathrm{r}\boldsymbol{T}_\mathrm{p} + \mathcal{L}^\mathrm{r}_\mathrm{F}\boldsymbol{u}(\boldsymbol{r})|_{\boldsymbol{r}=\boldsymbol{r}_\mathrm{p}} \quad \text{with} \quad \mathcal{L}^\mathrm{r}_\mathrm{F} = \frac{1}{2}\nabla\times \ , \tag{2.33}$$

where the formal notation $\nabla\times$ represents the tensor-like operator with Cartesian components $(\nabla\times)_{\alpha\beta} = -\sum_\gamma \varepsilon_{\alpha\beta\gamma}\nabla_\gamma$ (with $\varepsilon_{\alpha\beta\gamma}$ being the Levi-Civita tensor, $\alpha,\beta,\gamma = 1,2,3$ or x,y,z).[12] Note that Eq. (2.33) reproduces the Stokes law for rotation (2.19) with driving torque $\boldsymbol{T}_\mathrm{p}$ in the case $\boldsymbol{u} = \boldsymbol{0}$.

Assume now that particle i is subject to an external force $\boldsymbol{F}_i$ and torque $\boldsymbol{T}_i$. Then, to zeroth order, it moves with velocities

$$\boldsymbol{v}_i^0 = \mu^\mathrm{t}\boldsymbol{F}_i \,, \tag{2.34a}$$

$$\boldsymbol{\omega}_i^0 = \mu^\mathrm{r}\boldsymbol{T}_i \,, \tag{2.34b}$$

and it creates a flow field $\boldsymbol{u}^0(\boldsymbol{r})$ that is the superposition of Eqs. (2.15) and (2.18) with $\boldsymbol{v} = \boldsymbol{v}_i^0$ and $\boldsymbol{\omega} = \boldsymbol{\omega}_i^0$. This, in turn, influences the motion of a neighboring particle j. Its velocities including those caused by the flow field $\boldsymbol{u}^0(\boldsymbol{r})$ follow directly from the Faxén laws (2.32) and (2.33):

$$\boldsymbol{v}_j^1 = \mu^\mathrm{t}\boldsymbol{F}_j + \mathcal{L}^\mathrm{t}_\mathrm{F}\boldsymbol{u}^0(\boldsymbol{r})|_{\boldsymbol{r}=\boldsymbol{r}_j} \,, \tag{2.35a}$$

$$\boldsymbol{\omega}_j^1 = \mu^\mathrm{r}\boldsymbol{T}_j + \mathcal{L}^\mathrm{r}_\mathrm{F}\boldsymbol{u}^0(\boldsymbol{r})|_{\boldsymbol{r}=\boldsymbol{r}_j} \,. \tag{2.35b}$$

This motion generates an additional flow field $\boldsymbol{u}^1(\boldsymbol{r})$, following from Eqs. (2.15) and (2.18) with $\boldsymbol{v} = \boldsymbol{v}_j^1$ and $\boldsymbol{\omega} = \boldsymbol{\omega}_j^1$. The "incident" flow $\boldsymbol{u}^0(\boldsymbol{r})$ is said to be "reflected" by sphere j. The total flow field $\boldsymbol{u}^0(\boldsymbol{r}) + \boldsymbol{u}^1(\boldsymbol{r})$ satisfies the stick-boundary conditions on the surface of particle j when it translates with velocity $\boldsymbol{v}_j^1$ and rotates with velocity $\boldsymbol{\omega}_j^1$.

The stick-boundary conditions on the surface of particle i, however, are now (slightly) violated, which has to be corrected by a succeeding iteration step. The corrections to the velocities of particle i due to the additional flow field $\boldsymbol{u}^1(\boldsymbol{r})$ are given by the Faxén laws (2.32) and (2.33) with $\boldsymbol{F}_\mathrm{p}$ and $\boldsymbol{T}_\mathrm{p}$ set equal to zero, since the Stokesian velocities ($\boldsymbol{v}_\mathrm{p} = \mu^\mathrm{t}\boldsymbol{F}_\mathrm{p}$ and $\boldsymbol{\omega}_\mathrm{p} = \mu^\mathrm{r}\boldsymbol{T}_\mathrm{p}$) have already been accounted for in Eq. (2.34). Hence, the velocity corrections are calculated from

$$\boldsymbol{v}_i^2 = \mathcal{L}^\mathrm{t}_\mathrm{F}\boldsymbol{u}^1(\boldsymbol{r})|_{\boldsymbol{r}=\boldsymbol{r}_i} \,, \tag{2.36a}$$

$$\boldsymbol{\omega}_i^2 = \mathcal{L}^\mathrm{r}_\mathrm{F}\boldsymbol{u}^1(\boldsymbol{r})|_{\boldsymbol{r}=\boldsymbol{r}_i} \,, \tag{2.36b}$$

which create a further contribution $\boldsymbol{u}^2(\boldsymbol{r})$ to the fluid flow. Continuing this iterative procedure, we obtain the series expansion

$$\boldsymbol{u}(\boldsymbol{r}) = \boldsymbol{u}^0(\boldsymbol{r}) + \boldsymbol{u}^1(\boldsymbol{r}) + \boldsymbol{u}^2(\boldsymbol{r}) + \cdots \tag{2.37}$$

[12] This simply means that, acting on a vector $\boldsymbol{a}$, the operator $\nabla\times$ yields the derivative $\nabla\times\boldsymbol{a}$.

of the exact solution for the flow field (in powers of the inverse particle distance a/r_{ij}), where the level of accuracy increases with each step of iteration. The corresponding series expansions for the particle velocities are

$$\boldsymbol{v}_i = \boldsymbol{v}_i^0 + \boldsymbol{v}_i^2 + \cdots \quad \text{and} \quad \boldsymbol{v}_j = \boldsymbol{v}_j^1 + \boldsymbol{v}_j^3 + \cdots , \tag{2.38a}$$

$$\boldsymbol{\omega}_i = \boldsymbol{\omega}_i^0 + \boldsymbol{\omega}_i^2 + \cdots \quad \text{and} \quad \boldsymbol{\omega}_j = \boldsymbol{\omega}_j^1 + \boldsymbol{\omega}_j^3 + \cdots . \tag{2.38b}$$

It can be shown that this iterative scheme is convergent [158].[13] The resulting linear relations between the translational and rotational velocities and the external forces and torques then directly yield the complete set of mobility tensors [see Eq. (2.21)].

Striktly speaking, the above presentation of the method of reflections refers to the interactions between *two* spheres. For more than two particles, we additionally have to account for the case that the flow field reflected at particle j does not only have an effect on the original particle i, but on all other particles as well, which leads to *many-body* interactions.

The first iteration step (2.35) with the flow field $\boldsymbol{u}^0(\boldsymbol{r}) = \boldsymbol{A}(\boldsymbol{r} - \boldsymbol{r}_i) \cdot \boldsymbol{v}_i^0$ [see Eq. (2.15)] yields expressions for the mobilities that are exact up to order $(a/r_{ij})^3$, which is the so-called *Rotne-Prager approximation* [60]:

$$\boldsymbol{\mu}_{ii}^{\mathrm{tt}} = \mu^{\mathrm{t}} \mathbf{1} \qquad + \ \mathcal{O}(4) , \tag{2.39a}$$

$$\boldsymbol{\mu}_{ij}^{\mathrm{tt}} = \mu^{\mathrm{t}} \left[\frac{3}{4} \frac{a}{r_{ij}} (\mathbf{1} + \hat{\boldsymbol{r}}_{ij} \hat{\boldsymbol{r}}_{ij}) + \frac{1}{2} \left(\frac{a}{r_{ij}} \right)^3 (\mathbf{1} - 3\, \hat{\boldsymbol{r}}_{ij} \hat{\boldsymbol{r}}_{ij}) \right] \qquad + \ \mathcal{O}(4) , \tag{2.39b}$$

$$\boldsymbol{\mu}_{ii}^{\mathrm{rr}} = \mu^{\mathrm{r}} \mathbf{1} \qquad + \ \mathcal{O}(6) , \tag{2.39c}$$

$$\boldsymbol{\mu}_{ij}^{\mathrm{rr}} = -\mu^{\mathrm{r}} \frac{1}{2} \left(\frac{a}{r_{ij}} \right)^3 (\mathbf{1} - 3\, \hat{\boldsymbol{r}}_{ij} \hat{\boldsymbol{r}}_{ij}) \qquad + \ \mathcal{O}(6) , \tag{2.39d}$$

$$\boldsymbol{\mu}_{ii}^{\mathrm{tr}} = \mathbf{0} \qquad + \ \mathcal{O}(7) , \tag{2.39e}$$

$$\boldsymbol{\mu}_{ij}^{\mathrm{tr}} = \mu^{\mathrm{r}} a \left(\frac{a}{r_{ij}} \right)^2 \hat{\boldsymbol{r}}_{ij} \times \qquad + \ \mathcal{O}(5) , \tag{2.39f}$$

where $\mathcal{O}(n)$ denotes corrections of order $(a/r_{ij})^n$ (values taken from Ref. [176]).[14] The tensors $\boldsymbol{\mu}_{ij}^{\mathrm{rt}}$ not listed follow from the symmetry relations (2.25): $\boldsymbol{\mu}_{ij}^{\mathrm{rt}} =$

[13] The Faxén theorems (2.32) and (2.33) can also be written in the inverted form yielding the forces and torques, $\boldsymbol{F}_{\mathrm{p}} = \zeta^{\mathrm{t}}[\boldsymbol{v}_{\mathrm{p}} - \mathcal{L}_{\mathrm{F}}^{\mathrm{t}} \boldsymbol{u}(\boldsymbol{r})|_{\boldsymbol{r}=\boldsymbol{r}_{\mathrm{p}}}]$ and $\boldsymbol{T}_{\mathrm{p}} = \zeta^{\mathrm{r}}[\boldsymbol{\omega}_{\mathrm{p}} - \mathcal{L}_{\mathrm{F}}^{\mathrm{r}} \boldsymbol{u}(\boldsymbol{r})|_{\boldsymbol{r}=\boldsymbol{r}_{\mathrm{p}}}]$, which could be used to calculate the friction tensors by iteration. In this case, however, the method of reflections may fail to converge [118].

[14] For systems of only two spheres, the corrections to the cross-mobilities ($i \neq j$) occur at even higher orders: $\mathcal{O}(7)$ for $\boldsymbol{\mu}_{ij}^{\mathrm{tt}}$ and $\mathcal{O}(9)$ for $\boldsymbol{\mu}_{ij}^{\mathrm{rr}}$ [122, 176, 216]; for $\boldsymbol{\mu}_{ij}^{\mathrm{tr}}$, there is a discrepancy in the literature between $\mathcal{O}(10)$ [122, 216] and $\mathcal{O}(8)$ [176].

$(\boldsymbol{\mu}_{ji}^{\mathrm{tr}})^{\mathrm{T}}$. The tensor with components $(\hat{\boldsymbol{r}}_{ij}\times)_{\alpha\beta} = -\sum_\gamma \varepsilon_{\alpha\beta\gamma}(\hat{\boldsymbol{r}}_{ij})_\gamma$ is antisymmetric, $(\hat{\boldsymbol{r}}_{ij}\times)^{\mathrm{T}} = -\hat{\boldsymbol{r}}_{ij}\times = \hat{\boldsymbol{r}}_{ji}\times$, so one finally obtains the identity $\boldsymbol{\mu}_{ij}^{\mathrm{rt}} = \boldsymbol{\mu}_{ij}^{\mathrm{tr}}$.

To be more precise, only the translational part (superscripts tt) is referred to as *Rotne-Prager tensor* [208] (also known as *Yamakawa tensor* [247]). In the following, however, we mean Eq. (2.39) as a whole when we consider the mobility matrix in "Rotne-Prager approximation". At this level, only two-body interactions play a role. Many-body interactions need more reflections to build up so that, e.g., three-particle contributions to $\boldsymbol{\mu}_{ij}^{\mathrm{tt}}$ occur at orders $(a/r_{ik})^2(a/r_{jk})^2$ and higher [60].[15] Note that the self-mobilities $\boldsymbol{\mu}_{ii}^{\mathrm{tt}}$ and $\boldsymbol{\mu}_{ii}^{\mathrm{rr}}$ are given by the respective single-particle Stokes coefficients. In particular, translation and rotation are not coupled ($\boldsymbol{\mu}_{ii}^{\mathrm{tr}} = \boldsymbol{0}$). For an isolated sphere, the well-known Magnus effect only enters via the nonlinear term in the Navier-Stokes equation [110, 209] and thus does not occur in the linear Stokes regime. In the presence of a neighboring particle, however, there indeed exists a self-coupling of translation and rotation (i.e., $\boldsymbol{\mu}_{ii}^{\mathrm{tr}} \neq \boldsymbol{0}$) that is mediated by the other particle. But since this effect needs at least two reflections, it is of higher order than $(a/r_{ij})^3$ and hence not included in the Rotne-Prager approximation.

Originally, a variational principle minimizing the energy dissipation was used to derive the Rotne-Prager tensor [208]. Thus, this approximation gives an "upper bound" to the mobilities.

2.4.3 Method of induced forces

An alternative way to calculate the mobility tensors is the *method of induced forces*. As we are not using explicit expressions originating from this method, it shall only be sketched here very briefly. However, in our simulations, we make use of the library HYDROLIB [113], a numerical implementation that calculates the mobility or friction matrix for a given configuration of equal-sized spheres in an efficient scheme based on the method of induced forces [41].

Each suspended particle, moving with translational velocity $\boldsymbol{v}_i$ and rotational velocity $\boldsymbol{\omega}_i$, exerts on the fluid a force density $\boldsymbol{f}_i(\boldsymbol{r})$ that is *induced* by the stick-boundary condition on the particle surface. Hence, we can extend the fluid formally to the volume inside the particle surfaces, representing the rigid bodies entirely in terms of the induced forces. In this picture, the solution of the Stokes equations (2.14) with stick-boundary conditions on the particle surfaces is replaced by solving the flow equations in *all* space with an additional force distribution $\boldsymbol{f}(\boldsymbol{r}) = \sum_i \boldsymbol{f}_i(\boldsymbol{r})$ [75, 125]. The force density is chosen such that the fictitious fluid inside each particle surface moves with the rigid-body velocity of the particle, thus

$$\boldsymbol{u}(\boldsymbol{r}_i + \boldsymbol{x}) = \boldsymbol{v}_i + \boldsymbol{\omega}_i \times \boldsymbol{x} \quad \text{for} \quad |\boldsymbol{x}| \leq a\,. \tag{2.40}$$

[15] Considering the inverse problem, i.e., determining the friction tensors $\boldsymbol{\zeta}_{ij}^{\mathrm{tt}}$ etc., then three- and four-particle interactions already contribute at order $(a/r_{ij})^3$ [175].

Using the Oseen tensor, the formal solution of the Stokes equations for the (unknown) induced force density reads [see Eq. (2.29)]

$$\boldsymbol{u}(\boldsymbol{r}) = \sum_i \int \mathrm{d}^3 r' \, \boldsymbol{G}(\boldsymbol{r} - \boldsymbol{r}') \cdot \boldsymbol{f}_i(\boldsymbol{r}') \,. \tag{2.41}$$

The respective net force and torque that each moving particle exerts on the fluid is given by

$$\boldsymbol{F}_i = \int \mathrm{d}^3 r \, \boldsymbol{f}_i(\boldsymbol{r}) \,, \tag{2.42a}$$

$$\boldsymbol{T}_i = \int \mathrm{d}^3 r \, \boldsymbol{r} \times \boldsymbol{f}_i(\boldsymbol{r}) \,. \tag{2.42b}$$

Note that, for hard spheres, the induced forces can be assumed to be located at the particle surfaces.[16]

Because of the spherical shape of the particles, it is most appropriate to describe the force densities in spherical coordinates and expand them into vector spherical harmonics [4, 112]. This kind of multipole description of a vector field is a generalization of the common multipole expansion of a scalar field (as applied, e.g., to the charge density in electrostatics). In the method of induced-force multipoles, the expansion is done in terms of two infinite, complete sets of solutions of the *homogeneous* Stokes equations [Eqs. (2.14) with $\boldsymbol{f} = \boldsymbol{0}$], denoted as $\boldsymbol{e}^+_{lm\sigma}(\boldsymbol{r})$ and $\boldsymbol{e}^-_{lm\sigma}(\boldsymbol{r})$, respectively. The first set (superscript $+$) is regular at $\boldsymbol{r} = \boldsymbol{0}$ and divergent at infinity, while the second set (superscript $-$) is singular at $\boldsymbol{r} = \boldsymbol{0}$ and vanishes at infinity. These sets consist of complex functions (labeled by integers $l \geq 1$, $|m| \leq l$, and $\sigma = 0, 1, 2$), and they are themselves certain linear combinations of vector spherical harmonics [75, 125].

Using the regular functions $\boldsymbol{e}^+_{lm\sigma}(\boldsymbol{r})$, the velocity field at a point $\boldsymbol{r} = \boldsymbol{r}_i + \boldsymbol{x}$ on the surface of particle i can be expanded as

$$\boldsymbol{u}(\boldsymbol{r}_i + \boldsymbol{x}) = \boldsymbol{v}_i + \boldsymbol{\omega}_i \times \boldsymbol{x} = \sum_{l,m,\sigma} v_{i,lm\sigma} \boldsymbol{e}^+_{lm\sigma}(\boldsymbol{x}) \quad \text{for} \quad |\boldsymbol{x}| = a \tag{2.43}$$

with coefficients $v_{i,lm\sigma}$. The expansion of the Oseen tensor about the center of particle i is given by [125]

$$\boldsymbol{G}(\boldsymbol{r} - \boldsymbol{r}') = \frac{1}{\eta} \sum_{l,m,\sigma} \frac{1}{n^2_{lm}} \, \boldsymbol{e}^-_{lm\sigma}(\boldsymbol{r}_>) \boldsymbol{e}^{+\,*}_{lm\sigma}(\boldsymbol{r}_<) \,, \tag{2.44}$$

where n_{lm} are normalization constants, and the superscript $*$ denotes the complex conjugate. The arguments $\boldsymbol{r}_>$ and $\boldsymbol{r}_<$ refer, respectively, to the larger and smaller

[16] The pressure inside the spheres is set to zero and has thus discontinuities at their surfaces [176]. Therefore, a simple choice for the force density is $\boldsymbol{f}_i(\boldsymbol{r}_i + \boldsymbol{x}) = \boldsymbol{g}_i(\hat{\boldsymbol{x}})\delta(|\boldsymbol{x}| - a)$ with $\hat{\boldsymbol{x}} = \boldsymbol{x}/|\boldsymbol{x}|$.

of the relative position vectors $\boldsymbol{r}-\boldsymbol{r}_i$ and $\boldsymbol{r}'-\boldsymbol{r}_i$. Besides the velocity coefficients $v_{i,lm\sigma}$ as defined in Eq. (2.43), we introduce the force multipoles located on the surface of particle i by

$$f_{i,lm\sigma} = \int \mathrm{d}^3x \; \boldsymbol{e}^{+\,*}_{lm\sigma}(\boldsymbol{x}) \cdot \boldsymbol{f}_i(\boldsymbol{r}_i + \boldsymbol{x}) \,. \tag{2.45}$$

The forces $\boldsymbol{F}_i$ and the torques $\boldsymbol{T}_i$ acting on the particles are linear combinations of the first-order multipoles $f_{i,1m0}$ and $f_{i,1m1}$ [125]. Likewise, the velocities $\boldsymbol{v}_i$ and $\boldsymbol{\omega}_i$ correspond to linear combinations of $v_{i,1m0}$ and $v_{i,1m1}$.

With the above expansions, the formal solution (2.41) of the boundary-value problem can finally be reduced to an infinite set of algebraic equations of the form [75, 125]

$$\mathsf{v} = \mathsf{M} \cdot \mathsf{f} \quad \text{with} \quad \mathsf{M} = \mathsf{M}_0 + \mathsf{G} \,, \tag{2.46}$$

where v and f denote infinite-dimensional vectors containing all elements $v_{i,lm\sigma}$ and $f_{i,lm\sigma}$, respectively ($i = 1, \ldots, N$, $l \geq 1$, $|m| \leq l$, and $\sigma = 0, 1, 2$). The elements $G_{i,lm\sigma;\,i',l'm'\sigma'}$ of the matrix G arise from the Oseen tensor in Eq. (2.41) with $i \neq i'$, i.e., G is off-diagonal in the particle labels, while the matrix M_0 is diagonal and contains the single-sphere contributions ($i = i'$). Equation (2.46) is exact and is the analogue to Eq. (2.22).

If Eq. (2.46) could be solved exactly, the projection onto the $l = 1$ subspace would yield the exact N-body mobility matrix. However, since there are infinitely many multipole orders, we must approximate the equations by truncation at finite order $l = L$ [41]. It turns out that the velocity response to a force multipole $f_{i,lm\sigma}$ decays with distance as $1/r^{l+\sigma}$ [125]. Therefore, one must choose $L \geq 3$ to include all long-range effects (decaying no faster than $1/r^3$).[17]

Note that, in contrast to the aforementioned method of reflections, the concept of induced forces does not require the knowledge and therefore the explicit construction of the flow field.

2.4.4 Lubrication effects

The smaller the particle separations, the larger the number of reflections or the higher the multipole order that is required to get accurate results for the hydrodynamic interactions. Therefore, both the method of reflections and the multipole expansion are not feasible at distances close to contact.

In this regime, however, the dynamics of two neighboring particles moving relative to each other is dominated by *lubrication effects* [134]. These originate from the strong velocity gradients of the flow field in the gap between the two

[17] In our simulations using HYDROLIB, we choose $L = 3$ which corresponds to truncation errors of less than 1% [113].

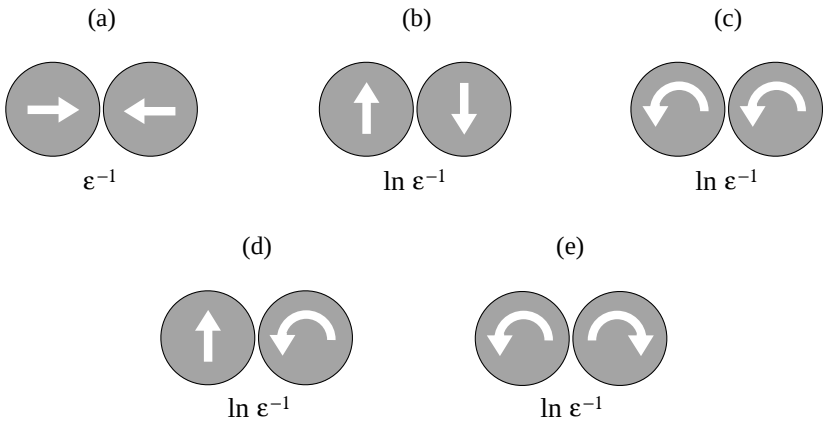

Figure 2.2 ■ Leading order of the lubrication expansion (in terms of the inverse gap ε^{-1}) for the diverging friction coefficients in "squeezing" (a) and "shearing" motions (b–d) of two particles close to contact. The rolling motion (e) also shows singular behavior.

spheres. Note that lubrication effects contribute only to *relative* motion; for collective motions, lubrication does not play a role. Moreover, since the lubrication zone is localized at the point of closest approach, lubrication effects are well accounted for by a superposition of pair interactions [66]. This kind of correction at small particle distances is included in the numerical library HYDROLIB [41, 113].

For a pair of spheres moving relative to each other, the frictional forces and torques diverge when the gap between the particles approaches zero ($r_{ij} \to 2a$). This is a result of lubrication theory, which yields an asymptotic expansion for the friction forces and torques in terms of ε^{-1}, where $\varepsilon = r_{ij}/a - 2 \ll 1$ is the dimensionless gap parameter [134].

We can essentially distinguish between two different types of motion that generate a lubrication zone (i.e., strong velocity gradients in the gap between the particle surfaces) and therefore cause divergent terms in the leading order of the lubrication expansion. The first type is the "squeezing" motion where the two particles approach each other along their line of centers [Fig. 2.2(a)]. The leading-order term of the hydrodynamic friction coefficient shows a singular behavior as ε^{-1} for $\varepsilon \to 0$ [122, 134]. The second type are "shearing" motions where the particles either (i) translate in opposite directions perpendicular to the line of centers [Fig. 2.2(b)] or (ii) rotate in the same sense about axes perpendicular to the line of centers [Fig. 2.2(c)] or where (iii) one particle translates and the other one rotates in directions perpendicular to the line of centers and perpendicular to each other [Fig. 2.2(d)]. In all these motions, the surface areas facing each other move in opposite directions. The corresponding hydrodynamic friction coeffients are weakly diverging as $\ln \varepsilon^{-1}$. Furthermore, it is interesting to note that the simple rolling motion, where the two spheres rotate in opposite sense about axes perpendicular to the line of centers [Fig. 2.2(e)], also leads to friction forces

with singularities of order $\ln \varepsilon^{-1}$ [122]. The friction coefficients corresponding to all other types of motion do not show a divergent behavior at small particle distances.[18]

Finally, it should be mentioned that, contrary to the friction coefficients, the mobilities reveal a smooth, non-divergent behavior at $\varepsilon \to 0$ for any type of motion [122].[19]

2.4.5 Mobilities of a two-sphere system

Consider a system of two identical spheres with center-center distance r. Let $\hat{\boldsymbol{r}} = \boldsymbol{r}/r$ be the unit vector along the line of centers, pointing from particle 1 to particle 2. Due to rotational symmetry about the axis $\hat{\boldsymbol{r}}$, the mobility tensors must be a linear combination of the tensors $\hat{\boldsymbol{r}}\hat{\boldsymbol{r}}$, $\hat{\boldsymbol{r}}\times$, and the unit tensor $\mathbf{1}$. However, we also have to account for the different parities of polar ($\boldsymbol{v}_i$ and $\boldsymbol{F}_j$) and axial vectors ($\boldsymbol{\omega}_i$ and $\boldsymbol{T}_j$). Multiplication with $\hat{\boldsymbol{r}}\hat{\boldsymbol{r}}$ leaves the parity of a vector unchanged, while the cross product $\hat{\boldsymbol{r}}\times$ changes parity from polar to axial and vice versa. Therefore, the purely translational (tt) and purely rotational mobility tensors (rr) must have the form [17, 122]

$$\boldsymbol{\mu}_{ij}^{\mathrm{tt}}(\boldsymbol{r}) = \mu_{ij}^{\mathrm{tt}\parallel}(r)\,\hat{\boldsymbol{r}}\hat{\boldsymbol{r}} + \mu_{ij}^{\mathrm{tt}\perp}(r)(\mathbf{1} - \hat{\boldsymbol{r}}\hat{\boldsymbol{r}})\,, \tag{2.47a}$$

$$\boldsymbol{\mu}_{ij}^{\mathrm{rr}}(\boldsymbol{r}) = \mu_{ij}^{\mathrm{rr}\parallel}(r)\,\hat{\boldsymbol{r}}\hat{\boldsymbol{r}} + \mu_{ij}^{\mathrm{rr}\perp}(r)(\mathbf{1} - \hat{\boldsymbol{r}}\hat{\boldsymbol{r}})\,, \tag{2.47b}$$

while the mixed mobilities[20] (tr) can be written as [122]

$$\boldsymbol{\mu}_{ij}^{\mathrm{tr}}(\boldsymbol{r}) = \mu_{ij}^{\mathrm{tr}\perp}(r)\,\hat{\boldsymbol{r}}\times \tag{2.47c}$$

(with $ij = 11, 12, 21, 22$). The mobility coefficients $\mu_{ij}^{\mathrm{tt}\parallel,\perp}$, $\mu_{ij}^{\mathrm{rr}\parallel,\perp}$, and $\mu_{ij}^{\mathrm{tr}\perp}$ are scalar functions of r. We distinguish between motions parallel and perpendicular to $\hat{\boldsymbol{r}}$ (superscripts $\parallel$ and $\perp$) as $\hat{\boldsymbol{r}}\hat{\boldsymbol{r}}$ projects onto the axis $\hat{\boldsymbol{r}}$ whereas $\mathbf{1} - \hat{\boldsymbol{r}}\hat{\boldsymbol{r}}$ yields the components perpendicular to $\hat{\boldsymbol{r}}$. The cross-product term $\hat{\boldsymbol{r}}\times$ vanishes for components parallel to $\hat{\boldsymbol{r}}$. Using the general symmetry relations (2.25) and the fact that the two particles are identical, the mobility coefficients must obey

$$\mu_{11}^{\mathrm{tt}\parallel,\perp} = \mu_{22}^{\mathrm{tt}\parallel,\perp}\,, \quad \mu_{11}^{\mathrm{rr}\parallel,\perp} = \mu_{22}^{\mathrm{rr}\parallel,\perp}\,, \quad \mu_{11}^{\mathrm{tr}\perp} = -\mu_{22}^{\mathrm{tr}\perp}\,, \tag{2.48a}$$

$$\mu_{12}^{\mathrm{tt}\parallel,\perp} = \mu_{21}^{\mathrm{tt}\parallel,\perp}\,, \quad \mu_{12}^{\mathrm{rr}\parallel,\perp} = \mu_{21}^{\mathrm{rr}\parallel,\perp}\,, \quad \mu_{12}^{\mathrm{tr}\perp} = -\mu_{21}^{\mathrm{tr}\perp}\,. \tag{2.48b}$$

Note that, due to these symmetries, the distance between two spheres driven by identical forces $\boldsymbol{F}_1 = \boldsymbol{F}_2$ (as in sedimentation, e.g.) does not change since the two velocities are the same, i.e., $\boldsymbol{v}_1 = \boldsymbol{v}_2$.

[18] For rotations of the particles in opposite sense about the line of centers, the friction does not diverge although this also causes some kind of "shearing" motion of the fluid.
[19] There are only singularities in the derivatives [122].
[20] The tensors $\boldsymbol{\mu}_{ij}^{\mathrm{rt}}$ are not discussed here explicitly since $\boldsymbol{\mu}_{ij}^{\mathrm{rt}} = (\boldsymbol{\mu}_{ji}^{\mathrm{tr}})^{\mathrm{T}} = \boldsymbol{\mu}_{ij}^{\mathrm{tr}}$.

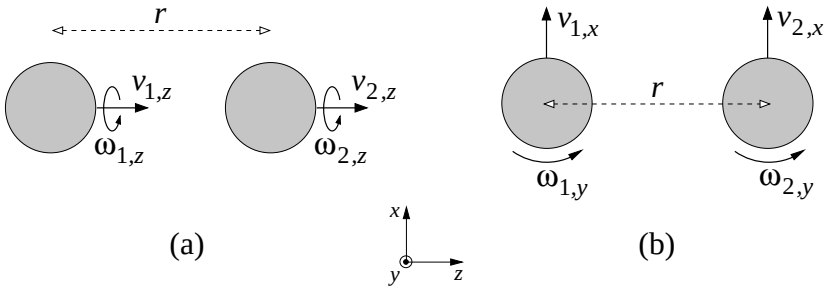

Figure 2.3 ■ Definition of the Cartesian coordinates for a system of two spheres. The z direction is along the center-center line of the particles. Longitudinal motions (a) decouple from transversal motions (b). Furthermore, there is no coupling of translation and rotation for longitudinal motions.

With the explicit expressions (2.47), the dynamics of the two-sphere system described by Eq. (2.21) separates into longitudinal motions parallel and transversal motions perpendicular to the particle-particle axis $\hat{\boldsymbol{r}}$, respectively. Note, moreover, that Eq. (2.47c) does not allow for a coupling between translations along and rotations about $\hat{\boldsymbol{r}}$.[21] In a Cartesian coordinate system with the z direction pointing along $\hat{\boldsymbol{r}}$ (see Fig. 2.3), we obtain from Eqs. (2.21), (2.47), and (2.48) for longitudinal motions

$$\begin{bmatrix} v_{1,z} \\ v_{2,z} \\ \omega_{1,z} \\ \omega_{2,z} \end{bmatrix} = \begin{bmatrix} \mu_{11}^{\mathrm{tt}\parallel} & \mu_{12}^{\mathrm{tt}\parallel} & 0 & 0 \\ \mu_{12}^{\mathrm{tt}\parallel} & \mu_{11}^{\mathrm{tt}\parallel} & 0 & 0 \\ 0 & 0 & \mu_{11}^{\mathrm{rr}\parallel} & \mu_{12}^{\mathrm{rr}\parallel} \\ 0 & 0 & \mu_{12}^{\mathrm{rr}\parallel} & \mu_{11}^{\mathrm{rr}\parallel} \end{bmatrix} \cdot \begin{bmatrix} F_{1,z} \\ F_{2,z} \\ T_{1,z} \\ T_{2,z} \end{bmatrix}, \tag{2.49}$$

where $v_{1,z}$ is the z component of the translational velocity of particle 1, etc. In transversal motions, translations along the x direction couple to rotations about the y axis:

$$\begin{bmatrix} v_{1,x} \\ v_{2,x} \\ \omega_{1,y} \\ \omega_{2,y} \end{bmatrix} = \begin{bmatrix} \mu_{11}^{\mathrm{tt}\perp} & \mu_{12}^{\mathrm{tt}\perp} & -\mu_{11}^{\mathrm{tr}\perp} & -\mu_{12}^{\mathrm{tr}\perp} \\ \mu_{12}^{\mathrm{tt}\perp} & \mu_{11}^{\mathrm{tt}\perp} & \mu_{12}^{\mathrm{tr}\perp} & \mu_{11}^{\mathrm{tr}\perp} \\ -\mu_{11}^{\mathrm{tr}\perp} & \mu_{12}^{\mathrm{tr}\perp} & \mu_{11}^{\mathrm{rr}\perp} & \mu_{12}^{\mathrm{rr}\perp} \\ -\mu_{12}^{\mathrm{tr}\perp} & \mu_{11}^{\mathrm{tr}\perp} & \mu_{12}^{\mathrm{rr}\perp} & \mu_{11}^{\mathrm{rr}\perp} \end{bmatrix} \cdot \begin{bmatrix} F_{1,x} \\ F_{2,x} \\ T_{1,y} \\ T_{2,y} \end{bmatrix}. \tag{2.50}$$

Translations along the y direction and rotations about the x axis obey an equivalent system of equations. Defining the appropriate four-dimensional velocity

[21] This can also be easily understood without using the explicit form (2.47c). A two-sphere system shows mirror symmetry with respect to a plane containing the centers of both spheres. Assume the particles rotate with frequencies $\boldsymbol{\omega}_i = \omega_i \hat{\boldsymbol{r}}$ and translate with velocities $\boldsymbol{v}_i = v_i \hat{\boldsymbol{r}}$. Then, in the mirrored system, the rotational velocities are $\boldsymbol{\omega}_i = -\omega_i \hat{\boldsymbol{r}}$, while the translations remains unchanged. Due to linearity [see Eqs. (2.21)], however, an inversion of the direction of rotation should also lead to an inversion of the translational motion. Therefore, a coupling of translation and rotation in longitudinal motions cannot exist.

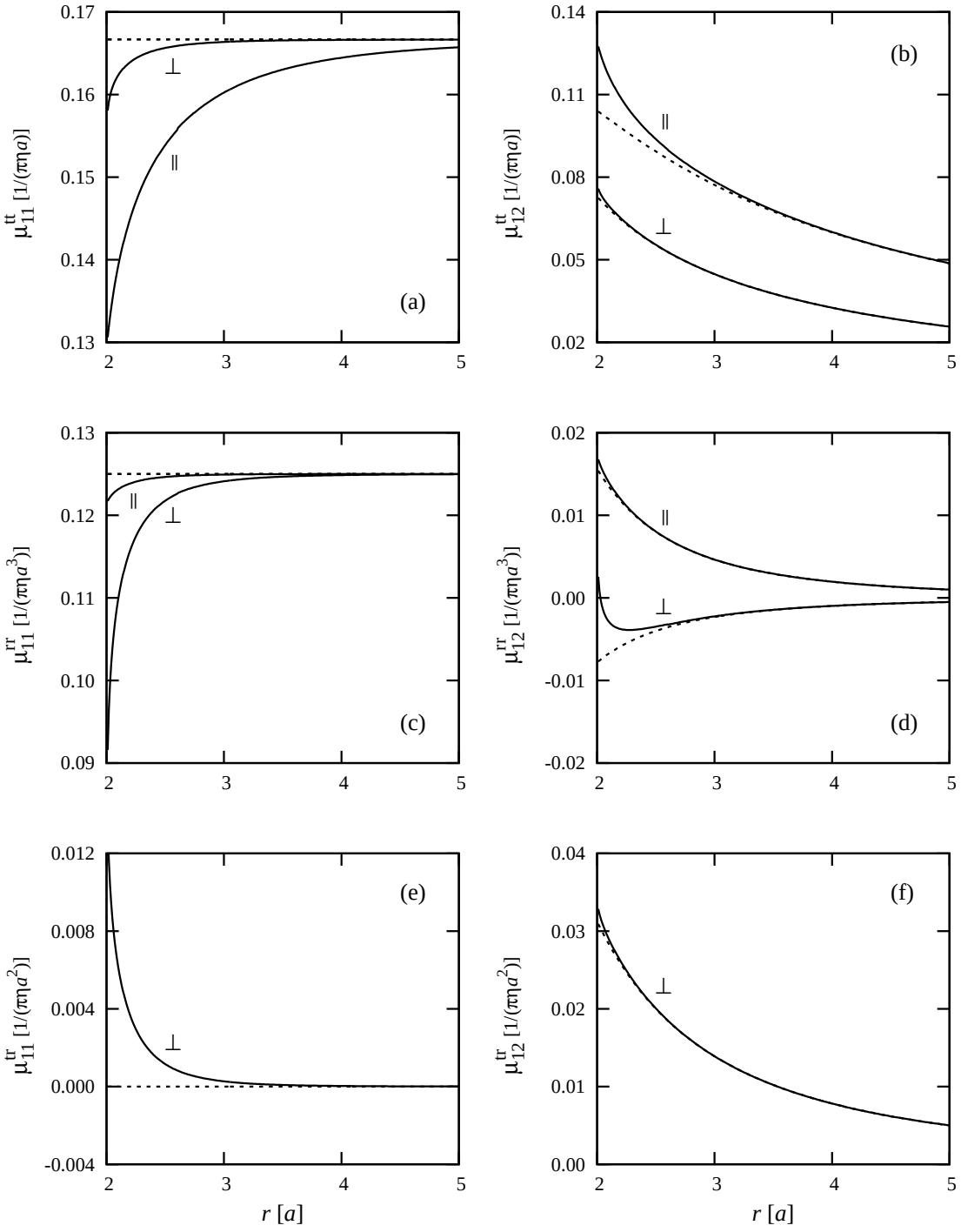

Figure 2.4 ■ Two-sphere mobilities as functions of the center-center distance r: multipole-expansion values calculated with HYDROLIB (solid lines) and Rotne-Prager approximation (dashed lines). Close to contact ($r \approx 2a$), lubrication corrections effects become important. In Rotne-Prager approximation, the translational (a) and rotational (c) self-mobilities are identical to the single-particle Stokes values, $\mu^{\mathrm{t}} = (6\pi\eta a)^{-1}$ and $\mu^{\mathrm{r}} = (8\pi\eta a^3)^{-1}$, respectively; there is no self-coupling of translation and rotation (e).

vector $\mathbf{v}^\sigma$ and force vector $\mathbf{f}^\sigma$ ($\sigma = \parallel, \perp$), we can abbreviate Eqs. (2.49) and (2.50), respectively, by

$$\mathbf{v}^\sigma = \mathbf{M}^\sigma \cdot \mathbf{f}^\sigma \,, \tag{2.51}$$

where the 4×4 mobility matrices $\mathbf{M}^\sigma$ are still symmetric. Thus, the rotational symmetry reduces the full 12×12 problem (2.22) to two 4×4 problems, where Eq. (2.49) is essentially a 2×2 problem.

Accordingly, the energy dissipation rate $\mathbf{f} \cdot \mathbf{M} \cdot \mathbf{f}$ [see Eq. (2.27)] splits up into a sum of three independent contributions (one for longitudinal and two for transversal motions) of the form $\mathbf{f}^\sigma \cdot \mathbf{M}^\sigma \cdot \mathbf{f}^\sigma$, so each of the reduced mobility matrices $\mathbf{M}^\sigma$ has to be positive-definite separately.

Figure 2.4 shows how the two-particle mobilities of the Rotne-Prager approximation (2.39) compare to the values obtained by a more accurate multipole expansion using HYDROLIB [113]. Clearly, the Rotne-Prager expressions work pretty well for particle distances larger than $r \approx 3a$. At very small separations, lubrication effects, incorporated in HYDROLIB, become dominant.

2.4.6 Mobility matrix for rigid clusters

Once the complete $6N \times 6N$ mobility matrix for a configuration of N single particles is known, the mobility matrix of a *rigid cluster* consisting of these particles can be readily calculated [42]. For the sake of clarity, we illustrate here only the case where all particles belong to the same cluster. However, the formalism can be easily extended to several clusters.

Let $\boldsymbol{v}_\mathrm{c}$ be the translational velocity of the center of mass of the rigid cluster and $\boldsymbol{\omega}_\mathrm{c}$ its rotational velocity. The velocities of the single constituents of the rigid cluster are then given by

$$\boldsymbol{v}_i = \boldsymbol{v}_\mathrm{c} + \boldsymbol{\omega}_\mathrm{c} \times (\boldsymbol{r}_i - \boldsymbol{r}_\mathrm{c}) \,, \tag{2.52a}$$

$$\boldsymbol{\omega}_i = \boldsymbol{\omega}_\mathrm{c} \,, \tag{2.52b}$$

where $\boldsymbol{r}_\mathrm{c}$ denotes the location of the center of mass. The total force and torque acting on the center of mass of the cluster are

$$\boldsymbol{F}_\mathrm{c} = \sum_i \boldsymbol{F}_i \,, \tag{2.53a}$$

$$\boldsymbol{T}_\mathrm{c} = \sum_i \left[\boldsymbol{T}_i + (\boldsymbol{r}_i - \boldsymbol{r}_\mathrm{c}) \times \boldsymbol{F}_i \right] . \tag{2.53b}$$

With the generalized cluster velocity $\mathbf{v}_\mathrm{c} = [\boldsymbol{v}_\mathrm{c}, \boldsymbol{\omega}_\mathrm{c}]$, Eqs. (2.52) can be written compactly as

$$\mathbf{v} = \mathcal{C} \cdot \mathbf{v}_\mathrm{c} \,, \tag{2.54}$$

where we introduced the $6N \times 6$ projection matrix

$$\mathcal{C} = \begin{bmatrix} \mathbf{1} & (\boldsymbol{r}_c - \boldsymbol{r}_1)\times \\ \vdots & \vdots \\ \mathbf{1} & (\boldsymbol{r}_c - \boldsymbol{r}_N)\times \\ \mathbf{0} & \mathbf{1} \\ \vdots & \vdots \\ \mathbf{0} & \mathbf{1} \end{bmatrix} . \tag{2.55}$$

In the same way, we can write Eqs. (2.53) as

$$\mathbf{f}_\mathrm{c} = \mathcal{C}^\mathrm{T} \cdot \mathbf{f} \tag{2.56}$$

with $\mathbf{f}_\mathrm{c} = [\boldsymbol{F}_\mathrm{c}, \boldsymbol{T}_\mathrm{c}]$, where the transformation matrix is now the transpose of $\mathcal{C}$. Using the generalized friction law $\mathbf{f} = \mathbf{Z} \cdot \mathbf{v}$ [see Eq. (2.24)], we obtain

$$\mathbf{f}_\mathrm{c} = \mathcal{C}^\mathrm{T} \cdot \mathbf{Z} \cdot \mathcal{C} \cdot \mathbf{v}_\mathrm{c} \,, \tag{2.57}$$

so by comparison with the friction law for the cluster,

$$\mathbf{f}_\mathrm{c} = \mathbf{Z}_\mathrm{c} \cdot \mathbf{v}_\mathrm{c} \,, \tag{2.58}$$

the effective 6×6 friction matrix of the rigid cluster is given by

$$\mathbf{Z}_\mathrm{c} = \mathcal{C}^\mathrm{T} \cdot \mathbf{Z} \cdot \mathcal{C} \,, \tag{2.59}$$

and the cluster mobility matrix finally reads

$$\mathbf{M}_\mathrm{c} = (\mathcal{C}^\mathrm{T} \cdot \mathbf{M}^{-1} \cdot \mathcal{C})^{-1} \,. \tag{2.60}$$

For a system of N_c clusters, $\mathcal{C}$ is an $N_\mathrm{c} \times N_\mathrm{c}$ matrix comprised of submatrices of the form (2.55), representing the different clusters.

2.5 Stokesian-dynamics simulations

2.5.1 Equation of motion

In the overdamped regime, where inertial effects are neglected, Newton's equation of motion reduces to the force and torque balance $\mathbf{f} + \mathbf{f}_\mathrm{h} = \mathbf{0}$, where $\mathbf{f}$ are external forces and torques or other non-hydrodynamic interactions of the suspended particles, and $\mathbf{f}_\mathrm{h}$ is the hydrodynamic friction given by Eq. (2.24), i.e., $\mathbf{f}_\mathrm{h} = -\mathbf{Z}\cdot\mathbf{v}$. Thus, the equation of motion for Stokesian dynamics has in principle already been established by Eqs. (2.21) or (2.22), respectively, relating the forces and torques linearly to the resulting translational and rotational velocities, viz. $\mathbf{v} = \mathbf{M} \cdot \mathbf{f}$.

We represent a particle of arbitrary shape (e.g., a rigid cluster composed of spheres) by its center-of-mass position $\boldsymbol{r}_i$ and a body-fixed orthonormal vector basis $\{\boldsymbol{e}_i^1, \boldsymbol{e}_i^2, \boldsymbol{e}_i^3\}$. For brevity, we group the coordinates of all particles together in the $12N$-dimensional vector $X = [\boldsymbol{r}_1, \boldsymbol{e}_1^1, \boldsymbol{e}_1^2, \boldsymbol{e}_1^3, \ldots, \boldsymbol{r}_N, \boldsymbol{e}_N^1, \boldsymbol{e}_N^2, \boldsymbol{e}_N^3]$. To describe the motion of the particles, we introduce the $6N$-dimensional generalized differential $\mathrm{d}\mathbf{r} = [\mathrm{d}\boldsymbol{r}_1, \ldots, \mathrm{d}\boldsymbol{r}_N, \mathrm{d}\boldsymbol{\phi}_1, \ldots, \mathrm{d}\boldsymbol{\phi}_N]$, where the vector $\mathrm{d}\boldsymbol{\phi}_i$ defines an infinitesimal rotation of particle i according to $\mathrm{d}\boldsymbol{e}_i^\alpha = \mathrm{d}\boldsymbol{\phi}_i \times \boldsymbol{e}_i^\alpha$ ($\alpha = 1, 2, 3$). The change in the configuration X can then be written in a compact notation as

$$\mathrm{d}X = \mathcal{P}(X) \cdot \mathrm{d}\mathbf{r}\,. \tag{2.61a}$$

The transformation matrix $\mathcal{P}$ consists of separate block matrices for each particle i that can be identified from

$$\begin{bmatrix} \mathrm{d}\boldsymbol{r}_i \\ \mathrm{d}\boldsymbol{e}_i^\alpha \end{bmatrix} = \begin{bmatrix} \mathbf{1} & \mathbf{0} \\ \mathbf{0} & -\boldsymbol{e}_i^\alpha \times \end{bmatrix} \cdot \begin{bmatrix} \mathrm{d}\boldsymbol{r}_i \\ \mathrm{d}\boldsymbol{\phi}_i \end{bmatrix}. \tag{2.61b}$$

The evolution equation that we use in the Stokesian-dynamics simulations can then be written in compact differential form as

$$\mathrm{d}\mathbf{r} = \mathbf{v}\,\mathrm{d}t \quad \text{with} \quad \mathbf{v} = \mathbf{M}(X) \cdot \mathbf{f}(X)\,, \tag{2.62a}$$

and the assigned incremental change $\mathrm{d}X = \mathcal{P} \cdot \mathrm{d}\mathbf{r}$ in the state of the particles is explicitely given by

$$\mathrm{d}\boldsymbol{r}_i = \boldsymbol{v}_i\,\mathrm{d}t\,, \tag{2.62b}$$

$$\mathrm{d}\boldsymbol{e}_i^\alpha = \boldsymbol{\omega}_i\,\mathrm{d}t \times \boldsymbol{e}_i^\alpha\,, \tag{2.62c}$$

where the translational and rotational velocities are stated in Eqs. (2.21a) and (2.21b), respectively.

As the dependence of the mobility matrix $\mathbf{M}$ on the particle coordinates is highly nonlinear, we use higher-order (and thus more stable) integration schemes for the numerical solution of the equation of motion, which are presented in the following. Note that we only consider forces and torques that do not depend on time explicitly (i.e., $\partial\mathbf{f}/\partial t = 0$).

2.5.2 Numerical integration schemes

The simplest choice for a discretized version (with respect to time t) of Eq. (2.62) is the well-known *Euler method*

$$\Delta\mathbf{r}_t = \mathbf{v}(X_t)\Delta t \tag{2.63}$$

with the assigned configuration update $X_{t+\Delta t} = X_t + \Delta X_t$, where $\Delta X_t = \mathcal{P}(X_t) \cdot \Delta \mathbf{r}_t$ according to Eq. (2.61). This procedure, however, is not very stable [198].[22] Therefore, one should always choose integration schemes of higher order in the time step Δt to avoid the accumulation of numerical errors.

Higher-order algorithms typically combine the information obtained from several Euler-like steps such that they match a Taylor expansion of the function to be determined up to some order Δt^n. The use of intermediate steps makes these procedures numerically much more stable since it corrects the errors that arise from a single Euler move. A procedure that is exact up to order Δt^2 is the *Heun algorithm* [97, 138] (which is equivalent to the second-order Runge-Kutta scheme [198, 218]). It first performs the predictor step

$$\Delta \mathbf{r}_* = \mathbf{v}(X_t)\Delta t\,, \tag{2.64a}$$

corresponding to a configurational change $\Delta X_* = \mathcal{P}(X_t) \cdot \Delta \mathbf{r}_*$. The intermediate configuration $X_t + \Delta X_*$ is then used to calculate the corrector step

$$\Delta \mathbf{r}_t = \tfrac{1}{2}[\mathbf{v}(X_t) + \mathbf{v}(X_t + \Delta X_*)]\Delta t \tag{2.64b}$$

and $\Delta X_t = \mathcal{P}(X_t) \cdot \Delta \mathbf{r}_t$, which leads to the final configuration $X_{t+\Delta t} = X_t + \Delta X_t$.

The by far most often used integration scheme is the *fourth-order Runge-Kutta algorithm* [4, 138, 198, 218], which matches the Taylor expansion up to order Δt^4. It consists of the intermediate Euler steps

$$\Delta \mathbf{r}_1 = \mathbf{v}(X_t)\Delta t\,, \tag{2.65a}$$

$$\Delta \mathbf{r}_2 = \mathbf{v}(X_t + \tfrac{1}{2}\Delta X_1)\Delta t\,, \tag{2.65b}$$

$$\Delta \mathbf{r}_3 = \mathbf{v}(X_t + \tfrac{1}{2}\Delta X_2)\Delta t\,, \tag{2.65c}$$

$$\Delta \mathbf{r}_4 = \mathbf{v}(X_t + \Delta X_3)\Delta t \tag{2.65d}$$

with the corresponding configurational changes $\Delta X_i = \mathcal{P}(\ldots) \cdot \Delta \mathbf{r}_i$, where the matrix $\mathcal{P}$ is evaluated at the same configuration as the velocity $\mathbf{v}$ in the respective equation for $\Delta \mathbf{r}_i$. The new configuration $X_{t+\Delta t} = X_t + \Delta X_t$ with $\Delta X_t = \mathcal{P}(X_t) \cdot \Delta \mathbf{r}_t$ is then finally obtained from the combined step

$$\Delta \mathbf{r}_t = \tfrac{1}{6}\Delta \mathbf{r}_1 + \tfrac{1}{3}\Delta \mathbf{r}_2 + \tfrac{1}{3}\Delta \mathbf{r}_3 + \tfrac{1}{6}\Delta \mathbf{r}_4\,. \tag{2.65e}$$

[22] The simple Euler method is, in particular, delicate in case of trajectories with a persistent curvature. This becomes immediately obvious when we consider a particle running on a circle, driven by tangential forces only, so there is no radial motion in the overdamped regime. However, due to the discretization of time, there will always be an unphysical drift in radial direction, as the integration step has a finite length and thus also a radial component.

3 Brownian motion

Colloidal particles suspended in a viscous fluid undergo erratic movements, the well-known *Brownian motion*, which has its origin in the bombardement by the fluid molecules. The stochastic character arises from the fact that the dynamics of the single fluid molecules is not resolved on the characteristic length and time scale of the moving colloidal particles.

On the molecular level, the dynamics is completely deterministic.[1] Thus, if we knew all initial conditions and also all types of interactions, we would be able to predict the entire future of a system. But as we know neither the starting point nor the interactions exactly, the dynamics is not predictable precisely. Moreover, chaos theory shows that even if we had all informations on the interactions and thus the complete equations of motions, any slight error in the initial conditions would be magnified exponentially. So, in fact, there is practically no predictability.

Furthermore, due to the different length and time scales of the dynamics of the fluid molecules on the one hand and the much larger and slower colloidal particles on the other hand, we are not interested in the detailed motion on the molecular level anyway, as this would be an exorbitant computational task (and, by the way, cannot be resolved experimentally). Instead of including all the molecular degrees of freedom, we switch to a statistical theory for the effective dynamics of the suspended particles only. The solvent enters this description by two effects. First, the fluid is considered to be continuous, which corresponds to averaging over a huge number of collisions of the suspended particles with the fluid molecules. This average results in the *deterministic* hydrodynamic forces and torques acting on moving particles, as discussed in detail in the previous chapter on Stokesian dynamics. Secondly, the solvent can be treated as a source of *noise* that causes random motions of the suspended particles due to the incessant bombardement by the fluid molecules.

This coarse-grained picture can be formulated theoretically by two different but equivalent concepts of statistical mechanics. The first approach is to complete Newton's equation of motion by hydrodynamic friction (as in Stokesian dynamics) and by *random forces and torques*. The resulting stochastic differential equation is referred to as *Langevin equation* [86, 190, 205]. Alternatively, if we are not interested in single phase-space trajectories but in ensemble averages, we can calculate the probability distribution of the system in phase space. Its time evolution is governed by a diffusion-type differential equation, the so-called

[1] at least in the classical picture, not considering quantum effects

Fokker-Planck equation, in the overdamped limit also known as *Smoluchowski equation* [86, 190, 205].

3.1 The Langevin equation

3.1.1 From Newton's second law to the Langevin equation

The Langevin equation can be considered as Newton's equation of motion including the interaction of the colloidal particles with a bath (namely the solvent). The latter leads to the deterministic hydrodynamic friction $\mathbf{f}_\mathrm{h}$ and, in addition, to rapidly fluctuating forces and torques $\tilde{\mathbf{f}}(t)$, the thermal noise. Newton's equation is then of the form

$$\mathbf{I} \cdot \dot{\mathbf{v}} = \mathbf{f}_\mathrm{h} + \tilde{\mathbf{f}}(t) + \mathbf{f} \,, \tag{3.1}$$

where the symmetric $6N \times 6N$ matrix $\mathbf{I}$ contains the masses m_i and moments of inertia $\boldsymbol{I}_i$ of the particles, and $\mathbf{f}$ are deterministic, non-hydrodynamic forces and torques. As in the previous chapter on Stokesian dynamics, we are going to neglect inertial effects in the end. For the time being, however, we keep the inertial term in order to clarify what the correct evolution equations of Brownian dynamics are.

Although derived from the static, *inertialess* Stokes equations (2.14) for the fluid, the steady-state friction law $\mathbf{f}_\mathrm{h} = -\mathbf{Z} \cdot \mathbf{v}$ is nevertheless a good approximation even for non-steady motion of particles with a *finite mass*, provided that the density ratio holds $(\rho/\rho_\mathrm{p})^{1/2} \ll 1$ [107, 175], where ρ is the mass density of the fluid and ρ_p the one of the suspended particles. In other words, we consider a time scale on which the momenta of the light fluid molecules are in equilibrium, while those of the suspended particles are not.[2] Thus, we finally obtain the *Langevin equation*

$$\mathbf{I} \cdot \dot{\mathbf{v}} + \mathbf{Z} \cdot \mathbf{v} = \tilde{\mathbf{f}}(t) + \mathbf{f} \,, \tag{3.2}$$

which is a stochastic differential equation of second order in time for the particle coordinates.

Recall that the friction matrix $\mathbf{Z}$ itself depends on the spatial particle configuration. If we consider only the noise contributions to the velocity and neglect inertia, then the Langevin equation reads $\mathbf{v} = \mathbf{Z}^{-1} \cdot \tilde{\mathbf{f}}(t)$. As the noise $\tilde{\mathbf{f}}(t)$ is multiplied by a configuration-dependent "coefficient", namely the mobility matrix $\mathbf{Z}^{-1}$, the random part of the Langevin equation is termed *multiplicative noise* [205]. Its consequences will be discussed later in Sect. 3.1.4.

[2] In general, the friction term has the time-retarded form $\mathbf{f}_\mathrm{h}(t) = -\int_{-\infty}^{t} \mathrm{d}t' \, \mathbf{Z}(t-t') \cdot \mathbf{v}(t')$ with the memory kernel $\mathbf{Z}(t-t')$ [107, 252], so the generalized Langevin equation is an integro-differential equation.

In the following, we will first establish correlations of the fluctuating forces and torques $\tilde{\mathbf{f}}(t)$ guaranteeing that the equipartition theorem of statistical mechanics is obeyed: the *fluctuation-dissipation theorem*. Subsequently, we will introduce the stochastic calculus of Wiener processes being used to treat the random trajectories analytically. As we will see (Sect. 3.1.4), the Langevin equation in the form (3.2) is meaningless in a strictly mathematical sense. Therefore, we shall represent the correct evolution equation in differential form (which can finally be implemented in Brownian-dynamics simulations).

3.1.2 Fluctuation-dissipation theorem

To calculate trajectories by integration of Eq. (3.2), we need to know some properties of the random noise $\tilde{\mathbf{f}}(t)$. By definition, interactions with the solvent that do not vanish in the ensemble average are assigned to the deterministic hydrodynamic part $\mathbf{f}_\mathrm{h}$. Therefore, we can set

$$\langle \tilde{\mathbf{f}}(t) \rangle = \mathbf{0}\,, \tag{3.3}$$

where $\langle \ldots \rangle$ denotes an ensemble average. Furthermore, the molecular collisions occur on a time scale by many orders of magnitude shorter than the colloidal time scale. The solvent time scale is of the order of 10^{-14} s [31, 60], while the shortest time scale of the colloidal particles is the momentum relaxation time, which is in the range of nanoseconds (see Sect. 2.1.4). Thus, it is a reasonable approximation to assume that the random forces at different times are uncorrelated.[3] This yields the so-called Gaussian white[4] noise, characterized by the time-correlation function [79, 175, 187]

$$\langle \tilde{\mathbf{f}}(t) \tilde{\mathbf{f}}(t') \rangle = 2 k_\mathrm{B} T\, \mathbf{Z}(X(t))\, \delta(t - t')\,, \tag{3.4}$$

where T is the temperature of the solvent and k_B the Boltzmann constant. The strength of the *stochastic* noise is related to the *deterministic* friction due to the common origin of dissipative and fluctuating forces and torques. The *fluctuation-dissipation theorem* (3.4) ensures that the equipartition theorem of statistical mechanics is fulfilled, i.e., the translational and rotational kinetic energies on average hold the relations $\langle \frac{1}{2} m_i \boldsymbol{v}_i^2 \rangle = \langle \frac{1}{2}\, \boldsymbol{\omega}_i \cdot \boldsymbol{I}_i \cdot \boldsymbol{\omega}_i \rangle = \frac{3}{2} k_\mathrm{B} T$ for all particles i. In other words, the work done by the random forces and torques on average balances the energy losses due to viscous dissipation, and thus, the mean kinetic energies remain constant.

At first glance, it might appear contradictory that the local random impacts of the fluid molecules on the colloidal particles can cause a long-range spatial

[3] In the general case (see footnote 2, p. 34), the fluctuation-dissipation relation takes the form $\langle \tilde{\mathbf{f}}(t) \tilde{\mathbf{f}}(t') \rangle = k_\mathrm{B} T\, \mathbf{Z}(t - t')$ [107, 252].

[4] According to the Wiener-Khinchin theorem, the power spectrum of the noise is given by the Fourier transform of its time-correlation function [86, 205]. For a δ-correlated noise, this spectrum is frequency-independent, which motivates the attribute "white".

correlation of the fluctuating forces and torques represented by the friction matrix $\mathbf{Z}$ in Eq. (3.4) that describes long-range hydrodynamic interactions. Naïvely, one might instead expect that the random kicks acting on separate particles are uncorrelated, i.e., $\langle\tilde{\mathbf{f}}(t)\tilde{\mathbf{f}}(t')\rangle \propto \mathbf{1}\delta(t-t')$, where $\mathbf{Z}$ in Eq. (3.4) is replaced by $\mathbf{Z} \propto \mathbf{1}$. Nonetheless, the Langevin equation, with fluctuating forces and torques satisfying the fluctuation-dissipation theorem, can be derived completely from and shown to be consistent with the equations of fluctuating hydrodynamics, i.e., the Navier-Stokes equation with a fluctuating stress tensor [79, 148, 187].

Alternatively, the Langevin equation (3.2) with the noise correlations (3.4) can also be derived from the Liouville equation of the complete system (i.e., including the coordinates of the single constituents of the bath) by means of a projection-operator technique that reduces the degrees of freedom to those of the colloidal particles, accompanied by a series expansion in the small parameter $(m_\mathrm{f}/m)^{1/2}$, where m_f is the mass of the light fluid molecules and m the mass of the heavier colloidal particles [58].

3.1.3 Brownian displacements and Wiener processes

Having established the time correlations of the fluctuating forces and torques, the question arises how they determine the random trajectories. In this section, we will derive the diffusive displacements due to thermal noise, a result which will finally enter the evolution equation.

Let us, for simplicity, consider first a single sphere with a constant friction coefficient ζ and not subject to external forces, i.e., we are only interested in the fluctuating part $\tilde{v} = v - \langle v\rangle$. The Langevin equation (in one dimension) in this case reads

$$m\dot{\tilde{v}} + \zeta\tilde{v} = \tilde{F}(t) \tag{3.5}$$

with white-noise correlations

$$\langle\tilde{F}(t)\tilde{F}(t')\rangle = 2k_\mathrm{B}T\zeta\delta(t-t')\,. \tag{3.6}$$

The velocity correlation function in thermal equilibrium, i.e., for times $t, t' \gg \tau_\mathrm{m}$, turns out to be[5] [205]

$$\langle\tilde{v}(t)\tilde{v}(t')\rangle = \frac{k_\mathrm{B}T}{m}\,\mathrm{e}^{-|t-t'|/\tau_\mathrm{m}}\,, \tag{3.7}$$

i.e., the fluctuating velocities are only correlated within a very narrow time window of order τ_m, where $\tau_\mathrm{m} = m/\zeta$ is the momentum relaxation time (see

[5] For $t = t'$, we obtain from Eq. (3.7) the equipartition theorem $\frac{1}{2}m\langle\tilde{v}^2(t)\rangle = \frac{1}{2}k_\mathrm{B}T$, which verifies the fluctuation-dissipation theorem (3.6) or, more general, (3.4).

Sect. 2.1.4). In the overdamped regime, however, such short time differences are not resolved. Thus, taking the limit $m \to 0$, we obtain

$$\langle \tilde{v}(t)\tilde{v}(t')\rangle = 2\,\frac{k_{\mathrm{B}}T}{\zeta}\,\delta(t-t')\,, \tag{3.8}$$

where we have used the representation $\lim_{\varepsilon\to 0}(1/\varepsilon)\mathrm{e}^{-|x|/\varepsilon} = 2\delta(x)$ of the δ-function [4]. Note that we could have obtained this result also directly from the Langevin equation with zero mass, i.e., $\tilde{v}(t) = \tilde{F}(t)/\zeta$.

Hence, if we study the stochastic dynamics on a time scale beyond momentum relaxation, we can neglect the inertial term $\mathbf{I}\cdot\dot{\mathbf{v}}$ in the generalized Langevin equation (3.2) from the beginning. The noise contributions to the velocity are thus considered to be instantaneous and directly given by

$$\tilde{\mathbf{v}}(t) = \mathbf{Z}^{-1}(X(t))\cdot\tilde{\mathbf{f}}(t) \tag{3.9}$$

with time correlations

$$\langle \tilde{\mathbf{v}}(t)\tilde{\mathbf{v}}(t')\rangle = 2k_{\mathrm{B}}T\,\mathbf{Z}^{-1}(X(t))\delta(t-t')\,, \tag{3.10}$$

according to the fluctuation-dissipation theorem (3.4). The resulting random displacements on a time interval $[t, t+\Delta t]$,

$$\Delta\tilde{\mathbf{r}}_t = \int_0^{\Delta t} \mathrm{d}\tau\,\tilde{\mathbf{v}}(t+\tau)\,, \tag{3.11}$$

do not lead to a net motion, because on average $\langle\tilde{\mathbf{f}}(t)\rangle = \mathbf{0}$ and thus

$$\langle\Delta\tilde{\mathbf{r}}_t\rangle = \mathbf{0}\,. \tag{3.12}$$

The covariance matrix of the displacements reads in general

$$\langle\Delta\tilde{\mathbf{r}}_t\Delta\tilde{\mathbf{r}}_t\rangle = \int_0^{\Delta t}\mathrm{d}\tau\int_0^{\Delta t}\mathrm{d}\tau'\,\langle\tilde{\mathbf{v}}(t+\tau)\tilde{\mathbf{v}}(t+\tau')\rangle\,. \tag{3.13}$$

Let Δt be sufficiently short such that the spatial particle configuration does not change significantly (but nevertheless still large compared to the momentum relaxation time). We can then assume the friction matrix to be approximately constant: $\mathbf{Z}(X(t)) \approx \mathbf{Z}(X(t+\Delta t))$, denoted briefly by $\mathbf{Z}(X_t)$. For the random displacements satisfying the fluctuation-dissipation theorem, we finally obtain a diffusive behavior

$$\langle\Delta\tilde{\mathbf{r}}_t\Delta\tilde{\mathbf{r}}_t\rangle = 2\mathbf{D}(X_t)\Delta t\,, \tag{3.14}$$

where we have introduced the diffusion matrix, related to the mobility and friction matrix, respectively, via the generalized *Einstein relation* [182]

$$\mathbf{D} = k_{\mathrm{B}}T\,\mathbf{M} = k_{\mathrm{B}}T\,\mathbf{Z}^{-1}\,. \tag{3.15}$$

A rigorous analytical treatment of the irregular dynamics can be given within the stochastic calculus of *Wiener processes* [86, 190, 194, 205]. A Wiener process, denoted by $W(t)$, is defined as a Gaussian variable with zero mean, $\langle W(t)\rangle = 0$, and time correlation

$$\langle W(t)W(t')\rangle = \min(t,t')\,, \tag{3.16}$$

where $\min(t,t')$ is the smaller of the two values t and t'. The increments $\Delta W_t = W(t+\Delta t) - W(t)$ are then Gaussian variables, too, for which one can readily derive the properties $\langle \Delta W_t\rangle = 0$ and

$$\langle \Delta W_t^2\rangle = \Delta t\,. \tag{3.17}$$

The increments at different times t are independent of each other. For our purposes, we define the $6N$-dimensional increment $\Delta\mathbf{w}_t$, each of whose components describes an independent Wiener process, thus having zero mean, i.e.,

$$\langle \Delta\mathbf{w}_t\rangle = \mathbf{0}\,, \tag{3.18}$$

and the covariance matrix is diagonal with

$$\langle \Delta\mathbf{w}_t \Delta\mathbf{w}_t\rangle = \mathbf{1}\Delta t\,. \tag{3.19}$$

Given these definitions, we can assign the correlated $6N$ displacements $\Delta\tilde{\mathbf{r}}_t$ the uncorrelated Wiener increments $\Delta\mathbf{w}_t$ by setting [86, 190]

$$\Delta\tilde{\mathbf{r}}_t = \mathbf{H}(X_t)\cdot\Delta\mathbf{w}_t\,, \tag{3.20a}$$

where the $6N\times 6N$ matrix $\mathbf{H}$ has to obey the relation

$$\mathbf{H}\cdot\mathbf{H}^{\mathrm{T}} = 2\mathbf{D}\,. \tag{3.20b}$$

With this choice, the correct mean value and covariance of $\Delta\tilde{\mathbf{r}}_t$, as given by Eqs. (3.12) and (3.14), respectively, are obtained.

To summarize this section, we note that the final result essentially has been derived such that the fluctuation-dissipation theorem (3.4) is satisfied. Hence, by random displacements obeying Eq. (3.20), the configurational space is sampled consistently with statistical mechanics.

3.1.4 Evolution equation of Langevin dynamics

So far, we applied the Langevin equation in a rather naïve manner. But we should be aware of the fact that Wiener processes are not differentiable. In a mean-square sense, Eq. (3.17) yields $\Delta W = \sqrt{\Delta t}$ and thus $\Delta W/\Delta t = 1/\sqrt{\Delta t}$, which diverges in the limit $\Delta t \to 0$. Therefore, the derivative $\mathrm{d}W/\mathrm{d}t$ does not exist. Physically, this behavior stems from the white noise, having zero correlation time, i.e., it can be considered as a sequence of peaked functions with zero width [205]. Hence, the stochastic trajectory jumps each time a peak occurs.

This shows that the Langevin equation in the form (3.2) containing time derivatives is, in a strictly mathematical sense, meaningless. Especially in the case of configuration-dependent friction (multiplicative noise), we have to tackle some subtle peculiarities of stochastic differential equations. It is not clear *a priori* which configuration is to be used to determine the friction matrix $\mathbf{Z}$ (or the diffusion matrix $\mathbf{D}$, respectively) [205]: the one just before or the one right after the jump, or somewhere in-between?

Therefore, the Langevin equation is better represented by a stochastic integral with the differential

$$\mathrm{d}\mathbf{r} = [(k_\mathrm{B}T)^{-1}\mathbf{D}\cdot\mathbf{f} + \partial_\mathbf{r}\cdot\mathbf{D}]\mathrm{d}t + \mathbf{H}\cdot\mathrm{d}\mathbf{w}\,, \tag{3.21}$$

where the according Wiener increments are defined by

$$\langle \mathrm{d}\mathbf{w}\rangle = \mathbf{0}\,, \tag{3.22}$$

$$\langle \mathrm{d}\mathbf{w}\mathrm{d}\mathbf{w}\rangle = \mathbf{1}\mathrm{d}t\,. \tag{3.23}$$

In addition, unlike for deterministic differential equations, we have to specify a rule for the integration, since different rules yield different forms for the differential $\mathrm{d}\mathbf{r}$ [86, 128, 190]. The above representation is to be interpreted in the *Itô sense*, i.e., the matrix $\mathbf{D}$ (and thus also $\mathbf{H}$) and the forces and torques $\mathbf{f}$ are evaluated at the beginning of the integration step. Alternatively, the Langevin equation could be interpreted in the *Stratonovich sense*, which uses the intermediate configuration after half an integration step. Both interpretations differ in the derivative $\partial_\mathbf{r}\cdot\mathbf{D}$ of the configuration-dependent diffusion matrix, an unexpected term which is yet to be explained.

The Langevin equation in the Itô representation (3.21) is obtained as follows from Eq. (3.2). The diffusive random displacements are of order $\sqrt{\mathrm{d}t}$, as can be seen from Eq. (3.14) (for $\Delta t \to \mathrm{d}t$). Therefore, the derivation of the correct evolution equation, i.e., exact up to order $\mathrm{d}t$, requires a second-order expansion in $\sqrt{\mathrm{d}t}$ [13, 70, 77, 94, 111]. Thus, it is essential to carry along the inertial term $\mathbf{I}\cdot\dot{\mathbf{v}}$ in Eq. (3.2) since it contains the second-order time derivatives of the particle coordinates; otherwise, the expansion would not be exact in second order. Keeping all terms of order $\sqrt{\mathrm{d}t}$ and $\mathrm{d}t$, Eq. (3.21) remains where the

inertial effects finally have been skipped (i.e., $\mathbf{I} = \mathbf{0}$), and we consider again the dynamics in the overdamped regime ($t \gg \tau_\mathrm{m}$).[6]

The first term in Eq. (3.21) is the deterministic, Stokesian-dynamics contribution, as $(k_\mathrm{B}T)^{-1}\mathbf{D}\cdot\mathbf{f} = \mathbf{M}\cdot\mathbf{f}$ is the drift velocity due to the deterministic forces and torques $\mathbf{f}$. The last term, $\mathbf{H}\cdot\mathrm{d}\mathbf{w}$, describes the Brownian displacement as discussed above [see Eq. (3.20)]. The second contribution, however, is not so obvious. The $6N$-dimensional vector $\partial_\mathbf{r}\cdot\mathbf{D}$ can be considered as the divergence of the diffusion matrix, where the symbol $\partial_\mathbf{r} = \mathrm{d}/\mathrm{d}\mathbf{r}$ denotes the $6N$-dimensional derivative related to the differential $\mathrm{d}\mathbf{r} = [\mathrm{d}\boldsymbol{r}_1, \ldots, \mathrm{d}\boldsymbol{r}_N, \mathrm{d}\boldsymbol{\phi}_1, \ldots \mathrm{d}\boldsymbol{\phi}_N]$. This additional term can be viewed as an additional drift velocity since it contributes linearly in $\mathrm{d}t$. In the literature, it is often refered to as *spurious drift* [190].[7] As it is proportional to the temperature T, this effect is *noise-induced*. Furthermore, it is already established on the time scale of momentum relaxation since it cannot be obtained from looking at a purely overdamped dynamics with zero mass.

3.1.5 Deterministic vs. diffusive motion

Equation (3.21) seems to suggest that the noise term ($\propto \sqrt{\mathrm{d}t}$) dominates the deterministic contribution ($\propto \mathrm{d}t$) when going to small time steps. However, the increasing strength of the noise is compensated by the increase in irregularity since more random events are needed to span a fixed time interval and thus the particles are kicked more often [91].

The relative importance of deterministic vs. random motion can be seen by writing Eq. (3.21) in a dimensionless form. The typical time that a particle needs to diffuse over a distance comparable to its own radius is given by a^2/D, where D is a characteristic value for the diffusion coefficient (typically the single-particle coefficient).[8] Using the dimensionless time step $\mathrm{d}t' = \mathrm{d}t/(a^2/D)$ and rescaling the other quantities in Eq. (3.21) according to $\mathrm{d}\mathbf{r}' = \mathrm{d}\mathbf{r}/a$, $\mathbf{f}' = \mathbf{f}/F$, $\mathbf{D}' = \mathbf{D}/D$, $\mathrm{d}\mathbf{w}' = \mathrm{d}\mathbf{w}/(a/\sqrt{D})$, and $\mathbf{H}' = \mathbf{H}/\sqrt{D}$, we obtain the dimensionless equation of motion [31, 113, 196]

$$\mathrm{d}\mathbf{r}' = (\mathrm{Pe}\,\mathbf{D}'\cdot\mathbf{f}' + \partial_{\mathbf{r}'}\cdot\mathbf{D}')\mathrm{d}t' + \mathbf{H}'\cdot\mathrm{d}\mathbf{w}'\,. \tag{3.24}$$

The dimensionless prefactor in front of the deterministic drift term is the *Péclet number* [60]

$$\mathrm{Pe} = \frac{Fa}{k_\mathrm{B}T}\,, \tag{3.25}$$

[6] An equivalent procedure to derive Eq. (3.21) considers overdamped dynamics from the very beginning but assumes at first a finite correlation time for the noise. At the end of the calculation, the limit of zero correlation time is taken [205].

[7] The attribute "spurious" may be misleading. It is not an unphysical effect, but part of the total drift observable in an experiment [211].

[8] For the sake of clarity, we restrict the discussion given here to *translational* degrees of freedom.

where F is a characteristic value for the force acting on the particles. Thus, the Péclet number compares the work needed to drive the particle a distance a to the thermal energy, i.e., it measures the importance of deterministic drift relative to diffusion. Introducing the characteristic drift velocity $v = (k_\mathrm{B}T)^{-1}DF$, Eq. (3.25) can also be written as

$$\mathrm{Pe} = \frac{va}{D} = \frac{a^2/D}{a/v} \,, \tag{3.26}$$

which is the ratio of the respective time that the particle needs to either diffuse or drift a distance comparable to its own radius.

Therefore, at large Péclet number, Brownian motion can be neglected, and we are in the regime of Stokesian dynamics [compare Eq. (2.62)], while at small Péclet number, the dynamics is predominantly governed by diffusion.[9]

3.2 The Smoluchowski equation

Instead of calculating explicit trajectories of a stochastic system by means of a Langevin equation, we can alternatively describe its stochastic dynamics by a probability distribution. In general, the evolution equation for the probability $p(X, P, t)$, where P denotes the conjugate momenta associated to the configurational coordinates X, is called *Fokker-Planck equation*. It is of the general form

$$\frac{\partial}{\partial t}\, p(X, P, t) = \mathcal{L}_\mathrm{FP}(X, P, t)\, p(X, P, t) \,, \tag{3.27}$$

where $\mathcal{L}_\mathrm{FP}$ is a differential operator with respect to all phase-space coordinates X and P. In the overdamped limit, where the particle momenta P are neglected, this equation is also called *Smoluchowski equation*:

$$\frac{\partial}{\partial t}\, p(X, t) = \mathcal{L}_\mathrm{S}(X, t)\, p(X, t) \,. \tag{3.28}$$

It can be shown that one can assign a unique Fokker-Planck equation to each Langevin equation [86, 190, 205]. Different Langevin equations that possess the same Fokker-Planck equation are stochastically and hence physically equivalent. The Smoluchowski equation that is equivalent to the Langevin equation (3.21) reads [70, 111, 182]

$$\frac{\partial}{\partial t}\, p(X, t) = \partial_\mathbf{r} \cdot \mathbf{D}(X) \cdot [\partial_\mathbf{r} - (k_\mathrm{B}T)^{-1}\mathbf{f}(X)\,]\, p(X, t) \,. \tag{3.29}$$

[9] Note that hydrodynamic interactions are often neglected at low Péclet numbers. However, it was demonstrated in simulations of sedimenting suspensions that hydrodynamic effects do play a role even at $\mathrm{Pe} = 0.1$ where viscous forces are much smaller than Brownian forces [191].

This equation can be interpreted as a diffusion equation [128], which is motivated as follows. Let us introduce the probability flux

$$\mathbf{j} = (\mathbf{M}\cdot\mathbf{f})p - \mathbf{D}\cdot\partial_{\mathbf{r}}p\,, \tag{3.30}$$

where the first term describes the deterministic drift with velocity $\mathbf{M}\cdot\mathbf{f}$, and the second term is a generalization of Fick's law, which assumes the diffusive probability flux to be linear in the gradient $\partial_{\mathbf{r}}p$. If the system is in thermal equilibrium, the distribution is stationary ($\partial p/\partial t = 0$), and the flux must vanish ($\mathbf{j} = \mathbf{0}$). Consider for the moment conservative forces $\mathbf{f} = -\partial_{\mathbf{r}}U$ with configuration-dependent potential energy U. Then, in equilibrium, the probability distribution must be given by the Boltzmann weight $p \propto \mathrm{e}^{-U/k_{\mathrm{B}}T}$. With $-U = k_{\mathrm{B}}T\ln p + \text{const}$, we can write the forces as

$$\mathbf{f} = k_{\mathrm{B}}T\,\partial_{\mathbf{r}}\ln p = k_{\mathrm{B}}T\,\frac{1}{p}\,\partial_{\mathbf{r}}p\,, \tag{3.31}$$

so the probability flux is now given by

$$\mathbf{j} = (k_{\mathrm{B}}T\,\mathbf{M} - \mathbf{D})\cdot\partial_{\mathbf{r}}p\,. \tag{3.32}$$

As thermal equilibrium requires $\mathbf{j} = \mathbf{0}$, we have to identify

$$\mathbf{D} = k_{\mathrm{B}}T\,\mathbf{M}\,, \tag{3.33}$$

which confirms the *Einstein relation* [17, 182] that we have already introduced in Sect. 3.1.3. It is stronlgy connected to the fluctuation-dissipation theorem since it also establishes a relation between the temperature-dependent fluctuations ($\mathbf{D}$) and the deterministic friction ($\mathbf{Z} = \mathbf{M}^{-1}$). From the continuity equation for the probability,

$$\frac{\partial p}{\partial t} + \partial_{\mathbf{r}}\cdot\mathbf{j} = 0 \quad \text{with} \quad \mathbf{j} = \mathbf{D}\cdot[(k_{\mathrm{B}}T)^{-1}\mathbf{f} - \partial_{\mathbf{r}}]p\,, \tag{3.34}$$

we finally obtain the Smoluchowski equation (3.29).

Assume that at time t the system occupies a definite state characterized by the configuration variable X_t. Then, the mean displacement during a short time interval Δt, $\langle\Delta\mathbf{r}_t\rangle = \mathcal{P}^{-1}(X_t)\cdot\Delta X_t$ [see Eq. (2.61a)] with

$$\begin{aligned}\langle\Delta X_t\rangle &= \int \mathrm{d}^{12N}X\, X[\,p(X,t+\Delta t) - p(X,t)] \\ &= \int \mathrm{d}^{12N}X\, X\Delta t\,\frac{\partial p(X,t)}{\partial t}\bigg|_{X=X_t}\end{aligned} \tag{3.35}$$

(neglecting higher orders in Δt), can be calculated with the help of Eq. (3.29). With $p(X,t) = \delta(X - X_t)$, we finally obtain [70]

$$\langle\Delta\mathbf{r}_t\rangle = [(k_{\mathrm{B}}T)^{-1}\mathbf{D}(X_t)\cdot\mathbf{f}(X_t) + \partial_{\mathbf{r}}\cdot\mathbf{D}(X_t)]\Delta t\,, \tag{3.36}$$

which is consistent with the results of Sect. 3.1. In particular, it reveals the spurious drift term $\partial_{\mathbf{r}} \cdot \mathbf{D}$ occuring in the differential Langevin equation (3.21). Calculating in the same way the second moment of the probability distribution $p(X,t)$ gives the diffusion law (3.14):[10]

$$\langle \Delta\mathbf{r}_t \Delta\mathbf{r}_t \rangle = 2\mathbf{D}(X_t)\Delta t\,. \tag{3.37}$$

3.3 Brownian-dynamics simulations

Brownian-dynamics simulations based on a Langevin equation can be considered as somewhere in-between Monte-Carlo and molecular-dynamics simulations, sharing the stochastic character with the former and the continuous trajectories with the latter. The concept of detailed balance (see, e.g., Ref. [186]), which plays a central role in equilibrium Monte-Carlo methods, is here replaced by the fluctuation-dissipation theorem (3.4).[11]

3.3.1 Numerical integration schemes

As in the case of deterministic differential equations, the simplest discretization scheme of the Langevin equation in the Itô form (3.21) is the *Euler step*

$$\Delta\mathbf{r}_t = [\mathbf{h}(X_t) + \partial_{\mathbf{r}} \cdot \mathbf{D}(X_t)]\Delta t + \mathbf{H}(X_t) \cdot \Delta\mathbf{w}_t\,, \tag{3.38}$$

which gives the configurational update $X_{t+\Delta t} = X_t + \Delta X_t$, given by $\Delta X_t = \mathcal{P}(X_t) \cdot \Delta\mathbf{r}_t$ according to Eq. (2.61). For brevity, we have introduced the notation

$$\mathbf{h}(X) = \mathbf{M}(X) \cdot \mathbf{f}(X) \tag{3.39}$$

for the deterministic drift velocity. As shown before, the diffusion matrix is given by the Einstein relation

$$\mathbf{D}(X) = k_{\mathrm{B}}T\,\mathbf{M}(X)\,, \tag{3.40}$$

where the mobility matrix $\mathbf{M}(X)$ is calculated by the methods presented in Chap. 2. The matrix $\mathbf{H}(X)$ as a solution of

$$2\mathbf{D}(X) = \mathbf{H}(X) \cdot \mathbf{H}^{\mathrm{T}}(X) \tag{3.41}$$

[10] To be more precise and consistent with the notation used in Sect. 3.1, we decompose the displacement into the deterministic part $\Delta\bar{\mathbf{r}}_t$ ($\propto \Delta t$) and the fluctuating part $\Delta\tilde{\mathbf{r}}_t$ ($\propto \sqrt{\Delta t}$), i.e., $\Delta\mathbf{r}_t = \Delta\bar{\mathbf{r}}_t + \Delta\tilde{\mathbf{r}}_t$. The second moment is given by $\langle \Delta\mathbf{r}_t \Delta\mathbf{r}_t \rangle = \langle \Delta\bar{\mathbf{r}}_t \Delta\bar{\mathbf{r}}_t \rangle + \langle \Delta\tilde{\mathbf{r}}_t \Delta\tilde{\mathbf{r}}_t \rangle$ since $\langle \Delta\tilde{\mathbf{r}} \rangle = \mathbf{0}$. Thus, to order Δt, $\langle \Delta\mathbf{r}_t \Delta\mathbf{r}_t \rangle = \langle \Delta\tilde{\mathbf{r}}_t \Delta\tilde{\mathbf{r}}_t \rangle$, so Eq. (3.37) is identical to Eq. (3.14).

[11] Hence, the temperature of the solvent is transferred to the suspended particles through the temperature dependence of the Brownian forces. In conventional molecular-dynamics simulations, the coupling to the heat bath is realized, e.g., through a Nosé-Hoover thermostat [81].

must be determined anew at each single step. This is most conveniently and efficiently done by *Cholesky decomposition* [70, 77], which will be described in Sect. 3.3.2. The Wiener increments $\Delta\mathbf{w}_t$ are $6N$ independent Gaussian random numbers each having zero mean and variance Δt. Furthermore, the increments at different times are independent of each other, too. We generate a new set of $6N$ independent random numbers ξ_i at each time step, obeying the Gaussian distribution[12]

$$p(\xi) = \frac{1}{2\pi}\,\mathrm{e}^{-\xi^2/2} \tag{3.42}$$

with zero mean and unit variance. Multiplying these numbers with $\sqrt{\Delta t}$, we obtain the correct Wiener increments,

$$\Delta\mathbf{w}_t = \begin{bmatrix} \xi_1 \\ \vdots \\ \xi_{6N} \end{bmatrix}_t \sqrt{\Delta t}\,, \tag{3.43}$$

satisfying the required properties (3.18) and (3.19). The algorithm we use to actually generate the Gaussian random numbers is presented in Sect. 3.3.3.

The main problem of this direct implementation is the enormous computational effort associated with the calculation of the multidimensional derivative $\partial_{\mathbf{r}} \cdot \mathbf{D}$ at each time step. Hence, the question arises how to avoid the explicit calculation of this term. If we calculate the hydrodynamic interactions in Oseen or Rotne-Prager approximation, the answer is readily given: The spurious drift vanishes identically since at that level only two-body interactions of identical spherical particles are taken into account (see Sect. 2.4.2), and thus $\partial_{\mathbf{r}} \cdot \mathbf{D} = \mathbf{0}$.[13] But for more accurate calculations (including many-body effects) of the hydrodynamic matrices, the divergence term has to be taken into account. By using two-step algorithms, however, it is possible to avoid the explicit calculation of $\partial_{\mathbf{r}} \cdot \mathbf{D}$ [13, 94, 117].

We use a predictor-corrector-type that is based on the concept of kinetic stochastic integrals [117]. First, the Euler step

$$\Delta\mathbf{r}_* = \mathbf{h}(X_t)\,\Delta t \,+\, \mathbf{H}(X_t) \cdot \Delta\mathbf{w}_t \tag{3.44a}$$

[12] For the Euler method (3.38), the random variables do not necessarily need to obey an exact Gaussian distribution [97, 190]. It is sufficient to use a uniform distribution with zero mean and unit variance, i.e., the first two moments have to be the same in order to obtain the same distribution of solutions.

[13] The positional components (i.e., the first $3N$ components related to $\mathrm{d}\boldsymbol{r}_i$) of the $6N$-dimensional vector $\partial_{\mathbf{r}} \cdot \mathbf{D}$ are given by sums of terms $\nabla_i \cdot \boldsymbol{D}^{\mathrm{tt}}_{ij}$. In the two-particle approximation, we can write $\boldsymbol{D}^{\mathrm{tt}}_{ij} = \boldsymbol{D}^{\mathrm{tt}}(\boldsymbol{r}_i - \boldsymbol{r}_j)$. Furthermore, for identical particles, the symmetry relation $\boldsymbol{D}^{\mathrm{tt}}_{ji} = \boldsymbol{D}^{\mathrm{tt}}_{ij}$ holds, so $\nabla_i \cdot \boldsymbol{D}^{\mathrm{tt}}_{ij} = \nabla_i \cdot \boldsymbol{D}^{\mathrm{tt}}(\boldsymbol{r}_i - \boldsymbol{r}_j) = \nabla_i \cdot \boldsymbol{D}^{\mathrm{tt}}(\boldsymbol{r}_j - \boldsymbol{r}_i) = -\nabla_i \cdot \boldsymbol{D}^{\mathrm{tt}}(\boldsymbol{r}_i - \boldsymbol{r}_j)$ and thus $\nabla_i \cdot \boldsymbol{D}^{\mathrm{tt}}_{ij} = \mathbf{0}$. The rotational terms (related to $\mathrm{d}\boldsymbol{\phi}_i$) do not play a role as long as we consider two-body interactions of particles with spherical shape and, in addition, without internal order that would break the spherical symmetry (like birefringent beads in an electric field).

is performed *without* the spurious drift. We then use the intermediate configuration $X_t + \Delta X_*$, with $\Delta X_* = \mathcal{P}(X_t) \cdot \Delta \mathbf{r}_*$, to calculate the corrector step

$$\begin{aligned} \Delta \mathbf{r}_t = {} & \tfrac{1}{2}[\mathbf{h}(X_t) + \mathbf{h}(X_t + \Delta X_*)]\Delta t \\ & + \tfrac{1}{2}[\mathbf{1} + \mathbf{D}(X_t + \Delta X_*) \cdot \mathbf{D}^{-1}(X_t)] \cdot \mathbf{H}(X_t) \cdot \Delta \mathbf{w}_t \,, \end{aligned} \tag{3.44b}$$

and we obtain the final configuration $X_{t+\Delta t} = X_t + \Delta X_t$, where $\Delta X_t = \mathcal{P}(X_t) \cdot \Delta \mathbf{r}_t$. By evaluating the diffusion matrix $\mathbf{D}$ at two different configurations (the initial configuration X_t and the mid-point configuration $X_t + \Delta X_*$, respectively), the divergence term $\partial_{\mathbf{r}} \cdot \mathbf{D}$ is implicitly accounted for. Note that the expression $\mathbf{H}(X_t) \cdot \Delta \mathbf{w}_t$ occuring in the corrector step is the same as the diffusive term that has already been calculated in the predictor step. Thus, computation time can be saved by calculating this term only once.

This two-step algorithm is weakly convergent to first order in Δt [117]. The term "weak convergence" means that not individual trajectories are of interest, but only the distribution of solutions of the stochastic differential equation [190]. For a constant diffusion matrix, the above scheme would actually be correct to order Δt^2. Note in this context that the deterministic part of this procedure is identical to the Heun algorithm (2.64).

There are also higher-order integration scheme of Runge-Kutta type available for stochastic differential equations [246]. These methods, however, require the time-consuming explicit calculation of the spatial derivatives of the diffusion matrix.

3.3.2 The Cholesky decomposition

For square matrices $\mathbf{A}$ that are symmetric and positive definite (as the diffusion matrix $\mathbf{D}$ is), there exists a very efficient triangular decomposition

$$\mathbf{A} = \mathbf{L} \cdot \mathbf{L}^{\mathrm{T}} \,, \tag{3.45}$$

where $\mathbf{L}$ is a lower triangular matrix. This procedure is referred to as *Cholesky decomposition*. In sloppy words, it can be considered as "taking the square root" of the matrix $\mathbf{A}$. The single elements of $\mathbf{L}$ can be determined recursively by applying the relations [198]

$$L_{ii} = \left(A_{ii} - \sum_{k=1}^{i-1} L_{ik}^2 \right)^{1/2} \,, \tag{3.46}$$

$$L_{ij} = \frac{1}{L_{ii}} \left(A_{ij} - \sum_{k=1}^{i-1} L_{ik} L_{jk} \right) \quad \text{for} \quad j = i+1, i+2, \ldots \tag{3.47}$$

in the order $i = 1, 2, \ldots$ Then, on the right-hand sides, only elements occur that have already been determined.

3.3.3 Generation of Gaussian random numbers

Suppose we generate a random number x with a given probability distribution $p(x)$ and want to know the probability distribution for a transformed variable $y = y(x)$. The transformation law for the probability is then simply $|p(y)\mathrm{d}y| = |p(x)\mathrm{d}x|$ or $p(y) = p(x)|\mathrm{d}x/\mathrm{d}y|$. The generalization to more than one dimension is straightforward. If $x_1, x_2, \ldots$ are random numbers with a joint probability distribution $p(x_1, x_2, \ldots)$ and if $y_1, y_2, \ldots$ are each functions of all the x_i, then the joint probability distribution of the y_i is given by [198]

$$p(y_1, y_2, \ldots) = p(x_1, x_2, \ldots) \left| \frac{\partial(x_1, x_2, \ldots)}{\partial(y_1, y_2, \ldots)} \right| , \tag{3.48}$$

where $\partial(\ldots)/\partial(\ldots)$ is the Jacobian determinant of the x_i with respect to the y_i (or the inverse of the Jacobian determinant of the y_i with respect to the x_i).

Now let x_1 and x_2 be two independent random numbers uniformly distributed on $(0, 1)$, and consider the transformation [30, 198]

$$y_1 = \sqrt{-2 \ln x_1} \, \cos 2\pi x_2 \, , \tag{3.49a}$$

$$y_2 = \sqrt{-2 \ln x_1} \, \sin 2\pi x_2 \tag{3.49b}$$

with the inversion

$$x_1 = \exp\left[-\frac{1}{2}(y_1^2 + y_2^2) \right] , \tag{3.50a}$$

$$x_2 = \frac{1}{2\pi} \arctan \frac{y_2}{y_1} \, . \tag{3.50b}$$

Then, the above transformation law for the probabilities yields

$$p(y_1, y_2) = \left| \det \begin{bmatrix} \frac{\partial x_1}{\partial y_1} & \frac{\partial x_1}{\partial y_2} \\ \frac{\partial x_2}{\partial y_1} & \frac{\partial x_2}{\partial y_2} \end{bmatrix} \right| = \frac{1}{\sqrt{2\pi}} \, \mathrm{e}^{-y_1^2/2} \cdot \frac{1}{\sqrt{2\pi}} \, \mathrm{e}^{-y_2^2/2} \, . \tag{3.51}$$

Thus, the so-called *Box-Muller method* (3.49) generates two independent random numbers satisfying each a *normal* or *Gaussian* distribution with zero mean and unit variance [30, 198].

There is a further trick to make the Box-Muller algorithm more efficient [198]. Instead of picking the random variables x_1 and x_2 on the unit square, we use points $(\bar{x}_1, \bar{x}_2)$ inside the unit circle around the origin, thus satisfying the condition $\bar{x}_1^2 + \bar{x}_2^2 < 1$. Then, the probability for the radial coordinate $r = \sqrt{\bar{x}_1^2 + \bar{x}_2^2}$ to be in $(r, r + \mathrm{d}r)$ is given by $2r\mathrm{d}r$, since the points $(\bar{x}_1, \bar{x}_2)$ are distributed homogeneously. Thus, r obeys the distribution $p(r) = 2r$. Transforming to the variable $s = r^2$, we must satisfy the condition $p(r)\mathrm{d}r = p(s)\mathrm{d}s$, where $\mathrm{d}s = \mathrm{d}(r^2) = 2r\mathrm{d}r$. By comparison, we obtain $p(s) = 1$, i.e., $s = \bar{x}_1^2 + \bar{x}_2^2$ is uniformly distributed on

$(0,1)$ and can be used instead of x_1. Obviously, the polar angle $\phi = \arctan \bar{x}_2/\bar{x}_1$ is a uniform random number, too, and can be used instead of $2\pi x_2$. The advantage of this transformation is that the cosine and sine in Eq. (3.49) can be now written as $\bar{x}_1/\sqrt{s}$ and $\bar{x}_2/\sqrt{s}$, respectively, thus avoiding calls of trigonometric functions. The Box-Muller method then reads: (i) pick two random numbers $\bar{x}_1$ and $\bar{x}_2$ uniformly distributed on $(-1,1)$; (ii) calculate $s = \bar{x}_1^2 + \bar{x}_2^2$ and accept $(\bar{x}_1, \bar{x}_2)$ only if $s < 1$ (otherwise, pick new numbers); (iii) the two independent Gaussian random numbers y_1 and y_2 are then given by $y_i = \sqrt{-2 \ln s/s}\, \bar{x}_i$.

This algorithm is implemented in the routine `gasdev` [198], which itself uses the widespread routine `ran1` [198] to generate the uniform deviates $\bar{x}_1$ and $\bar{x}_2$.

B | Two-point microrheology ■ Hydrodynamic coupling of rotating beads in optical traps

Abstract ■ We study the hydrodynamic coupling of two equal-sized colloidal spheres immersed in a Newtonian liquid at low Reynolds numbers. The particles are assumed to be harmonically trapped with respect to both their positions and orientations. By taking into account the rotational motion, we obtain a rich spectrum of collective eigenmodes whose properties we determine on the basis of pure symmetry arguments. Extending recent investigations on translational correlations [15, 179], we derive the complete set of self- and cross-correlation functions. We draw special attention to the rotational degree of freedom and how it couples to translational motion. An important feature of our system is the self-coupling of translation and rotation of one particle mediated by the neighboring particle. It thus shows a characteristic time delay that is clearly visible in the appropriate self-correlation function. We compare our analytical results with correlation functions determined from both Brownian-dynamics simulations and experiments.

4 Optical tweezers and microrheology

Complex fluids, such as colloidal suspensions, colloid-polymer mixtures, or soft biomaterials like cells, can act, to some degree, both like fluids and solids, depending on how one puts forces on them. Traditional rheology measures the combined viscous and elastic properties of a viscoelastic material by imposing an external shear strain. This, however, requires quite a considerable amount of the substance to be analyzed.

In recent years, a new method called *microrheology* has been developed and applied to several complex fluids, especially to biological materials. This technique requires only small amounts of substance. The outstanding advantage of microrheology is that it broadens our microscopic understanding of these complex materials on characteristic length scales of the constituents (e.g., the mesh size of filament networks). By monitoring the trajectories of embedded probe particles (tracers) and calculating the time-dependent positional and also orientational correlations, the rheological properties of the host medium can be determined.

To emphasize the context of this work, we point out that, in particular, hydrodynamic interactions and their effects on the particle dynamics can be measured systematically by this technique. (An overview of such experiments will be given in Sect. 4.3.)

Besides passive microrheology where one studies the thermal fluctuations of the probe particles, there are also active techniques where the tracer is pulled through the medium and the drag force or torque is measured. The manipulation of both particle positions and orientations can be performed by means of so-called *optical tweezers*, a powerful technique whose basics are illustrated in the subsequent sections.

4.1 Optical tweezers

4.1.1 Trapping of dielectric particles in a laser spot

The extremely high gradients in the electric field occuring near the waist of a tightly focused laser beam are associated with strong forces that can capture polarizable dielectric particles in three dimensions [5, 6, 181, 220]. This effect enables colloidal particles to be picked up and moved around by a laser beam. Therefore, the name *optical tweezer* has established for this technique. The forces

can be divided into those having their origin in the scattering of light (pointing in the direction of the incident beam) and those arising from intensity gradients (pointing in the direction of the latter). For particles of higher refractive index than the surrounding medium, the gradient forces dominate and the particles are pulled to the focus of the laser beam.

Tightly focused light generates a trapping potential that is harmonic over a fraction of the wavelength [206]. Thus, for sufficiently small displacements $\boldsymbol{r}$ of the trapped particle out of the focus (at $\boldsymbol{r} = \mathbf{0}$), the restoring tweezer potential can be considered, in good approximation, to be given by

$$U^{\mathrm{t}}(\boldsymbol{r}) = \frac{1}{2} \sum_{\alpha} k_{\alpha}^{\mathrm{t}} r_{\alpha}^2 \,, \tag{4.1}$$

where, in general, the trap stiffnesses k_{α}^{t} are different for the directions along the beam and perpendicular to it ($\alpha = x, y, z$). The superscript t symbolizes that this energy refers to translational motion. The stiffnesses can be determined experimentally from the mean-square displacements of the fluctuating particle via the equipartition theorem $\frac{1}{2} k_{\mathrm{B}} T = \frac{1}{2} k_{\alpha}^{\mathrm{t}} \langle r_{\alpha}^2 \rangle$.

A recent study shows good quantitative agreement between electromagnetic theory and the experimentally measured trap stiffnesses [206]. Overall, the trapping strength is proportional to the laser power. In beam direction, the trap is weaker than in the lateral directions as the field gradient along the beam is smaller than perpendicular to it. Furthermore, optical traps also reveal an asymmetry in the lateral trap stiffnesses and thus in the lateral extents of the trapping potential due to linear polarization of the laser beam. This effect, however, vanishes for particles whose size is comparable to the lateral focus extent, which is basically set by the wavelength of the trapping light.

Laser tweezers are widely used to study soft biomaterials [220]. In a number of experiments, colloidal beads are attached to cells or even single biomolecules, so forces can be exerted on these systems by trapping the beads optically and moving the laser focus. With this technique, one can perform single-molecule biomechanics and investigate, e.g., the stretching and unwinding of DNA [34, 96]. In particular, important insight has been gained in recent years how motor proteins work [178]. Laser-tweezer experiments can reveal, e.g., the force that a single molecular motor (here: RNA polymerase) exerts as it crawls along a DNA strand translating the code into RNA (the so-called transcription process) [241]. Furthermore, even bacteria and viruses can be trapped and manipulated in optical tweezers [7].

If the trapped particle has helical shape, deflection of light leads to a rotation of the particle, physically analogous to the rotation of windmills. This effect was demonstrated with complex "microturbines" built of light-curing resins by photopolymerization [83]. Another way to manipulate the orientation of trapped particles is to use polarized light and birefringent materials, as discussed in the following.

4.1.2 Rotation of birefringent particles in polarized traps

Due to the anisotropy in the dielectric polarizability, birefringent particles can couple to an external electric field, resulting in an orientation-dependent torque. Hence, orientational fluctuations can be suppressed by applying a constant electric field. On the other hand, if the field direction is rotated at a fixed frequency, a constant torque can be exerted on the birefringent particle.

Birefringent particles show a characteristic, orientation-dependent optical texture when viewed under crossed polarizers, which can be used to detect the orientation of the particle. It was demonstrated in several experiments that uniaxially birefringent particles, such as micron-sized quartz beads or polymerized liquid-crystalline droplets, e.g., are spinning in a circularly polarized laser beam [27, 28, 38, 127, 149, 213]. The hindered rotational diffusion of polymerized liquid-crystalline beads in an external field was investigated by applying a constant electric field, showing good agreement with theoretical results based on the Smoluchowski equation [180].

The potential energy density of a nematic liquid crystal with director field $\boldsymbol{n}$ in an electric field $\boldsymbol{E}$ is given by [90]

$$u^{\mathrm{LC}}(\boldsymbol{n}) = -\frac{\Delta\varepsilon}{8\pi}(\boldsymbol{n}\cdot\boldsymbol{E})^2\,, \tag{4.2}$$

where $\Delta\varepsilon = \varepsilon^{\parallel} - \varepsilon^{\perp}$ is the dielectric anisotropy of the liquid-crystalline material in the nematic phase ($\varepsilon^{\parallel}$ and $\varepsilon^{\perp}$ refer, respectively, to polarization parallel and perpendicular to $\boldsymbol{n}$). Therefore, the director preferably aligns (anti-)parallel to the field. The dependence of u^{LC} on $\boldsymbol{E}$ is quadratic since it is the energy of dipoles *induced* by the electric field.

Consider now a colloidal sphere of radius a with frozen (by polymerization) internal nematic order. Due to the curved boundaries, the director field is presumably not uniform. Thus, we define now $\boldsymbol{n}$ to be the *mean* orientation of the director field inside the particle. To correct for the deviations of the local director from $\boldsymbol{n}$, we have to introduce a geometric factor $g \leq 1$ [180]. Then, the total potential energy of the particle (i.e., integrated over the whole volume $\frac{4\pi}{3}a^3$) reads

$$U^{\mathrm{r}}(\boldsymbol{n}) = -\frac{1}{2}k^{\mathrm{r}}(\boldsymbol{n}\cdot\hat{\boldsymbol{E}})^2 \tag{4.3}$$

with the orientational trap stiffness $k^{\mathrm{r}} = \frac{1}{3}ga^3\Delta\varepsilon E^2$, and $\hat{\boldsymbol{E}} = \boldsymbol{E}/E$. The superscript r indicates that this potential applies to rotational motion of the particle. The factor g can also account for the fact that the electric field is not necessarily uniform, which is, e.g., the case for particles trapped in focused laser spots, obviously having a non-uniform intensity profile. In practice, the effective trap constant k^{r} is determined from orientational fluctuations by applying the equipartition theorem to the mean-square angular displacements.

4.2 Concepts of microrheology

The technique of optical tweezers presented above is perfectly suited for microrheology and has been very successfully applied in many experiments. In principle, we distinguish between *one-* [173] and *two-point microrheology* [50]. The former only considers the motion of a single probe particle, while the latter investigates the correlated dynamics of two particles which has several advantages that will be discussed below.

4.2.1 One-point microrheology

A simple experiment is to put a small tracer particle in a purely viscous fluid and study its thermal motion. The mean-square displacement of the tracer grows linearly in time, where the growth rate is determined by the diffusion constant. Thus, if temperature and particle size are known, viscosity can be measured.

Now imagine that we repeat the same experiment, but in a purely elastic medium. In this case, the tracer particle performs a random path in a confined region and never actually diffuses through the sample. In fact, the distance how far it can move (measured by the mean-square displacement in the long-time limit) is directly linked to the elasticity of the medium through the equipartition theorem applied to the potential energy, similar to the stretching of a spring.

In general, the motion of small tracer beads in a viscoelastic material can be directly related to the viscoelastic moduli characterizing the material. The same quantity, the mean-square displacement, is measured and analyzed to determine both viscous and elastic properties. From its nontrivial time dependence, the frequency dependence of the viscoelastic moduli can be obtained [162, 173]. Quite a number of experiments were performed using this approach to measure the viscoelastic shear moduli of complex fluids as, e.g., polymer gels [92, 174] or actin networks [85]. Furthermore, it has been demonstrated experimentally that the rotational diffusion of a colloidal bead in a viscoelastic host medium reveals the same rheological properties as translational diffusion [3].

So far, we described passive microrheology, which simply analyzes the thermal fluctuations of the tracer particles. An alternative method to measure the frequency dependence of the material properties directly is active microrheology, where an external force or torque oscillating with a fixed frequency is imposed and the (complex) amplitude of the particle motion is measured [151, 214].

4.2.2 Two-point microrheology

The microrheology technique as sketched above, however, may fail since many complex materials are inhomogeneous on small length scales. Thus, whenever the probe particle is smaller than the characteristic length scale of the inhomogeneities, it will explore the viscoelastic properties of the local environment rather

than those of the bulk material. In particular, the probe particles themselves may cause inhomogeneities if they disturb the complex fluid in some way.[1]

However, these problems can be circumvented by investigating the correlated motion of two probe particles placed at different positions [50]. Each particle performs Brownian motion, and if the particles are sufficiently close to each other, their motions are correlated. In a purely viscous fluid, the origin of these correlations are hydrodynamic interactions, while in a purely elastic medium, they stem from deformations of the elastic matrix. Generally speaking, the correlations depend on the viscoelastic moduli of the bulk material. It can be shown analytically that the *inter-particle* correlations are insensitive to the local particle environment and thus provide a more reliable method to investigate the bulk properties than do single-particle fluctuations [151]. One further advantage of this approach is that it does not depend on the size and shape of the tracer particles and not even on the coupling between the tracer and the medium at distances large compared to the tracer size [50]. Hence, this novel technique called *two-point microrheology* means a great improvement in the analysis of soft materials.

The combined application of one- and two-point microrheology can be exploited to gain important information on the local structure of the material. The differences in the measured friction coefficients of colloidal beads in polymer solutions, e.g., may give a hint that the nature of the shear coupling between the probe particle and the medium differs in the one- and two-particle situations. While the two-particle motions yield the bulk properties of the solution, the one-particle fluctuations are sensitive to the local interfacial zone immediately surrounding the particle. Hence, it was suggested that the discrepancies in the friction coefficients reflect the existence of a depletion zone (with lower polymer concentration) close to the particle [226]. Therefore, the medium might be better described by slip rather than stick boundary conditions. Furthermore, as one- and two-point microrheology are sensitive to different length scales, they probe different viscoelastic fluctuations having different relaxation time scales, which in turn leads to different frequency dependencies of the measured viscoelastic moduli [85].

4.3 Experiments measuring hydrodynamic interactions

The method of microrheology can be employed to study systematically the influence and characteristics of hydrodynamic interactions in viscous fluids. In a first

[1] A detailed scaling analysis [166] gives an estimate what size the tracer beads should at least have (depending on the characteristic length scales of the material to be analyzed, as, e.g., the persistence length of polymers) in order to measure the correct macroscopic values of the viscoelastic moduli instead of some local values. These theoretical findings were also confirmed experimentally [215].

experiment, the free diffusion of two spheres was recorded, and the diffusion coefficients was measured as a function of particle distance [49]. The results showed good agreement with the theoretical expectations obtained from the far-field expansion in powers of $1/r$ (see Sect. 2.4.2). Another type of experiments considers the hydrodynamically coupled translations of two beads that are trapped in separate optical tweezers [15, 108, 179]. This setup allows for a very accurate measurement of the distance dependence of the two-particle mobilities. It was also checked whether the presence of a polymer layer adsorbed or anchored on the particle surface (which is a common method of stabilizing colloids) modifies the hydrodynamic interactions [15].

Further experiments study the dynamics of colloidal beads close to flat walls. Theory predicts that, due to the hydrodynamic interaction of a particle with a wall, even the single-particle mobilities become position dependent [195]. In addition, also the inter-particle mobilities are modified [29, 44]. These predictions were tested experimentally for the diffusion of a single sphere between two parallel walls [22, 65] as well as for the two-particle interactions in the vicinity of a single wall [64] or confined between two walls [51, 61]). In the latter case, the hydrodynamic interactions between two particles are "screened" such that they decay to leading order as $1/r^2$ (instead of $1/r$ like in the case of an infinitely extended fluid). All these experiments reveal good agreement with existing theoretical predictions.

5 Theory of coupled motions of two trapped beads

So far, the *rotational* degree of freedom of colloidal particles and its coupling to translation has rarely been studied in the literature [56, 124, 139]. In particular, microrheological experiments and the accompanying theories investigating in detail the hydrodynamic interactions of two particles (as presented in Sec. 4.3) have exclusively considered *translational* motions [15, 108, 179]. In the following, we will therefore extend these investigations and give a complete analytical description of the coupled translational and rotational dynamics of two trapped particles. Thus, we will lay the basis for experimental studies including rotational motions.

5.1 Tweezer setup and dynamics of trapped particles

We consider two identical birefringent beads that are trapped with respect to both their positions and orientations by means of linearly polarized optical tweezers. As pointed out in Sect. 4.1.2, the particle orientations can be detected under crossed polarizers. We define a coordinate system such that the polarization $\hat{\boldsymbol{E}}$ of the traps sets the x direction and the center-center axis $\hat{\boldsymbol{r}}$ of the two beads coincides with the z direction, as illustrated in Fig. 5.1.

Due to the uniaxial symmetry of the two-sphere system, longitudinal motions parallel and transversal motions perpendicular to the particle-particle axis decouple from each other, as shown in Sect. 2.4.5. This greatly reduces the complexity of the problem, which can thus be split into (i) the decoupled translations along and rotations about z direction, and (ii) the coupled translations in x direction and rotations about the y axis. The coordinate system introduced in Fig. 5.1 is consistent with the one underlying the analysis presented in Sect. 2.4.5, thus we can immediately adopt the notation of Eqs. (2.49) and (2.50).

5.1.1 Forces and translational motion

By means of the harmonic potential (4.1), the trapping force on particle i in direction α is readily given by

$$F_{i,\alpha} = -k^{\mathrm{t}} r_{i,\alpha} \,, \tag{5.1}$$

where $r_{i,\alpha}$ is the displacement relative to the center of the trap. This linear approximation is valid for displacements that are small compared to the size of

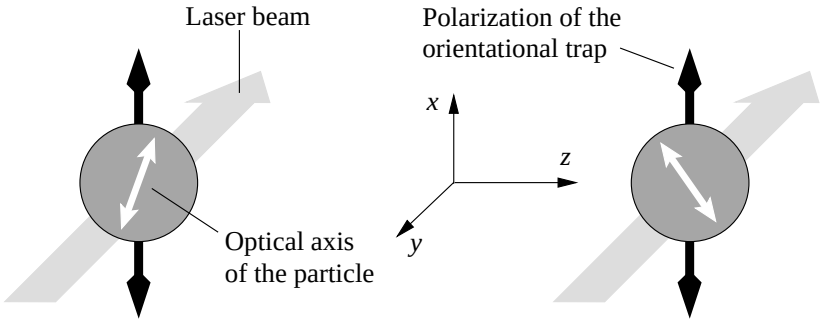

Figure 5.1 ■ Sketch of a setup to monitor rotational correlations of two birefringent particles. The particles are situated on the z axis. The laser beam of the orientational optical trap is directed along the y axis and its polarization points into x direction. To monitor the coupled transversal translations and rotations, the direction of observation is along the y axis. The purely rotational longitudinal motions are only observable along the z axis.

the laser spot, which is the case for thermal fluctuations in a sufficiently stiff trap. The translational velocities of the two beads can be directly identified as

$$v_{i,\alpha} = \dot{r}_{i,\alpha} \,. \tag{5.2}$$

Note that, in general, the trap stiffness k^{t} is different for different directions α. However, as the particles used in the experiment have a diameter comparable to the focal width of the trapping laser spot, this anisotropy between motions in x and z direction is not observed (see discussion in Sect. 4.1.1). Hence, we skip the indices α for the trap constants throughout our analysis.[1]

5.1.2 Torques and rotational motion

For small orientational fluctuations of the particles (i.e., $\boldsymbol{n}_i \approx \boldsymbol{e}_x$), we can decompose the rotational motions into separate rotations about the three coordinate axes, described by angles $\chi_{i,\alpha}$, as illustrated in Fig. 5.2. Due to the restoring potential $U^{\mathrm{r}}(\boldsymbol{n}_i)$ generated by the polarized trap, the angles $\chi_{i,y}$ and $\chi_{i,z}$ are restricted such that $\langle \chi_{i,y}^2 \rangle = \langle \chi_{i,z}^2 \rangle \ll 1$. They can be identified to leading order with the components of the vector $\boldsymbol{n}_i$, namely $n_{i,y} \approx \chi_{i,z}$ and $n_{i,z} \approx -\chi_{i,y}$ (see Fig. 5.2). The normalization condition $|\boldsymbol{n}_i| = 1$ then yields for the x component $n_{i,x}^2 \approx 1 - (\chi_{i,y}^2 + \chi_{i,z}^2)$, and thus, the orientational trap potential (4.3) to leading order reads

$$U^{\mathrm{r}}(\chi_{i,y}, \chi_{i,z}) \approx \frac{1}{2} k^{\mathrm{r}} (\chi_{i,y}^2 + \chi_{i,z}^2 - 1) \,. \tag{5.3}$$

[1] Translations in y direction do not play a role as they cannot be recorded in the setup shown in Fig. 5.1 (with observation along the y axis). As they do not couple to motions in the other directions, we can neglect them in our analysis.

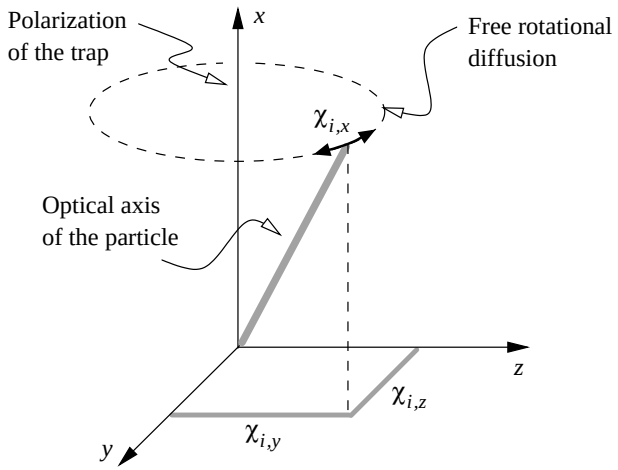

Figure 5.2 ■ While the rotation of the optical axis of the trapped particle about the direction of the trap polarization (pointing along the x axis in our setup) is free, the deviation from x direction is restricted by the trap, and therefore, the angular displacements $\chi_{i,y}$ and $\chi_{i,z}$ are small. On the relaxational time scale, the free rotational diffusion about the x axis can be neglected (see text).

Hence, the torques with respect to rotations about the y and z axis, respectively, are in harmonic approximation given by

$$T_{i,\alpha} = -k^{\mathrm{r}} \chi_{i,\alpha} \,. \tag{5.4}$$

As long as the angular displacements are small ($\langle \chi_{i,\alpha}^2 \rangle \ll 1$), we can relate them to the rotational velocities via

$$\omega_{i,\alpha} = \dot{\chi}_{i,\alpha} \,. \tag{5.5}$$

The above statements using independent angles $\chi_{i,\alpha}$ contain a nontrivial assumption and require some further explanation. The optical axis $\boldsymbol{n}_i$ of the birefringent particle aligns with the polarization $\hat{\boldsymbol{E}}$ of the laser trap, pointing along the x axis. Any deviation of the particle orientation from the x direction, described by the angles $\chi_{i,y}$ and $\chi_{i,z}$, relaxes in the optical trap on the time scale[2] $(\mu^{\mathrm{r}} k^{\mathrm{r}})^{-1}$. Rotations about the x axis, however, are not subject to the trap, i.e., the angle $\chi_{i,x}$ corresponds to free rotational diffusion. Since this diffusion of the particle axis also changes the angular displacements $\chi_{i,y}$ and $\chi_{i,z}$ (see Fig. 5.2), Eq. (5.5) obviously does not hold in general. Nevertheless, in the limit of strong trapping considered here, the orientational relaxation is a much faster process than the free diffusion. Hence, on the relaxation time scale, the free diffusion can be neglected and relation (5.5) is applicable. To verify this, we note that the free rotational diffusion takes place on the time scale[3] $(k_{\mathrm{B}} T \mu^{\mathrm{r}})^{-1}$. Thus, requiring

[2]The time scale of the orientational relaxation about y and z axis is set by the overdamped equation of motion $\dot{\chi}_{i,\alpha} = \omega_{i,\alpha} = \mu^{\mathrm{r}} T_{i,\alpha} = -\mu^{\mathrm{r}} k^{\mathrm{r}} \chi_{i,\alpha}$.

[3]The free rotation obeys the (short-time) diffusion law $\langle \chi_{i,x}^2 \rangle = 2 D^{\mathrm{r}} t$ (with $D^{\mathrm{r}} = k_{\mathrm{B}} T \mu^{\mathrm{r}}$). Note that D^{r} has the dimension of an inverse time, i.e., $1/D^{\mathrm{r}}$ directly sets the diffusive time scale.

the separation of the two time scales, i.e., $(k_\mathrm{B}T\mu^\mathrm{r})^{-1} \gg (\mu^\mathrm{r}k^\mathrm{r})^{-1}$, imposes the trap strength to satisfy the condition $k_\mathrm{B}T/k^\mathrm{r} \ll 1$. By means of the equipartition theorem $\langle\chi_{i,y}^2\rangle = \langle\chi_{i,z}^2\rangle = k_\mathrm{B}T/k^\mathrm{r}$, we finally recover the initial premise $\langle\chi_{i,\alpha}^2\rangle \ll 1$ for all directions α,[4] which proves the consistency of all assumptions.

5.2 Relaxational eigenmodes of two trapped spheres

Due to the decoupling of longitudinal and transversal motions, we can describe their dynamics by two independent sets of coordinates, represented by the four-dimensional vectors $\mathbf{q}^\parallel = [r_{1,z}, r_{2,z}, \chi_{1,z}, \chi_{2,z}]$ and $\mathbf{q}^\perp = [r_{1,x}, r_{2,x}, \chi_{1,y}, \chi_{2,y}]$. Analogously, we define the force and torque vectors $\mathbf{f}^\sigma$ ($\sigma = \parallel, \perp$) in directions parallel and perpendicular to the center-center axis [see Eqs. (2.49) and (2.50)]. The linear relations (5.1) and (5.4) can thus be written compactly as

$$\mathbf{f}^\sigma = -\mathbf{K}^\sigma \cdot \mathbf{q}^\sigma \tag{5.6}$$

with the diagonal matrix of trap constants

$$\mathbf{K}^\parallel = \mathbf{K}^\perp = \begin{bmatrix} k^\mathrm{t} & 0 & 0 & 0 \\ 0 & k^\mathrm{t} & 0 & 0 \\ 0 & 0 & k^\mathrm{r} & 0 \\ 0 & 0 & 0 & k^\mathrm{r} \end{bmatrix} . \tag{5.7}$$

The motion of the two spheres takes place at low Reynolds number, and the trajectories are measured on a time scale beyond momentum relaxation. According to Eqs. (5.2) and (5.5), the velocities in the present notation read $\dot{\mathbf{q}}^\sigma = \mathbf{v}^\sigma$, so using Eq. (2.51), both longitudinal and transversal dynamics is governed by a differential equation of the form

$$\dot{\mathbf{q}}^\sigma + \mathbf{M}^\sigma \cdot \mathbf{K}^\sigma \cdot \mathbf{q}^\sigma = \mathbf{0}\,, \tag{5.8}$$

where $\mathbf{M}^\sigma$ is the appropriate 4×4 mobility matrix given by Eqs. (2.49) and (2.50), respectively. For small spatial displacements of the fluctuating particles, the matrix $\mathbf{M}^\sigma$ can be considered constant and approximated by its values at equilibrium particle separation.[5] Hence, Eq. (5.8) is linear in $\mathbf{q}^\sigma$ and can be analyzed in terms of its eigenmodes.

The fundamental solutions of the first-order differential equation (5.8) are relaxational eigenmodes

$$\mathbf{q}_i^\sigma(t) = \mathrm{e}^{-\lambda_i^\sigma t}\mathbf{a}_i^\sigma \tag{5.9}$$

[4] The separation of diffusive and relaxation time scale implies that $\langle\chi_{i,x}^2\rangle \ll \langle\chi_{i,y}^2\rangle = \langle\chi_{i,z}^2\rangle$.

[5] Under typical experimental conditions, the root-mean-square displacement ranges from some 10 to 100 nm, while the particle separation is of the order of several μm [15, 108, 172].

with relaxation rates λ_i or relaxation times λ_i^{-1}, respectively ($i = 1, \ldots, 4$). They are determined by the eigenvalue problem

$$\mathbf{M}^\sigma \cdot \mathbf{K}^\sigma \cdot \mathbf{a}_i^\sigma = \lambda_i^\sigma \mathbf{a}_i^\sigma \,. \tag{5.10}$$

Note that, in general, the 4×4 matrix $\mathbf{M}^\sigma \cdot \mathbf{K}^\sigma$ is no longer symmetric. Therefore, its eigenvectors $\mathbf{a}_i^\sigma$ are not necessarily perpendicular to each other. In the next two sections, we will analyze the types of eigenmodes for longitudinal and transversal motions in detail.

5.2.1 Longitudinal modes

For longitudinal motions, translation (coordinates $q_1^\parallel = r_{1,z}$ and $q_2^\parallel = r_{2,z}$) and rotation ($q_3^\parallel = \chi_{1,z}$ and $q_4^\parallel = \chi_{2,z}$) are decoupled, as discussed in Sect. 2.4.5. This manifests itself in the structure of the mobility matrix $\mathbf{M}^\parallel$, which can be subdivided into two 2×2 matrices [see Eq. (2.49)]. As a consequence, the eigenvalue problem of the 4×4 matrix $\mathbf{M}^\parallel \cdot \mathbf{K}^\parallel$ essentially separates into two eigenvalue problems of symmetric 2×2 submatrices (one for purely translational and one for purely rotational motions):

$$\mathbf{M}^\parallel \cdot \mathbf{K}^\parallel = \begin{bmatrix} k^\mathrm{t} \begin{bmatrix} \mu_{11}^{\mathrm{tt}\parallel} & \mu_{12}^{\mathrm{tt}\parallel} \\ \mu_{12}^{\mathrm{tt}\parallel} & \mu_{11}^{\mathrm{tt}\parallel} \end{bmatrix} & \mathbf{0} \\ \mathbf{0} & k^\mathrm{r} \begin{bmatrix} \mu_{11}^{\mathrm{rr}\parallel} & \mu_{12}^{\mathrm{rr}\parallel} \\ \mu_{12}^{\mathrm{rr}\parallel} & \mu_{11}^{\mathrm{rr}\parallel} \end{bmatrix} \end{bmatrix} . \tag{5.11}$$

Thus, all eigenvectors are mutually perpendicular. We can immediately write down the complete set of eigenvalues and eigenvectors:

$$\lambda_{1/2}^\parallel = \left(\mu_{11}^{\mathrm{tt}\parallel} \pm \mu_{12}^{\mathrm{tt}\parallel}\right) k^\mathrm{t} \,, \qquad \mathbf{a}_{1/2}^\parallel = \begin{bmatrix} 1 \\ \pm 1 \\ 0 \\ 0 \end{bmatrix} , \tag{5.12a}$$

$$\lambda_{3/4}^\parallel = \left(\mu_{11}^{\mathrm{rr}\parallel} \pm \mu_{12}^{\mathrm{rr}\parallel}\right) k^\mathrm{r} \,, \qquad \mathbf{a}_{3/4}^\parallel = \begin{bmatrix} 0 \\ 0 \\ 1 \\ \pm 1 \end{bmatrix} . \tag{5.12b}$$

We can distinguish between relative ($-$) and collective ($+$) eigenmodes. Intuitive arguments allow a comparison of the respective relaxation rates. When the spheres translate in opposite directions (relative translational mode $\mathbf{a}_2^\parallel$), some fluid has to be pulled into or squeezed out of the region between the two particles; when they rotate in opposite directions (relative rotational mode $\mathbf{a}_4^\parallel$), the

fluid between the spheres has to be sheared. On the other hand, when the spheres translate or rotate collectively (modes $\mathbf{a}_1^{\parallel}$ or $\mathbf{a}_3^{\parallel}$), the fluid surrounding the spheres is just "displaced" or "rotated" as a whole. So the collective modes experience less hydrodynamic friction and therefore relax faster than the relative modes. This is in accordance with Eqs. (5.12) which give $\lambda_1^{\parallel} > \lambda_2^{\parallel}$ and $\lambda_3^{\parallel} > \lambda_4^{\parallel}$.

5.2.2 Transversal modes

The appropriate coordinates to treat transversal eigenmodes are $\mathbf{q}^{\perp} = [r_{1,x}, r_{2,x}, \chi_{1,y}, \chi_{2,y}]$, and the mobility matrix $\mathbf{M}^{\perp}$ is given by Eq. (2.50). However, the diagonalization of the nonsymmetric 4×4 matrix

$$\mathbf{M}^{\perp} \cdot \mathbf{K}^{\perp} = \begin{bmatrix} k^{\mathrm{t}} \begin{bmatrix} \mu_{11}^{\mathrm{tt}\perp} & \mu_{12}^{\mathrm{tt}\perp} \\ \mu_{12}^{\mathrm{tt}\perp} & \mu_{11}^{\mathrm{tt}\perp} \end{bmatrix} & k^{\mathrm{r}} \begin{bmatrix} -\mu_{11}^{\mathrm{tr}\perp} & -\mu_{12}^{\mathrm{tr}\perp} \\ \mu_{12}^{\mathrm{tr}\perp} & \mu_{11}^{\mathrm{tr}\perp} \end{bmatrix} \\ k^{\mathrm{t}} \begin{bmatrix} -\mu_{11}^{\mathrm{tr}\perp} & \mu_{12}^{\mathrm{tr}\perp} \\ -\mu_{12}^{\mathrm{tr}\perp} & \mu_{11}^{\mathrm{tr}\perp} \end{bmatrix} & k^{\mathrm{r}} \begin{bmatrix} \mu_{11}^{\mathrm{rr}\perp} & \mu_{12}^{\mathrm{rr}\perp} \\ \mu_{12}^{\mathrm{rr}\perp} & \mu_{11}^{\mathrm{rr}\perp} \end{bmatrix} \end{bmatrix} \tag{5.13}$$

is not immediately obvious. Nevertheless, symmetry arguments help to identify the eigenvectors $\mathbf{a}_i^{\perp}$ rather quickly. At first, since the two particles are identical, the amplitudes of the two translational components (denoted by $a^{\mathrm{t}\perp}$) must be the same, and likewise the two rotational ones (denoted by $a^{\mathrm{r}\perp}$). Secondly, since spatial and angular coordinates possess different parities, we can only combine symmetric translations (i.e., the two translational components have the same sign) with antisymmetric rotations (i.e., the two rotational components have opposite sign) and vice versa. Thus, the eigenvectors can only be of the form $[a^{\mathrm{t}\perp}, a^{\mathrm{t}\perp}, a^{\mathrm{r}\perp}, -a^{\mathrm{r}\perp}]$ or $[a^{\mathrm{t}\perp}, -a^{\mathrm{t}\perp}, a^{\mathrm{r}\perp}, a^{\mathrm{r}\perp}]$. This constraint simplifies the determination of the eigenmodes considerably. There are two eigenmodes of the first type showing symmetric translation and antisymmetric rotation,

$$\lambda_{1/2}^{\perp} = \frac{1}{2}\Big[\mu_{+}^{\mathrm{tt}\perp} k^{\mathrm{t}} + \mu_{-}^{\mathrm{rr}\perp} k^{\mathrm{r}} \pm \sqrt{\left(\mu_{+}^{\mathrm{tt}\perp} k^{\mathrm{t}} - \mu_{-}^{\mathrm{rr}\perp} k^{\mathrm{r}}\right)^2 + 4\left(\mu_{-}^{\mathrm{tr}\perp} k^{\mathrm{t}} k^{\mathrm{r}}\right)^2}\,\Big], \tag{5.14a}$$

$$\mathbf{a}_{1/2}^{\perp} = \begin{bmatrix} a_{1/2}^{\mathrm{t}\perp} \\ a_{1/2}^{\mathrm{t}\perp} \\ a_{1/2}^{\mathrm{r}\perp} \\ -a_{1/2}^{\mathrm{r}\perp} \end{bmatrix} \tag{5.14b}$$

with amplitudes

$$a_{1/2}^{\mathrm{t}\perp} = -2\mu_{-}^{\mathrm{tr}\perp} k^{\mathrm{r}}\,, \tag{5.14c}$$

$$a_{1/2}^{\mathrm{r}\perp} = -\left(\mu_{+}^{\mathrm{tt}\perp} k^{\mathrm{t}} - \mu_{-}^{\mathrm{rr}\perp} k^{\mathrm{r}}\right) \pm \sqrt{\left(\mu_{+}^{\mathrm{tt}\perp} k^{\mathrm{t}} - \mu_{-}^{\mathrm{rr}\perp} k^{\mathrm{r}}\right)^2 + 4\left(\mu_{-}^{\mathrm{tr}\perp}\right)^2 k^{\mathrm{t}} k^{\mathrm{r}}}\,. \tag{5.14d}$$

Here, we introduced the abbreviations $\mu_{\pm}^{\mathrm{tt}\perp} = \mu_{11}^{\mathrm{tt}\perp} \pm \mu_{12}^{\mathrm{tt}\perp}$, etc. The two modes of the second type with antisymmetric translation and symmetric rotation are

$$\lambda_{3/4}^{\perp} = \frac{1}{2}\left[\mu_{-}^{\mathrm{tt}\perp} k^{\mathrm{t}} + \mu_{+}^{\mathrm{rr}\perp} k^{\mathrm{r}} \pm \sqrt{\left(\mu_{-}^{\mathrm{tt}\perp} k^{\mathrm{t}} - \mu_{+}^{\mathrm{rr}\perp} k^{\mathrm{r}}\right)^2 + 4\left(\mu_{+}^{\mathrm{tr}\perp}\right)^2 k^{\mathrm{t}} k^{\mathrm{r}}}\right], \tag{5.15a}$$

$$\mathbf{a}_{3/4}^{\perp} = \begin{bmatrix} a_{3/4}^{\mathrm{t}\perp} \\ -a_{3/4}^{\mathrm{t}\perp} \\ a_{3/4}^{\mathrm{r}\perp} \\ a_{3/4}^{\mathrm{r}\perp} \end{bmatrix} \tag{5.15b}$$

with amplitudes

$$a_{3/4}^{\mathrm{t}\perp} = -2\mu_{+}^{\mathrm{tr}\perp} k^{\mathrm{r}}\,, \tag{5.15c}$$

$$a_{3/4}^{\mathrm{r}\perp} = -\left(\mu_{-}^{\mathrm{tt}\perp} k^{\mathrm{t}} - \mu_{+}^{\mathrm{rr}\perp} k^{\mathrm{r}}\right) \pm \sqrt{\left(\mu_{-}^{\mathrm{tt}\perp} k^{\mathrm{t}} - \mu_{+}^{\mathrm{rr}\perp} k^{\mathrm{r}}\right)^2 + 4\left(\mu_{+}^{\mathrm{tr}\perp}\right)^2 k^{\mathrm{t}} k^{\mathrm{r}}}\,. \tag{5.15d}$$

We note that all eigenvalues of $\mathbf{M}^{\perp} \cdot \mathbf{K}^{\perp}$ are positive, so in fact we only have relaxational modes. To prove this statement, we require $\lambda_i^{\perp} > 0$ in Eqs. (5.14a) and (5.15a) and find the conditions $\mu_{\pm}^{\mathrm{tt}\perp}\mu_{\mp}^{\mathrm{rr}\perp} > (\mu_{\mp}^{\mathrm{tr}\perp})^2$, which are basically the same guaranteeing that the mobility matrix itself is positive-definite[6] as they do not depend on k^{t} and k^{r} anymore.

Without relying on the exact values of all the mobility coefficients (which stronlgy depend on the particle separation), we can already infer the qualitative characteristics of the eigenmodes based on general arguments. As can be seen directly from Eqs. (5.14d) and (5.15d) without any further assumptions, the signs of the rotational components $a_{1-4}^{\mathrm{r}\perp}$ are independent of the mobility coefficients:

$$a_1^{\mathrm{r}\perp} > 0\,, \quad a_2^{\mathrm{r}\perp} < 0\,, \quad a_3^{\mathrm{r}\perp} > 0\,, \quad a_4^{\mathrm{r}\perp} < 0\,. \tag{5.16}$$

[6]The positive definiteness of the mobility matrices $\mathbf{M}^{\sigma}$ was shown in Sect. 2.4.5.

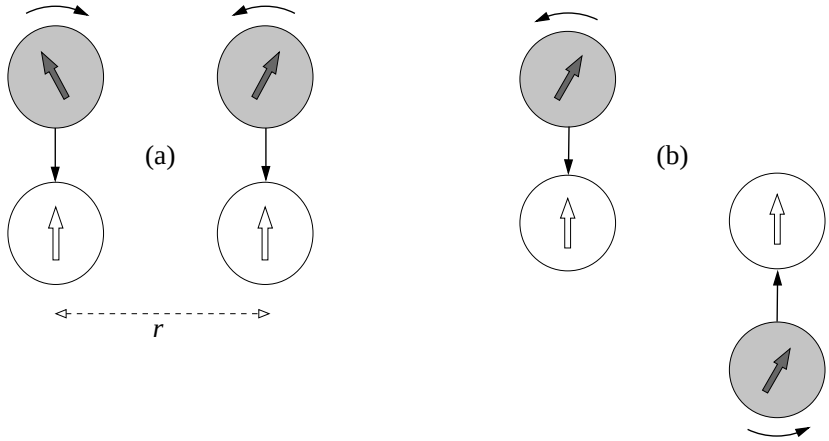

Figure 5.3 ■ Transversal eigenmodes of two trapped spheres (white: relaxed equilibrium state). There are two modes with collective (i.e., symmetric) translation and relative (i.e., antisymmetric) rotation (a) and two modes with relative translation and collective rotation (b). For each mode shown, there is a complementary mode with opposite direction of rotation.

The signs of the translational components $a_{1-4}^{\mathrm{t}\perp}$ depend on the signs of the mobilities $\mu_{\pm}^{\mathrm{tr}\perp}$ of coupled translation and rotation. In Sect. 2.4.2, we already discussed on the basis of the reflection method that the absolute value of the cross-mobility $\mu_{12}^{\mathrm{tr}\perp}$ is larger than the self mobility $\mu_{11}^{\mathrm{tr}\perp}$ since the latter is mediated by the second particle and requires thus at least one reflection of the flow field. Furthermore, for the special case $T_{2,y} > 0$ and $F_{1,x} = F_{2,x} = T_{1,y} = 0$, Eq. (2.50) yields $v_{1,x} = -\mu_{12}^{\mathrm{tr}\perp} T_{2,y}$ (for the geometry, see Fig. 2.3). Obviously, the resulting translational motion points in negative x direction ($v_{1,x} < 0$), so we infer that $\mu_{12}^{\mathrm{tr}\perp}$ is positive. Thus, $\mu_{+}^{\mathrm{tr}\perp} > 0$ and $\mu_{-}^{\mathrm{tr}\perp} < 0$, and we find

$$a_1^{\mathrm{t}\perp} > 0\,, \quad a_2^{\mathrm{t}\perp} > 0\,, \quad a_3^{\mathrm{t}\perp} < 0\,, \quad a_4^{\mathrm{t}\perp} < 0\,. \tag{5.17}$$

The eigenmodes described by Eqs. (5.14b) and (5.15b) are illustrated in Fig. 5.3. The mode shown in Fig. 5.3(a) corresponds to the eigenvector $\mathbf{a}_1^{\perp}$, and the one in Fig. 5.3(b) to $\mathbf{a}_3^{\perp}$. Each of the modes is complemented by a mode with opposite direction of rotation corresponding to the eigenvectors $\mathbf{a}_2^{\perp}$ and $\mathbf{a}_4^{\perp}$, respectively. Figure 5.3 shows the faster modes, i.e., $\lambda_1^{\perp} > \lambda_2^{\perp}$ and $\lambda_3^{\perp} > \lambda_4^{\perp}$. The reason for this is simply that the relaxations described by $\mathbf{a}_1^{\perp}$ and $\mathbf{a}_3^{\perp}$ show qualitatively the same behavior as if the particles were not trapped with respect to their orientations, which can be easily seen by taking the limit $k^{\mathrm{r}} \to 0$. Hence, $\mathbf{a}_2^{\perp}$ and $\mathbf{a}_4^{\perp}$ correspond to modes where the orientational relaxation is opposite to this "natural" direction of rotation. Therefore, these modes are slower compared to their respective partners $\mathbf{a}_1^{\perp}$ and $\mathbf{a}_3^{\perp}$. Furthermore, the mode represented by $\mathbf{a}_1^{\perp}$ is expected to be the fastest of all four modes since its translational and rotational components relax all collectively [Fig. 5.3(a)],[7] whereas the mode represented by

[7] "Collectively" means that the flow fields in-between the two beads superimpose *constructively*.

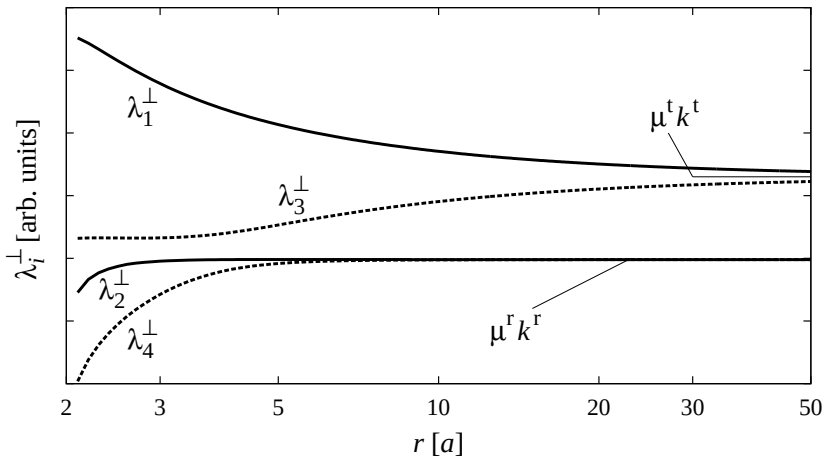

Figure 5.4 ■ Eigenvalues of the transversal modes [Eqs. (5.14a) and (5.15a)] as a function of the center-center distance r (in units of the particle radius a) in a semi-logarithmic plot. The mobilities were calculated using the numerical library HYDROLIB. The trap constants are chosen here as $k^r = k^t a^2$.

$\boldsymbol{a}_4^\perp$ is expected to be the slowest one since translational and rotational relaxations all counteract each other [Fig. 5.3(b) with opposite directions of rotation]. For collective motions, the velocity gradients and thus the shear stresses in-between the two spheres are rather small, while they are large for counteracting motions.

These qualitative findings are in agreement with exact numbers for the eigenvalues which we plot in Fig. 5.4 as a function of the particle distance. Furthermore, for large distances, rotational and translational motions decouple since $\lambda_1^\perp$ and $\lambda_3^\perp$ tend towards the single-particle translational relaxation rate $\mu^t k^t$ whereas $\lambda_2^\perp$ and $\lambda_4^\perp$ assume the corresponding rotational value $\mu^r k^r$. As obvious from the figure, this decoupling occurs for rotational motion at shorter distances compared to translational motion since rotational flow fields decay faster ($|\boldsymbol{u}(\boldsymbol{r})| \propto 1/r^2$) than translational ones ($|\boldsymbol{u}(\boldsymbol{r})| \propto 1/r$ for $r \gg a$).

5.3 Correlated Brownian motion of two trapped spheres

To treat the Brownian motion of the two trapped spheres, time-dependent random forces and torques $\tilde{\mathbf{f}}^\sigma(t)$ mimicking the microscopic degrees of freedom of the surrounding fluid have to be added to the harmonic trap forces and torques [Eq. (5.6)]. The total generalized force and torque vector is then

$$\mathbf{f}^\sigma = -\mathbf{K}^\sigma \cdot \mathbf{q}^\sigma + \tilde{\mathbf{f}}^\sigma(t)\,. \tag{5.18}$$

Thus, extending Eq. (5.8), we obtain the Langevin equation

$$\dot{\mathbf{q}}^\sigma + \mathbf{M}^\sigma \cdot \mathbf{K}^\sigma \cdot \mathbf{q}^\sigma = \tilde{\mathbf{v}}^\sigma(t)\,, \tag{5.19}$$

where

$$\tilde{\mathbf{v}}^\sigma(t) = \mathbf{M}^\sigma \cdot \tilde{\mathbf{f}}^\sigma(t) \tag{5.20}$$

are the velocities induced by the thermal noise. The random forces and torques $\tilde{\mathbf{f}}^\sigma(t)$ are assumed to be a Gaussian white noise with zero mean and correlations given by the fluctuation-dissipation theorem (3.4). This implies the following correlations for the noise-induced velocities:

$$\langle \tilde{\mathbf{v}}^\sigma(t)\tilde{\mathbf{v}}^\sigma(t')\rangle = 2k_\mathrm{B}T\,\mathbf{M}^\sigma\delta(t-t')\,. \tag{5.21}$$

Equation (5.19) is a linear first-order stochastic differential equation and describes a so-called *Ornstein-Uhlenbeck process* [86, 205].[8] Its complete solution formally reads

$$\mathbf{q}^\sigma(t) = \mathrm{e}^{-\mathbf{M}^\sigma\cdot\mathbf{K}^\sigma t}\cdot\mathbf{q}^\sigma(0) + \int_0^t \mathrm{d}t'\,\mathrm{e}^{-\mathbf{M}^\sigma\cdot\mathbf{K}^\sigma(t-t')}\cdot\tilde{\mathbf{v}}^\sigma(t')\,, \tag{5.22}$$

where the exponential of a square matrix $\mathbf{A}$ is defined by its Taylor series $\mathrm{e}^{\mathbf{A}} = \sum_{n=0}^{\infty}(1/n!)\mathbf{A}^n$. Since we are only interested in the fluctuating part of $\mathbf{q}^\sigma(t)$, we omit the deterministic relaxation $\mathrm{e}^{-\mathbf{M}^\sigma\cdot\mathbf{K}^\sigma t}\cdot\mathbf{q}^\sigma(0)$ due to an initial displacement by setting $\mathbf{q}^\sigma(0) = \mathbf{0}$. On average, we should anyway expect $\langle\mathbf{q}^\sigma(0)\rangle = \mathbf{0}$, which is the equilibrium state of the trapped particles. In calculating the correlation matrix of the displacements, we employ Eq. (5.21) and obtain[9]

$$\langle\mathbf{q}^\sigma(t)\mathbf{q}^\sigma(t')\rangle = k_\mathrm{B}T\left[\mathrm{e}^{-\mathbf{M}^\sigma\cdot\mathbf{K}^\sigma|t-t'|} - \mathrm{e}^{-\mathbf{M}^\sigma\cdot\mathbf{K}^\sigma(t+t')}\right]\cdot(\mathbf{K}^\sigma)^{-1}\,, \tag{5.23}$$

In the long-time limit ($\lambda_i^\sigma t \gg 1$), where the system has relaxed to thermal equilibrium, we can neglect the second term in Eq. (5.23), so the time correlation finally depends only on the time lag $\tau = |t-t'|$:

$$\langle\mathbf{q}^\sigma(t+\tau)\mathbf{q}^\sigma(t)\rangle = k_\mathrm{B}T\,\mathrm{e}^{-\mathbf{M}^\sigma\cdot\mathbf{K}^\sigma\tau}\cdot(\mathbf{K}^\sigma)^{-1} \quad \text{with} \quad \tau \geq 0\,. \tag{5.24}$$

Note that the condition $\tau \geq 0$ is not a restriction since the correlation matrix is symmetric, i.e., $\langle\mathbf{q}^\sigma(t+\tau)\mathbf{q}^\sigma(t)\rangle = \langle\mathbf{q}^\sigma(t)\mathbf{q}^\sigma(t+\tau)\rangle$, as can be immediately seen from Eq. (5.23).

To express the correlation functions explicitly in coordinates, we introduce the dual eigenvectors $\mathbf{b}_i^\sigma$ satisfying

$$(\mathbf{M}^\sigma\cdot\mathbf{K}^\sigma)^\mathrm{T}\cdot\mathbf{b}_i^\sigma = \lambda_i^\sigma\mathbf{b}_i^\sigma\,. \tag{5.25}$$

[8] Note that we are not concerned with the spurious drift $\partial_{\mathbf{q}^\sigma}\cdot\mathbf{D}^\sigma$ (see Sect. 3.1.4) since we assume the mobility to be constant in this linear approximation.

[9] Here we used the identity $\mathbf{A}\cdot\mathrm{e}^{\mathbf{B}\cdot\mathbf{A}} = \mathrm{e}^{\mathbf{A}\cdot\mathbf{B}}\cdot\mathbf{A}$ for two square matrices $\mathbf{A}$ and $\mathbf{B}$, which can be easily derived from the series representation of the matrix exponential.

Together with the eigenvectors $\mathbf{a}_i^\sigma$ of the matrix $\mathbf{M}^\sigma \cdot \mathbf{K}^\sigma$, they fulfill the orthonormality and completeness relations[10]

$$\mathbf{a}_i^\sigma \cdot \mathbf{b}_j^\sigma = \delta_{ij} \quad \text{and} \quad \sum_{i=1}^{4} \mathbf{a}_i^\sigma \mathbf{b}_i^\sigma = \mathbf{1}\,. \tag{5.26}$$

Representing the matrix exponential by its spectral decomposition,

$$\mathrm{e}^{-\mathbf{M}^\sigma \cdot \mathbf{K}^\sigma t} = \sum_{i=1}^{4} \mathrm{e}^{-\lambda_i^\sigma t} \mathbf{a}_i^\sigma \mathbf{b}_i^\sigma\,, \tag{5.27}$$

we obtain from Eq. (5.24) the coordinate form

$$\langle q_m(t+\tau) q_n(t)\rangle = \frac{k_\mathrm{B}T}{K_{nn}^\sigma} \sum_{i=1}^{4} \mathrm{e}^{-\lambda_i^\sigma \tau} a_{i,m}^\sigma b_{i,n}^\sigma\,, \tag{5.28}$$

where $a_{i,m}^\sigma$ ($b_{i,n}^\sigma$) is the mth (nth) component of the vector $\mathbf{a}_i^\sigma$ ($\mathbf{b}_i^\sigma$) and K_{nn}^σ the nth element of the diagonal matrix $\mathbf{K}^\sigma$ ($K_{nn}^\sigma = k^\mathrm{t}, k^\mathrm{t}, k^\mathrm{r}, k^\mathrm{r}$). Normalizing the correlation function to the square roots of the mean-square displacements $\langle (q_n^\sigma)^2\rangle = k_\mathrm{B}T/K_{nn}^\sigma$, we finally arrive at

$$\frac{\langle q_m^\sigma(t+\tau) q_n^\sigma(t)\rangle}{\sqrt{\langle (q_m^\sigma)^2\rangle \langle (q_n^\sigma)^2\rangle}} = \sqrt{\frac{K_{mm}^\sigma}{K_{nn}^\sigma}} \sum_{i=1}^{4} \mathrm{e}^{-\lambda_i^\sigma \tau} a_{i,m}^\sigma b_{i,n}^\sigma\,. \tag{5.29}$$

5.3.1 Longitudinal fluctuations

Longitudinal motions ($\sigma = \parallel$) are characterized by the eigenvectors and eigenvalues in Eq. (5.12). As the eigenvectors $\mathbf{a}_i^\parallel$ are all mutually perpendicular to each other, the dual eigenvectors $\mathbf{b}_i^\parallel$ are identical to $\mathbf{a}_i^\parallel$. We recall that translations and rotations are decoupled. So finally, the auto- and cross-correlation functions for rotational motions only (coordinates $q_3^\parallel = \chi_{1,z}$ and $q_4^\parallel = \chi_{2,z}$) are given by

$$\frac{\langle \chi_{1,z}(t+\tau)\chi_{1,z}(t)\rangle}{\langle \chi_{1,z}^2\rangle} = \frac{1}{2}\left[\mathrm{e}^{-(\mu_{11}^{\mathrm{rr}\parallel}+\mu_{12}^{\mathrm{rr}\parallel})k^\mathrm{r}\tau} + \mathrm{e}^{-(\mu_{11}^{\mathrm{rr}\parallel}-\mu_{12}^{\mathrm{rr}\parallel})k^\mathrm{r}\tau}\right], \tag{5.30a}$$

$$\frac{\langle \chi_{1,z}(t+\tau)\chi_{2,z}(t)\rangle}{\langle \chi_{1,z}^2\rangle} = \frac{1}{2}\left[\mathrm{e}^{-(\mu_{11}^{\mathrm{rr}\parallel}+\mu_{12}^{\mathrm{rr}\parallel})k^\mathrm{r}\tau} - \mathrm{e}^{-(\mu_{11}^{\mathrm{rr}\parallel}-\mu_{12}^{\mathrm{rr}\parallel})k^\mathrm{r}\tau}\right], \tag{5.30b}$$

with mean-square angular displacements $\langle \chi_{1,z}^2\rangle = \langle \chi_{2,z}^2\rangle = k_\mathrm{B}T/k^\mathrm{r}$. For translations (coordinates $q_1^\parallel = r_{1,z}$ and $q_2^\parallel = r_{2,z}$), the correlation functions are the same,

[10] This can be shown as follows. Let $\mathbf{a}_i$ be the eigenvectors of an arbitrary square matrix $\mathbf{A}$ with eigenvalues λ_i, i.e., $\mathbf{A}\cdot\mathbf{a}_i = \lambda_i \mathbf{a}_i$. The transpose matrix $\mathbf{A}^\mathrm{T}$ has the same eigenvalues; its eigenvectors $\mathbf{b}_i$ thus satisfy the relation $\mathbf{A}^\mathrm{T}\cdot\mathbf{b}_j = \lambda_j \mathbf{b}_j$. From this, we obtain $\lambda_i \mathbf{a}_i\cdot\mathbf{b}_j = (\mathbf{A}\cdot\mathbf{a}_i)\cdot\mathbf{b}_j = \mathbf{a}_i\cdot(\mathbf{A}^\mathrm{T}\cdot\mathbf{b}_j) = \lambda_j(\mathbf{a}_i\cdot\mathbf{b}_j)$. Thus, for $i=j$, we obtain $\mathbf{a}_i\cdot\mathbf{b}_i = 1$. In general, $\lambda_i \neq \lambda_j$ for $i \neq j$, and hence $\mathbf{a}_i\cdot\mathbf{b}_j = 0$. Altogether, we finally obtain $\mathbf{a}_i\cdot\mathbf{b}_j = \delta_{ij}$, which was to be proven.

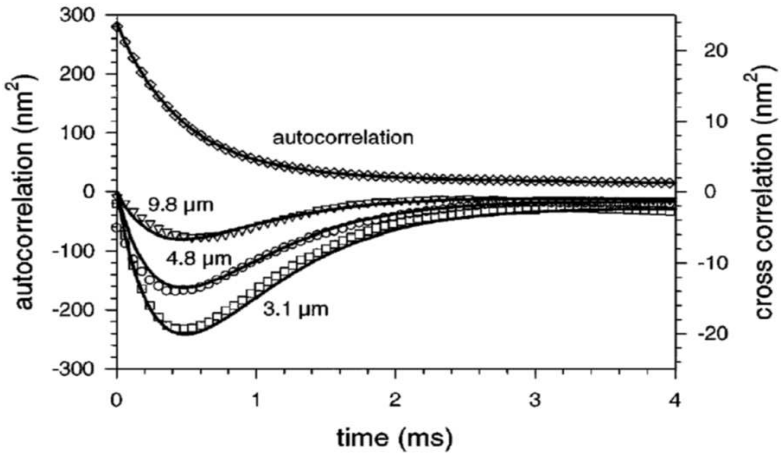

Figure 5.5 ■ Correlation functions for longitudinal translations, $\langle r_{1,z}(t+\tau)r_{1,z}(t)\rangle$ and $\langle r_{1,z}(t+\tau)r_{2,z}(t)\rangle$ (redrawn from Ref. [179]). The symbols represent experimental data, and the solid lines are the theoretical predictions. The lower curves show the cross-correlation functions for particle separations $r = 9.8$, 4.8, and 3.1 μm, respectively; the particle radius was $a = 0.5$ μm. The depth of the minimum decays to leading order as $1/r$.

except that the relaxation rates $(\mu_{11}^{\mathrm{rr}\parallel} \pm \mu_{12}^{\mathrm{rr}\parallel})k^{\mathrm{r}}$ are replaced by the respective translational eigenvalues $(\mu_{11}^{\mathrm{tt}\parallel} \pm \mu_{12}^{\mathrm{tt}\parallel})k^{\mathrm{t}}$ [15, 179].

The correlations for translational motions have already been measured experimentally and compared with theoretical predictions (see Fig. 5.5) [15, 108, 179]. These works reveal good agreement between theory and experiment. The correlation functions for rotational motions, as illustrated in Fig. 5.6, show the same qualitative behavior, however with some quantitative differences.

First of all, we realize that the strength of the cross-correlations decreases with increasing particle separation. This is explained by the decrease of the cross-mobility $\mu_{12}^{\mathrm{rr}\parallel}$, which essentially represents the hydrodynamic coupling of the two beads, due to the spatial decay of the flow fields created by the particle rotation. Compared to translational motions, this decrease is more pronounced since rotational flow fields decay stronger than their translational counterparts (see Sect. 2.2).

Secondly, while the auto-correlation function (5.30a) reveals the typical monotonous decay, the cross-correlation function (5.30b) features an interesting behavior. It is negative (denoted as "anti-correlation" in Ref. [179]) since the relative modes decay more slowly than the collective ones, as already mentioned in Sect. 5.2.1. Therefore, the negative second term in the cross-correlation function (5.30b) dominates.

The most interesting feature of the cross-correlation function is that it exhibits a "memory effect". It vanishes at $\tau = 0$, in contrast to what one would initially expect for the *instantaneous* hydrodynamic forces in Stokesian dynamics, and then shows a distinct time-delayed extremum (located at τ^* in Fig. 5.6). This

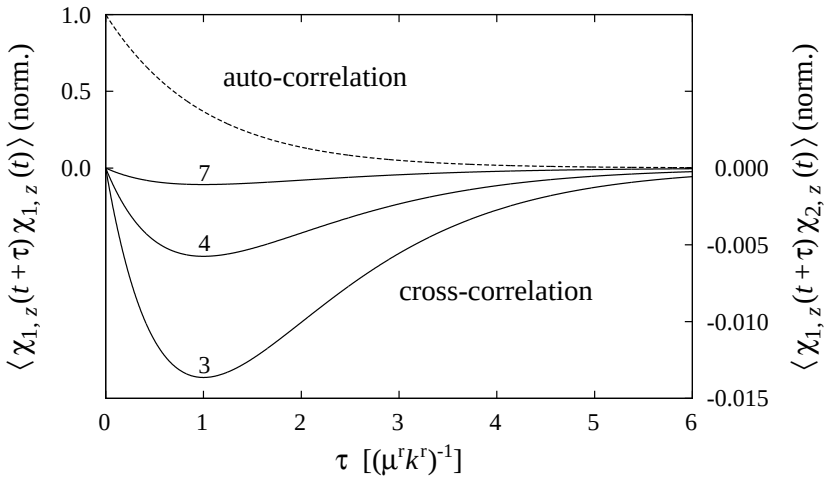

Figure 5.6 ■ Correlation functions for longitudinal rotations. The curve labels indicate the dimensionless center-center distance r/a. The time is measured in units of the orientational relaxation time $(\mu^{\mathrm{r}}k^{\mathrm{r}})^{-1}$. The correlation functions are normalized to the mean-square angular displacement $\langle\chi_{i,z}^2\rangle = k_{\mathrm{B}}T/k^{\mathrm{r}}$. The depth of the minimum decays to leading order as $1/r^3$.

behavior can be understood as follows. The motion of particle 1 creates a fluid flow which instantaneously reaches particle 2. However, due to the trap, particle 2 can only "react" in a finite time, so the past history of particle 1 is somehow "encoded" in the present state of particle 2 [179]. Thus, the correlation evolves on a characteristic time scale which is related to the relaxation times and thereby to the trap stiffness. Since the "memory" is "stored" in the trap, it obviously cannot last longer than the typical relaxation time. Hence, the correlation decays to zero for times larger than τ^*.

For sufficiently large particle distances, the self-mobility $\mu_{11}^{\mathrm{rr}\parallel}$ is much bigger than the cross-mobility $\mu_{12}^{\mathrm{rr}\parallel}$. Then, to leading order, the characteristic time scale is given by the single-particle rotational relaxation time, i.e., $\tau^* = (\mu^{\mathrm{r}}k^{\mathrm{r}})^{-1}$, in analogy to the translational case [15, 179]. Indeed, according to Fig. 5.6, the time lag τ^* depends only very weakly on the particle distance. Nevertheless, the cross-mobility $\mu_{12}^{\mathrm{rr}\parallel}$ is sufficiently large to separate the time scales $[(\mu_{11}^{\mathrm{rr}\parallel}+\mu_{12}^{\mathrm{rr}\parallel})k^{\mathrm{r}}]^{-1}$ and $[(\mu_{11}^{\mathrm{rr}\parallel}-\mu_{12}^{\mathrm{rr}\parallel})k^{\mathrm{r}}]^{-1}$ of the two eigenmodes, which is the origin of the "anti-correlation". The depth of the extremum in the cross-correlation function at τ^*, however, is strongly distance-dependent. To leading order, it is given by $\mathrm{e}^{-1}\mu_{12}^{\mathrm{rr}\parallel}/\mu_{11}^{\mathrm{rr}\parallel}$ [15, 179] and hence decays as $1/r^3$ (in contrast to $1/r$ in case of the translational correlations).

5.3.2 Transversal fluctuations

The transversal eigenmodes ($\sigma = \perp$) are characterized by Eqs. (5.14) and (5.15), respectively. Since the two types of eigenvectors are orthogonal to each other,

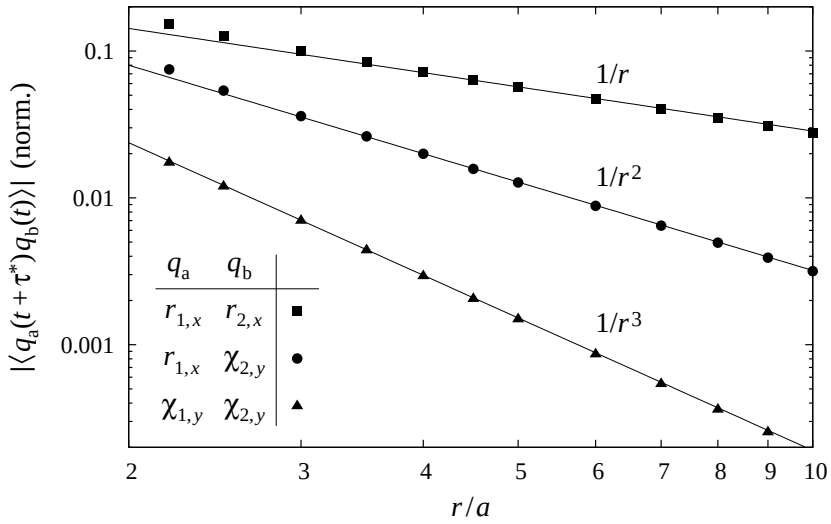

Figure 5.7 ■ Strength of transversal cross-correlations, plotted as a function of particle distance r (in units of the particle radius a). The symbols denote the height/depth $|\langle q_a(t+\tau^*)q_b(t)\rangle|$ of the time-delayed peak/dip in the correlation functions at time lag τ^*, extracted from calculated correlation functions (with trap constants $k^r = k^t a^2$). The values are normalized to the square roots of the mean-square displacements $\langle q_a^2\rangle$ and $\langle q_b^2\rangle$. The solid lines indicate the respective asymptotic decay. The translation-translation coupling ($q_a = r_{1,x}$, $q_b = r_{2,x}$) decays as $1/r$, the translation-rotation coupling ($q_a = r_{1,x}$, $q_b = \chi_{2,y}$) as $1/r^2$, and the rotation-rotation coupling ($q_a = \chi_{1,y}$, $q_b = \chi_{2,y}$) as $1/r^3$.

i.e., $\mathbf{a}^\perp_{1/2} \cdot \mathbf{a}^\perp_{3/4} = 0$, the dual vectors $\mathbf{b}^\perp_{1/2}$ are linear combinations of $\mathbf{a}^\perp_1$ and $\mathbf{a}^\perp_2$ only; the equivalent holds for $\mathbf{b}^\perp_{3/4}$. One finds the relation

$$\mathbf{b}^\perp_i = \frac{|\mathbf{a}^\perp_{i'}|^2 \mathbf{a}^\perp_i - (\mathbf{a}^\perp_i \cdot \mathbf{a}^\perp_{i'})\mathbf{a}^\perp_{i'}}{|\mathbf{a}^\perp_i|^2 |\mathbf{a}^\perp_{i'}|^2 - (\mathbf{a}^\perp_i \cdot \mathbf{a}^\perp_{i'})^2} \,, \tag{5.31}$$

where the index combinations are $(i|i') = (1|2), (2|1), (3|4), (4|3)$. The correlation functions for the coordinates $q^\perp_1 = r_{1,x}$, $q^\perp_2 = r_{2,x}$, $q^\perp_3 = \chi_{1,y}$, and $q^\perp_4 = \chi_{2,y}$ are obtained from Eq. (5.29). They are superpositions of four exponential decays.

The auto-correlation functions, $\langle r_{1,x}(t+\tau)r_{1,x}(t)\rangle$ and $\langle \chi_{1,y}(t+\tau)\chi_{1,y}(t)\rangle$, show qualitatively the same monotonous decay as in the case of longitudinal fluctuations (see Figs. 5.5 and 5.6, upper curves). All the other correlation functions exhibit the features of the longitudinal cross-correlations discussed in Sect. 5.3.1, in particular the characteristic peak or dip with time delay τ^*.

The amplitude of the peak or dip in the correlation functions depends on the particle distance. In Fig. 5.7, we compare the asymptotic behavior of the amplitudes $\langle r_{1,x}(t+\tau^*)r_{2,x}(t)\rangle$, $\langle r_{1,x}(t+\tau^*)\chi_{2,y}(t)\rangle$, and $\langle \chi_{1,y}(t+\tau^*)\chi_{2,y}(t)\rangle$ as functions of the distance r. As could be expected, the translation-translation correlation decays as $1/r$, the translation-rotation correlation as $1/r^2$, and the rotation-rotation correlation as $1/r^3$. This is consistent with the leading-order

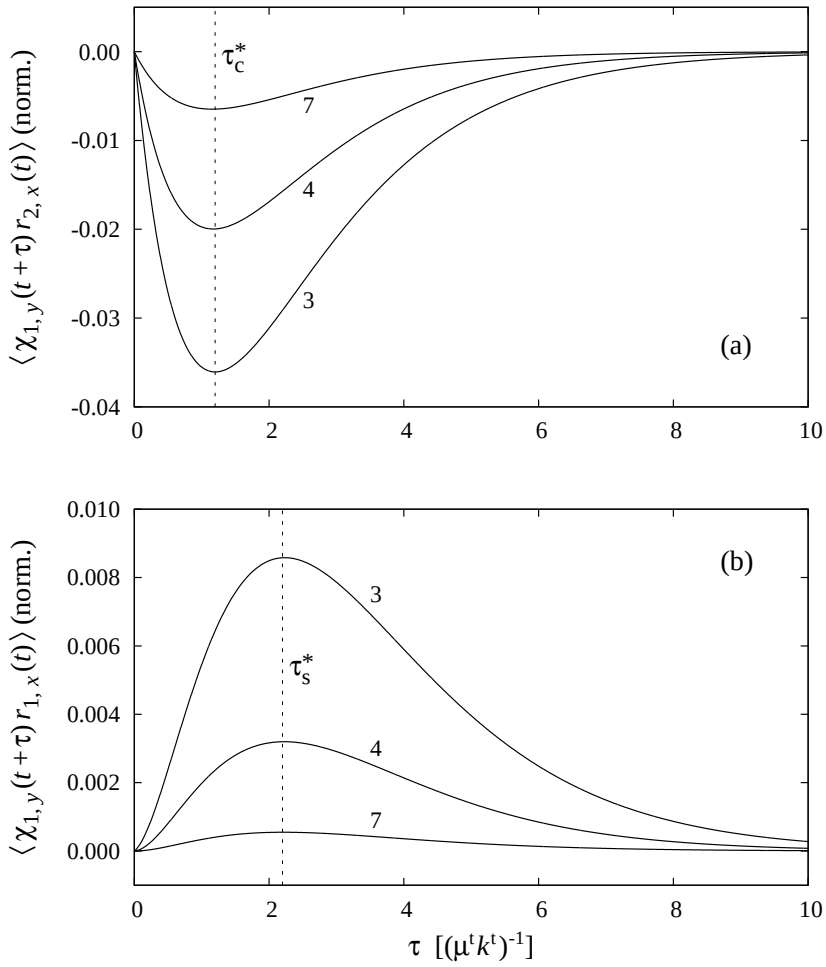

Figure 5.8 ■ Correlation functions for transversal motions. The curves shown are the mixed cross- (a) and self-correlation (b) for angle and position. The trap constants were chosen as $k^r = k^t a^2$. The curve labels indicate the dimensionless center-center distance r/a. The time is measured in units of the positional relaxation time $(\mu^t k^t)^{-1}$. The correlation functions are normalized to the square roots of the mean-square displacements $\langle \chi_{i,y}^2 \rangle = k_B T/k^r$ and $\langle r_{i,x}^2 \rangle = k_B T/k^t$ [see Eq. (5.29)].

terms of the mobilities $\boldsymbol{\mu}_{ij}^{tt}$, $\boldsymbol{\mu}_{ij}^{tr}$, and $\boldsymbol{\mu}_{ij}^{rr}$, respectively [see Eq. (2.39)], which are the essential coupling constants.

The respective signs of the correlation functions can be understood as follows. As discussed in Sect. 5.2.2, the relaxational mode represented by the eigenvector $\boldsymbol{a}_4^{\perp}$ [Fig. 5.3(b) with opposite angular displacements, i.e., $\chi_{i,y} > 0$] is the slowest of all four transversal modes. Therefore, it determines the long-time behavior and thus the signs of the correlation functions. So, for instance, $\langle \chi_{1,y}(t+\tau) r_{2,x}(t) \rangle < 0$ since $\chi_{1,y} > 0$ and $r_{2,x} < 0$ in this mode, or $\langle \chi_{1,y}(t+\tau) r_{1,x}(t) \rangle > 0$ since $\chi_{1,y} > 0$ and $r_{1,x} > 0$ (compare Figs. 5.8).

As representative examples, the correlation functions for rotations about the y axis and translations along x direction, $\langle \chi_{1,y}(t+\tau) r_{1,x}(t) \rangle$ and $\langle \chi_{1,y}(t+\tau) r_{2,x}(t) \rangle$,

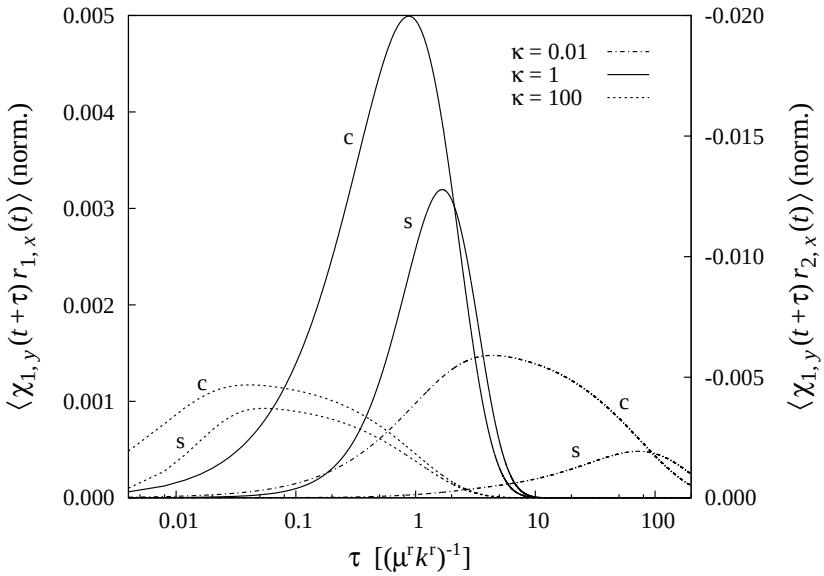

Figure 5.9 ■ Mixed self- (label s) and cross-correlation (label c) for various trap-constant ratios $\kappa = k^{\mathrm{t}}a^2/k^{\mathrm{r}}$. The force constant k^{t} was varied, while the torque constant k^{r} was kept fixed. The time is measured in units of the orientational relaxation time $(\mu^{\mathrm{r}}k^{\mathrm{r}})^{-1}$. The qualitative behavior of the functions (discussion see text) is the same for different particle distances (here: $r = 4a$). Note the different scaling of the two vertical axes.

are plotted in Fig. 5.8. In the following, we will refer to them briefly as mixed self- and cross-correlation, describing the self- and cross-coupling of rotation and translation, respectively. Both correlation functions show a distinct time-delayed extremum, denoted, respectively, by τ_{s}^* and τ_{c}^* in Fig. 5.8.

The most striking feature, however, is revealed by the mixed self-correlation. For a single bead, translation and rotation are not coupled at vanishing Reynolds number[11] due to the spherical symmetry [110, 209], so the mixed (self-)correlation vanishes. In the two-sphere system, however, there exists a mixed self-correlation, as shown in Fig. 5.8, that is mediated by the neighboring particle. This correlation is weaker than the mixed cross-correlation since the flow field created by particle 1 has to be reflected by particle 2.[12] As discussed before, particle 2 "reacts" with a finite delay due to the trap stiffness. Then, in addition, particle 1 also has a finite "reaction time." Hence, we always expect $\tau_{\mathrm{s}}^* > \tau_{\mathrm{c}}^*$.

We also studied the influence of the trap stiffnesses k^{t} and k^{r} on the correlation functions. As illustrated in Fig. 5.9, the difference in the delay times τ_{s}^* and

[11] The transverse force acting on a sphere translating with linear velocity $\boldsymbol{v}$ and spinning with angular velocity $\boldsymbol{\omega}$ is proportional to $\boldsymbol{v}\times\boldsymbol{\omega}$ and thus a quadratic effect in the velocities [110, 209]. Hence, this coupling only occurs when the nonlinear term in the Navier-Stokes equation (2.8) is taken into account (i.e., $\mathrm{Re} > 0$).

[12] Note that the mixed self-correlations cannot be treated within the Rotne-Prager approximation. They constitute an additional effect of higher order, as mentioned in Sect. 2.4.2.

τ_c^* decreases with increasing ratio $\kappa = k^t a^2/k^r$, which can be understood as follows. The leading-order contributions to the correlations are of translational nature. Hence, the time scale on which particle 2 reacts to motions of particle 1 is essentially determined by k^t. In the limit $k^t \to \infty$ (i.e., $\kappa \to \infty$ at fixed k^r), the "reaction" times approach zero and thus also the difference between τ_s^* and τ_c^*. Furthermore, we observe that the correlations are strongest for $\kappa \approx 1$.

6 Brownian-dynamics simulations and experiments

6.1 Brownian-dynamics simulations

We also performed Brownian-dynamics simulations to estimate the amount of data that is necessary to obtain a good statistics (i.e., suitable to make quantitative comparisons with theory) of the correlation functions in the two-particle system considered in the previous chapter. This serves as a helpful input to experiments.

6.1.1 Trap forces and torques

The tweezer setup used in the simulations is identical to the one in the previous chapter (see Fig. 5.1). The trapping potential generated by the focused laser beam is given by the harmonic form (4.1). Furthermore, we assume isotropic trap stiffnesses,[1] so the trapping forces are

$$\boldsymbol{F}_i = -k^{\mathrm{t}}(\boldsymbol{r}_i - \bar{\boldsymbol{r}}_i)\,, \tag{6.1}$$

where $\boldsymbol{r}_i$ is the position of particle i ($i = 1, 2$) and $\bar{\boldsymbol{r}}_i$ the center of the respective laser focus.

The restoring potential for the particle orientations $\boldsymbol{n}_i$ due to the linear polarization (direction $\hat{\boldsymbol{E}}$) of the traps was introduced by Eq. (4.3). To derive the torques generated by this potential, we consider the optical axis $\boldsymbol{n}_i$ as a point on the unit sphere. Hence, when this point moves away from its equilibrium position (located at one of the poles of the sphere, i.e., $\boldsymbol{n}_i = \pm\hat{\boldsymbol{E}}$), it experiences the restoring "force" $-\nabla_{\boldsymbol{n}_i} U^{\mathrm{r}}(\boldsymbol{n}_i)$, which causes the torque

$$\boldsymbol{T}_i = \boldsymbol{n}_i \times [-\nabla_{\boldsymbol{n}_i} U^{\mathrm{r}}(\boldsymbol{n}_i)] = k^{\mathrm{r}}(\boldsymbol{n}_i \cdot \hat{\boldsymbol{E}})\, \boldsymbol{n}_i \times \hat{\boldsymbol{E}} \tag{6.2}$$

with respect to the center of the sphere. Note that the gradient $\nabla_{\boldsymbol{n}_i}$ also yields radial contributions in direction $\boldsymbol{n}_i$, but these do not play a role due to the cross product $\boldsymbol{n}_i \times$ in Eq. (6.2).

[1] This assumption is justified as follows. First, we note that the stiffnesses in x and z direction are the same for particles having the same size as the focal width of the laser spot (see Sect. 4.1.1). Second, translations in y diretion do not play a role as we will only consider longitudinal motions in z direction and transveral motions with translations along x direction and rotation about the y axis, which all do not couple to translations along y direction.

Given these forces and torques, fully three-dimensional Brownian-dynamics simulations were performed by means of the two-step algorithm (3.44) yielding the spatial and orientational trajectories, $\boldsymbol{r}_i(t)$ and $\boldsymbol{n}_i(t)$, respectively.[2] The mobility matrix was calculated at each time step using the library HYDROLIB.

6.1.2 Correlation functions

While the spatial coordinates $r_{i,\alpha}$ are immediately given by $\boldsymbol{r}_i$, the orientation of the optical axis $\boldsymbol{n}_i$ has to be mapped to angles $\chi_{i,\alpha}$ in a way consistent with the previous chapter. We define $\chi_{i,y}$ to be the angle between the x axis and the projection of $\boldsymbol{n}_i$ onto the xz plane (Fig. 5.2), thus it is determined by the relation

$$\tan \chi_{i,y} = -\frac{n_{i,z}}{n_{i,x}} \ , \tag{6.3}$$

where the minus sign is needed to measure the angle in mathematically positive sense. Accordingly, the angle $\chi_{i,z}$ is given by

$$\tan \chi_{i,z} = \frac{n_{i,y}}{n_{i,x}} \ . \tag{6.4}$$

Representative examples for correlation functions[3] of spatial and angular coordinates obtained from the Brownian-dynamics trajectories are shown in Fig. 6.1. The translational and rotational auto-correlations, $\langle r_{1,\alpha}(t+\tau) r_{1,\alpha}(t)\rangle$ $(\alpha = x, z)$ and $\langle \chi_{1,\beta}(t+\tau)\chi_{1,\beta}(t)\rangle$ $(\beta = y, z)$, respectively, agree perfectly with the theoretical expectation (data not shown). The purely translational cross-correlations $\langle r_{1,\alpha}(t+\tau) r_{2,\alpha}(t)\rangle$ [Fig. 6.1(a) for $\alpha = x$] and also the mixed cross-correlations $\langle r_{1,x}(t+\tau)\chi_{2,y}(t)\rangle$ of transversal translations and rotations [Fig. 6.1(b)] show a very good agreement with the theoretical curves, too. For the purely rotational cross-correlations $\langle \chi_{1,\beta}(t+\tau)\chi_{2,\beta}(t)\rangle$, however, a much better statistics is needed since the rotational coupling is too weak at the relatively large separation $r = 3\,a$, and the same holds for the self-coupling of translation and rotation described by $\langle r_{1,x}(t+\tau)\chi_{1,y}(t)\rangle$ (data not shown).

[2] Using the notation of Sect. 2.5, the optical axis $\boldsymbol{n}_i$ is identified with one of the vectors $\boldsymbol{e}_i^{\alpha}$.

[3] The correlation functions were calculated very efficiently by means of fast Fourier transformation (FFT) [198]. Instead of calculating the correlation of two functions $f(t)$ and $g(t)$ directly, given by the time integral $\langle f(t+\tau)g(t)\rangle \propto h(\tau) = \int \mathrm{d}t\, f(t+\tau)g(t)$, we can employ the convolution theorem of Fourier analysis which states that in Fourier space the correlation integral $h(\tau)$ becomes the direct product $H(\omega) = F(\omega)G^*(\omega)$, where F, G, and H are the Fourier transforms of f, g, and h, respectively. This fact can be used to reduce the computational effort tremendously. For data sets discretized in time t, the very efficient method of FFT can be applied. It can be shown that the computational effort to calculate the correlation functions from data sets of length N via FFT is of order $N \log N$ [45], compared to N^2 for the direct way summing up terms $f(t+\tau)g(t)$, a difference which is immense for large N. Ready-to-use implementations of FFT and its application to the calculation of correlation functions are available for most programming languages such as C, PERL, etc.

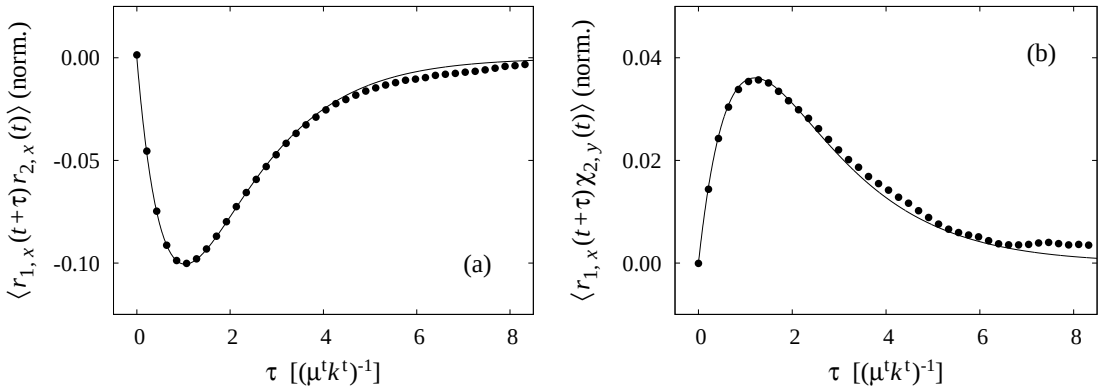

Figure 6.1 ■ Correlation functions for transversal fluctuations determined from Brownian-dynamics simulations (points) in comparison with the analytical result (lines) according to Eq. (5.29). The curves shown are the purely translational (a) and the mixed cross-correlation (b). The particle separation was $r = 3\,a$. The trap constants were chosen as $k^{\mathrm{r}} = k^{\mathrm{t}}a^2$, and the temperature was set to $k_{\mathrm{B}}T = 10^{-2}\,k^{\mathrm{t}}a^2$. The resulting spatial and angular fluctuations are then of order $\langle r_{i,\alpha}^2\rangle^{1/2} \approx 0.1\,a$ and $\langle \chi_{i,\alpha}^2\rangle^{1/2} \approx 6°$, respectively. (Not every data point is shown.)

It turns out from the simulations that the required amount of data should cover at least several 10,000 characteristic correlation times (given by the position of the positive or negative peak in the cross-correlations) to obtain a reasonable statistics for the correlation functions. The correlation functions shown in Fig. 6.1 were calculated from data sets covering in total about 100,000 correlation times. In case of rotational couplings, the required amount of data is much higher as the strength of the coupling is weaker. For comparison, the experimental curves shown in Fig. 5.5 were calculated from data sets covering about 40,000 correlation times [179].

6.2 Experiments

The experimental results that we shall present here very briefly are courtesy of S. Martin and T. Gisler [172]. They use fast video microscopy (with 125 frames per second) to track the motions of two colloidal spheres with diameters of about 3 to 4 μm suspended in water at 15 °C. The particles are liquid-crystal droplets whose nematic order was locked by polymerization [213]. The optical traps are generated by splitting a laser beam into two focal spots [72]. The distance of the trapped particles to the walls of the sample cell is about 20 μm. Imaging the birefringent spheres under crossed polarizers (see Sect. 4.1.2) allows to determine positions and orientations of the particles simultaneously.

The correlation functions shown in Fig. 6.2 are averages over about 10,000 correlation times. The purely translational cross-correlation $\langle r_{1,x}(t+\tau)r_{2,x}(t)\rangle$ of transversal motions reproduces the theoretical expectation very well, at least

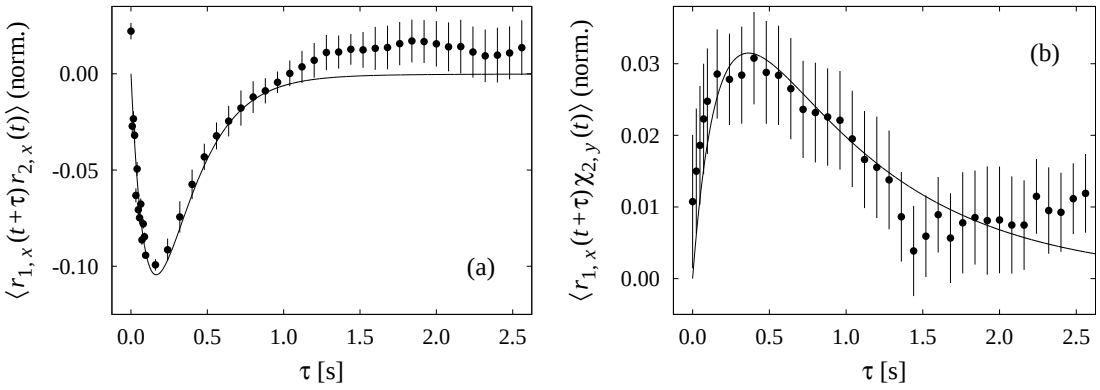

Figure 6.2 ■ Correlation functions for transversal fluctuations measured in the experiment (data courtesy of S. Martin [172]) in comparison with the theoretical prediction. The curves shown are the purely translational (a) and the mixed cross-correlation (b). The beads had a radius of $a = 2.0\ \mu$m, and the particle separation was $r = 5.8\ \mu\text{m} = 2.9\,a$. The trap stiffnesses were $k^{\text{t}} = 2.6 \times 10^{-7}\ \text{N}\,\text{m}^{-1}$ and $k^{\text{r}} = 2.5 \times 10^{-19}\ \text{N}\,\text{m} = 0.24\,k^{\text{t}}a^2$. For comparison, the translational relaxation time scale of a single particle in this setup is $(\mu^{\text{t}}k^{\text{t}})^{-1} = 0.16$ s. (Not every data point is shown.)

concerning the position and depth of the dip. For larger time lags τ, the statistics is poorer. The correlations of the cross-coupling of translation and rotation are weaker and thus would need more data to get a better statistics. Nevertheless, the characteristic peak is fitting quite well.

7 Conclusions I

In this part, we have presented the complete solution for the hydrodynamically coupled translational and rotational motions of two colloidal spheres that are trapped with respect to both their positions and orientations.

Based on pure symmetry arguments and without relying on explicit values of the mobilities, we have determined all the 12 collective eigenmodes and qualitatively discussed their relaxation times. The analysis relies on the eigenvalue problem of nonsymmetric matrices. Whereas the properties of the longitudinal modes are reminiscent to a system with purely translational degrees of freedom, the transversal modes exhibit a characteristic coupling of translation and rotation.

In a detailed Langevin analysis, we have derived the full set of correlation functions characterizing the Brownian motion of the trapped particles. Explicit examples for the correlation functions at different particle separations have been calculated based on mobilities which we obtained from the numerical library HYDROLIB [113].

The longitudinal fluctuations (both translation and rotation) exhibit the features already mentioned in Refs. [15, 108, 179], namely a "memory effect" in the cross-correlations. The transversal fluctuations are governed by the coupling of translations and rotations. As the most striking feature, this coupling is also visible in the mixed self-correlations which are governed by a second delay time in addition to the one observed in the cross-correlations. The self-coupling of translation and rotation for one sphere has to be mediated by a second sphere and is thus an effect of higher order.

Correlation functions involving rotational degrees of freedom are weaker compared to purely translational correlations since the flow field of a single rotating sphere decays as $1/r^2$, compared to translating particles where the decay is $1/r$. However, the strength of the correlations increases for decreasing particle separation which is more pronounced whenever rotations are involved. Furthermore, at sufficiently small distances, lubrication theory (see Sect. 2.4.4) becomes important, and the system introduced in this paper may help to check its predictions. Due to the rather weak coupling of rotational motions, this might be a challenging experimental task. The recent experimental data we have presented, however, look promising.

In the beginning of this part, we have already mentioned the field of microrheology. An extension of our work to viscoelastic media [151, 214] seems appealing. We have pointed out the rotational degree of freedom and its influ-

ence on hydrodynamic interactions. In addition, the rotations of probe particles in a viscoelastic environment result in an interesting deformational mode since they introduce some torsion in the surrounding medium. It therefore can yield additional information about the viscoelastic properties.

C Drafting of colloids ■ The benefits of hydrodynamic interactions

Abstract ■ We study the dynamics of three (and more) colloidal spheres that are driven by a constant force along a circular trap. It is shown that hydrodynamic interactions between the circling particles determine their interesting collective behavior. A linear stability analysis is performed to investigate the stability of regular particle clusters, and we illustrate the periodic limit cycle to which the system converges. We clarify that drafting effects of particle doublets are essential for the understanding of the limit cycle. When we apply a spatially periodic sawtooth potential along the circular trap, in addition to the constant force, we find a novel caterpillar-like motional sequence that is dominated by the long-range hydrodynamic interactions and that promotes the surmounting of potential barriers by the particles.

8 Colloidal particles orbiting in circular optical traps

In Part B, we studied fluctuations and hydrodynamic interactions in a colloidal system at thermal equilibrium. Now, we shall focus on the dynamics of colloidal particles that are driven *far from equilibrium* under the influence of external forces. Moreover, the nonlinear character of hydrodynamic interactions and their long-range nature (see Chap. 2) give rise to many interesting collective phenomena in driven colloidal systems, such as (almost) temporally periodic motions [37, 222] or even transient chaotic dynamics [120] of sedimenting three-particle clusters. Furthermore, hydrodynamic interactions lead to pattern formation of rotating colloidal motors [101], featuring a possible two-dimensional melting [150].

The physical system we have in mind are colloidal particles that are captured in a circular trap and driven by tangential forces, so they perform a circling motion along the trap [Fig. 8.1(a)]. As the particles are confined in radial direction, their dynamics is almost one-dimensional along the circumference of the trap, and hence, they cannot pass each other. We are particularly interested in collective types of motion and how the particle dynamics benefits from hydrodynamic interactions. To analyze the impact of hydrodynamic coupling systematically and to elaborate the crucial points, we shall consider only few-particle systems.

In the following, we first sketch two possible experimental realizations of such a system. They are both based on the principle of optical tweezing, i.e., the manipulation of colloidal particles by means of focused laser beams, which was already introduced in Sect. 4.1.1.

8.1 Optical vortices

Our work on circling particles was initially motivated by recent experimental studies on *optical vortices* [52, 53, 54]. In addition to spin angular momentum associated with circular polarization,[1] the photons in light modes with *helical* wave fronts (notably Laguerre-Gaussian modes) also carry *orbital angular momentum* associated with the spatial distribution of the electromagnetic field [1, 2, 59, 98, 192]. This arises from the fact that the phase fronts are inclined with respect to the propagation axis of the light beam [Fig. 8.1(b)].

[1] This property is exploited in experiments where birefringent particles are rotated by means of circularly polarized optical tweezers (see Sect. 4.1.2).

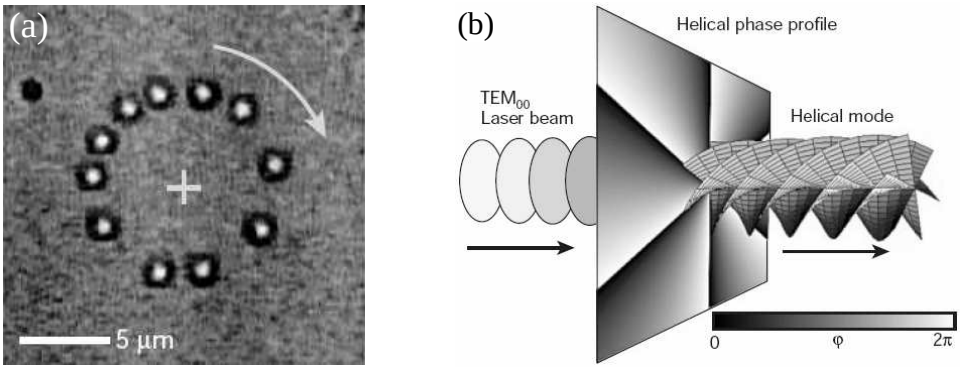

Figure 8.1 ■ Colloidal particles trapped and circling in an optical vortex (pictures redrawn from Ref. [98]). The particles are trapped inside the circular focus, and they are driven by the transfer of orbital angular momentum carried by the laser beam (a). The helical light mode generating an optical vortex can be created by a holographic phase mask (b).

The phase of a Laguerre-Gaussian mode is essentially given by $e^{i(kz-m\phi)}$, where k is the wave number of the laser beam propagating in z direction, and ϕ is the azimuthal angle about the beam axis. Each photon in the beam carries an orbital angular momentum $m\hbar$ [1, 21],[2] where m is an integral winding number known as *topological charge* of the vortex.

Such helical light modes focus to rings, rather than to points. To good approximation, the radius of the principal maximum of the intensity increases linearly with the topological charge m [53]. Due to the scattering of light, optical vortices can transfer orbital angular momentum to colloidal particles that are trapped inside the circular focus [Fig. 8.1(a)], which corresponds to tangential driving forces acting persistently on all particles. This force increases with the topological charge m.

Optical vortices can be created from linearly polarized light by a set of optical lenses [21, 192] or by means of computer-generated holograms [Fig. 8.1(b)] that imprint the phase shifts onto the wave fronts [52, 53, 54]. The holographic technique was applied to build arrays of optical vortices [142] that can assemble colloidal particles into "microoptomechanical pumps" to be employed in microfluidic systems. Furthermore, the hydrodynamic coupling of particles circling in concentric optical vortices was studied [143].

However, there are several experimental disadvantages concerning the use of optical vortices to study in detail the dynamics of circling particles as we propose in this work. In the first place, the driving force and the strength of the trapping onto the circular focus are given by the intensity of the beam and can therefore not be varied independently. Secondly, the driving force and the radius of the focal ring are coupled to each other via the topological charge m of the vortex

[2] Using holographic techniques to generate the Laguerre-Gaussian beam, the topological charge can reach values up to $m \approx 200$ [53].

[53]. Thirdly, for vortices generated by the holographic technique, the intensity variations along the circumference of the vortex are rather high (at least in the experiments performed so far) [143], and hence the tangential driving force is not well-defined. Moreover, the focus is very close to the surface of the sample cell,[3] which alters the hydrodynamic interactions due to wall effects [51, 61, 64].

8.2 Circulating optical tweezer

An alternative (and for our purposes more promising) method to generate a circular optical trap is to use a single circulating laser tweezer. This can be achieved by deflecting the beam at two synchronously oscillating galvanometric mirrors, thus scanning a planar circle inside the sample cell (for experimental details, see Refs. [74, 160]).

As one moves the focus of a laser beam rather slowly, a particle trapped inside follows the focal spot. However, if the tweezer moves too fast, such that the viscous drag acting on the particle becomes of the order of the tweezing force, the particle may eventually escape from the trap.[4] For a circulating laser beam, the tweezer focus can then be considered as being "smeared out", forming a circular trapping potential.

In fact, it was verified both theoretically and experimentally that this approach is capable of trapping colloidal particles on a circle [74]. Depending on the revolution frequency ω_t of the circulating tweezer, the particle drifts along the circle. At low frequencies (regime I in Fig.8.2), the particle can follow the motion of the trap and hence simply runs on a circle of radius R with tangential velocity $v_p = R\omega_t$. At intermediate frequencies (regime II), the particle cannot follow the trap, but it still experiences regular kicks by the laser at each revolution. Between these kicks, the particle diffuses freely, but does not have enough time to diffuse away from the circle before the return of the trap. It is thus captured in radial direction and moves along the circle with a well-defined mean velocity; the detailed analysis reveals that $v_p \propto 1/\omega_t$. This can be considered as driving the particle with a constant tangential force. At high angular frequencies (regime III), the particle cannot follow the tweezer at all. However, it is still trapped in radial direction and therefore diffuses freely along the circle.

The circulating-tweezer setup in the purely diffusive regime was applied successfully to study the diffusion of particles restricted to one dimension [159, 160]. This problem, known as single-file diffusion, is encountered in various fields (such as ion transport in biological membranes or channeling in zeolithes [244]).

[3] Typically, the distance h of the focus from the surface of the sample cell is of the order of microns and hence amounts only a few particle radii a (in Ref. [143], e.g., $h = 3a$). Otherwise, the intensity of the trap would not be sufficient to trap particles.

[4] Typically, the trapping forces for micron-sized beads suspended in water are of order pN. Then, the critical velocity of the focal spot is of order 100 μm/s [74].

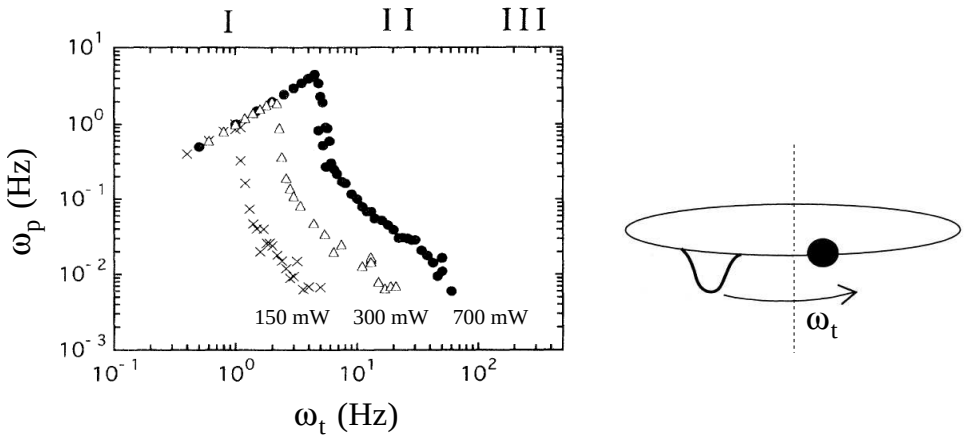

Figure 8.2 ■ Circling velocity ω_p of a particle driven by a laser tweezer circulating with velocity ω_t and forming a circular trap with radius 6.2 μm (pictures redrawn from Ref. [74]). At low frequencies ω_t (regime I), the particle follows the trap, i.e., $\omega_p = \omega_t$. At intermediate frequencies (regime II), the particle cannot follow the trap, but is driven with velocity $\omega_p \propto 1/\omega_t$ along the circular trajectory of the laser focus. At high frequencies (regime III), the particle diffuses freely on the circle. The different symbols denote measurements at different laser powers.

The advantage of applying this technique over using optical vortices is, first of all, that the relevant parameters can be varied almost independently. The strength of the radial trapping is set by the laser power, and the tangential driving can be tuned by the circulation frequency of the laser. Trivially, the radius of the circular trap is adjusted by inclination of the rotating mirrors that deflect the beam. Furthermore, the laser can be focused on a spot far enough (yet with sufficiently high intensity) from the surface of the sample cell to avoid effects of the walls on the hydrodynamic coupling.

The most important advantage of such a setup is that the intensity of the laser beam can be modulated along the circle, thus provinding the possibility to generate arbitrary spatial and temporal potentials to drive the particles. The feasibility of this idea was already demonstrated: A sawtooth-shaped modulation can indeed generate a "static" potential and thus create a well-functioning thermal ratchet by switching the modulation on and off (with the circulation frequency of the laser being in the fast regime III) [73].

So far, the dynamics of only a single particle in such a ratchet has been studied in order to avoid effects that stem from hydrodynamic interactions [73]. In the context of this work, however, these are exactly the effects we are interested in. Experiments with three particles (using the same type of setup as described above) were performed recently by C. Lutz and C. Bechinger [160]. In this case, the laser beam was rotated at intermediate frequencies (regime II). The modulation of the laser intensity then effectively generates a tilted sawtooth potential due to the additional constant driving force. In fact, it was verified experimentally that this model assumption is valid (see Chap. 10).

9 Collective drafting dynamics of circling particles

At first, we study the dynamics of particles driven on a circle by *constant* external forces. We consider *non-Brownian*, equal-sized beads moving in a viscous fluid in the overdamped regime, whose mutual coupling is solely of hydrodynamic origin.

9.1 Model system

The basic features of the experimental realizations sketched in Sects. 8.1 and 8.2, respectively, are mimicked by applying a constant tangential force[1] F to each particle. In addition, the particles are kept on a ring of radius R by means of a harmonic radial potential (corresponding to the lateral intensity profile of the laser beam) with force constant K [Fig. 9.1(a)]. The particle motion is effectively two-dimensional[2] in the plane of the ring ($z = 0$). Thus, the particle positions are best described by polar coordinates, r_i and ϕ_i. With the radial and tangential unit vectors at the position of particle i, $\boldsymbol{e}_i^r = [\cos\phi_i, \sin\phi_i, 0]$ and $\boldsymbol{e}_i^\phi = [-\sin\phi_i, \cos\phi_i, 0]$, the total external force acting on particle i then reads

$$\boldsymbol{F}_i = F\boldsymbol{e}_i^\phi - K(r_i - R)\boldsymbol{e}_i^r \,. \tag{9.1}$$

The radial oscillations out of the circular trap are rather small ($|r_i - R| < 0.1\,a$) for the trap stiffnesses K and driving forces F that we apply.

In order to prevent that particles overlap in the simulations, we add a short-range repulsive interaction which becomes relevant only when two particles are very close to each other. We use a hard-sphere-type interaction potential where a "hard core" with diameter $2a$ is surrounded by a "soft" repulsive potential [Fig. 9.1(b)]:

$$U_{\mathrm{rep}}(\boldsymbol{r}_i, \boldsymbol{r}_j) = A\left[\left(\frac{r_{ij}}{2a}\right)^n - 1\right]^{-1} \,. \tag{9.2}$$

Here, $r_{ij} = |\boldsymbol{r}_i - \boldsymbol{r}_j|$ is the center-center distance between particles i and j, and a is the particle radius. The repulsive force generated by this potential diverges

[1] Note that, in case of an optical vortex (Sect. 8.1), the assumption of a constant tangential force is a rough approximation since the intensity profile of an optical vortex is modulated along the ring, as determined by the topological charge m [53]. However, if m is large so that the period of the modulations is small compared to the particle size, then our approximation seems to be reasonable.

[2] Nevertheless, the surrounding fluid flow is still three-dimensional.

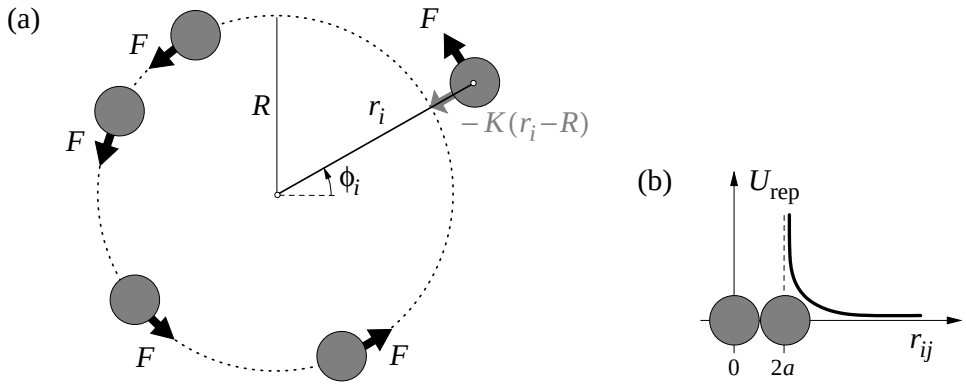

Figure 9.1 ■ Definition of our model system. (a) The particles are driven by a constant tangential force F and trapped on a circle with radius R by a harmonic radial potential characterized by the force constant K. (b) In order to avoid overlapping particles, they repel each other at very short distances. The repulsive potential U_{rep} is given by Eq. (9.2).

at contact ($r_{ij} = 2a$). This choice is primarily due to numerical reasons, but can nevertheless be justified from the physical point of view since even hard-sphere-like colloids show a "soft" repulsive potential at very short distances [35]. We choose the commonly used Lennard-Jones exponent $n = 12$, so the repulsion only acts at very short distances, and we tune the prefactor A such that the minimal inter-particle gap $r_{ij} - 2a$ in the simulations turns out to be of order $10^{-4}a$.

In the overdamped regime at low Reynolds number, the dynamics of the particles is governed by Eq. (2.21). As there are no external torques in our model, i.e., $\boldsymbol{T}_i = \boldsymbol{0}$, and as we are not interested in the rotational motion of the particles, the remaining equations of motion for our problem are

$$\dot{\boldsymbol{r}}_i = \sum_{j=1}^{N} \boldsymbol{\mu}_{ij}^{\text{tt}}(\boldsymbol{r}_1, \ldots, \boldsymbol{r}_N) \cdot \boldsymbol{F}_j \,. \tag{9.3}$$

Since the mobility tensors $\boldsymbol{\mu}_{ij}^{\text{tt}}$ are nonlinear functions of all particle positions, Eq. (9.3) describes the coupled nonlinear dynamics of N particles.

In our simulations, we use the numerical library HYDROLIB [113] (see Sect. 2.4.3) to calculate the required mobilities $\boldsymbol{\mu}_{ij}^{\text{tt}}$. For the numerical integration of the highly nonlinear equations of motion (9.3), we apply the fourth-order Runge-Kutta scheme as listed in Eq. (2.65). The time step Δt is chosen such that the corresponding change in the particle position is of the order of $0.1a$.

9.2 Stability of regular clusters

In this section, we study the dynamics and, in particular, the stability of regular N-particle clusters. By "regular" we mean configurations with N-fold symmetry, like the ones shown in Fig. 9.2.

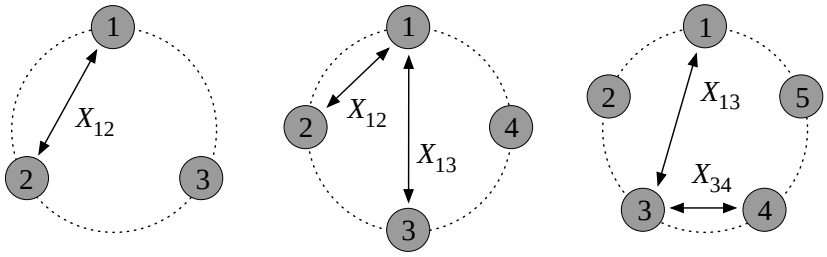

Figure 9.2 ■ Regular clusters with exemplary distances X_{ij}.

9.2.1 Dynamics of regular clusters

Due to the N-fold symmetry, all particle positions in a regular cluster are equivalent, i.e., the orbital angular velocity $\dot{\phi}_i$ has to be the same for all particles. The radial positions of the particles do not change either, which can also be justified by a simple symmetry argument. Let us start with a regular configuration where $r_i = R$ for all particles, so there is no radial force component in Eq. (9.1). Due to linearity, $\dot{r}_i \propto F$, which means that changing the direction of F inverts the direction of $\dot{r}_i$. However, since there is no difference if the cluster rotates clockwise or counterclockwise, the radial velocity must be the same for both directions. Therefore, $\dot{r}_i = 0$ and $r_i(t) = R$. Hence, a regular cluster remains unchanged and rotates with constant frequency $\dot{\phi}_i = \Omega_N$ that depends on the number of particles in the ring.

In regular clusters, the particles are well separated for sufficiently large radius R, and we may approximate the hydrodynamic interactions (to leading order with respect to the reduced inverse particle distance a/r_{ij}) by the Oseen tensor (2.30):

$$\boldsymbol{\mu}_{ij}^{\mathrm{tt}} = \frac{3\mu^{\mathrm{t}}}{4}\frac{a}{r_{ij}}\left(\mathbf{1} + \hat{\boldsymbol{r}}_{ij}\hat{\boldsymbol{r}}_{ij}\right) , \tag{9.4}$$

and $\boldsymbol{\mu}_{ii}^{\mathrm{tt}} = \mu^{\mathrm{t}}\mathbf{1}$ [with $\mu^{\mathrm{t}} = (6\pi\eta a)^{-1}$]. The positions of the particles in a rotating regular clusters are given by

$$r_i(t) = R\,, \tag{9.5a}$$

$$\phi_i(t) = \frac{2\pi}{N}\,i + \Omega_N t\,. \tag{9.5b}$$

With $\boldsymbol{F}_i = F\boldsymbol{e}_i^{\phi}$, we derive from (9.3) the rotational frequency of an N-particle cluster,

$$\frac{\Omega_N}{\Omega_1} = 1 + \frac{3}{4}\sum_{j\neq i}\frac{1}{X_{ij}}\,\frac{1+3\cos\Phi_{ij}}{2} \quad \text{with} \quad \Omega_1 = \frac{\mu^{\mathrm{t}}F}{R}\ , \tag{9.6}$$

where $X_{ij} = \sqrt{2}(R/a)\sqrt{1-\cos\Phi_{ij}}$ and $\Phi_{ij} = (2\pi/N)(j-i)$ are the respective spatial and angular distances between particles i and j in the regular configuration (Fig. 9.2).

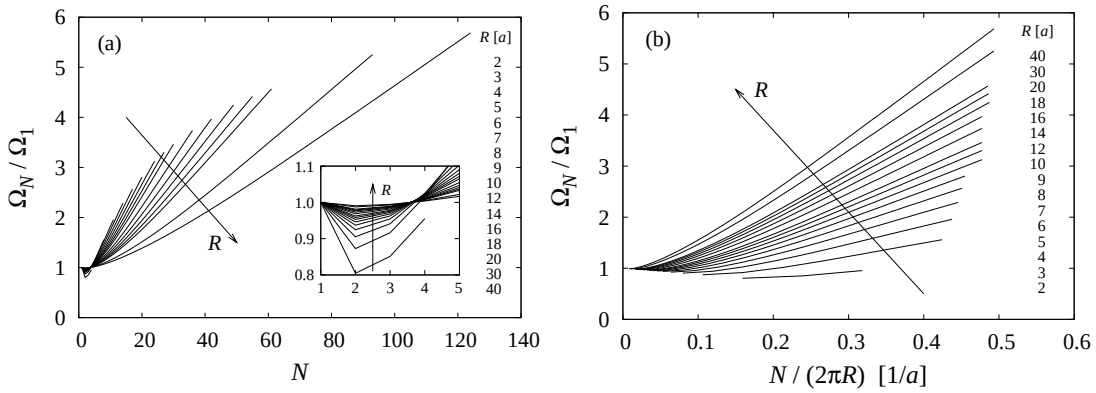

Figure 9.3 ■ Circling frequencies Ω_N of regular N-particle clusters (normalized to the frequency Ω_1 of a single sphere), as obtained from simulations. The two plots show the same data: (a) as a function of particle number N, (b) as a function of particle line density $N/(2\pi R)$. The arrow gives the direction of increasing ring radius R.

In Fig. 9.3(a), we study the circling frequencies of regular clusters as a function of particle number N for different ring radii R. The data shown were obtained from simulations. At constant radius, the frequency increases with the number of particles since then the particles are closer together which reduces the drag. Note that for less than four particles, the frequency is reduced relative to the single particle value. Here, hydrodynamic interactions across the ring increase the drag on the particles. This effect is clearly more pronounced for small rings.

At constant particle distance $2\pi R/N$ [or constant line density of the particles, $N/(2\pi R)$], the drag is reduced when the ring radius increases, as Fig. 9.3(b) clearly shows. This is due to the fact that, in a ring with larger radius and thus smaller curvature, the particles are better "aligned" behind each other, and therefore, the drag reduction is more effective.

9.2.2 Eigenmodes of perturbed clusters

To investigate the stability of regular N-particle clusters against small radial and angular particle displacements, we introduce

$$r_i(t) = R\,[1 + \delta\rho_i(t)]\,, \tag{9.7a}$$

$$\phi_i(t) = \frac{2\pi}{N}\,i + \Omega_N t + \delta\phi_i(t)\,. \tag{9.7b}$$

Using the forces (9.1) and the Oseen tensor (9.4), we linearize the equation of motion (9.3) in terms of the small perturbations $\delta\rho_i, \delta\phi_i \ll 1$. This yields the linear evolution equation

$$\frac{\mathrm{d}}{\mathrm{d}\tau}\,\mathbf{q}(\tau) = \mathbf{\Lambda}\cdot\mathbf{q}(\tau) \tag{9.8}$$

for the $2N$-dimensional vector $\mathbf{q} = [\delta\rho_1, \ldots, \delta\rho_N, \delta\phi_1, \ldots, \delta\phi_N]$, where $\tau = \Omega_1 t$ is the reduced time.[3] The $2N \times 2N$ matrix $\mathbf{\Lambda}$ is composed of the $N \times N$ submatrices $\mathbf{\Lambda}^{\mathrm{tt}}$, $\mathbf{\Lambda}^{\mathrm{tr}}$, $\mathbf{\Lambda}^{\mathrm{rt}}$, and $\mathbf{\Lambda}^{\mathrm{rr}}$,

$$\mathbf{\Lambda} = \begin{bmatrix} \mathbf{\Lambda}^{\mathrm{tt}} & \mathbf{\Lambda}^{\mathrm{tr}} \\ \mathbf{\Lambda}^{\mathrm{rt}} & \mathbf{\Lambda}^{\mathrm{rr}} \end{bmatrix}, \tag{9.9a}$$

with elements[4]

$$\Lambda^{\mathrm{tt}}_{ii} = -\kappa\,, \tag{9.9b}$$

$$\Lambda^{\mathrm{tt}}_{ij} = +\frac{3}{4}\frac{1}{X_{ij}}\left(\frac{(5-3\cos\Phi_{ij})\sin\Phi_{ij}}{4(1-\cos\Phi_{ij})} + \kappa\,\frac{1-3\cos\Phi_{ij}}{2}\right), \tag{9.9c}$$

$$\Lambda^{\mathrm{tr}}_{ii} = -\frac{3}{4}\sum_{j\neq i}\frac{1}{X_{ij}}\,\frac{3(1-\cos\Phi_{ij})}{4}\,, \tag{9.9d}$$

$$\Lambda^{\mathrm{tr}}_{ij} = +\frac{3}{4}\frac{1}{X_{ij}}\,\frac{3(1-\cos\Phi_{ij})}{4}\,, \tag{9.9e}$$

$$\Lambda^{\mathrm{rt}}_{ii} = -\left(1+\frac{3}{4}\sum_{j\neq i}\frac{1}{X_{ij}}\,\frac{3(1+3\cos\Phi_{ij})}{4}\right), \tag{9.9f}$$

$$\Lambda^{\mathrm{rt}}_{ij} = -\frac{3}{4}\frac{1}{X_{ij}}\left(\frac{1+3\cos\Phi_{ij}}{4} + \kappa\,\frac{3\sin\Phi_{ij}}{2}\right), \tag{9.9g}$$

$$\Lambda^{\mathrm{rr}}_{ii} = 0\,, \tag{9.9h}$$

$$\Lambda^{\mathrm{rr}}_{ij} = -\frac{3}{4}\frac{1}{X_{ij}}\,\frac{(7-3\cos\Phi_{ij})\sin\Phi_{ij}}{4(1-\cos\Phi_{ij})}\,. \tag{9.9i}$$

The dimensionless parameter

$$\kappa = \frac{KR}{F} \tag{9.10}$$

measures the strength of the radial trap relative to the driving force.

The stability of the regular cluster is determined by the character of the $2N$ eigenmodes of Eq. (9.8), which have the form

$$\mathbf{q}_i(\tau) = \mathrm{e}^{\lambda_i \tau}\mathbf{a}_i\,. \tag{9.11}$$

The corresponding eigenvalue problem

$$\mathbf{\Lambda}\cdot\mathbf{a}_i = \lambda_i\mathbf{a}_i \tag{9.12}$$

[3] As the driving force F merely sets the characteristic time scale Ω_1^{-1} of the circling dynamics, we keep F constant in all our simulations.

[4] Note that the matrix $\mathbf{\Lambda}$ is not symmetric.

N	(i) $\lambda_i = 0$	(ii) $\lambda_i < 0$	(iii) $\lambda_i > 0$	(iv) Re $\lambda_i < 0$	(v) Re $\lambda_i > 0$
odd	1	1	—	$N-1$	$N-1$
even	1	2	1	$N-2$	$N-2$

Table 9.1 ■ Number of eigenmodes classified by their eigenvalues λ_i for even and odd particle numbers N. (i) constant angular shift, (ii/iii) non-oscillating damped or unstable modes, (iv/v) oscillating damped or unstable modes.

was solved numerically by using the computer-algebra package MAPLE [171]. This analysis reveals that the stable and unstable eigenmodes for the coupled displacements $\mathbf{q}$ can be categorized as follows (depending on the number of particles): (i) a constant angular shift, (ii/iii) non-oscillating damped/unstable, and (iv/v) oscillating damped/unstable. In Table 9.1, we give the number of eigenmodes classified by their eigenvalues λ_i for even and odd particle numbers. Figure 9.4 shows an example of an unstable oscillating mode (type v).

The occurence of stable and unstable modes can be compared to a saddle point in the framework of the analysis of dynamic systems. A cluster configuration with arbitrary small radial and angular displacements of the particles is practically unstable since contributions of unstable modes will always grow, while stable modes will relax to zero.

For $N = 3$, we also determined the eigenvalues analytically by an expansion to first order in a/R:

$$\lambda_1 = 0 \qquad \text{(type i)}\,, \tag{9.13a}$$

$$\lambda_2 = -\kappa\left(1 - \frac{\sqrt{3}}{10}\,\frac{a}{R}\right) \qquad \text{(type ii)}\,, \tag{9.13b}$$

$$\lambda_{3/4} = -\kappa - \left[\left(\frac{\sqrt{3}}{20} + \frac{27\sqrt{3}}{32}\frac{1}{\kappa}\right) \pm \mathrm{i}\,\frac{13\sqrt{3}}{32}\right]\frac{a}{R} \qquad \text{(type iv)}\,, \tag{9.13c}$$

$$\lambda_{5/6} = \left(\frac{27\sqrt{3}}{2}\,\frac{1}{\kappa} \pm \mathrm{i}\,\frac{17\sqrt{3}}{32}\right)\frac{a}{R} \qquad \text{(type v)}\,. \tag{9.13d}$$

In this case, a non-oscillating unstable mode (type iii) does not exist; it only occurs for even N (see Table 9.1).

The oscillating unstable mode shown in Fig. 9.4 illustrates that the oscillation frequency is by an order of magnitude lower than the frequency of the cluster circulation.[5] For the special case of three particles, we see from Eqs. (9.13c)

[5]Note that the time axis in Fig. 9.4 is normalized to the periodic time $T_4 = 2\pi/\Omega_4$ of the cluster rotation, so t/T_4 gives essentially the number of cluster rotations.

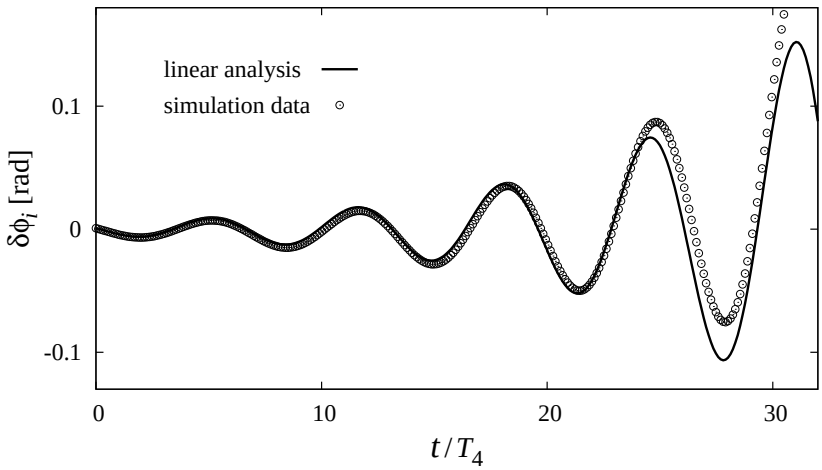

Figure 9.4 ■ Representative example of the angular coordinate of an unstable oscillating mode (here: $N = 4$, $R/a = 10$, $\kappa = 10$). The time scale is normalized to the periodic time of the circulating cluster ($T_4 = 2\pi/\Omega_4$). The linear theory and the simulations (see Sect. 9.3) agree very well up to amplitudes of several percent of $2\pi/N$. (Not every data point of the simulation is shown.)

and (9.13d) that the oscillation frequencies, given by $\omega_i = \operatorname{Im}\lambda_i$, are of order a/R (measured on the reduced time scale and thus relative to the single-particle frequency Ω_1) and therefore much smaller than the circling frequency Ω_3 of the cluster.

In case of infinitely stiff radial trapping, the radial displacements are suppressed (i.e., $\delta\rho_i = 0$). Equation (9.13d) reveals that there are no growing modes in the limit $\kappa \to \infty$. This was also confirmed numerically for $N > 3$: For modes of type (iii) and (v), $\operatorname{Re}\lambda_i \to 0$ if $\kappa \to \infty$. Hence, radial oscillations are essential for the occurrence unstable modes, so the latter cannot be obtained from an analysis only considering angular displacements.

9.3 Nonlinear dynamics and periodic limit cycle

The amplitude of an unstable mode grows up to a certain magnitude in agreement with the linear analysis, until the nonlinear contributions to the dynamics take over (see Fig. 9.4). The amplitudes saturate, and the system finally tends towards a periodic limit cycle with oscillating particle distances. This behavior was also demonstrated experimentally [160].

9.3.1 Dynamic transition to periodic limit cycle

In Fig. 9.5 we show an example of such a dynamic transition from an unstable linear mode to the periodic limit cycle by plotting the angular coordinate $\phi_i(t)$,

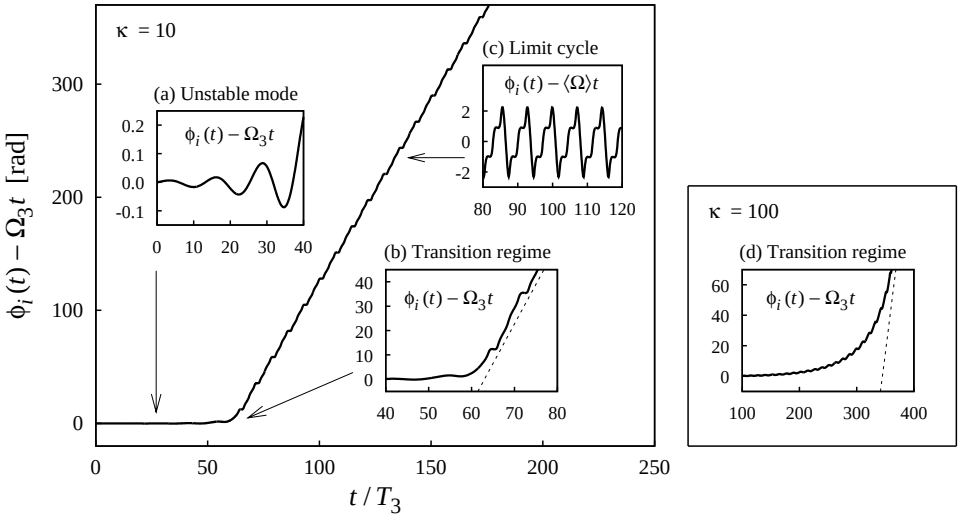

Figure 9.5 ■ Dynamic transition in the angular coordinate from an unstable linear mode to the periodic limit cycle for three particles ($R/a = 10$). The main curve and the insets (a), (b), and (d) show the angle $\phi(t)$ relative to $\Omega_3 t$ as a function of time. In the inset (c), $\phi(t) - \langle\Omega\rangle t$ is plotted. Plots (a)–(c) correspond to a stiffness of $\kappa = 10$. For comparison with (b), the transition regime for $\kappa = 100$ is shown in (d). The dashed lines in (b) and (d) indicate the limit cycles (slope $\langle\Omega\rangle$).

relative to the cluster rotation $\Omega_N t$, as a function of time. Note that Ω_N is the rotational frequency of the regular N-particle cluster introduced in Eq. (9.6).

The mean slope of $\phi_i(t)$ in each of the two regimes (linear mode and limit cycle) gives a well-defined mean orbital frequency $\langle\Omega\rangle$. For the linear mode, it is given by the cluster frequency Ω_N. Clearly, $\langle\Omega\rangle$ and therefore the mean velocity of the particles increases during the transition to the limit cycle, which means that the mean drag force on the particles is reduced (for the underlying dynamic mechanism, see below).

The character of the transition depends on the radial trap stiffness K. It is quite sharp for weaker traps, where the transition takes place within a few oscillations, as shown in Fig. 9.5(b). For stronger traps, the mean frequency increases smoothly from the linear regime to the limit cycle, as illustrated in Fig. 9.5(d). Furthermore, the onset of the transition is shifted to larger times when the trap becomes stiffer. This is due to the fact that unstable modes need more time to grow in a stiffer trap [for three particles, see Eq. (9.13d)].

9.3.2 Enhanced particle motion due to drafting effects

In Fig. 9.6, we visualize the basic mechanism underlying the periodic limit cycle. Two particles in close contact move faster than a single particle [Figs. 9.6(a–c)] since the friction per particle is reduced due to the well-known effect of *drafting*. When such a pair reaches the third particle, they form a triplet for a short time

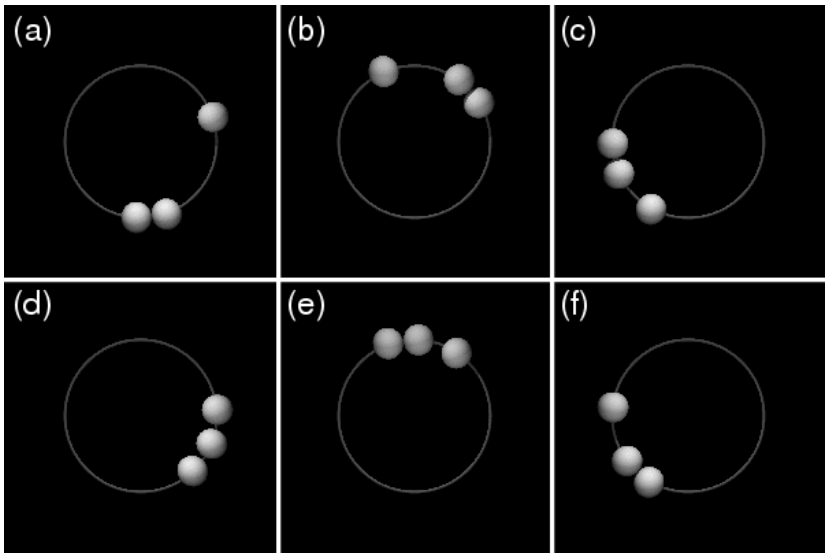

Figure 9.6 ■ Snapshots of the simulation illustrating the basic mechanism of the periodic limit cycle. The particles circulate counterclockwise. The thin ring is drawn as a guide to the eye and represents the circular harmonic trap with radius R. (a–c) Two particles in close contact move faster than a single particle. (d) When this pair reaches the third particle, they form an intermediate triplet. (e,f) Finally, the first two particles escape as a new pair.

[Fig. 9.6(d)]. In this configuration, the mobility of the middle particle is larger since it is "screened" from the fluid flow by the outer particles. It therefore pushes the particle in front, so that the first two particles "escape" from the last one [Figs. 9.6(e,f)]. The same principle also holds for more than three particles. In these cases, there can be more than one pair of particles.

This characteristic limit cycle was also observed in experiments by C. Lutz and C. Bechinger [160], who used a circulating tweezer to generate the circular trap (see Sect. 8.2). It should be mentioned, however, that the limit cycle as described above is absent when the experiment is performed close to the surface of the sample cell. We believe that this is due to the fact that hydrodynamic interactions are altered [64] or even "screened" [51, 61] close to walls.

In the limit cycle, the mean orbital frequency $\langle\Omega\rangle$ is larger compared to the velocity Ω_N of the corresponding regular configuration. The quantitative effect is illustrated in Fig. 9.7 for the case of three particles. We attribute this to the drafting of particle doublets which reduces their drag force. We observe that the dependence of the limit-cycle velocity on both the ring radius R and the trap stiffness K is rather weak.

9.3.3 Harmonic analysis of the limit cycle

For the limit cycle, we have performed a harmonic analysis using fast Fourier transformation [198]. In order to separate the fast orbital dynamics of the parti-

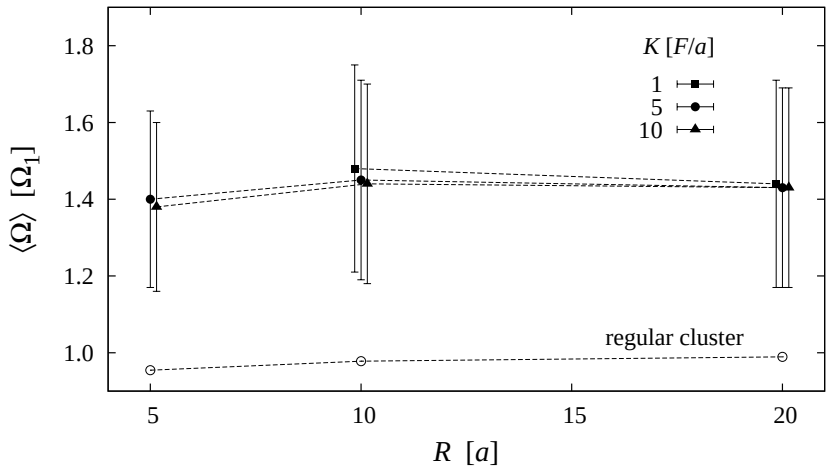

Figure 9.7 ■ Mean circling frequencies $\langle\Omega\rangle$ of three particles in the periodic limit cycle (normalized to the frequency Ω_1 of a single sphere). The upper three curves are plotted for different trap stiffnesses K (in units of F/a). For comparison, the lower curve shows the values for the regular three-particle cluster, i.e., Ω_3. The errorbars indicate the range within which the orbital velocities vary in the limit cycle.

cles (characterized by the mean angular velocity $\langle\Omega\rangle$) from their relative motions, we calculate the Fourier transform of the relative angular coordinate, given by the cos- and sin-coefficients, $a(\omega)$ and $b(\omega)$, respectively:[6]

$$\phi_i(t) - \langle\Omega\rangle t = \sum\!\!\!\!\!\!\int_{\omega} [a(\omega)\cos\omega t + b(\omega)\sin\omega t]\,. \tag{9.14}$$

This yields the fingerprint of the dynamics relative to the mean circling motion. In Fig. 9.8, we present the corresponding Fourier spectrum for three particles.[7] The spectrum features equidistant peaks, indicating that the dynamics of the limit cycle is indeed periodic. Besides the characteristic frequency ω^*, the higher harmonics $2\omega^*$ and $3\omega^*$ are very pronounced, too. The frequency ratio $\omega^*/\langle\Omega\rangle$ is of the order of 0.1, i.e., it takes about 10 circulations to break up a two-particle cluster and to rebuild the *same* one again. Thus, a drafting doublet circulates about 3 times before it breaks up and a new one is formed.[8]

The absolute value of the characteristic frequency ω^* decreases with increasing ring radius, as shown in Fig. 9.9(a), because it takes longer for a particle pair to reach the third particle on a larger ring. At constant ring radius, the characteristic frequency increases with the trap stiffness since particles in a stronger trap are

[6] The notation $\sum\!\!\!\!\!\!\int$ in Eq. (9.14) symbolizes that the integral of the Fourier transformation becomes a sum in case of finite and discrete data sets.

[7] We also calculated the frequency spectrum in case of four and five particles. The results look very similar to those shown in Fig. 9.8.

[8] The sequence $ij = 12 \to 23 \to 31 \to 12$ of drafting doublets takes 10 revolutions. Therefore, it takes $10/3 \approx 3$ revolutions to break up one of the doublets and form the next one.

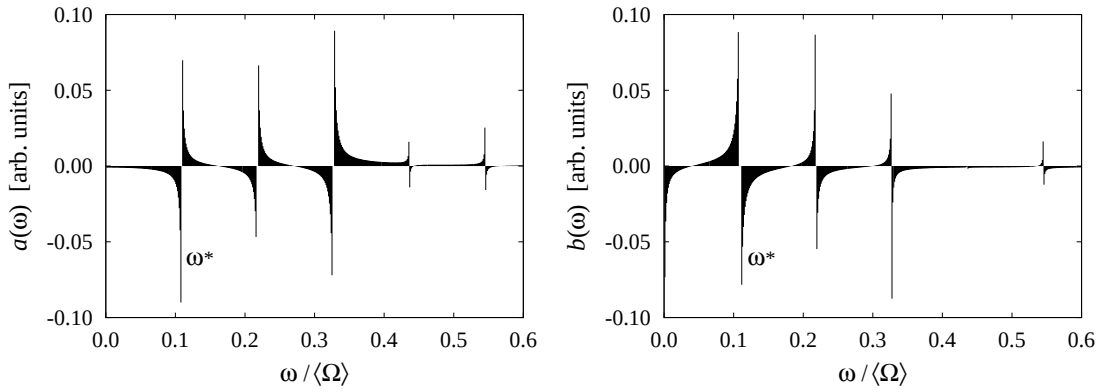

Figure 9.8 ■ Fourier spectrum [cos-coefficients $a(\omega)$ and sin-coefficients $b(\omega)$] of the periodic limit cycle of three particles. Note that the frequencies ω are defined relative to the mean orbital frequency $\langle\Omega\rangle$.

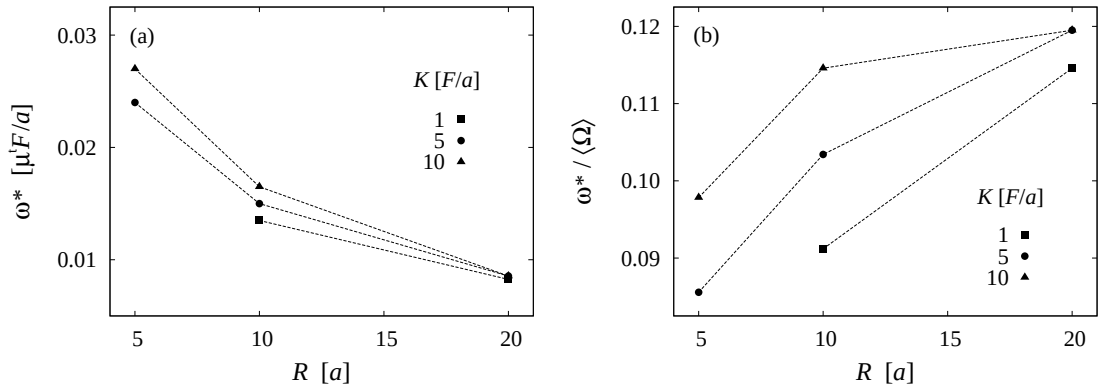

Figure 9.9 ■ Characteristic frequency ω^* of the periodic limit cycle of three particles vs. ring radius R. The different curves are related to different trap stiffnesses K. Both graphs show the same data but with different normalization of the frequencies. In (a), the absolute values of ω^* are plotted [$a/(\mu^t F)$ is the time that a single bead needs to drift its own radius], while (b) shows the relative values compared to the respective mean circling frequency $\langle\Omega\rangle$ (see Fig. 9.7).

better aligned along the ring, which makes the mechanism of the limit cycle more effective. Note that this is in contrast to the mean circling velocity that does not depend significantly on K (see Fig. 9.7).

Figure 9.9(b) presents the same data as Fig. 9.9(a), but the frequencies are here normalized to the respective mean circling frequency $\langle\Omega\rangle$, which was shown in Fig. 9.7. The increase of the ratio $\omega^*/\langle\Omega\rangle$ with growing R reveals that breaking up a doublet and forming a new one requires less circulations in larger rings.

9.3.4 Clustering in weak radial traps

If the strength of the radial trap is decreased, the radial displacements of the particles increase so that they can pass each other. This happens at a reduced

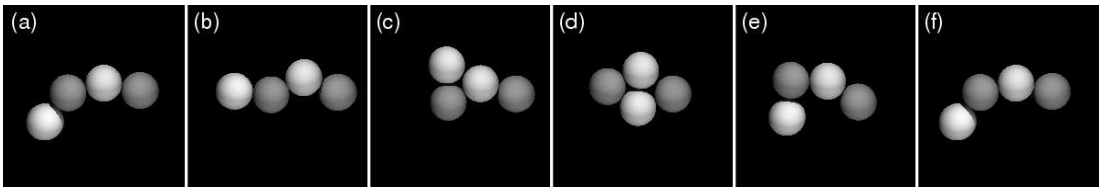

Figure 9.10 ■ Dynamics of four particles at medium radial trap stiffness ($\kappa = 5$). The motion shown is relative to the mean rotation (with frequency $\langle\Omega\rangle$) along the ring trap. Only the relevant part of the ring is shown, the center of the ring is located at the bottom of the snapshots. The particles are running from right to left. During one cycle, the first and the third particle are exchanged. The particles are shaded differently in order to distinguish them.

trap stiffness $\kappa = KR/F$ of the order of 1. For three particles and four particles, the limit cycle then consists of a compact triangular or rhombic-shaped cluster circling and rotating in the trap.

For four particles, we also find the limit cycle illustrated in Fig. 9.10. It occurs if the radial trap has medium strength such that compact particle clusters can be formed but only with a finite "life time". The first particle on the left is pushed in outward radial direction by the particles behind it [Fig. 9.10(b)] and subsequently passed by the second particle [Fig. 9.10(c)]. It then pushes the third one in inward radial direction [Fig. 9.10(d)], which in turn takes over the lead of the chain [Fig. 9.10(e)]. Finally, the initial state is rebuild, where the first and the third particle are exchanged [Fig. 9.10(f)]. Note that there is an intermediate state where the particles form a compact rhombic-shaped cluster [Fig. 9.10(d)], which, however, is not stable at this intermediate trap strength.

10 Dynamics in a sawtooth potential supported by drafting

After having demonstrated hydrodynamic effects in case of a *constant driving force*, we now want to investigate the cooperative motion of particles in the presence of a more complicated force profile. On top of the constant force, we now apply a static, spatially periodic *sawtooth potential*. In total, the particles thus move in a tilted sawtooth landscape, featuring both "steep" *drift* and "flat" *diffusive* regimes. In contrast to the purely deterministic dynamics considered in the previous chapter, we now have to take *Brownian motion* into account.

In general, nonequilibrium systems that perform thermally induced motions (such as diffusion or thermal-activation processes) in spatially asymmetric potentials are known as *thermal ratchets* or *Brownian motors* [8, 9, 10, 202, 203]. Extracting directed motion out of unbiased thermal fluctuations is a task of great interest for dynamics at the microscopic level, especially in biological physics. The most intensively studied systems described by ratchet models are molecular motors such as myosin and kinesin/dynein, carrying loads along actin filaments and microtubules, respectively [9, 26, 126, 185].

To our knowledge, the role of hydrodynamic interactions in ratchet systems has not yet been investigated. However, since biological motors, e.g., operate in aqueous environments, neighboring motors might be coupled via the surrounding fluid and perform thus cooperative motions that benefit from hydrodynamic interactions. In this chapter, we clarify how drafting affects the dynamics of particles moving in a sawtooth potential.

10.1 Model system

10.1.1 Sawtooth-modulated circular trap

The sawtooth potential that we apply is introduced in Fig. 10.1, where $s = R\phi$ is the circumferential coordinate along the contour line of the circular trap. In the regime $0 \leq s < L_\downarrow$, the potential $U_{\text{saw}}(s)$ generates the force $F_{\text{saw}} = F_\downarrow > 0$, supporting the driving force $F_0 > 0$. For $L_\downarrow \leq s < L$, the sawtooth force $F_{\text{saw}} = -F_\uparrow < 0$ counteracts F_0. The total force along the cirular trap is thus

$$F(s) = F_0 + F_{\text{saw}}(s) = \begin{cases} F_0 + F_\downarrow & \text{for} \quad 0 \leq s < L_\downarrow \\ F_0 - F_\uparrow & \text{for} \quad L_\downarrow \leq s < L \end{cases} \tag{10.1}$$

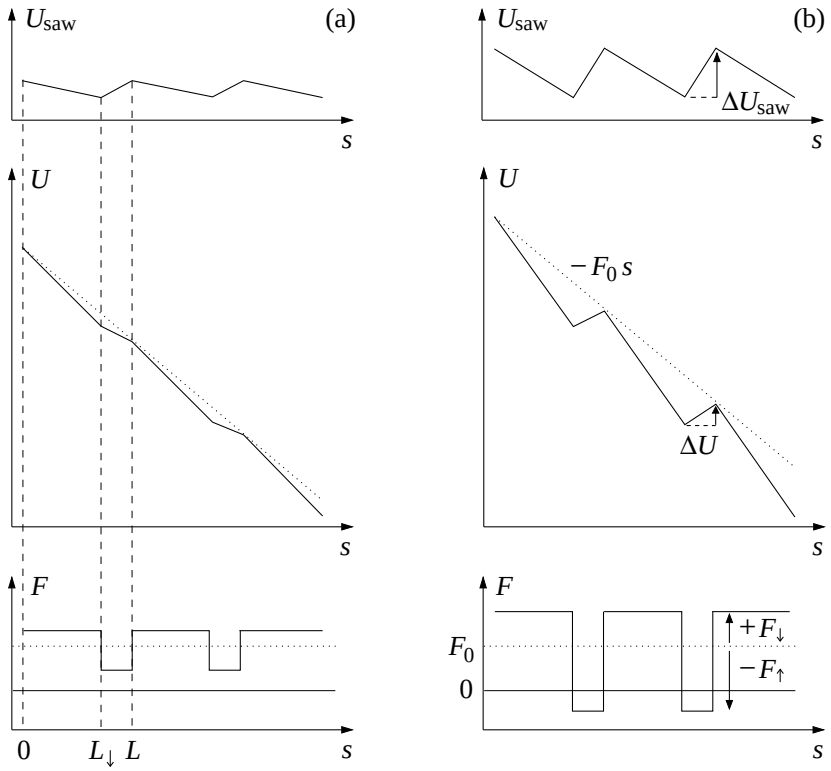

Figure 10.1 ■ Sawtooth potential as a function of the contour coordinate s along the circular trap. (a) For $\varepsilon < 1$, the net driving force $F(s) = -\mathrm{d}U(s)/\mathrm{d}s = F_0 - \mathrm{d}U_{\mathrm{saw}}(s)/\mathrm{d}s$ always points in positive s direction, so the particle performs a drift motion. (b) In the case $\varepsilon > 1$, the particle experiences an energy barrier since the net force on the "uphill" segment points in negative s direction.

(to be continued with period L). This corresponds, via $F(s) = -\mathrm{d}U(s)/\mathrm{d}s$, to the tilted sawtooth potential

$$U(s) = -F_0 s + U_{\mathrm{saw}}(s)\,. \tag{10.2}$$

We characterize the sawtooth potential by two dimensionless parameters, ε and ξ. The force $F_\uparrow$ counteracting the driving force F_0 is set by the ratio

$$\varepsilon = \frac{F_\uparrow}{F_0}\,, \tag{10.3}$$

Hence, ε is essentially a measure for the amplitude of the sawtooth potential (provided that L and $L_\downarrow$ are kept fixed). For $\varepsilon < 1$, the total force always points in forward direction [Fig. 10.1(a)], so the particle predominantly performs a drift motion, while for $\varepsilon > 1$, there exists an effective energy barrier $\Delta U > 0$ even in the tilted sawtooth potential [Fig. 10.1(b)], which a captured particle can only overcome by a *thermally activated* jump. The value $\varepsilon = 1$ represents the case where the net force in the "uphill" regime ($L_\downarrow \le s < L$) vanishes exactly, i.e.,

$F = F_0 - F_\uparrow = 0$, so the particle *diffuses* freely until it resumes the drift motion on the "downhill" segment ($0 \le s < L_\downarrow$).

The asymmetry of the sawtooth potential $U_{\rm saw}(s)$ is described by the dimensionless parameter

$$\xi = \frac{L_\uparrow}{L} \,, \tag{10.4}$$

where $L_\uparrow = L - L_\downarrow$. Since the force $F_\downarrow$ must obey the condition $F_\downarrow L_\downarrow = F_\uparrow L_\uparrow$ (setting the depth of the sawtooth potential), we obtain

$$F_\downarrow = \frac{\xi}{1-\xi} F_\uparrow = \frac{\xi}{1-\xi} \varepsilon F_0 \,. \tag{10.5}$$

Hence, the smaller the value of ξ, the larger the ratio $F_\uparrow/F_\downarrow = \xi^{-1} - 1$. For $\xi = \frac{1}{2}$, the sawtooth potential $U_{\rm saw}(s)$ is symmetric (i.e., $F_\uparrow = F_\downarrow$).

The energy barrier of the bare sawtooth potential, $\Delta U_{\rm saw} = F_\downarrow L_\downarrow = F_\uparrow L_\uparrow$, is lowered by the contribution of the driving force F_0, so the effective energy barrier of the tilted potential reads

$$\Delta U = (F_\uparrow - F_0) L_\uparrow = (\varepsilon - 1) \xi F_0 L \,. \tag{10.6}$$

Thus, $\Delta U > 0$ for $\varepsilon > 1$, and there exists no barrier ($\Delta U < 0$) for $\varepsilon < 1$. Note that $F_0 L$ is the energy that a particle moving under the influence of the potential $U(s)$ dissipates during one period.[1]

In addition to the force generated by the driving potential $U(s)$, we still have the circular harmonic trapping with force constant K as in the previous chapter [see Eq. (9.1)]. However, since we consider here also thermal fluctuations, which occur in all spatial directions, the dynamics of a particle placed in the trap is now fully three-dimensional. Its position is best described in cylindrical coordinates, $\boldsymbol{r}_i = r_i \boldsymbol{e}_i^r + z_i \boldsymbol{e}^z = [r_i \cos\phi_i, r_i \sin\phi_i, z_i]$, and the total force generated by the circular trap finally reads

$$\boldsymbol{F}_i^{\circlearrowleft} = F(s_i) \boldsymbol{e}_i^\phi - K[(r_i - R)\boldsymbol{e}_i^r + z_i \boldsymbol{e}^z] \,. \tag{10.7}$$

We shall concentrate on the dynamics induced by the sawtooth potential along the circular trap. Therefore, we choose a rather large value for the stiffness K such that the thermal fluctuations out of the ring, in radial and in z direction, are negligibly small.[2]

[1] The energy dissipated per period is given by $\int_L {\rm d}s\, F(s) = (F_0 + F_\downarrow) L_\downarrow + (F_0 - F_\uparrow) L_\uparrow = F_0 L$ since $F_\downarrow L_\downarrow = F_\uparrow L_\uparrow = \Delta U_{\rm saw}$.

[2] The stiffness of the toroidal trap that we applied in all simulations presented in the following was $K = 10\, F_0/a$. Both the radial fluctuations, $|r_i - R|$, and the out-of-plane fluctuations, $|z_i|$, then turn out to be smaller than $0.05\, a$ in our simulations. (Note that the chosen value of K is not adjusted to the experiment; however, the radial stiffness affects the tangential dynamics only marginally, as can be seen from Fig. 9.7, and thus does not play a crucial role.)

10.1.2 Electrostatic interaction

To make our results comparable to experimental data, we include electrostatic repulsion between the particles.[3] The interaction of like-charged colloids is well-described by a screened Coulomb potential (also known as Yukawa potential) [57, 238],

$$U^{\lightning}(\boldsymbol{r}_i, \boldsymbol{r}_j) = A \, \frac{\mathrm{e}^{-r_{ij}/\ell_\mathrm{D}}}{r_{ij}/\ell_\mathrm{D}} \,, \tag{10.8}$$

which decays on distances $r_{ij} = |\boldsymbol{r}_i - \boldsymbol{r}_j|$ comparable to the Debye screening length ℓ_D. The prefactor A is related to physical parameters via

$$A = k_\mathrm{B} T Z^2 \, \frac{\ell_\mathrm{B}}{\ell_\mathrm{D}} \left(\frac{\mathrm{e}^{a/\ell_\mathrm{D}}}{1 + a/\ell_\mathrm{D}} \right)^2 \,, \tag{10.9}$$

where Z is the effective charge of the suspended particles and ℓ_B the Bjerrum length of the solvent.[4] The repulsive force is then given by

$$\boldsymbol{F}_i^{\lightning} = -\sum_{j \neq i} \nabla_j \, U^{\lightning}(\boldsymbol{r}_i, \boldsymbol{r}_j) = -A \sum_{j \neq i} \left(1 + \frac{\ell_\mathrm{D}}{r_{ij}} \right) \frac{\mathrm{e}^{-r_{ij}/\ell_\mathrm{D}}}{r_{ij}} \, \hat{\boldsymbol{r}}_{ij} \,, \tag{10.10}$$

where ∇_j denotes the gradient with respect to the coordinates of particle j, and $\hat{\boldsymbol{r}}_{ij} = (\boldsymbol{r}_j - \boldsymbol{r}_i)/r_{ij}$.

In experiments performed by C. Lutz and C. Bechinger [160] (see Sect. 10.2), the radius of the colloidal particles is $a = 1.5$ μm. The Debye length is approximately $\ell_\mathrm{D} = 300$ nm; for our simulations, we use the corresponding rescaled value $\ell_\mathrm{D} = 0.2\,a$. The prefactor A of the screened coulomb potential (10.8) is tuned such that the center-center distance between circling particles, driven by constant force F_0, does not fall below about $3\,a$ as observed in the experiments. This turns out to be the case for the value $A = 10^6 \, F_0 a$.[5] With the Bjerrum length $\ell_\mathrm{B} = 2.3$ nm for ethanol at room temperature [152], we obtain from Eq. (10.9) an effective particle charge of about $Z = 5000$.

10.1.3 Brownian-dynamics simulations

Since the sawtooth-modulated system features both deterministic drift and stochastic thermal motions (diffusion or thermally activated jumps across barriers),

[3] This replaces the "auxiliary" repulsive potential defined by Eq. (9.2).

[4] The Bjerrum length refers to the distance where electrostatic interactions between two particles are comparable to thermal noise. Its value is given by $\ell_\mathrm{B} = e^2/(4\pi\varepsilon_0\varepsilon_\mathrm{r} k_\mathrm{B} T)$, where e is the elementary charge, ε_0 the vacuum permittivity, and ε_r the relative dielectric constant of the solvent.

[5] This value of A formally corresponds to a *static* force equilibrium between the driving force F_0 and the electrostatic repulsion at particle distance $r_{ij} = 2.6\,a$.

it is essential to include Brownian motion in our calculations. As thermal noise also exerts torques on the particles, we now have to take rotational motions into account, too.[6] The system is thus described by the complete $6N$-dimensional Langevin equation (see Sect. 3.1), where the deterministic part of the forces and torques (denoted by $\mathbf{f}$) is given by

$$\boldsymbol{F}_i = \boldsymbol{F}_i^{\circlearrowleft} + \boldsymbol{F}_i^{\downarrow} \,, \tag{10.11a}$$

$$\boldsymbol{T}_i = \mathbf{0} \,. \tag{10.11b}$$

The Brownian-dynamics simulations were performed by applying the numerical integration scheme listed in Eq. (3.44). The time step Δt was chosen such that the drift displacements in the steep "downhill" regime are of order $0.05\,a$. (The diffusive steps are by one order of magnitude smaller for the temperature values that we use.)

As mentioned in the previous section, the strength of the electrostatic repulsion was tuned such that the particle distances are larger than $3\,a$. Therefore, the mobility matrix $\mathbf{M}$ (and thus the diffusion matrix $\mathbf{D} = k_\mathrm{B}T\mathbf{M}$) is to a good approximation given by the Rotne-Prager tensors listed in Eq. (2.39).[7]

If not stated otherwise, we use in our simulations the same parameter values as given by the experiment (see below). It was shown in Sect. 3.1.5 that driving force and temperature are not independent of each other, but enter the Langevin equation in terms of the Péclet number (3.25). Since we have defined all forces in terms of F_0, the dynamics in our model system is essentially characterized by the ratio $\mathrm{Pe}_0 = F_0 a/(k_\mathrm{B}T)$. In accordance with the experimental parameters, we set $\mathrm{Pe}_0 = 100$. If we normalize the resulting velocities to $v_0 = \mu^\mathrm{t} F_0 = F_0/(6\pi\eta a)$, the absolute value of F_0 is arbitrary. The bath temperature is given by $k_\mathrm{B}T = F_0 a/\mathrm{Pe}_0 = 0.01\,F_0 a$.

Note that the Péclet number in the "downhill" regime is very large, $\mathrm{Pe}_\downarrow = (F_0 + F_\downarrow)a/(k_\mathrm{B}T) \geq \mathrm{Pe}_0 \gg 1$, i.e., the dynamics there is almost deterministic, while in the "uphill" regime, the Péclet number $\mathrm{Pe}_\uparrow = |F_0 - F_\downarrow|\,a/(k_\mathrm{B}T) = |1-\varepsilon|\,\mathrm{Pe}_0$ becomes small and thus the motion diffusive if $\varepsilon \approx 1$.

The only not clearly fixed quantity is the asymmetry parameter ξ. We will use this in Sect. 10.3 as a free fit parameter to *map* the experimental potential (with "rounded edges") to an *effective* perfect sawtooth (with "sharp edges", as defined in Fig. 10.1).

[6] However, rotational fluctuations will only have a minor effect on the *tangential* dynamics since rotations only couple to translations that are *perpendicular* to the center-center axis of two particles (see Sect. 2.4.5) and, furthermore, rotational hydrodynamic couplings decay faster with distance than purely translational ones (see Sect. 2.4.2).

[7] The comparison of the Rotne-Prager mobilities with the more accurate values obtained by a higher-order multipole expansion is shown in Fig. 2.4. They agree quite well for particle distances larger than $3\,a$.

10.2 Experimental realization and validation of the model

The system introduced above was realized experimentally by C. Lutz and C. Bechinger [160]. A circular trap with radius $R = 9.86\ \mu$m (or, rescaled with respect to the particle size, $R = 7\,a$) was generated by a single laser tweezer scanned at intermediate frequency such that it exerts a driving force on colloidal particles inside the trap (see Sect. 8.2). The velocity of a particle driven by the unmodulated tweezer was $v_0 = 7.24\ \mu$m/s, corresponding to the force $F_0 = 6\pi\eta a v_0 = 0.245$ pN for particles with radius $a = 1.5\ \mu$m immersed in ethanol solution. The particles were tracked by videomicroscopy. Since the displacement by a single kick of the optical trap is estimated to be about $0.08\,a$, the particle motion is rather smooth. To avoid wall effects, the focus of the laser beam was placed about $27\,a$ away from the surface of the sample cell.

The additional sawtooth potential on top of the constant driving was achieved by weakly modulating ($\pm 10\%$) the intensity of the laser beam. This was accomplished by means of a function generator that was synchronized with the scanning motion of the laser. The number of potential wells along the circle was six, so the circumferential period length was $L = 2\pi R/6 = 10.3\ \mu$m.

It was demonstrated by C. Lutz and C. Bechinger that their experimental approach indeed allows to simultaneously apply a constant drift force and an additional quasi-static periodic potential to colloidal particles, as we will illustrate in the following. The energy dissipated by a moving particle due to hydrodynamic friction is given by the integral

$$W_{\mathrm{diss}}(s) = -\int_0^s \mathrm{d}s'\, F_{\mathrm{h}}(s') = \int_0^s \mathrm{d}s'\, F(s')\,, \tag{10.12}$$

where the friction force F_{h} and the driving force F, respectively, are related to the particle velocity via the Stokes law

$$F(s) = -F_{\mathrm{h}}(s) = \zeta^{\mathrm{t}} v(s) \tag{10.13}$$

with the friction coefficient $\zeta^{\mathrm{t}} = 6\pi\eta a$ [see Eqs. (2.16) and (2.17)]. According to Eq. (10.12), the dissipated energy corresponds to the tilted sawtooth potential $U(s)$ driving the particle:[8]

$$U(s) = -W_{\mathrm{diss}}(s)\,. \tag{10.14}$$

Thus, by measuring the position-dependent single-particle velocity $v(s)$ along the trap, one can determine the effective potential acting on the particle.

The result of this analysis is shown in Fig. 10.2. The upper inset [Fig. 10.2(b)] shows the particle velocity obtained from the recorded trajectories. In the main

[8] Note that W_{diss} also contains small contributions from the stochastic motion of the particles that can be neglected (see Fig. 10.2).

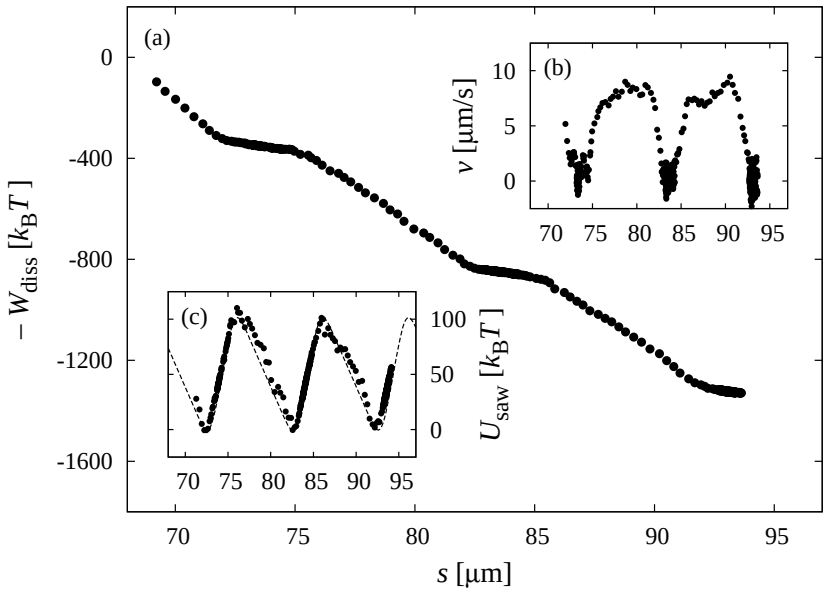

Figure 10.2 ■ (a) Dissipated energy $W_{\mathrm{diss}}(s)$ of a single particle driven by a constant force in a sawtooth potential. The values were calculated from the measured position-dependent velocity $v(s)$ shown in inset (b). Subtraction of the contribution of the constant driving force F_0 to the total energy yields the sawtooth potential $U_{\mathrm{saw}}(s)$ represented by the symbols in inset (c); for comparison, the dashed line represents the potential calculated directly from the intensity variation along the contour of the trap. All the data presented here are courtesy of C. Lutz [160].

graph [Fig. 10.2(a)], the corresponding energy dissipation is plotted that was determined via Eq. (10.12).[9] After subtraction of the linear contribution $F_0 s$, given by the mean particle velocity $v_0 = F_0/\zeta^{\mathrm{t}}$ that was measured *without* intensity modulation, we finally obtain the sawtooth potential $U_{\mathrm{saw}}(s)$, represented by the symbols in the lower inset [Fig. 10.2(c)]. Taking into account the size of the laser focus and that of the particles (both effects lead to some "rounding" of the "edges" in the potential [160, 236]), C. Lutz and C. Bechinger also calculated the effective potential acting on the particles directly from the sawtooth-shaped modulation of the laser intensity. The result is shown as dashed line in Fig. 10.2(c), which reveals good agreement with the measurements. Hence, it was verified experimentally that an intensity-modulated laser tweezer in fact generates simultaneously a constant driving force and a spatially modulated potential.

10.3 Single-particle dynamics

We first study the characteristic dynamics of a single particle in the tilted sawtooth potential $U(s)$. The single-particle velocity, as a function of the barrier

[9] Note that $W_{\mathrm{diss}}(s)$ also contains small contributions from the stochastic motion of the particle. These, however, are negligible in comparison with the absolute values of the energy.

height ε, will serve later as a reference to which the three-particle dynamics is compared. Furthermore, it will be used to determine an effective value for the asymmetry parameter ξ from the experimental data. The analytic expression for the single-particle velocity was derived by H. Stark [224] as follows.

Since the particle moves on a circle (i.e., we have periodic boundary conditions), the system reaches a stationary state, so the probability $p(s)$ to find the particle at position s becomes time-independent. It thus obeys the stationary Smoluchowski equation [Eq. (3.29) with $\partial p/\partial t = 0$]

$$\frac{\mathrm{d}}{\mathrm{d}s}\left[\left(\frac{\mathrm{d}}{\mathrm{d}s} - \frac{1}{k_\mathrm{B}T}F(s)\right)p(s)\right] = 0\,. \tag{10.15}$$

The corresponding probability flux $j(s)$ [see Eq. (3.30)] then reads

$$\frac{j}{D^\mathrm{t}} = \frac{1}{k_\mathrm{B}T}F(s)p(s) - \frac{\mathrm{d}}{\mathrm{d}s}p(s) = \text{const}\,, \tag{10.16}$$

where $D^\mathrm{t} = k_\mathrm{B}T\mu^\mathrm{t}$. For simplicity, we consider here a one-dimensional dynamics, thus neglecting effects of fluctuations in radial direction.[10] Solving the differential equation (10.16) for $p(s)$ piecewise on the two segments $0 \le s < L_\downarrow$ and $L_\downarrow \le s < L$ yields the probability distributions $p_\downarrow(s)$ and $p_\uparrow(s)$, respectively. They must satisfy the matching conditions $p_\downarrow(0) = p_\uparrow(L)$ and $p_\downarrow(L_\downarrow) = p_\uparrow(L_\downarrow)$, and the normalization $\int_L \mathrm{d}s\, p(s) = 1$. According to Eq. (10.16), the probability flux $j(s) = p(s)v(s)$ is constant, so the mean velocity $\langle v\rangle = \int_L \mathrm{d}s\, p(s)v(s)$ of the particle is simply [202]

$$\langle v\rangle = jL\,. \tag{10.17}$$

Finally, one obtains[11]

$$\frac{\langle v\rangle}{v_0} = \left[1 + \frac{\varepsilon^2}{(1-\varepsilon)[1-(1-\varepsilon)\xi]} \times\left(\xi - \frac{1-\mathrm{e}^{-w(1-\varepsilon)\xi}}{w(1-\varepsilon)[1-(1-\varepsilon)\xi]}\right)\right]^{-1}, \tag{10.18}$$

where $v_0 = \mu^\mathrm{t}F_0 = F_0/(6\pi\eta a)$, and $w = F_0L/k_\mathrm{B}T$ is the dissipative work per period normalized to the thermal energy.

Regarding Eq. (10.18) as a function of the barrier height ε, we can determine an effective asymmetry parameter ξ by a least-mean-square fit to the experimental data. Thus, we *map* the experimental potential to an *effective* perfect sawtooth. As Fig. 10.3 reveals, the agreement of the fitted theoretical curve with

[10] This is validated *a posteriori* by comparing the result of the one-dimensional analysis with data obtained from complete, three-dimensional Brownian-dynamics simulations (see Fig. 10.3).
[11] Equation (10.18) is equivalent to the relation presented in Ref. [167] [*ibid.*, Eq. (3)].

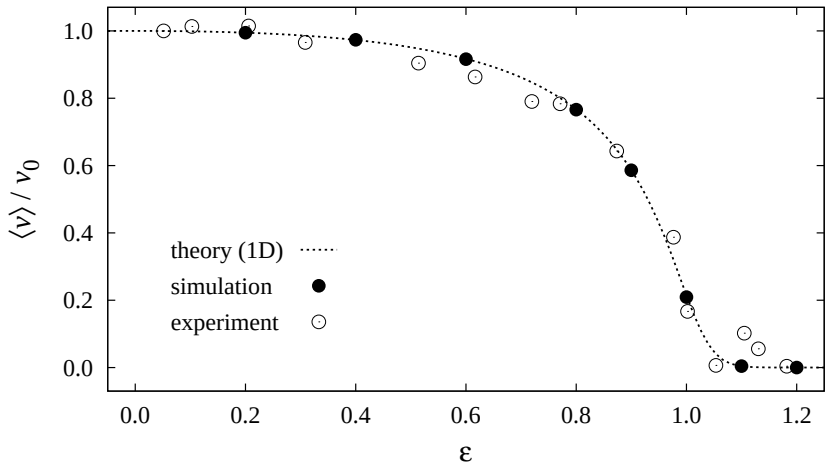

Figure 10.3 ■ Time-averaged single-particle velocity as a function of the sawtooth amplitude ε. The open circles show experimental data (courtesy of C. Lutz [160]). The dashed curve represents the theoretical result of the one-dimensional Smoluchowski analysis [Eq. (10.18)]. For comparison, the solid circles show data from three-dimensional Brownian-dynamics simulations.

the experimental data is excellent. The so obtained value is $\xi = 0.1$; if not stated otherwise, we use this value for ξ in all simulations.

In addition, Fig. 10.3 shows that the mean velocities calculated from the one-dimensional theory coincide with the ones determined by fully three-dimensional Brownian-dynamics simulations, validating the theoretical ansatz that neglected radial fluctuations.

10.4 Cooperative motion of drafting and thermal jumps

We now consider the dynamics of *three* particles in the sawtooth-modulated circular trap. Our interest is focused on the regime $\varepsilon > 1$ where particles are captured in potential wells. Similar to the case of constant forcing (see Sect. 9.3.2), the particles perform drafting motions and change their relative distances as a function of time. In contrast to Fig. 9.6, however, we do not observe the same periodic limit cycle, but rather a novel type of collective motion, induced by the sawtooth landscape, which enhances the dynamics compared to the single particle.

10.4.1 The "caterpillar" mode

For sawtooth amplitudes $\varepsilon > 1$, we find the following "caterpillar"-like motion of particle clusters. Assume that particle 2 drifts into a potential well which is already occupied by particle 1 [Fig. 10.4(a)]. Due to a combined effect of electrostatic repulsion and hydrodynamic interactions, particle 2 will push particle 1 over the barrier [Fig. 10.4(b)]. The drift motion of particle 1, in turn, causes

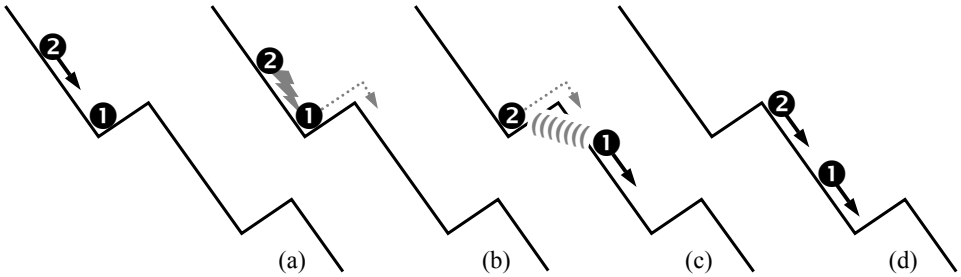

Figure 10.4 ■ Sketch of the motional sequence of a cluster comprised of two particles. Due to hydrodynamic interactions and electrostatic repulsion, a caterpillar-like motion is observed which facilitates the surmounting of potential barriers.

a hydrodynamic drag that particle 1 exerts on particle 2 [(Fig. 10.4(c)] which pulls the latter across the barrier [Fig. 10.4(d)]. Note that the process depicted in Fig. 10.4(c) would not be observed if hydrodynamic interactions did not exist. The motional sequence just described is reminiscent of a caterpillar which first stretches out, adheres at the front, and then bends the tail towards the head.

Once such a mode is initiated (by a thermally induced jump), the outlined motion may last over several sawtooth periods until the particles finally become again trapped in separate potential minima. This is caused by thermal fluctuations in their distance which reduce the effectivity of drafting. The motion stops until the situation described in Fig. 10.4(a) is initiated by a spontaneous jump of particle 2 into the potential well occupied by particle 1.[12]

Figure 10.5 shows representative trajectories (arc-length coordinates s_i) of three particles moving in a sawtooth potential with amplitude $\varepsilon = 1.1$. Note that this value corresponds to a rather high effective energy barrier, namely $\Delta U \approx 7\, k_{\mathrm{B}}T$. Nevertheless, the caterpillar can persist over several periods before breaking apart, as the time span marked in Fig. 10.5 (intervals I, II, and III) strikingly reveals. After quite a long break where all three particles were trapped, the motion is initiated by a thermal jump of particle 3 across the barrier. It kicks the neighboring particle 2 out of its potential well (interval I), and subsequently, also particle 1 is actuated. Then, a cluster is formed of particle 1 and particle 2, and the resulting caterpillar mode persists over about six sawtooth periods (interval II). When the cluster reaches the resting particle 3, the caterpillar keeps running, but the cluster is now comprised of particle 3 and particle 1, and particle 2 gets trapped (interval III). Finally, the caterpillar is "ruptured" by thermal fluctuations.

We point out that the screened electrostatic repulsion is only of minor importance. It is rather the long-range hydrodynamic interactions that generate a pushing force exerted by the rear particle on the particle in front, as illustrated in

[12] For sufficiently low energy barriers, it might also happen that particle 1 jumps first and pulls particle 2 across the barrier by hydrodynamic drag.

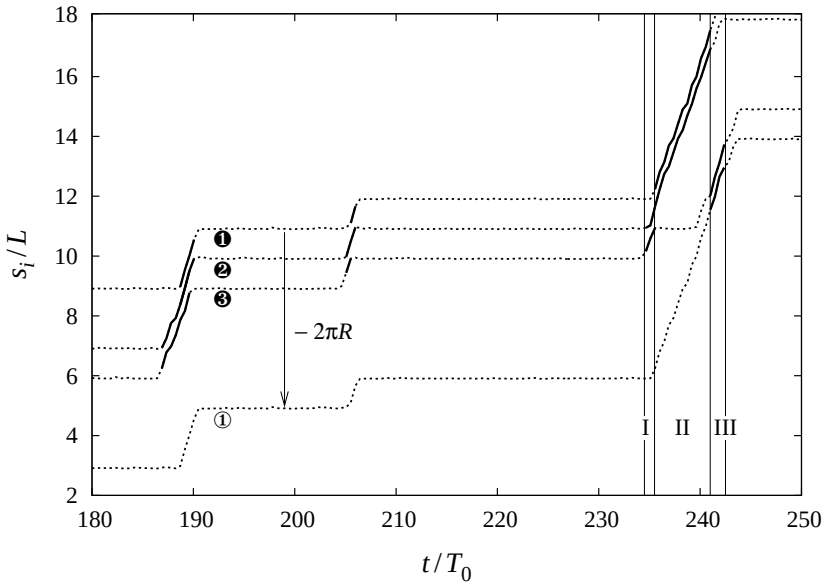

Figure 10.5 ■ Trajectories $s_i(t)$ of three particles in a sawtooth potential with $\varepsilon = 1.1$. The arc-length coordinates are normalized to the period length L, and the time is given in units of $T_0 = L/v_0$, i.e., the time that a single particle needs to drift along one period under the influence of the constant force F_0. The complete trajectories are drawn as dashed lines. The parts where the particles move in the caterpillar mode, satisfying the cluster criterion $\Delta s/L \leq \delta$ with $\delta = 0.7$, are marked as solid lines. The lowermost curve is the trajectory of particle 1 (uppermost curve) shifted by one circumferential length of the trap $[s_1(t) - 2\pi R]$.

Fig. 10.4(b), and thus predominantly trigger the caterpillar mode.[13] We obtain qualitatively the same kind of dynamics in simulations where the prefactor of the electrostatic interaction potential was reduced by two orders of magnitude.[14]

10.4.2 Enhanced cluster dynamics

To analyze the benefits of drafting effects in the caterpillar mode quantitatively, we calculate the mean velocity of the particles.[15] This averaging, however, requires some further consideration. For sawtooth amplitudes $\varepsilon > 1$, the particles spend a substantial amount of time being trapped in potential wells (horizon-

[13]The dominant term of the electrostatic forces is exponentially damped, $F^{\sharp}(r) = -\mathrm{d}U^{\sharp}(r)/\mathrm{d}r \propto \mathrm{e}^{-r/\ell_\mathrm{D}}/r$ (since $r > a \gg \ell_\mathrm{D}$), while hydrodynamic interactions decay asymptotically as $1/r$ (see Sect. 2.4.1).

[14]If the electrostatic repulsion is stronlgy reduced, the distances between adjacent particles can become very small ($r_{ij} \geq 2.1\,a$ for $A = 2 \times 10^4\, F_0 a$). Hence, the Rotne-Prager tensors are no longer a good approximation. Instead, we use the numerical library HYDROLIB [113] to calculate the mobilities by means of the more accurate multipole expansion, including lubrication corrections at very small distances.

[15]As the radial fluctuations are very small, we consider only the velocity components tangential to the centerline of the circular trap, $v_i = \dot{s}_i = R\dot{\phi}_i$.

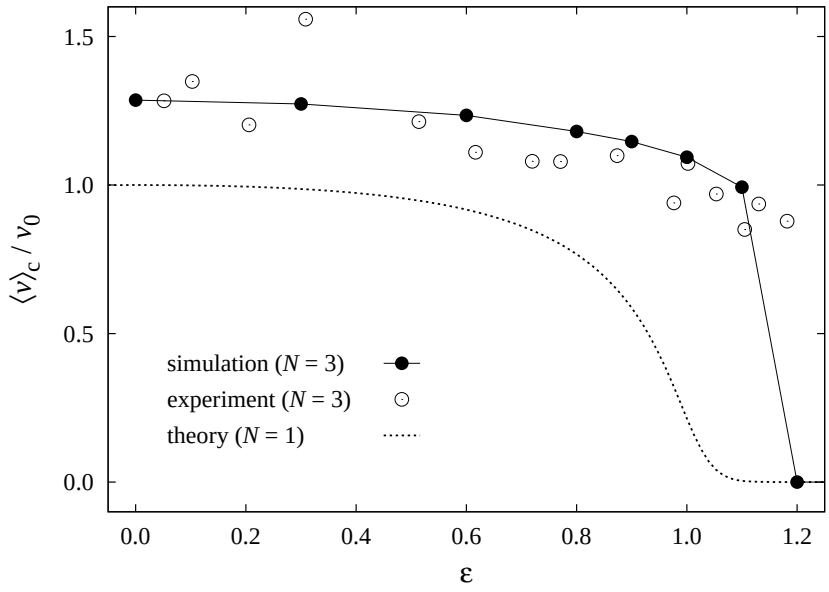

Figure 10.6 ■ Mean velocity of two-particle clusters in the caterpillar mode as a function of the sawtooth amplitude ε. The solid circles represent the result obtained from Brownian-dynamics simulations (the statistical error is of the order of the symbol size). The open circles show the velocities measured in the experiment (data courtesy of C. Lutz [160]). For comparison, the single-particle velocity from Fig. 10.3 is replotted (dashed curve).

tal parts of the trajectories shown in Fig. 10.5), i.e., the velocity in this case is zero. On the other hand, when they move in the collective caterpillar mode, their well-defined velocity is rather large. Roughly speaking, the distribution of the velocities exhibits two distinct peaks, so the simple average over all times[16] ($t = 0 \ldots T$) and particles ($i = 1 \ldots N$),

$$\langle v \rangle = \frac{1}{N} \sum_{i=1}^{N} \frac{1}{T} \fint_{t=0}^{T} v_i(t) \,, \tag{10.19}$$

is rather meaningless. Instead, we define a *cluster* or *caterpillar average* $\langle v \rangle_\mathrm{c}$ where only particles satisfying the criterion

$$\frac{\Delta s}{L} \leq \delta \quad \text{with} \quad \delta < 1 \tag{10.20}$$

are taken into account, i.e., the arc-length distance Δs between adjacent particles is less than one period length L of the sawtooth potential. For our data analysis, we choose the value $\delta = 0.7$. In Fig. 10.5, we have marked the parts of the trajectories that meet this criterion. Clearly, this is only a small fraction in comparison to the total simulation time.

[16] The combined symbol $\fint$ denotes that the time average $T^{-1} \int_0^T \mathrm{d}t \, v_i(t)$ becomes the sum $M^{-1} \sum_{j=1}^{M} v_i(t_j)$ (with $t_1 = 0$ and $t_M = T$) in case of discrete data sets.

The result of this analysis, applied to data obtained from Brownian-dynamics simulations, is presented in Fig. 10.6. In addition, we show the corresponding velocities measured in the experiment [160]. Obviously, the cluster velocity is larger than the single-particle velocity, which is again a result of drag reduction by hydrodynamic drafting effects. What is actually surprising, is the fact that, even when the single-particle velocity suddenly drops to zero around $\varepsilon \approx 1$ (because the particle becomes trapped in a potential well), the cluster velocity varies only by about 20% in that range of ε, and the caterpillar seems to overcome potential barriers of several $k_\mathrm{B}T$ with ease ($\Delta U \approx 7\, k_\mathrm{B}T$ for $\varepsilon = 1.1$).

10.4.3 On the role of hydrodynamic interactions

To demonstrate the crucial role of the hydrodynamic coupling, we also performed simulations *without* hydrodynamic interactions.[17] The resulting velocities are shown in Fig. 10.7 (open symbols). The different types of symbols denote different types of averaging, as discussed in the following.

Calculating the mean *cluster* velocities as before, we obtain the graph plotted with open circles in Fig. 10.7. As expected, the values of $\langle v \rangle_\mathrm{c}$ are always well below the corresponding curve where hydrodynamic interactions are incluced (solid circles). However, the "observation" that the particles still move significantly at $\varepsilon \geq 1$ even without hydrodynamic interactions is an artefact of our cluster analysis, since we "artificially" pick only particles that are accidentally moving as a short-lived cluster where the rear particle starts drafting down the seceding flank [Fig. 10.4(a)], kicks the front particle by electrostatic repulsion over the barrier [Fig. 10.4(b)], and then stops since the hydrodynamic drag [Fig. 10.4(c)] is missing.

Thus, to be precise and consistent, we have to calculate the average $\langle v \rangle$ over *all* times and particles to make a meaningful comparison with the single-particle dynamics, since the theory for the latter considers an ensemble average and thus an average over all times. While the complete dynamics *including* hydrodynamic interactions also in this type of averaging still reveals an enhancement (Fig. 10.7, solid squares), the mean velocities of particles *without* hydrodynamic coupling collapse on the single-particle curve (Fig. 10.7, open squares).

This can be understood quantitatively as follows. If we neglect hydrodynamic interactions, the velocity of particle i is directly given by

$$v_i(t) = \mu^\mathrm{t}[F_i^{\circlearrowleft}(t) + F_i^{\lightning}(t) + \tilde{F}_i(t)]\,. \tag{10.21}$$

According to Newton's third law, "actio = reactio", the electrostatic pair interactions cancel if we perform the sum over all particles:

$$\sum_{i=1}^{N} F_i^{\lightning}(t) = 0\,. \tag{10.22}$$

[17] $\boldsymbol{\mu}_{ii}^{\mathrm{tt}} = \mu^\mathrm{t}\mathbf{1}$ and $\boldsymbol{\mu}_{ii}^{\mathrm{rr}} = \mu^\mathrm{r}\mathbf{1}$; all the other mobilities vanish.

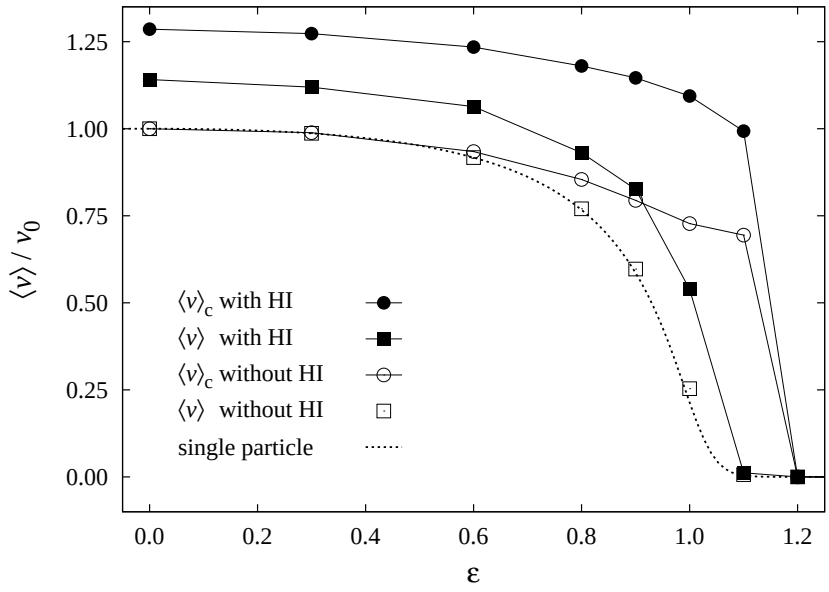

Figure 10.7 ■ Comparison of velocities in a three-particle system with and without hydrodynamic interactions (HI). The solid/open symbols represent data obtained from simulations with/without hydrodynamic interactions. The circles are cluster averages (the solid circles are the same data as in Fig. 10.6), while the squares show the average over all times and particles. For comparison, the single-particle velocity from Fig. 10.3 is replotted (dashed curve).

Furthermore, the time average of the fluctuating forces vanishes:

$$\frac{1}{T}\sum_{t=0}^{T}\!\!\!\!\!\!\int \tilde{F}_i(t) = 0\,. \tag{10.23}$$

Therefore, the overall average reads

$$\langle v\rangle_N = \frac{1}{N}\sum_{i=1}^{N}\frac{1}{T}\sum_{t=0}^{T}\!\!\!\!\!\!\int v_i(t) = \frac{1}{N}\sum_{i=1}^{N}\frac{1}{T}\sum_{t=0}^{T}\!\!\!\!\!\!\int \mu^{\mathrm{t}} F_i^{\circlearrowleft}(t)\,. \tag{10.24}$$

The subscript N here explicitly symbolizes that we consider a system of N particles. However, realizing that $\mu^{\mathrm{t}} F_i^{\circlearrowleft}(t)$ simply represents the velocity of a single particle driven along the circular trap, we have

$$\frac{1}{T}\sum_{t=0}^{T}\!\!\!\!\!\!\int \mu^{\mathrm{t}} F_i^{\circlearrowleft}(t) = \langle v\rangle_1\,, \tag{10.25}$$

and we finally obtain

$$\langle v\rangle_N = \langle v\rangle_1\,. \tag{10.26}$$

Hence, the mean velocity of N particles *without* hydrodynamic interactions is equal to the one of a *single* particle, so electrostatic repulsion does not play a

significant role.[18] This clearly demonstrates that, without hydrodynamic interactions, the particles on average move *independently*; or, reversely, hydrodynamic interactions are crucial for the enhancement of the dynamics.

In addition, to get a quantitative measure for the *cooperativity* of the dynamics, we calculate the velocity correlation function[19]

$$C_{ij}(\tau) = \frac{\langle \Delta v_i(t+\tau)\Delta v_j(t)\rangle}{\sqrt{\langle \Delta v_i^2\rangle\langle \Delta v_j^2\rangle}} \,, \tag{10.27}$$

where $\Delta v_i(t) = v_i(t) - \langle v_i\rangle$ is the deviation of the velocity of particle i from its time average. The correlation functions $C_{21}(\tau) = C_{32}(\tau) = C_{13}(\tau)$ describe situations like the one depicted in Fig. 10.4(b): First the rear particle moves and then pushes the front particle. The functions $C_{12}(\tau) = C_{23}(\tau) = C_{31}(\tau)$ sense the opposite situation as shown in Fig. 10.4(c): First the front particle moves and then drags the rear particle.

The result of this analysis is presented in Fig. 10.8, which reveals some characteristic features. Overall, the comparison of the correlation functions calculated from simulations with (black curves) and without hydrodynamic interactions (gray curves) confirms that the particles in principle move independently if hydrodynamic interactions are not present since their velocities are not correlated. In the following, we discuss the shape of the curves in detail.

We first consider the case where hydrodynamic interactions are included (black curves). Without sawtooth potential ($\varepsilon = 0$), the correlation functions would be periodic (with constant amplitude) in the absence of thermal noise, where the period is given by the time span that a two-particle cluster needs to break up and rebuild again (which is of the order of ten circulations[20]). Thermal fluctuations diminish the amplitude, as can be seen in Fig. 10.8(a). The interpretation of the absolute peak positions, however, is not so obvious since they result from a complex superposition of several dynamic situations.[21]

If the sawtooth amplitude approaches $\varepsilon = 1$, the correlations get reduced. For $\varepsilon = 0.9$, the dynamics is still a rather deterministic drift motion (with Péclet

[18]The only significant influence of electrostatic repulsion at all is that it sets the minimum particle distance and thus the drafting velocity. If we compare the value of $\langle v\rangle$ at $\varepsilon = 0$ in Fig. 10.7 with the values in Fig. 9.7 (the ordinates of both figures are equivalent), we see that $\langle v\rangle/v_0 \approx 1.1$ in the first case, i.e., with repulsion, and $\langle v\rangle/v_0 \approx 1.4$ in the latter case. This corresponds to the difference in the coupling coefficient $\mu_{12}^{\mathrm{tt}\parallel}$ for $r \approx 2\,a$ and $r \approx 3\,a$, respectively; from Fig. 2.4, we obtain $\mu_{12}^{\mathrm{tt}\parallel}(2\,a) \approx 1.5\,\mu_{12}^{\mathrm{tt}\parallel}(3\,a)$.

[19]The correlation functions were calculated by means of fast Fourier transformation (see footnote 3 on p. 76).

[20]see also Sect. 9.3.3

[21]If particle 1 and particle 2, e.g., move as a cluster and particle 3 moves separately, then C_{12} measures the velocity correlation inside a two-particle cluster. On the other hand, when the cluster breaks up after a while and a new cluster is formed of particle 1 and particle 3, then C_{12} measures correlations between the cluster and the single particle 2. This is only one example how different situations mix up in the correlation functions.

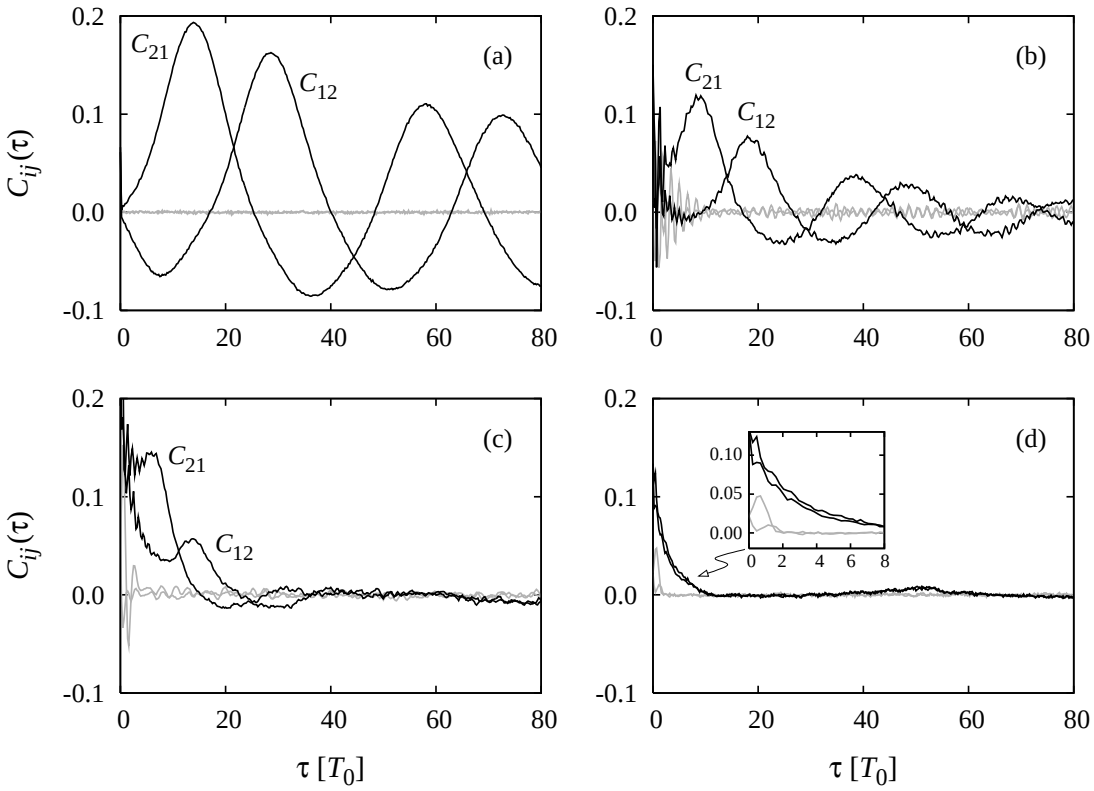

Figure 10.8 ■ Velocity correlations at different sawtooth amplitudes: (a) $\varepsilon = 0$, (b) $\varepsilon = 0.9$, (c) $\varepsilon = 1$, and (d) $\varepsilon = 1.1$. The black/gray curves were obtained from Brownian-dynamics simulations with/without hydrodynamic interactions. The time lag τ is given in units of the time $T_0 = L/v_0$ that a particle needs to drift one period L in case the sawtooth is switched off. The inset in Fig. (d) enlarges the initial decay of the correlations.

number $\mathrm{Pe}_\uparrow = 10$), and the characteristic features of the unmodulated trap are still visible [Fig. 10.8(b)]. At $\varepsilon = 1$, where the particles diffuse freely in the "uphill" regime, only a single significant peak remains in the correlation functions [Fig. 10.8(c)].

For $\varepsilon > 1$, an effective energy barrier $\Delta U > 0$ exists, so velocity correlations are destroyed if a particle gets trapped in a potential well. The decay time of the correlation functions shown in Fig. 10.8(d) can be interpreted as the characteristic life time of the caterpillar mode (until it is interrupted). The value of this correlation time corresponds to a cooperative motion that persists over about five sawtooth periods L. This coincides with observations made from video animations of the simulated particle trajectories.[22]

The small short-time oscillations with constant amplitude and time period $\Delta\tau \approx T_0 = L/v_0$ that are superimposed on all correlation functions for $\varepsilon > 0$ [Figs. 10.8(b–d)] are simply induced by the spatial periodicity L of the sawtooth

[22] see also the trajectories plotted in Fig. 10.5

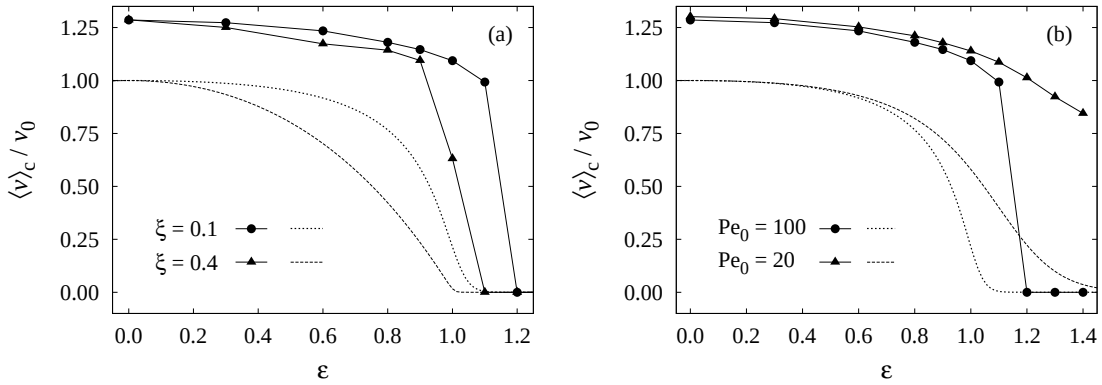

Figure 10.9 ■ Dependence of the cluster velocity on the sawtooth asymmetry (a) and the temperature (b). The solid circles denote the same data as those shown in Fig. 10.6 (according to the experimental parameters). In Fig. (a), the asymmetry parameter ξ is changed from 0.1 to 0.4 (for $\xi = 0.5$, the sawtooth would be symmetric). In Fig. (b), the temperature is increased by a factor of 5, corresponding to a decrease of the Péclet number $\mathrm{Pe}_0 = F_0 a/(k_\mathrm{B}T)$ from 100 to 20. For comparison, the dashed curves show the single-particle velocity for the respective parameter values.

potential. Note that, even if the particles did not interact at all, their velocities would be periodic in time due to the spatially periodic potential (provided that the particles perform drift motions only, i.e., for $0 < \varepsilon < 1$), and thus, the particles would appear to be somehow "correlated".

In the case where hydrodynamic interactions are neglected (gray curves), the correlation functions reveal a few peaks at short times. They result from events where the rear particle pushes the front particle due to electrostatic repulsion. Hence, these peaks are more pronounced for $C_{21}(\tau)$, describing the electrostatic push [Fig. 10.4(b)], and they almost vanish for $C_{12}(\tau)$ since the corresponding event, namely the hydrodynamic drag [Fig. 10.4(c)], is missing. For $\varepsilon \geq 1$ [Figs. 10.8(c,d)], there is only one such short-time peak caused by occasional electrostatic pushes; there are no further peaks since the correlation decays within one period L. Thus, we can consider the particle motion without hydrodynamic interactions to be almost uncorrelated.

10.4.4 Influence of sawtooth asymmetry and temperature

So far, we have used in our simulations the same parameter values as given by the experiment. In this last section, we want to discuss briefly the influence of sawtooth asymmetry and temperature on the particle dynamics.

In Fig. 10.9(a), we compare the average cluster velocities in a very asymmetric sawtooth (with parameter $\xi = 0.1$, as before) with a rather symmetric potential ($\xi = 0.4$). Significant differences in the cluster velocities for the two ξ values emerge for $\varepsilon \geq 1$, i.e., when energy barriers are present. Thus, asymmetry

clearly supports the collective caterpillar mode. Note that, although the single-particle velocities depend very sensitively on the value of ξ, the cluster velocities at different ξ do not differ significantly for $\varepsilon < 1$.

An increase of the temperature [or a decrease of the Péclet number $\mathrm{Pe}_0 = F_0 a/(k_\mathrm{B}T)$] effectively corresponds to a reduction of the energy barriers. The influence of temperature on the cluster velocities becomes significant only for $\varepsilon \geq 1.2$, as Fig. 10.9(b) reveals. Thus, for $\varepsilon < 1.2$, thermal activation does not seem to play a dominant role; in this regime, the caterpillar (once it is initiated) sustains itself by hydrodynamic pulling and pushing. For $\varepsilon \geq 1.2$, however, the caterpillar needs the additional support by thermal noise to overcome the barriers.

11 Conclusions II

This part was focusing on the enhancement of few-particle motions by hydrodynamic interactions in a colloidal system driven far from equilibrium. We modeled the circling motion of colloids in a circular trap and illustrated how hydrodynamic interactions lead to interesting nonlinear behavior of the coupled particle dynamics.

It was shown that practically any initial particle configuration driven by constant force is unstable and finally tends towards a periodic limit cycle. The latter is completely governed by hydrodynamic interactions, featuring a considerable drag reduction by drafting effects. Furthermore, we mentioned the clustering of particles for the case of weak radial trapping which can also lead to interesting collective phenomena.

By adding a static, spatially periodic sawtooth potential to the constant driving force, we observe a novel caterpillar-like motional sequence, which is also in quantitative agreement with experiments. We demonstrated that this phenomenon is predominantly triggered by hydrodynamic interactions, favoring the surmounting of rather large potential barriers. The caterpillar mode appears as an interplay between the pushing and pulling forces due to hydrodynamic interactions. While this observation represents an exclusively *dynamic* effect, a recent study also analyzed the role of a harmonic coupling (like a "spring") between two particles in a thermal ratchet [240]. Our results indicate that the motion of particles in thermal ratchets might be largely affected by hydrodynamic interactions.

Such thermal ratchets can be utilized as a tool to separate particles of different size via the differences in their mobilities or diffusivities, respectively. By varying a spatially asymmetric potential in time, the unbiased Brownian motion of particles can be converted into a directed flux, and the direction of this flux depends on the relevant parameters defining the potential and on the time scales involved [40, 202]. The ratchet (with appropriate shape of the potential) can be tuned such that different particles move in different directions and thus separate. In this context, it might be very interesting to study the role of hydrodynamic interactions and their influence on the particle motion. To our knowlegde, hydrodynamic interactions have not been included yet in the existing theories and have been avoided in quantitative experiments by considering only very dilute dispersions.

Besides a better microscopic understanding of hydrodynamic interactions in few-particle systems, our results are also of relevance for the dynamics of biolog-

ical, molecular motors that can be well described as thermal ratchets [9, 10, 126, 202]. Indeed, recent *in-vivo* experiments demonstrate that the speed of coupled motor proteins is increased compared to the speed of a single motor [141]. The underlying mechanism, however, has not been explained yet.

We now can make a "smooth crossover" to the subject of Part D. The biomolecular engines that drive swimming microorganisms, such as bacterial cells, can also be viewed as Brownian motors [10]. Filaments attached to these motors act as paddles propelling the organism. As we shall demonstrate for screw-like filaments driven by rotary motors, their motions are synchronized owing to hydrodynamic interactions.

D Swimming of microorganisms ■ Synchronization of rotating helical flagella

Abstract ■ Many types of bacteria use rotating helical flagella to swim. The motion of such organisms takes place in the regime of low Reynolds numbers where viscous effects dominate over inertia and where the dynamics is governed by hydrodynamic interactions. Typically, rotating flagella form bundles, which means that their rotations must be synchronized. The aim of this study is to investigate whether hydrodynamic interactions can be at the origin of such a synchronization. In a first approach, we consider two stiff helices that are modeled by rigidly connected beads, neglecting any elastic deformations. They are driven by constant and equal torques, and they are fixed in space by anchoring their ends in harmonic traps. We observe that, for finite anchoring strength, hydrodynamic interactions do indeed synchronize the rotations of the helices. It turns out, however, that the speed of phase synchronization decreases with increasing trap stiffness; in the limit of infinite trap stiffness, the speed is zero and the helices do not synchronize. As a second step, we refine our model and make the helices intrinsically flexible. Again, the dynamics of the rotating helices is synchronized. Analyzing the dependence of the synchronization process on the stiffness parameters, we find the expectation confirmed that flexibility enhances the synchronization process. Besides the phase locking of the helices, we furthermore observe the "onset" of flagellar bundling.

12 Locomotion of microorganisms

Swimming motions in water are well categorized by their Reynolds numbers. For an object with a characteristic linear dimension a moving with velocity v through a Newtonian fluid (with density ρ and viscosity η), the ratio $\mathrm{Re} = \rho v a/\eta$ [Eq. (2.10)] quantifies the relative importance of inertial and viscous forces. In Table 12.1, we list the Reynolds numbers of representative natural swimmers.

Propulsion mechanisms that are successful in the macroscopic world ($\mathrm{Re} \gg 1$) where inertial effects dominate the dynamics are not necessarily suitable for microorganisms ($\mathrm{Re} \ll 1$) where viscous forces govern the patterns of motion.[1] A large animal, such as a whale, moving at very high Reynolds number, coasts several meters after a single flap with its tail fin, utilizing strong inertial effects. This simple strategy of coasting, however, does not work at all for microorganisms, which becomes immediately obvious if we look at numbers. A micron-sized swimmer that runs at full speed (typically several microns per second) and then suddenly switches off its motor will stop after about 0.1 μs, and within that time, it will have traveled a distance of about 0.1 Å [199], i.e., less than the diameter of an atom! Hence, inertial effects indeed do not play a role at very low Reynolds numbers, and the thrust pushing the object forward must result solely from viscous forces. Swimming of microorganisms is thus fundamentally different from what we know from our own (macroscopic) experience.

Besides the fascinating physics behind, the investigation of swimming motions at the micron scale is also of biological, medical, and technological relevance. There is obvious interest in understanding how bacteria, e.g., move from one point to another, which is important in disease control and thus a concern in public health. Furthermore, the swirling dynamics of microorganisms can be utilized to mix fluids at low Reynolds number, which is one of the challenging problems in microfluidics [229]. Recently, it was demonstrated that the mass transport in a microfluidic device can be strongly enhanced by the presence of swimming microorganisms [55].[2] Last but not least, swimming at low Reynolds number is also an issue of medical research. There is the (futuristic) idea to design self-propelled "microbots" at the scale of biological cells [19, 20, 67, 140]. Injected into the human ureter, e.g., such a microrobot, so is the vision, can be utilized to destroy kidney stones.

[1] For intermediate Reynolds numbers ($\mathrm{Re} = 1 \ldots 100$), simulations predict that forward thrust is primarily generated by inertia, while resistance is rather caused by viscous drag [177].

[2] Such a device consists of bacterial cells whose bodies are attached to a surface, but whose propulsion units are still "paddling" freely, thus generating a fluid flow [55].

	whale	human	jellyfish	plankton	bacterium
size	10 m	1 m	10 cm	1 mm	1 μm
Re	10^8	10^5	10^3	10^1	10^{-5}

Table 12.1 ■ Reynolds numbers of swimming motions in nature (for characteristic length scales and typical swimming speeds). Inertial effects are relevant down to the millimeter scale (plankton with Re = 10). Microorganisms, such as bacteria, swim at very low Reynolds number (Re = 10^{-5}), where viscosity dominates over inertia.

12.1 Principles of swimming at low Reynolds number

In general, swimming is necessarily a cyclic deformation of the body. At higher Reynolds numbers, the motional pattern is typically some kind of flapping motion. At first, a fast power stroke is performed, such as a scallop closes its shell or as a jellyfish contracts its bell (like closing an umbrella). This is then followed by a slower recovery stroke (the scallop opens its shell again, or the jellyfish widens its bell). Due to inertia, this results in a net displacement in direction of the "hinge". However, this principle will not work at all for micron-sized swimmers for the following reason.

In the regime of low Reynolds number, the flow dynamics is governed by the Stokes equations (2.14). Since these are *time-independent* (neglecting inertial effects), the pattern of motion is the same, whether a stroke is performed slow or fast, whether forward or backward in time [157, 199].[3] This fact is also known as Purcell's "scallop theorem", which is depicted in Fig. 12.1(a). The displacement to the right after the first half of the cycle is equal to the displacement to the left after the second half, thus the net displament is zero, independent of the flapping speeds.

Therefore, patterns of motion that are to be successful at low Reynolds numbers must satisfy the criterion that they are *not reciprocal in time*, i.e., time-reversed pattern is not the same as the original one. The (hypothetical) pattern illustrated in Fig. 12.1(b), known as Purcell's "three-link swimmer" [199], is in fact cyclic but not reciprocal. For the sequence shown here, the swimmer is expected to move to the right [199],[4] which was also demonstrated experimentally by a mechanical realization of the three-link swimmer [116]. This can be understood by regarding the cycle as a "traveling wave", propagating from right to left, thus propelling the swimmer from left to right [18].

[3]The time-reversibility of Stokes flow was impressively demonstrated in several experiments by Taylor in his famous lecture on low-Reynolds-number flows [234].

[4]For very large flapping angles (where each stroke consists of nearly a full rotation of the flapping link), however, numerical results indicate that the swimming direction points to the left [18].

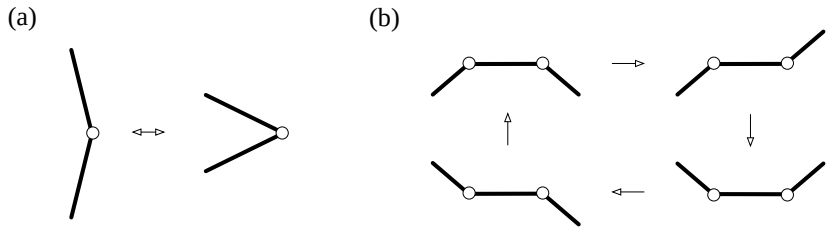

Figure 12.1 ■ (a) Reciprocal flapping motion with only one joint. At low Reynolds number, the displacement to the right after the first half of the cycle is equal to the displacement to the left after the second half, thus the net displament is zero. (b) In order to perform a non-reciprocal flapping motion, one more joint, i.e., at least three links, are necessary. The pattern of motion is not the same if processed forward or backward in time. After one complete cycle, the three-link swimmer as illustrated here has moved to the right.

In recent years, many variants of such a plain, hypothetical low-Reynolds-number swimmer, also calld "artificial animalcules", have been proposed and realized both theoretically and experimentally [11, 12, 62, 63, 88, 89, 135, 169, 184] (for a short state-of-the-art review, see Ref. [245]).

12.2 Flagellar propulsion

Microorganisms, such as bacteria and many eukaryotic cells, propel themselves with whip-like appendages, known as *flagella*, which can exhibit a variety of structures and motional patterns.[5] While, e.g., spermatozoa swim by undulating a single flagellum, other cells, such as bacteria, typically use several flagella.

We can distinguish basically three different strategies of nature to elude the "scallop theorem" by flagellar propulsion: (i) to undulate a flexible tail as shown in Fig. 12.2(a), (ii) to beat with a flexible oar[6] as sketched in Fig. 12.2(b), or (iii) to rotate a screw-like appendage as illustrated in Fig. 12.2(c). All these motions are cyclic but not reciprocal. In case (i), a wave of lateral displacements travels down the filament, and in case (iii) a helical wave. The fluid coupled to the filament moves rearward with the wave, and thus the cell is pushed forward [233].

The phenomenology of swimming by rotating flagella [Fig. 12.2(c)], as performed by certain types of bacteria, will be explained in detail below in Sect. 12.2.2. But at first, we describe briefly the beating pattern shown in Fig. 12.2(b), which is referred to as ciliary beating.

[5]Note that there are also microorganisms whose swimming mechanisms are not based on flagellar propulsion. *Spiroplasma*, e.g, swims by changes in the helicity of its chiral cytoskeleton, leading to kinks that propagate along the whole cell as a wave of lateral displacement [219].
[6]Beating with a *rigid* oar would not generate a net propulsion. The *bending* of the undulating flexible tail, however, breaks the forward-backward symmetry, so that the resulting motional pattern is *not reciprocal*.

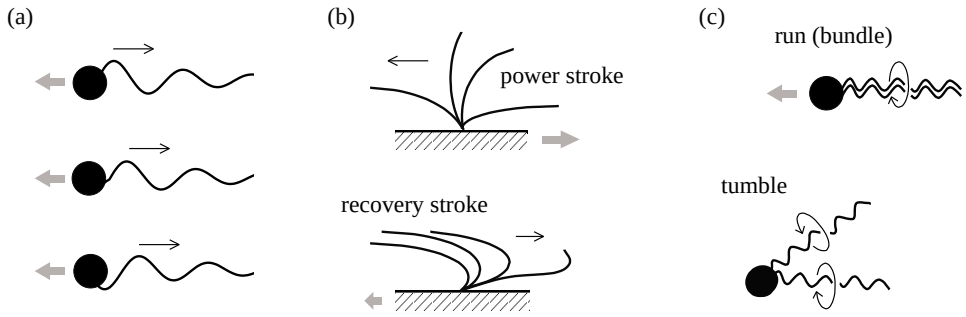

Figure 12.2 ■ Low-Reynolds-number swimming strategies implemented by nature. (a) The undulation of a single flagellum generates a bending wave that propagates down the tail and thus pushes the cell forward. (b) Motional pattern of beating cilia. In the power stroke, the cilium moves stretched out like a stiff rod, so the viscous drag (and thus the thrust to the right) is rather large. In the recovery stroke, the cilium rolls back in a more or less tangential motion close to the cell wall, hence reducing the viscous drag. Each image shows a sequences of four subsequent cilia configurations. (c) Propulsion by rotating helical flagella. During a run, the flagella all rotate in synchrony and form a bundle, leading to a forward thrust. A tumble occurs when one of the motors reverses, so the bundle flies apart and the cell changes its swimming direction randomly.

12.2.1 Ciliary beating

Certain cells possess surfaces that are densely coated with beating flagella, which are called *cilia* in this context.[7] The mechanism of ciliary beating relies essentially on the difference of the viscous friction of a slender rod moving either lengthwise or sidewise.[8] During the power stroke, the cilium moves almost like a straight rod, and during the recovery stroke, it rolls back to its starting position in a tangential motion close to the cell wall [221], as illustrated in Fig. 12.2(b).[9] The power stroke (also called effective stroke) thus encounters a strong viscous drag and therefore generates thrust, while the recovery stroke avoids viscous friction.

Paramecium, e.g., uses ciliary beating for locomotion, and epithelial cells such as those in the respiratory tract utilize their densely ciliated surfaces to transport fluids [155]. Furthermore, the hydrodynamic flows generated by cilia also play a key role during the morphogenesis of higher organisms such as mammalians. The left-right symmetry of the vertebrate body plan is broken with the help of nodal cilia (located in the midline of the early embryo). The ciliary beating generates a fluid flow to one side that transports signaling molecules and thus breaks the symmetry [227]. It was demonstrated that the left-right asymmetry is randomized

[7] Note that there are also microorganisms with only a few cilia. *Chlamydomonas*, e.g., has two cilia, and the beating pattern is reminiscent of human breast stroke [155].
[8] For a long and thin rigid rod, the friction coefficient for motion perpendicular to the rod is approximately twice as large as for parallel motion [16, 47].
[9] Typically, the power stroke is performed more or less in one plane, while the cilium moves out of this plane during the recovery stroke [221].

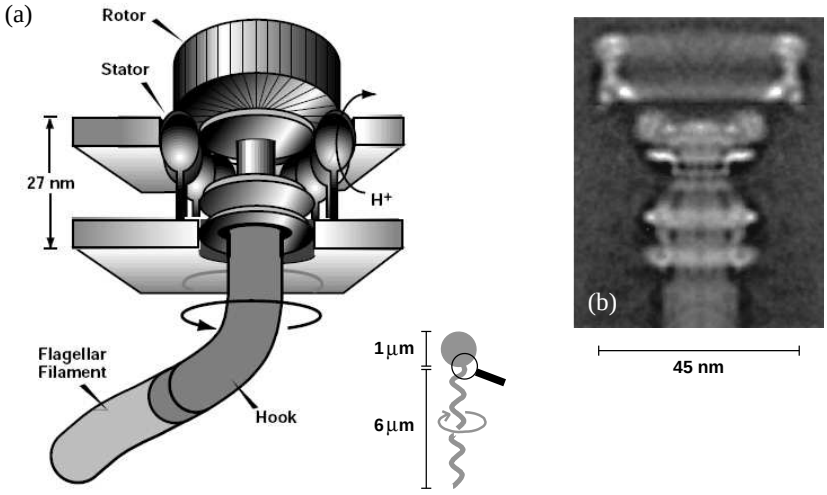

Figure 12.3 ■ Flagellar motor of *E. coli*. (a) The complete flagellum consists of a reversible rotary motor (powered by a proton flow) embedded in the cell wall, the helical filament that acts as propellor, and in-between a short flexible coupling called the proximal hook (picture redrawn from Ref. [129]). (b) Eletron-micrograph of the basal body (picture redrawn from Ref. [24]).

if the cilia are immotile due to gene manipulation [71, 188]. Furthermore, inducing an artificial rightward flow results in a reverse of the left-right bias in the early embryonic stages [189].

12.2.2 Phenomenology of propulsion by rotating helical flagella

Many types of bacteria, such as certain strains of *Escherichia coli* (*E. coli*) or *Salmonella typhimurium*, swim by rotating helical flagellar filaments, which are several micrometers long and about 20 nm in diameter (the size of the cell body is about 1 μm) [23, 24, 25, 165, 237]. The complete flagellum consists of three parts (Fig. 12.3): the basal body which is a reversible rotary motor embedded in the cell wall, the helical filament that acts as propellor, and in-between a short flexible coupling called the proximal hook.[10] The motor is powered by protons moving down an electrochemical gradient across the bacterial membrane, which generates a constant torque almost independent of the dynamic load [24, 25, 165, 170]. The rotation rates for the flagella of freely moving bacteria are of the order of 100 Hz. The filaments are polymers with high flexural and torsional stiffness; however, they are flexible enough to switch between different helical forms with distinct curvature and twist [24, 25, 165, 237]. The number of filaments attached to a cell varies from one individual to the other and ranges typically from one to five.[11]

[10] Recently, the molecular structures of the flagellar filament [250] and the proximal hook [212] were resolved.

[11] A detailed counting statistics yields that the number of filaments per *E. coli* cell is 3.3 ± 1.8 (mean $\pm$ standard deviation) [237].

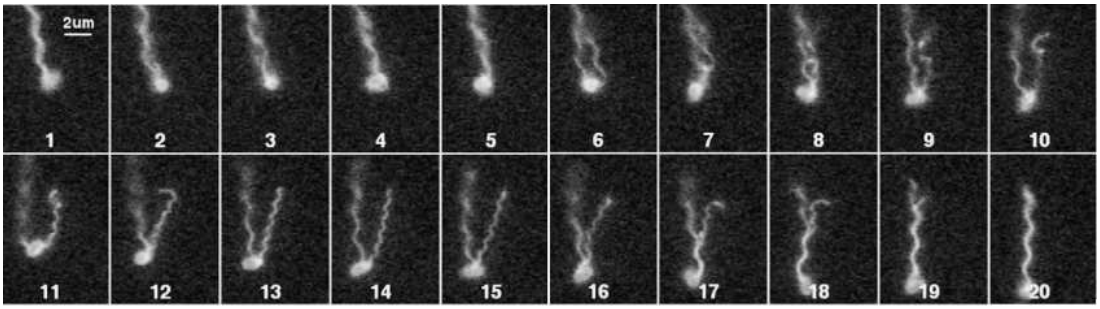

Figure 12.4 ■ Swimming *E. coli* cell with two flagellar filaments (picture redrawn from Ref. [237]). Images 1–5: Bundle of flagella rotating in synchrony. Images 6–15: The motor of the filament on the right reverses its direction of rotation; the filament separates from the bundle and undergoes several polymorphic transformations (changing handedness, pitch, and radius). Images 16–20: The motor of the filament on the right switches back to its original direction of rotation; the filament wraps around the normal filament on the left and rejoins the bundle as it reverts to the normal conformation. Note that the cell swam into the field of view in 5 o'clock direction and leaves it towards the 6 o'clock position. The images are taken at a frame rate of 60 Hz.

E. coli and other bacteria manage to swim because of the subtle dynamics of their multiple rotating flagella, as shown in Fig. 12.4. They bundle and de-bundle as their rotary motors change the rotational direction. During a so-called *run* [see Fig. 12.2(c) and images 1–5 of Fig. 12.4], all filaments are left-handed (with equal pitch and radius) and turn counterclockwise when viewed from behind towards the head. They rotate in synchrony, i.e., the helices are *locked in phase* so that they can form a *bundle* [23, 25, 237]. As a result, the cell is propelled smoothly at swimming speeds of about 30 μm/s. When one (or more) of the flagellar motors reverses its rotational direction and turns clockwise, the bundle flies apart and thus the cell *tumbles* [see Fig. 12.2(c) and images 6–15 of Fig. 12.4]. Such a tumbling event effectively randomizes the orientation of the cell. In addition, the motor reversal initiates a sequence of polymorphic transformations of the filament (several changes in helicity, pitch, and radius) [24, 25, 164, 237]. Once all motors rotate counter-clockwise again, the bundle is rebuilt (images 16–20 of Fig. 12.4).

Hence, the overall movement of a bacterium is the result of altering intervals of random tumbles and straight runs. Chemotaxis steers the bacterium by just regulating the tumbling frequency so that the net motion heads for a more favorable food environment [24, 25].

12.3 Hydrodynamic interactions in flagellar systems

At the low Reynolds numbers associated with flagellar motion, viscous forces dominate, and the dynamics is expected to be predominantly governed by long-range hydrodynamic interactions.

In a pioneering work [233], Taylor modeled the hydrodynamics of undulating sheets in the regime of low Reynolds number, having in mind the propulsion mechanism of spermatozoa [see Fig. 12.2(a)]. He analyzed the propagation of lateral waves along the sheets and showed for the first time that a wiggling tail can indeed generate propulsive forces even in the overdamped regime, i.e., without relying on inertial effects. In particular, for the case of two neighboring undulating sheets, he demonstrated that hydrodynamic interactions *synchronize* the phases of the lateral waves traveling down the tails. Moreover, the overall friction in the system is reduced by this synchronization.

In fact, there is experimental evidence that flagella of adjacent spermatozoa move in phase [95, 207]. Furthermore, swimming spermatozoa can form self-organized spatiotemporal patterns, and this large-scale coordination of cells is believed to be regulated purely through hydrodynamic interactions (without chemical signals) [204].

Beating cilia reveal coordinated strokes of neighboring filaments, known as *metachronal waves*, i.e., beats with a constant phase difference between neighboring cilia [114, 161]. Several analytical and numerical studies support the notion that this synchronized beating pattern is triggered by hydrodynamic interactions [102, 103, 135, 146, 239] and, furthermore, that metachronism reduces the energy expenditure required for beating [104].

In analogy to these examples, it has been suggested that hydrodynamic interactions may also play an important role in how bacterial flagellar filaments synchronize their rotational motion so that they can form bundles. It was found in experiments that, if the viscosity of the medium is increased, the bacteria swim faster and less erratically, and furthermore, they scatter more light [23]. These observations were explained by arguing that the increased viscous stresses cause more filaments to join bundles.

Recently, a quantitative image analysis of bacterial motion revealed that the average tumble duration is roughly inversely proportional to the run speed, which is consistent with the assumption that the reassembly of the flagellar bundle is largely governed by hydrodynamic effects (rather than biochemical processes) [225]. Furthermore, the bundling of nearby rotating "filaments" was studied in detail in macroscopic-scale experiments using stiff helical wires in highly viscous silicone oil [131, 133, 163]. The phenomenon of tumbling and bundling due to motor reversal was also observed in recent numerical simulations [78].

Overall, there is strong evidence that hydrodynamic interactions play a crucial role in flagellar propulsion. Therefore, we are interested in the open question whether hydrodynamic interactions can be at the origin of the synchronization of rotating flagella and can thus support flagellar bundling.

13 Synchronized rotation of rigid helical filaments

In a recent paper, the hydrodynamic coupling of two rotating helices was studied within the framework of slender-body theory [132]. The helices were considered as rigid and prevented from translation by appropriate external forces, such that their axes were always parallel. The key result of this work was that there is no phase synchronization if the two helices are driven with the same torque.

In this chapter, we consider a model that also consists of two *stiff* helices, thus neglecting any effects of elastic deformations. The helices are modeled by single beads that are rigidly connected to each other and are driven by *constant and equal torques* as well. In contrast to Ref. [132], however, we "fix" the helices in space by anchoring their terminal beads in harmonic traps. This allows for slight shifts and tilts of the helix axes and thus implies some kind of "flexibility", which is the major difference to Ref. [132]. As we will show, the phases of the rotating helices do indeed synchronize in this setup, and the state of zero phase difference possesses lowest friction.

13.1 Model system

We consider two identical helices built of equal-sized beads [Fig. 13.1(a)] that are connected to each other by (virtual) rigid bonds.[1] Thus, the helices cannot deform elastically. The centers of the beads are aligned along the backbone of the helix, with equal distances between successive beads.

To describe the dynamics of the helices, we introduce body-fixed coordinate axes, given by the orthonormal vectors $\boldsymbol{\alpha}_i$, $\boldsymbol{\beta}_i$, and $\boldsymbol{\gamma}_i = \boldsymbol{\alpha}_i \times \boldsymbol{\beta}_i$ $(i = 1, 2)$. The central axis of a helix is represented by $\boldsymbol{\alpha}_i$, and the orientation of the perpendicular vector $\boldsymbol{\beta}_i$ shall describe the phase of the helix, i.e., the rotation about its own axis [Fig. 13.1(b)]. The key quantities to detect synchronization effects are the phase angles ϕ_i, defined as the projection of $\boldsymbol{\beta}_i$ onto the xy plane [Fig. 13.1(c)]. The angle between $\boldsymbol{\alpha}_i$ and the z axis is the tilt angle θ_i.

The center-of-mass coordinates of the two helices are denoted by $\boldsymbol{r}_i$. The positions of the individual beads (helix index i, bead index ν) are then given by

$$\boldsymbol{r}_{i[\nu]} = \boldsymbol{r}_i + a_\nu \boldsymbol{\alpha}_i + b_\nu \boldsymbol{\beta}_i + c_\nu \boldsymbol{\gamma}_i \tag{13.1}$$

[1] The theory for a *continuous* model of flagellar hydrodynamics was established in Refs. [153, 154], representing the fluid flow by a curvilinear distribution of elementary flow fields (generated by the local linear force density) along the centerline of the flagellum.

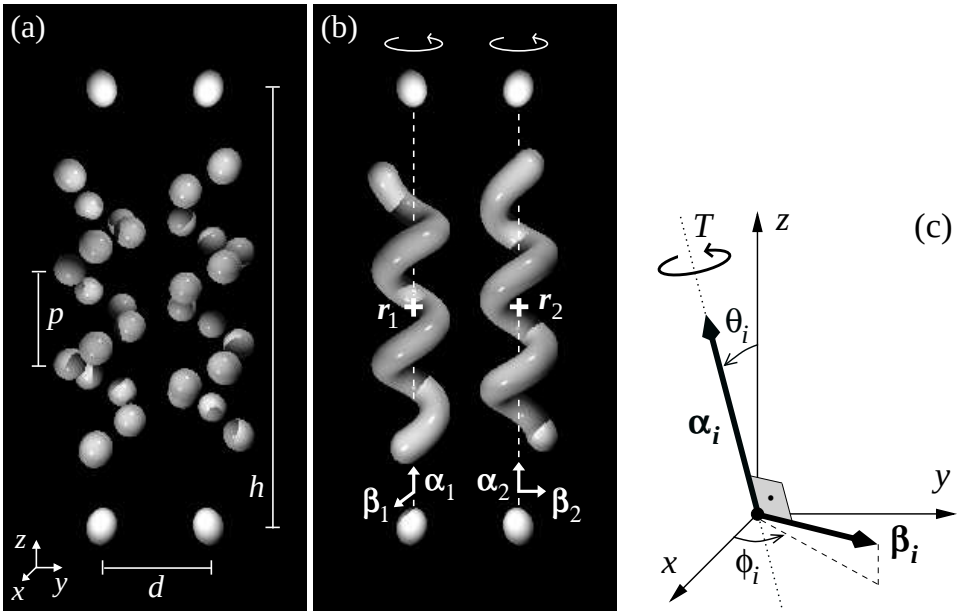

Figure 13.1 ■ Visualization of the helix geometry used in the simulations (here with a phase difference of $\pi/2$). (a) All beads of one helix are connected rigidly to each other. (b) For the sake of clarity, the beads are "smeared" out along the helix. The top and bottom beads are anchored in harmonic traps. The illustrated helices are in their equilibrium positions and orientations (i.e., in the absence of driving torques). (c) The tilt of the helix axis $\boldsymbol{\alpha}_i$ against z direction (i.e., the equilibrium orientation) is described by the angle θ_i. The phase ϕ_i measures the angle between the xy-plane projection of the phase vector $\boldsymbol{\beta}_i$ and the x axis.

with the internal coordinates

$$a_\nu = \frac{p}{m}\left(\nu - \frac{nm-1}{2}\right), \tag{13.2a}$$

$$b_\nu = r\cos\frac{2\pi}{m}\nu, \tag{13.2b}$$

$$c_\nu = r\sin\frac{2\pi}{m}\nu, \tag{13.2c}$$

where r is the radius of the helix and p its pitch. The bead index ν runs from 0 to $nm-1$ for each helix, with m being the number of beads per winding and n the number of windings.

The helices are driven by constant and equal torques that are always parallel to the respective central helix axis, i.e., the driving torques are given by

$$\boldsymbol{T}_i^{\circlearrowleft} = T\boldsymbol{\alpha}_i \tag{13.3}$$

with a fixed parameter T. Note that the assumption of a constant torque agrees (at least to good approximation) with experimental studies of real flagellar motors

[24, 170]. To "fix" the helices in space, we attach single beads at the top and bottom end of each helix axis [Figs. 13.1(a,b)] and anchor them in harmonic traps with equal force constants K. In equilibrium, both helix axes are parallel along z direction, and their distance is denoted by d. The coordinates of the anchoring beads are denoted by $\boldsymbol{r}_{i[\sigma]}$, where the index σ refers to "top" or "bottom". If one of these beads is displaced from the center $\bar{\boldsymbol{r}}_{i[\sigma]} = \pm\frac{1}{2}d\boldsymbol{e}^y \pm \frac{1}{2}h\boldsymbol{e}^z$ of the respective trap (where h is the overall length of a helix along its central axis, including the terminal beads), the restoring *single-particle* force is

$$\boldsymbol{F}_{i[\sigma]} = -K(\boldsymbol{r}_{i[\sigma]} - \bar{\boldsymbol{r}}_{i[\sigma]})\,. \tag{13.4}$$

This corresponds to *center-of-mass* forces and torques

$$\boldsymbol{F}_i^{\parallel} = \sum_{\sigma} \boldsymbol{F}_{i[\sigma]}\,, \tag{13.5a}$$

$$\boldsymbol{T}_i^{\parallel} = \sum_{\sigma} (\boldsymbol{r}_{i[\sigma]} - \boldsymbol{r}_i) \times \boldsymbol{F}_{i[\sigma]}\,, \tag{13.5b}$$

providing the parallel alignment of the helix axes at fixed positions. Finally, the total forces and torques acting on the rigid helices are

$$\boldsymbol{F}_i = \boldsymbol{F}_i^{\parallel}\,, \tag{13.6a}$$

$$\boldsymbol{T}_i = \boldsymbol{T}_i^{\circlearrowleft} + \boldsymbol{T}_i^{\parallel}\,. \tag{13.6b}$$

As the swimming motions of microorganisms occur at very low Reynolds numbers, we can apply Stokesian-dynamics simulations to study the hydrodynamically coupled motions of the two rotating helices.[2] According to Eq. (2.21), the translational and rotational velocities satisfy the relations

$$\boldsymbol{v}_i = \sum_j (\boldsymbol{\mu}_{ij}^{\mathrm{tt}} \cdot \boldsymbol{F}_j + \boldsymbol{\mu}_{ij}^{\mathrm{tr}} \cdot \boldsymbol{T}_j)\,, \tag{13.7a}$$

$$\boldsymbol{\omega}_i = \sum_j (\boldsymbol{\mu}_{ij}^{\mathrm{rt}} \cdot \boldsymbol{F}_j + \boldsymbol{\mu}_{ij}^{\mathrm{rr}} \cdot \boldsymbol{T}_j)\,. \tag{13.7b}$$

In Sect. 2.4.6, we developed a projection formalism to derive the mobility matrix of arbitrary rigid clusters of beads (with reduced degrees of freedom) from the mobility matrix for the individual beads. In case of two clusters, the rigid-body condition $\mathbf{v} = \mathcal{C} \cdot \mathbf{v}_{\mathrm{c}}$ [Eq. (2.54)] explicitly reads

$$\begin{bmatrix} \boldsymbol{v}_{1[\cdot]} \\ \boldsymbol{v}_{2[\cdot]} \\ \boldsymbol{\omega}_{1[\cdot]} \\ \boldsymbol{\omega}_{2[\cdot]} \end{bmatrix} = \begin{bmatrix} \mathbf{1} & (\boldsymbol{r}_1 - \boldsymbol{r}_{1[\cdot]})\times & \mathbf{0} & \mathbf{0} \\ \mathbf{0} & \mathbf{0} & \mathbf{1} & (\boldsymbol{r}_2 - \boldsymbol{r}_{2[\cdot]})\times \\ \mathbf{0} & \mathbf{1} & \mathbf{0} & \mathbf{0} \\ \mathbf{0} & \mathbf{0} & \mathbf{0} & \mathbf{1} \end{bmatrix} \cdot \begin{bmatrix} \boldsymbol{v}_1 \\ \boldsymbol{v}_2 \\ \boldsymbol{\omega}_1 \\ \boldsymbol{\omega}_2 \end{bmatrix}, \tag{13.8}$$

[2] Note that we do not consider effects of thermal noise.

where $\boldsymbol{v}_i$ and $\boldsymbol{\omega}_i$ are the translational and rotational velocities of the two *clusters*. The short notation $\boldsymbol{r}_{i[\cdot]}$ symbolizes the complete set of *single-particle* coordinates of cluster i, $\{\boldsymbol{r}_{i[0]}, \ldots, \boldsymbol{r}_{i[nm-1]}, \boldsymbol{r}_{i[\text{top}]}, \boldsymbol{r}_{i[\text{bottom}]}\}$. Accordingly, $\boldsymbol{v}_{i[\cdot]}$ and $\boldsymbol{\omega}_{i[\cdot]}$ are the linear and angular velocities of the individual beads.

Given the projection matrix $\mathcal{C}$ by Eq. (13.8), we can calculate the effective mobility matrix for the coupled center-of-mass translations and rotations of the two rigid clusters from Eq. (2.60). In our simulations, we use the numerical library HYDROLIB [113] (see Sect. 2.4.3) to calculate the complete mobility matrix of the individual beads. It also accounts for the (virtual) rigid bonds defining the clusters, thus providing the effective mobility tensors (based on the formalism just illustrated).

Hence, the indices i and j in Eq. (13.7) refer to the two rigid helices (for brevity, we skip an explicit index c denoting cluster mobilities). Each of the effective mobility tensors $\boldsymbol{\mu}_{ij}^{\text{tt}}$, $\boldsymbol{\mu}_{ij}^{\text{tr}}$, $\boldsymbol{\mu}_{ij}^{\text{rt}}$, and $\boldsymbol{\mu}_{ij}^{\text{rr}}$ now depends on the center-of-mass coordinates $\boldsymbol{r}_1$ and $\boldsymbol{r}_2$ as well as on the orientations $\boldsymbol{\alpha}_1$, $\boldsymbol{\alpha}_2$, $\boldsymbol{\beta}_1$, and $\boldsymbol{\beta}_2$.

With the forces and torques given in Eq. (13.6), we directly obtain the linear and angular velocities of the helices. The translational motion of the centers of mass is then governed by

$$\dot{\boldsymbol{r}}_i = \boldsymbol{v}_i \,. \tag{13.9}$$

The rotational motion of the body-fixed axes, i.e., the helix axes $\boldsymbol{\alpha}_i$ and the phase vectors $\boldsymbol{\beta}_i$, follows from

$$\dot{\boldsymbol{\alpha}}_i = \boldsymbol{\omega}_i \times \boldsymbol{\alpha}_i \,, \tag{13.10a}$$

$$\dot{\boldsymbol{\beta}}_i = \boldsymbol{\omega}_i \times \boldsymbol{\beta}_i \,. \tag{13.10b}$$

We integrate these equations in time by applying the Heun algorithm (2.64). Note that the mobility matrices have to be evaluated at each time step since the positions and orientations of the helices change.

While the trap constant K was varied to study the influence of the anchoring strength on the helix dynamics, the driving torque T was kept fixed since it merely sets the time scale (given by the rotational frequency ω_0 of an isolated helix). The relevant quantity is thus the dimensionless stiffness $K/(T/a^2)$, where a is the bead radius. The time step of the numerical integration was chosen to correspond to roughly 1/360th of a revolution of a single helix.

The geometry of the two helices is shown in Fig. 13.1. Their backbones have a radius of $r = 2.0\,a$ and a pitch of $p = 6.0\,a$. The number of windings is $n = 3$, and the number of beads per winding is $m = 5$. The distance between the anchoring beads and the helix is the same as the pitch. The equilibrium separation of the helices, i.e., the distance of the upper/lower anchoring traps, is $d = 7.0\,a$.

Note that the calculation of the mobility matrix is the most time consuming part in the simulations. Therefore, we had to restrict the number of beads in

one helix. Furthermore, we will only present results for the set of geometry parameters just introduced and concentrate on the essential variable, namely the trap stiffness K.

13.2 Symmetry considerations

Consider for the moment two helices whose axes are completely fixed in space, i.e., translation and tilt are prevented by appropriate forces and torques. In this case, the only remaining degrees of freedom are rotations about the axes of the helices (aligned parallel to the z axis). They are described by the phase angles ϕ_i and the angular velocities $\dot{\phi}_i = \omega_i$. We introduce the phase difference

$$\psi(t) = \phi_2(t) - \phi_1(t) \tag{13.11}$$

as the phase of the right helix relative to the left helix, when viewed as in Fig. 13.2(a,b) (left part).

According to Eq. (13.7), the rotational velocities ω_i are functions of the phase angles ϕ_i since the mobility tensors depend on the spatial configuration. As the helices are driven by the same torques $T_i = T$ about their axes, the synchronization rate is given by

$$\dot{\psi} = \omega_2(\phi_1, \phi_2) - \omega_1(\phi_1, \phi_2) = \mu(\phi_1, \phi_2)T\,, \tag{13.12}$$

where the effective mobility $\mu(\phi_1, \phi_2)$ is 2π-periodic in ϕ_i. We choose this careful definition because we now want to derive symmetry properties of $\mu(\phi_1, \phi_2)$.

We use the fact that the dynamics of the two-helix system must not change under arbitrary rotations of the whole geometry since the surrounding fluid is isotropic. By applying the two operations illustrated in Fig. 13.2, we create new configurations with left and right helices whose known dynamics we use to infer properties of the mobility $\mu(\phi_1, \phi_2)$.

In the first case, we rotate the two-helix system by 180° about the z axis, as illustrated in Fig. 13.2(a). The velocities of the left and right helix are exchanged, i.e., $\omega_1 \leftrightarrow \omega_2$ and thus $\dot{\psi} \to -\dot{\psi}$. On the other hand, the phase angles of the new left and right helix are, respectively, $\phi_2 + \pi$ and $\phi_1 + \pi$. Combining both statements, Eq. (13.12) yields

$$\mu(\phi_2 + \pi, \phi_1 + \pi) = -\mu(\phi_1, \phi_2)\,. \tag{13.13}$$

If the phases of the helices differ by π ($\phi_2 = \phi_1 + \pi$), one therefore obtains $\mu(\phi_1, \phi_1 + \pi) = -\mu(\phi_1, \phi_1 + \pi) = 0$ or

$$\dot{\psi} = 0 \quad \text{for} \quad \psi = \pi\,, \tag{13.14}$$

i.e., the synchronization speed vanishes for any ϕ_1 and ϕ_2 whenever $\phi_2 - \phi_1 = \pi$.

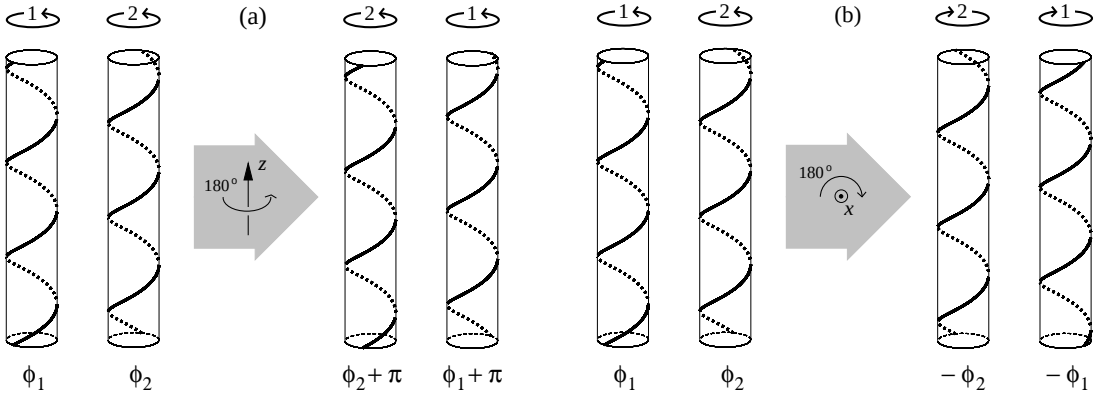

Figure 13.2 ■ Rotation of the two-helix system by 180° about the z axis (a) and about the x axis (b). The circular arrows (indexed with $i = 1, 2$) on top of the helices denote that the respective helix is driven with torque T_i and rotates with velocity ω_i in the indicated direction. The tubes are drawn as guide to the eye.

Let us now rotate the two-helix system by 180° about the x axis [Fig. 13.2(b)]. Then the velocities of the left and right helix are exchanged and reversed, i.e., $\omega_1 \leftrightarrow -\omega_2$, so the synchronization speed $\dot{\psi} = -\omega_1 - (-\omega_2) = \omega_2 - \omega_1$ remains the same. On the other hand, the angles transform as $\phi_1 \leftrightarrow -\phi_2$, and the driving torques are reversed, i.e., $T \to -T$. Again, combining both statements, Eq. (13.12) yields $\mu(-\phi_2, -\phi_1)(-T) = \mu(\phi_1, \phi_2)T$, and thus

$$\mu(-\phi_2, -\phi_1) = -\mu(\phi_1, \phi_2)\,. \tag{13.15}$$

For helices of infinite length, the dynamics can only depend on the phase difference ψ and not on the single phases ϕ_i. This is obvious since a phase shift of both helices is equivalent to a translation along the helix axes, which does not change the dynamics. Hence, Eq. (13.15) reads $\mu(\psi) = -\mu(\psi) = 0$, i.e., for parallel helices of infinite length, the synchronization rate $\dot{\psi} = \mu(\psi)T$ vanishes at *any* phase difference ψ, and therefore, they do not synchronize.[3]

13.3 Synchronization dynamics

13.3.1 Phase synchronization

We now study the rotational dynamics of two helices whose terminal beads are anchored in harmonic traps of *finite* strength, as introduced in Sect. 13.1. Thus, the helices can be shifted and tilted, and their axes undergo a precession-like

[3]The same result with similar methods was obtained by employing the concept of kinematic reversibility of Stokes flow [132] that manifests itself, e.g., in Eq. (13.12). That means, to arrive at Eq. (13.15), we also make use of this concept when the torque on the helices is reversed.

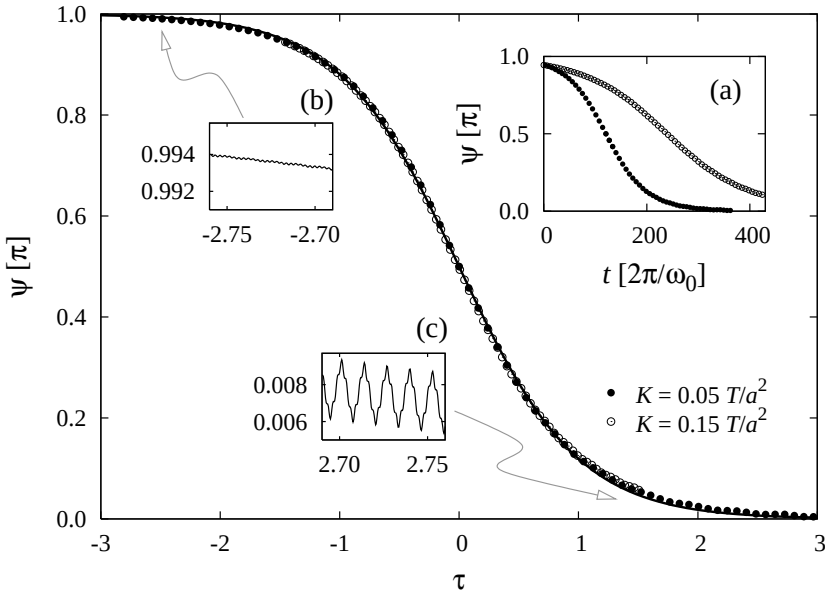

Figure 13.3 ■ Synchronization of the helix rotations. The phase difference of the two helices tends towards zero, starting from ψ slightly smaller than π. The main graph shows the same data as inset (a), but plotted against the reduced time τ [see Eq. (13.17)]; in (a), the time t is measured in units of $2\pi/\omega_0$, where ω_0 is the rotational frequency of an isolated helix. The symbols are simulation data at two different trap strengths K. (For clarity, not every data point is plotted.) The solid line shows the master curve of Eq. (13.16). The insets enlarge the small oscillations at (b) $\psi \approx \pi$ and (c) $\psi \approx 0$ (here for the case $K = 0.05\,T/a^2$, but the amplitudes do not depend strongly on K). Note that the scaling of the two insets is the same.

motion while each helix itself is rotating about its respective axis. The orientations of the helices in space are described by the vectors $\boldsymbol{\alpha}_i$ and $\boldsymbol{\beta}_i$ and the corresponding angles θ_i and ϕ_i, as defined in Fig. 13.1(c).

Figure 13.3 shows the time evolution of the phase difference $\psi = \phi_2 - \phi_1$ for two trap stiffnesses K. Starting with ψ slightly smaller than π, the phase difference decreases continuously (with steepest slope at $\psi = \pi/2$) and finally approaches zero, i.e., the two helices do indeed *synchronize* their phases. In particular, the weaker the anchoring traps are, the faster proceeds the synchronization [Fig. 13.3(a)]. Furthermore, the simulations reveal that the dynamics does not depend significantly on the phases ϕ_i themselves, but is predominantly determined by the phase *difference* ψ.[4] To be concrete, we observe that the rotational velocities $\dot{\phi}_i$ undergo oscillations of only about 1% around a mean value during one rotational period. Their amplitude does not depend on the trap stiffness K, i.e., the oscillations originate from the slight dependence on the phases themselves (and not from the precession of the axes). Therefore, starting with different values for ϕ_i but the same value of ψ yields the same curve [except for

[4]Note that this feature may be expected since the dynamics of parallel helices of *infinite* length can only depend on ψ as explained in Sec. 13.2.

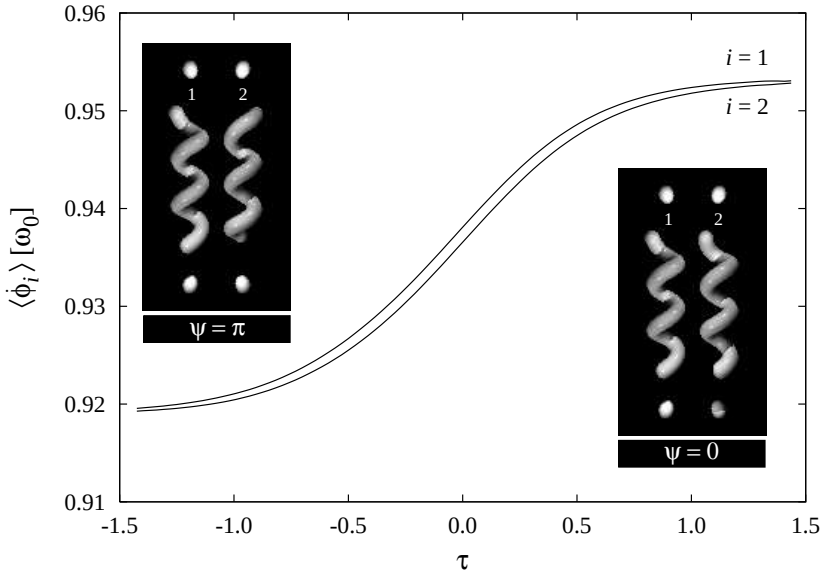

Figure 13.4 ■ Mean rotational velocities, averaged over one revolution (in units of the rotational frequency ω_0 of an isolated helix). The oscillations about the mean value are of the order of a few percent; they decrease slightly during the synchronization process. The example shown is for trap strength $K = 0.15\,T/a^2$. Note that the rotational velocities do not depend strongly on K, but nevertheless, the small difference $\dot{\psi} = \dot{\phi}_2 - \dot{\phi}_1$ does so.

differences in the very small oscillations illustrated in Figs. 13.3(b,c)].

The mean rotational velocities, averaged over one rotational period, increase during the synchronization process from about $0.92\,\omega_0$ at $\psi \approx \pi$ to about $0.95\,\omega_0$ at $\psi \approx 0$ (Fig. 13.4). Thus, the hydrodynamic drag acting on the helices is minimized during phase synchronization (see also Ref. [132]). Since the torques are constant, the dissipation rate $\sum_i \boldsymbol{T}_i \cdot \boldsymbol{\omega}_i$ is thus maximized.

In Sect. 13.2, we showed for fixed parallel helices, based on pure symmetry arguments, that their synchronization rate vanishes for a phase difference of $\psi = \pi$ [see Eq. (13.14)]. In that case, the two-helix configuration is symmetric with respect to a rotation by 180° about the z axis [see Fig. 13.2(a)]. Our reasoning of Sect. 13.2 can be straightforward extended to the case of non-parallel helix axes. Whenever we start with a configuration that is symmetric with respect to a rotation by 180° about the z axis, this symmetry remains preserved (even if the helix axes are tilted). Hence, the phase difference does not change and is always exactly π, i.e., the small oscillations enlarged in Fig. 13.3(b) are not present in this case. However, $\psi = \pi$ does not correspond to a stable state. Starting with ψ marginally smaller than π, the system tends towards phase difference zero. The simulation with $K = 0.05\,T/a^2$ in Fig. 13.3, e.g., was launched at $\psi = 0.994\,\pi$ with both helices in equilibrium position and orientation, as shown in Fig. 13.1.

On the other hand, the synchronized state $\psi = 0$ is stable against small perturbations since configurations with ψ between 0 and $-\pi$ synchronize towards

zero phase difference, too. This was checked by simulations, but can also be derived from Eq. (13.13). The corresponding rotation of Fig. 13.2(a) creates new left and right helices with a change in sign for ψ and $\dot{\psi}$ with respect to the original helices which explains our statement. Furthermore, starting a simulation with exactly $\psi = 0$, the helices remain synchronized on average (i.e., $\langle\psi\rangle = 0$), but there are still small oscillations as illustrated in Fig. 13.3(c).

Averaging over the small oscillations, we find that the resulting smoothed curves for the phase difference ψ obey an empirical law of the form

$$\psi(\tau) = \frac{\pi}{2}\left(1 - \tanh\tau\right), \tag{13.16}$$

where

$$\tau = \tau(t, K) = \frac{2}{\pi}\left(t - t_{\pi/2}\right)\left|\dot{\psi}(t = t_{\pi/2})\right|_K \tag{13.17}$$

is the reduced time, and $t_{\pi/2}$ denotes the time where $\psi = \pi/2$, i.e., the location of the inflection point of $\psi(t)$. Its slope $|\dot{\psi}(t = t_{\pi/2})|$ (where the dot denotes the derivative with respect to t) depends on the trap stiffness K and so does τ. As Fig. 13.3 strikingly reveals, this law works very well. By plotting the phase difference ψ versus the respective reduced time τ, the curves collapse on the master curve given by Eq. (13.16).

Since the dynamics at low Reynolds numbers is completely overdamped, we expect this law to follow from a differential equation which is of first order in time. Taking the first derivative of Eq. (13.16) with respect to τ, we find that $\psi(\tau)$ obeys the nonlinear equation

$$\frac{\mathrm{d}}{\mathrm{d}\tau}\,\psi(\tau) = \frac{2}{\pi}\psi(\tau)[\pi - \psi(\tau)]\,, \tag{13.18}$$

known as the Verhulst equation and originally proposed to model the development of a breeding population [4]. However, it is not clear how to derive this equation from first principles in our case.

Note that all results presented here refer to helices whose rotational direction is as given in Fig. 13.1(b). Reversing the direction of rotation, however, does not change the dynamics of the two-helix system as this can also be achieved by the operation shown in Fig. 13.2(b) that does not change the synchronization speed.

13.3.2 On the role of "flexibility"

Besides the observation that hydrodynamic interactions can indeed synchronize the rotations of the two helices, another essential result of our study is that the speed of the synchronization process decreases with increasing trap stiffness K. The values plotted in Fig. 13.5 for different K^{-1} are the slopes $|\dot{\psi}(t = t_{\pi/2})|$ extracted from simulation data at the inflection point with relative phase $\psi \approx$

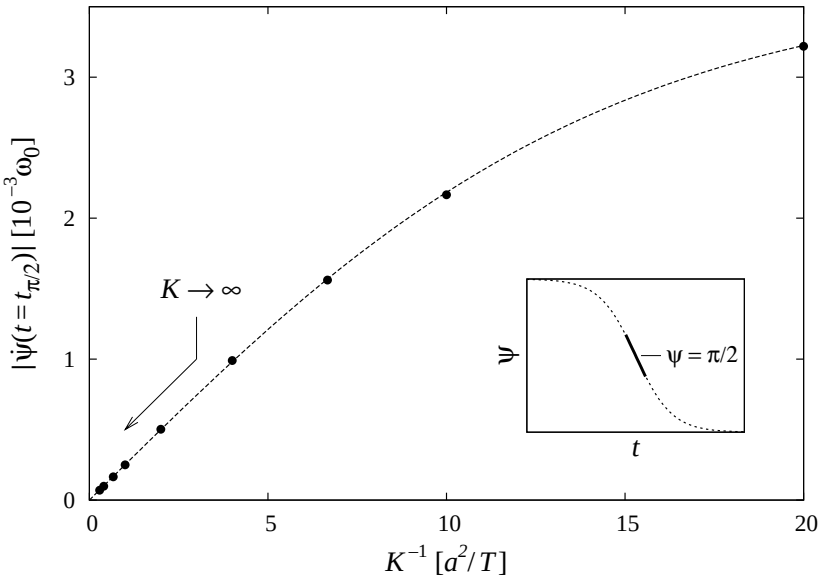

Figure 13.5 ■ Synchronization speed (taken at a relative phase $\psi \approx \pi/2$, as illustrated in the inset) as a function of inverse trap strength K^{-1}. The frequency scale ω_0 for the synchronization speed is the angular velocity of an isolated helix. The symbols indicate values extracted from simulations at different K. The dashed line is an empirical fit (see text).

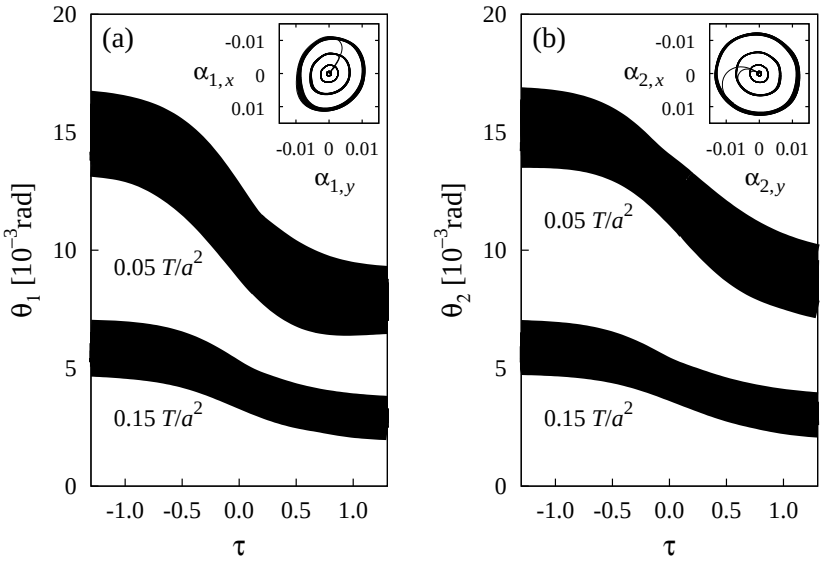

Figure 13.6 ■ Tilt of (a) left and (b) right helix axis for $K = 0.05$ and $0.15\,T/a^2$ as a function of reduced time τ. The fast periodic oscillations of the tilt angles θ_i yield the black bands since they cannot be resolved on the time scale used here. The insets visualize the precession of the helix axes by showing the tip of the vectors $\boldsymbol{\alpha}_i$ (at $\psi \approx \pi/2$). From the outer to the inner "circular" orbit, the trap stiffness assumes the values $K = 0.05$, 0.1, 0.15, and $1.0\,T/a^2$. (Since the simulations were started with both axes aligned along their equilibrium direction, the trajectories $[\alpha_{i,x}, \alpha_{i,y}]$ first move radially away from the origin and then enter the "precession orbit".)

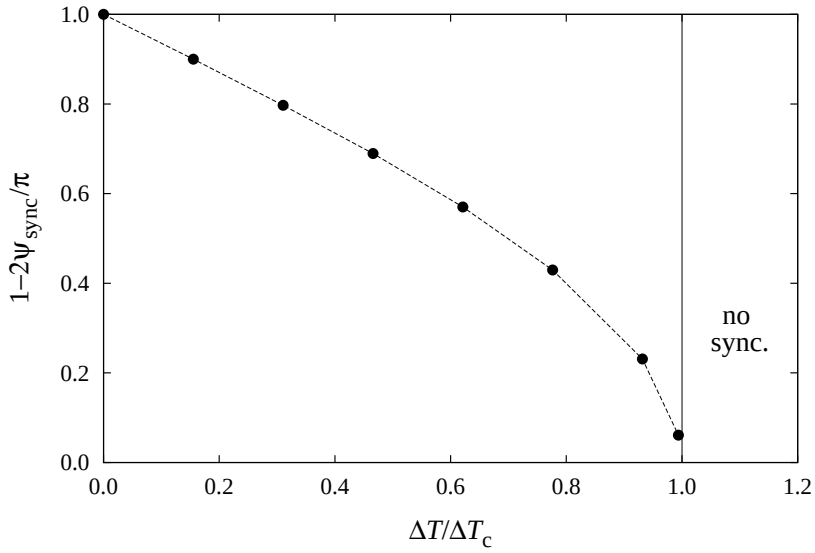

Figure 13.7 ■ Phase difference ψ_{sync} (plotted as $1-\psi_{\mathrm{sync}}/\frac{\pi}{2}$) of the synchronized state as a function of the torque difference ΔT. The phase difference increases from $\psi_{\mathrm{sync}}=0$ to $\pi/2$ (or $1-\psi_{\mathrm{sync}}/\frac{\pi}{2}$ decreases from 1 to 0) with increasing torque difference. For $\Delta T>\Delta T_{\mathrm{c}}$, there is no synchronization.

$\pi/2$. The curve in Fig. 13.5 can be interpolated by the analytic form $c_1 \tanh c_2 K^{-1}$ (dashed curve), where the fit parameters assume the values $c_1 = 3.67\times10^{-3}\,\omega_0$ and $c_2 = 0.0685\,T/a^2$. In the limit of infinite trap strength, i.e., for $K^{-1}\to 0$, the synchronization speed clearly tends towards zero, i.e., an infinitely strong anchoring of the helix axes does not allow for phase synchronization.

In Fig. 13.6, we illustrate how the tilt angles θ_i of the helix axes [for their definition, see Fig. 13.1(c)] vary during the synchronization process. The mean tilt angle as well as the amplitude of its periodic oscillations decrease when the phase difference approaches zero. Obviously, the dynamics of the helices depends on the stiffness of the harmonic anchoring of the top and bottom terminal beads. In a weaker trap, the tilt of the helix axes away from their equilibrium orientation is more pronounced compared to a stronger trap. The insets in Fig. 13.6 track the precession-like motions of the helix axes. The stronger the trap, the smaller the radius of the "orbit" or the tilt angle.

13.3.3 Robustness against torque differences

In real flagellar motors, the torques on the two filaments are not exactly the same. To test whether the phenomenon of synchronization still occurs, we now consider slightly different driving torques for the two helices. The first helix is driven with torque $T_1 = T$, while the second helix is driven with $T_2 = T+\Delta T$ ($\Delta T>0$).

We observe that, for torque differences ΔT below a critical value ΔT_{c}, the two helices indeed still synchronize towards a well-defined phase difference $\psi_{\mathrm{sync}}=$

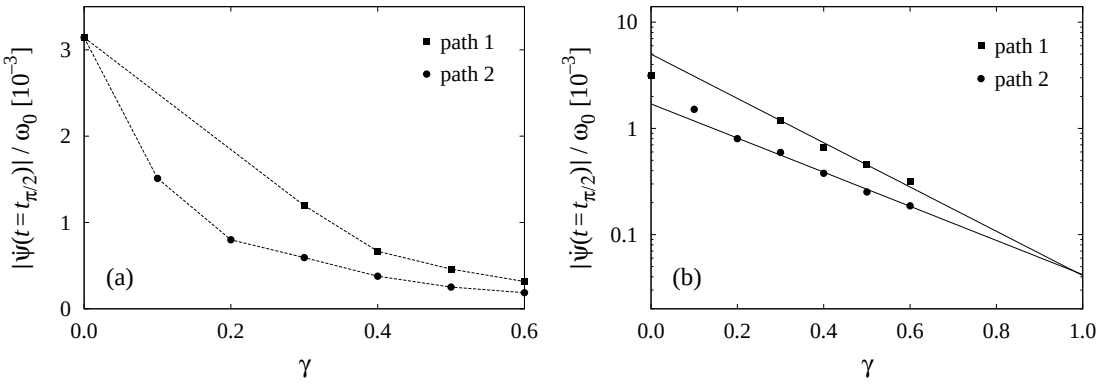

Figure 13.8 ■ (a) Synchronization speeds $\dot{\psi}$ (at $\psi = \pi/2$), relative to the rotational speed ω_0 of the respective isolated helix, for two different paths in the parameter space (r, p) connecting our "fat" helix (path parameter $\gamma = 0$: radius $r_0 = 2\,a$, pitch $p_0 = 6\,a$) with the "slender" flagellum ($\gamma = 1$: $r_1 = 20\,a$, $p_1 = 200\,a$). In both cases, the helix radius was interpolated linearly: $r(\gamma) = r_0 + (r_1 - r_0)\gamma$. In path 1, the pitch was interpolated quadratically, i.e., $p(\gamma) = p_0 + (p_1 - p_0)\gamma^2$, while in path 2, we prescribed the ratio $p(\gamma)/r(\gamma) = p_0/r_0 + (p_1/r_1 - p_0/r_0)\gamma$. The separation of the two helices was $d(\gamma) = 2\,r(\gamma) + 3\,a$. The trap stiffness was $K = 0.05\,T/a^2$. (b) Exponential extrapolation of the same data towards the real flagellum ($\gamma \to 1$) in a semilogarithmic plot.

$\psi(t \to \infty)$, which, in general, is not zero. The results are shown in Fig. 13.7, where we plot $1 - \psi_{\text{sync}}/\frac{\pi}{2}$ as a function of $\Delta T/\Delta T_c$. With increasing torque difference ΔT, the phase lag ψ_{sync} increases from zero to $\pi/2$. For $\Delta T > \Delta T_c$, there is no synchronization, and the phase difference grows continuously.

The reduced critical torque difference $\Delta T_c/T = 3.22 \times 10^{-3}$ corresponds to the reduced frequency difference $\dot{\psi}/\omega_0 = (\omega_2 - \omega_1)/\omega_0$ observed at $\psi = \pi/2$ for equal torques ($\Delta T = 0$). At the critical torque difference, the helices synchronize towards a phase lag of $\psi_{\text{sync}} = \pi/2$. This means that ΔT_c just compensates the difference in the effective mobilities of the two helices, which is largest for $\psi = \pi/2$ (see Fig. 13.4); thus the helices rotate with the same speed.

13.3.4 "Extrapolation" to real flagella

The helix geometry used in our numerical investigation with radius $r = 2\,a$ and pitch $p = 6\,a$ is far from the values of a real bacterial filament with $r = 20\,a$ and $p = 200\,a$, where a is now half the filament diameter. Therefore, we tried two different paths in the parameter space (r, p) to connect both cases, i.e., our "fat" helix and the real, "slender" helix, and to extrapolate along these paths from "fat" towards "slender". In Fig. 13.8(a), we show the synchronization speeds as obtained from simulations for the two paths. The number of beads per winding was always adjusted such that the separation of adjacent beads was as small as possible (without contact). The distance d between the two helix axes was chosen such that the "gap" between the two helices, $d - 2(r + a)$, was always the same.

We observe that making the helix more slender decreases the synchronization speed relative to the rotational speed of the respective isolated helix. This makes sense since the induced flow from the rotation of slender helices is smaller. To reduce computer time, we extrapolated the synchronization speeds for the two paths in the (r, p) space towards the real helical flagellum [$\gamma \to 1$ in Fig. 13.8(b)] and found that the speed is reduced by a factor of about 70 compared to the results reported in this chapter (corresponding to $\gamma = 0$).

Furthermore, we made a comparison of the resistance matrix of a real flagellum modeled by a sequence of spheres with the one obtained from resistive force theory as summarized, e.g., in Ref. [123]. We found that for motion and rotation along the helix axis, the single matrix elements differ by less than a factor of 2. This convinces us that modeling a flagellum with the method presented here is appropriate. For our fat helix, however, the deviations are larger since the filament is relatively thick compared to radius and pitch of the helix. So the conditions for the validity of resistive force theory are not satisfied so well.

14 Synchronization of flexible flagella

In the previous chapter, we demonstrated that hydrodynamic interactions do indeed synchronize the rotations of two *rigid* helices, provided that their axes can jiggle around (i.e., the anchoring strength of the helix ends is finite) which features some kind of "flexibility". We observed that the synchronization is enhanced if the anchoring strength is reduced or, in other words, if "flexibility" is increased.

Therefore, we now consider the dynamics of two intrinsically *flexible* helices (with finite bending and twisting elasticity), thus modeling the flagellar filaments more realistically. For that purpose, we develop a discrete version (i.e., a bead-spring model) of the so-called *helical worm-like chain* model.

14.1 Model system

14.1.1 The Frenet-Serret equations

Parametrized space curves $\boldsymbol{r}(s)$, where s is the arc-length parameter, are commonly described by the well-known Frenet-Serret formalism [228, 230]. If the curve is smooth, we can define at each point an orthonormal, right-handed vector basis $\{\boldsymbol{t}(s), \boldsymbol{n}(s), \boldsymbol{b}(s)\}$. The first vector is the tangent $\boldsymbol{t}(s) = \boldsymbol{r}'(s)$ ($|\boldsymbol{t}(s)| = 1$), where the prime denotes the derivative with respect to s. The normal vector is defined as $\boldsymbol{n}(s) = \boldsymbol{t}'(s)/\kappa(s)$ with the *curvature* $\kappa(s) = |\boldsymbol{t}'(s)|$. Note that $\boldsymbol{n}(s)$ points towards the center of the local circle of curvature. The curvature $\kappa(s)$ quantifies how strongly the curve bends, and its inverse $1/\kappa(s)$ is the local radius of curvature. The binormal vector $\boldsymbol{b}(s) = \boldsymbol{t}(s) \times \boldsymbol{n}(s)$ is perpendicular to the osculating plane, which is spanned locally by $\boldsymbol{t}(s)$ and $\boldsymbol{t}(s + \mathrm{d}s)$. The *torsion* $\tau(s) = -\boldsymbol{b}'(s) \cdot \boldsymbol{n}(s)$ measures how fast the curve is winding out of the local osculating plane.[1]

A circular helix with radius r and pitch p is a space curve that has a constant curvature $\kappa(s) = \kappa_\mathrm{e}$ and a constant torsion $\tau(s) = \tau_\mathrm{e}$. The explicit values of these parameters are related to the helix geometry (represented by its radius and pitch) via $r = \kappa_\mathrm{e}/\sqrt{\kappa_\mathrm{e}^2 + \tau_\mathrm{e}^2}$ and $p = 2\pi\tau_\mathrm{e}/\sqrt{\kappa_\mathrm{e}^2 + \tau_\mathrm{e}^2}$ [249]. The latter relation shows that the sign of the intrinsic torsion τ_e sets the helicity, i.e., whether the helix is right-handed or left-handed.

Any regular space curve is completely defined (except for its position and orientation in space) by specifying the curvature $\kappa(s)$ and the torsion $\tau(s)$, provided

[1] The definition of $\boldsymbol{b}(s)$ yields $\boldsymbol{b}'(s) = \boldsymbol{t}(s) \times \boldsymbol{n}'(s)$. Since $|\boldsymbol{n}(s)| = 1$, the derivative $\boldsymbol{n}'(s)$ is perpendicular to $\boldsymbol{n}(s)$, and therefore $\boldsymbol{b}'(s) \propto \boldsymbol{t}(s) \times \boldsymbol{b}(s) = -\boldsymbol{n}(s)$.

that everywhere $\kappa(s) > 0$. The vectors $\boldsymbol{t}(s)$, $\boldsymbol{n}(s)$, and $\boldsymbol{b}(s)$ are then governed by the *Frenet-Serret equations* [228, 230]

$$\frac{\mathrm{d}}{\mathrm{d}s}\begin{bmatrix}\boldsymbol{t}(s)\\ \boldsymbol{n}(s)\\ \boldsymbol{b}(s)\end{bmatrix} = \begin{bmatrix}0 & +\kappa(s) & 0\\ -\kappa(s) & 0 & +\tau(s)\\ 0 & -\tau(s) & 0\end{bmatrix}\cdot\begin{bmatrix}\boldsymbol{t}(s)\\ \boldsymbol{n}(s)\\ \boldsymbol{b}(s)\end{bmatrix}, \tag{14.1}$$

which follow directly from the definitions of the vectors $\boldsymbol{n}(s)$ and $\boldsymbol{b}(s)$ given above. The Frenet-Serret equations can be rewritten as [228]

$$\frac{\mathrm{d}}{\mathrm{d}s}\boldsymbol{f}(s) = \boldsymbol{\Omega}(s)\times\boldsymbol{f}(s) \quad \text{with} \quad \boldsymbol{f}\in\{\boldsymbol{t},\boldsymbol{n},\boldsymbol{b}\} \tag{14.2}$$

and thus be interpreted as a rigid rotation of the local triad $\{\boldsymbol{t}(s),\boldsymbol{n}(s),\boldsymbol{b}(s)\}$ with the local rotation vector (also known as Darboux vector)

$$\boldsymbol{\Omega}(s) = \tau(s)\boldsymbol{t}(s) + \kappa(s)\boldsymbol{b}(s)\,. \tag{14.3}$$

However, the Frenet-Serret formalism fails at points with vanishing curvature, i.e., $\kappa(s) = 0$. In this case, $\boldsymbol{t}'(s) = \boldsymbol{0}$, so the normal vector $\boldsymbol{n}(s)$ is not defined, and neither is the binormal vector $\boldsymbol{b}(s)$.[2] Therefore, the *helical worm-like chain* model provides a generalization of the Frenet-Serret equations, which we will introduce in the following.

14.1.2 Helical worm-like chain model

We consider a filament with small but finite (and, in general, noncircular) cross section that is modeled as an inextensible but deformable space curve. To each point $\boldsymbol{r}(s)$ along the space curve, we affix an orthonormal, right-handed triad $\{\boldsymbol{e}^1(s),\boldsymbol{e}^2(s),\boldsymbol{e}^3(s)\}$, whose component $\boldsymbol{e}^3(s)$ is chosen to coincide with the local tangent, i.e.,

$$\boldsymbol{e}^3(s) = \frac{\mathrm{d}}{\mathrm{d}s}\boldsymbol{r}(s)\,, \tag{14.4}$$

and the vectors $\boldsymbol{e}^1(s)$ and $\boldsymbol{e}^2(s)$ are directed along the principal axes of the cross section [193, 248, 249]. This formalism provides a complete description of the space curve described by the centerline of the filament, as well as of the rotation of the cross section about this curve related to *twist* deformations.

[2] In the discretized version of the Frenet-Serret formalism, curvature is represented by the angle between adjacent tangent vectors $\boldsymbol{t}_i$ and $\boldsymbol{t}_{i+1}$ (where $\boldsymbol{t}_i$ is the direction of the bond between vertex $i-1$ and i), and torsion is described by the angle between neighboring binormal vectors $\boldsymbol{b}_{i-1}\propto\boldsymbol{t}_{i-1}\times\boldsymbol{t}_i$ and $\boldsymbol{b}_i\propto\boldsymbol{t}_i\times\boldsymbol{t}_{i+1}$ (i.e., $\boldsymbol{b}_i$ is perpendicular to the plane spanned by the vertices $i-1$, i, and $i+1$) [201]. In simulations, this model behaves erratically if neighboring tangents become nearly aligned due to deformations of the helical structure.

The rotation of the triad as one moves along the chain is governed by the *generalized Frenet-Serret equations*

$$\frac{\mathrm{d}}{\mathrm{d}s}\,\boldsymbol{e}^{\alpha}(s) = \boldsymbol{\Omega}(s) \times \boldsymbol{e}^{\alpha}(s) \tag{14.5}$$

with $\alpha \in \{1,2,3\}$, which is in its form identical to Eq. (14.2), but the rotation vector $\boldsymbol{\Omega}(s)$ now has components along all three directions of the local triad,

$$\boldsymbol{\Omega}(s) = \sum_{\alpha} \Omega^{\alpha}(s)\boldsymbol{e}^{\alpha}(s)\,, \tag{14.6}$$

which can be viewed as a generalization of the Darboux vector introduced in Eq. (14.3) [193, 248, 249].

The genuine and the generalized Frenet-Serret frame are related to each other through a rotation about the common tangent direction $\boldsymbol{e}^{3}(s) = \boldsymbol{t}(s)$ which defines the *twist angle* $\varphi(s)$ [193]:

$$\boldsymbol{e}^{1}(s) = \sin\varphi(s)\,\boldsymbol{n}(s) + \cos\varphi(s)\,\boldsymbol{b}(s)\,, \tag{14.7a}$$

$$\boldsymbol{e}^{2}(s) = \cos\varphi(s)\,\boldsymbol{n}(s) - \sin\varphi(s)\,\boldsymbol{b}(s)\,, \tag{14.7b}$$

$$\boldsymbol{e}^{3}(s) = \boldsymbol{t}(s)\,. \tag{14.7c}$$

Substituting these relations into Eq. (14.5) and using the Frenet-Serret equations (14.1), we can link the *generalized curvatures* $\Omega^{\alpha}(s)$ to the curvature $\kappa(s)$, the torsion $\tau(s)$, and the twist angle $\varphi(s)$ via [193]

$$\Omega^{1}(s) = \kappa(s)\cos\varphi(s)\,, \tag{14.8a}$$

$$\Omega^{2}(s) = \kappa(s)\sin\varphi(s)\,, \tag{14.8b}$$

$$\Omega^{3}(s) = \tau(s) + \frac{\mathrm{d}}{\mathrm{d}s}\,\varphi(s)\,, \tag{14.8c}$$

or, vice versa,

$$\kappa(s) = \sqrt{[\Omega^{1}(s)]^{2} + [\Omega^{2}(s)]^{2}}\,, \tag{14.9a}$$

$$\tau(s) = \Omega^{3}(s) - \frac{\mathrm{d}}{\mathrm{d}s}\,\arctan\frac{\Omega^{2}(s)}{\Omega^{1}(s)}\,. \tag{14.9b}$$

We consider an elastic filament whose stress-free (undeformed) reference state is described by *intrinsic* curvatures $\Omega_{\mathrm{e}}^{\alpha}$. The elastic energy associated with the actual configuration of the filament is (to leading order) quadratic in the deformations $\Omega^{\alpha}(s) - \Omega_{\mathrm{e}}^{\alpha}$,

$$H = \frac{1}{2}\sum_{\alpha}\int \mathrm{d}s\, A^{\alpha}[\Omega^{\alpha}(s) - \Omega_{\mathrm{e}}^{\alpha}]^{2}\,, \tag{14.10}$$

with elastic moduli A^α [193, 248, 249].[3] For isotropic bending elasticity (as, e.g., in case of filaments with circular cross section), $A^1 = A^2$.

14.1.3 Discrete bead-spring model of a flexible helix

To include hydrodynamic interactions between separate helices and between different parts of a helix, we discretize[4] the helical worm-like chain model introduced above and develop a helical bead-spring model. The hydrodynamic interactions of the helices are then described as the ones between the single beads. (The bonds connecting the beads are assumed to be of vanishing volume.)

The complete set of coordinates for a helix built of N beads consists of the spatial coordinates $\boldsymbol{r}_i$ ($i \in [0, N-1]$) and $N-1$ orthonormal, right-handed triads $\{\boldsymbol{e}_i^1, \boldsymbol{e}_i^2, \boldsymbol{e}_i^3\}$ ($i \in [1, N-1]$). In analogy to the continuous model presented in the previous section, we identify the vector $\boldsymbol{e}_i^3$ with the direction of the bond between particles $i-1$ and i, i.e.,

$$\boldsymbol{e}_i^3 = \frac{\boldsymbol{r}_i - \boldsymbol{r}_{i-1}}{|\boldsymbol{r}_i - \boldsymbol{r}_{i-1}|} \,. \tag{14.11}$$

In our model, the rotation of the triad along the chain splits up into two distinct rotations as depicted in Fig. 14.1. The bending deformations are localized on the vertices, while the twist deformations are localized on (or spread along) the bonds.[5] In order to discretize the generalized Frenet-Serret equation (14.5), we apply the analytical procedure described in the following.

When stepping along the chain from particle $i-1$ to particle i, the triad $\{\boldsymbol{e}_i^1, \boldsymbol{e}_i^2, \boldsymbol{e}_i^3\}$ is at first rotated about the bond direction $\boldsymbol{e}_i^3$ by an angle φ_i [see Fig. 14.1(a)], representing the *twist* of the chain. We symbolize this rotation by the 3×3 transformation matrix $\boldsymbol{\Phi}_i$ and denote the rotated triad by

$$\tilde{\boldsymbol{e}}_i^\alpha = \boldsymbol{\Phi}_i \cdot \boldsymbol{e}_i^\alpha \,, \tag{14.12}$$

which explicitly reads

$$\tilde{\boldsymbol{e}}_i^{1/2} = \cos\varphi_i \, \boldsymbol{e}_i^{1/2} + \sin\varphi_i \, (\boldsymbol{e}_i^3 \times \boldsymbol{e}_i^{1/2}) \,. \tag{14.13}$$

(Note that $\tilde{\boldsymbol{e}}_i^3 = \boldsymbol{e}_i^3$.) The twist angle φ_i is then the angle between $\boldsymbol{e}_i^1$ and $\tilde{\boldsymbol{e}}_i^1$ (or, equivalently, the angle between $\boldsymbol{e}_i^2$ and $\tilde{\boldsymbol{e}}_i^2$). However, the relation $\cos\varphi_i = \boldsymbol{e}_i^1 \cdot \tilde{\boldsymbol{e}}_i^1$

[3] In general, the intrinsic curvatures Ω_e^α may also depend on the arc-length coordinate s. For helical filaments with fixed radius and pitch, however, the curvatures are constant.

[4] Note that continuous and discrete models do not necessarily lead to the same dynamics even in the limit of the discretization length approaching zero [136]. This is due to the fact that, in a discrete chain, bending and twisting are localized, whereas in a continuous model, the deformations are spread smoothly along the space curve.

[5] This decomposition of twist and bending deformations is similar to the model applied in Ref. [137].

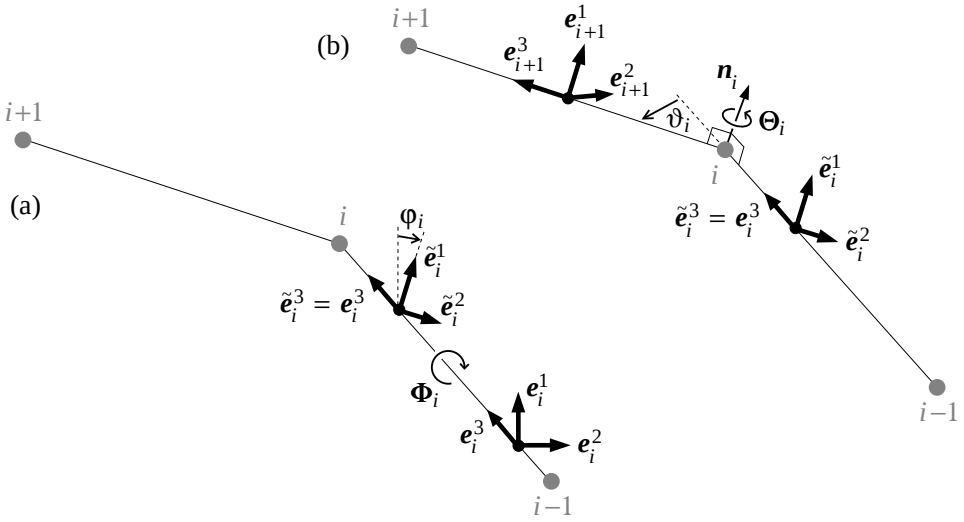

Figure 14.1 ■ Twist and bending deformations in the bead-spring model of a flexible filament. (a) When stepping along the chain from particle $i-1$ to particle i, the triad $\{\boldsymbol{e}_i^1, \boldsymbol{e}_i^2, \boldsymbol{e}_i^3\}$ is first rotated by the twist angle φ_i about the bond direction $\boldsymbol{e}_i^3$. (b) Subsequently, the twisted triad $\{\tilde{\boldsymbol{e}}_i^1, \tilde{\boldsymbol{e}}_i^2, \tilde{\boldsymbol{e}}_i^3\}$ is rotated by the bending angle ϑ_i about the direction $\boldsymbol{n}_i$, where $\boldsymbol{n}_i$ is perpendicular to the plane spanned by particles $i-1$, i, and $i+1$. In equilibrium, the twisted normal vector $\tilde{\boldsymbol{e}}_i^1$ is chosen to coincide with the bending vector $\boldsymbol{n}_i$.

does not yield information about the sign of φ_i and hence cannot distinguish between clockwise and counter-clockwise twist. Therefore, we determine the twist angle from the relation

$$\sin\varphi_i = \tilde{\boldsymbol{e}}_i^1 \cdot \boldsymbol{e}_i^2 \,, \tag{14.14}$$

which in fact preserves the sign of φ_i.

Thereafter, the triad is rotated such that the bond orientation $\boldsymbol{e}_i^3$ is transformed into the consecutive direction $\boldsymbol{e}_{i+1}^3$ [Fig. 14.1(b)], thus describing the *curvature* of the chain. We abbreviate this transformation by

$$\boldsymbol{e}_{i+1}^\alpha = \boldsymbol{\Theta}_i \cdot \tilde{\boldsymbol{e}}_i^\alpha \,, \tag{14.15}$$

where $\boldsymbol{\Theta}_i$ is the appropriate 3×3 rotation matrix. The respective bending angle ϑ_i is given by

$$\cos\vartheta_i = \boldsymbol{e}_i^3 \cdot \boldsymbol{e}_{i+1}^3 \,, \tag{14.16}$$

and the direction of rotation is represented by the unit vector

$$\boldsymbol{n}_i = \frac{\boldsymbol{e}_i^3 \times \boldsymbol{e}_{i+1}^3}{\sin\vartheta_i} \,. \tag{14.17}$$

Given the angle ϑ_i and the axis $\boldsymbol{n}_i$ of the rigid rotation $\boldsymbol{\Theta}_i$, the transformation $\tilde{\boldsymbol{e}}_i^\alpha \to \boldsymbol{e}_{i+1}^\alpha$ reads

$$\boldsymbol{e}_{i+1}^\alpha = \boldsymbol{n}_i\boldsymbol{n}_i \cdot \tilde{\boldsymbol{e}}_i^\alpha + \cos\vartheta_i\,(\mathbf{1} - \boldsymbol{n}_i\boldsymbol{n}_i) \cdot \tilde{\boldsymbol{e}}_i^\alpha + \sin\vartheta_i\,(\boldsymbol{n}_i \times \tilde{\boldsymbol{e}}_i^\alpha) \,, \tag{14.18}$$

which can be obtained by simple geometric considerations.[6] (Note that the dyadic product $\boldsymbol{n}_i\boldsymbol{n}_i$ projects $\tilde{\boldsymbol{e}}_i^{\alpha}$ onto $\boldsymbol{n}_i$.)

In analogy to the continuous model, the elastic energy related to the twist and bending deformations of the filament reads

$$H^{\mathrm{curv}} = \frac{1}{2}\sum_{\alpha} A^{\alpha} \sum_{i} (\Omega_i^{\alpha} - \Omega_{\mathrm{e}}^{\alpha})^2 \,. \tag{14.19}$$

We identify Ω_i^1 and Ω_i^2 with the components of the bending vector $\vartheta_i\boldsymbol{n}_i$ viewed from the basis $\{\boldsymbol{e}_i^1, \boldsymbol{e}_i^2, \boldsymbol{e}_i^3\}$,

$$\Omega_i^1\boldsymbol{e}_i^1 + \Omega_i^2\boldsymbol{e}_i^2 = \vartheta_i\boldsymbol{n}_i \,, \tag{14.20}$$

thus representing the "curvature" of the chain.[7] By multiplication with $\boldsymbol{e}_i^1$ and $\boldsymbol{e}_i^2$, respectively, we obtain using Eq. (14.17)

$$\Omega_i^1 = -\frac{\vartheta_i}{\sin\vartheta_i}\,\boldsymbol{e}_i^2 \cdot \boldsymbol{e}_{i+1}^3 \,, \tag{14.21a}$$

$$\Omega_i^2 = +\frac{\vartheta_i}{\sin\vartheta_i}\,\boldsymbol{e}_i^1 \cdot \boldsymbol{e}_{i+1}^3 \,. \tag{14.21b}$$

The third deformational degree of freedom is the twist, thus

$$\Omega_i^3 = \varphi_i \,. \tag{14.22}$$

The twist angle φ_i is given by Eq. (14.14). To calculate it for a given chain configuration, we have to "reverse" the bending step, represented by the transformation (14.15), in order to reconstruct the required auxiliary vector

$$\tilde{\boldsymbol{e}}_i^1 = \boldsymbol{\Theta}_i^{-1} \cdot \boldsymbol{e}_{i+1}^1 \,. \tag{14.23}$$

The inverted step $\boldsymbol{e}_{i+1}^1 \to \tilde{\boldsymbol{e}}_i^1$ follows directly from Eq. (14.18) by replacing ϑ_i with $-\vartheta_i$ (or, alternatively, $\boldsymbol{n}_i$ with $-\boldsymbol{n}_i$):

$$\tilde{\boldsymbol{e}}_i^1 = \boldsymbol{n}_i\boldsymbol{n}_i \cdot \boldsymbol{e}_{i+1}^1 + \cos\vartheta_i\,(\mathbf{1} - \boldsymbol{n}_i\boldsymbol{n}_i) \cdot \boldsymbol{e}_{i+1}^1 - \sin\vartheta_i\,(\boldsymbol{n}_i \times \boldsymbol{e}_{i+1}^1) \,. \tag{14.24}$$

With this, we finally obtain from Eq. (14.14)

$$\Omega_i^3 = \arcsin\Bigg[\cos\vartheta_i\,(\boldsymbol{e}_i^2 \cdot \boldsymbol{e}_{i+1}^1) - (\boldsymbol{e}_i^2 \cdot \boldsymbol{e}_{i+1}^3)(\boldsymbol{e}_i^3 \cdot \boldsymbol{e}_{i+1}^1) \tag{14.25}$$

$$+ \frac{(\boldsymbol{e}_i^1 \cdot \boldsymbol{e}_{i+1}^3)(\boldsymbol{e}_i^3 \cdot \boldsymbol{e}_{i+1}^2)}{1 + \cos\vartheta_i}\Bigg] \,. \tag{14.26}$$

[6] see, e.g., Ref. [93] [*ibid.*, Eq. (4-92)]

[7] Note that there is no component of $\vartheta_i\boldsymbol{n}_i$ in direction of $\boldsymbol{e}_i^3$ since $\boldsymbol{n}_i \propto \boldsymbol{e}_i^3 \times \boldsymbol{e}_{i+1}^3$.

For numerical reasons, we assume slightly extensible bonds, described by the stretching energy

$$H^{\mathrm{bond}} = \frac{1}{2} B \sum_i (L_i - L_\mathrm{e})^2 \,, \tag{14.27}$$

where

$$L_i = |\boldsymbol{r}_i - \boldsymbol{r}_{i-1}| \tag{14.28}$$

is the length of the bond between particles $i-1$ and i, and L_e is its equilibrium value. The stiffness B is chosen such that the extensions $L_i - L_\mathrm{e}$ of the bonds turn out to be negligibly small in the simulations (typically of order $10^{-4}\, L_\mathrm{e}$).

14.1.4 Equilibrium configuration

To be comparable to the results of Chap. 13 for rigid helices, we use here the same helix geometry [see Sect. 13.1 and Fig. 13.1(a)], corresponding to the equilibrium bond length $L_\mathrm{e} = 2.6\, a$ (where a is the bead radius) and the bending angle $\vartheta_\mathrm{e} = 63°$.

As we consider filaments with "circular cross section" (i.e., built of beads), the equilibrium twist angle φ_e is not fixed *a priori*. Hence, we can choose the normal vectors[8] $\boldsymbol{e}_i^1$ such that the twisted triad $\tilde{\boldsymbol{e}}_i^\alpha = \boldsymbol{\Phi}_i \cdot \boldsymbol{e}_i^\alpha$ obeys the identity $\tilde{\boldsymbol{e}}_i^1 = \boldsymbol{n}_i$ (see Fig. 14.1). The vector $\tilde{\boldsymbol{e}}_i^1$ is thus invariant under the bending rotation $\boldsymbol{\Theta}_i$ (as it rotates the twisted triad about the axis $\boldsymbol{n}_i$), so $\boldsymbol{e}_{i+1}^1 = \tilde{\boldsymbol{e}}_i^1 = \boldsymbol{n}_i$. Therefore, the normal vectors in the equilibrium state of the chain are set by the relation

$$\boldsymbol{e}_{i+1}^1 = \frac{\boldsymbol{e}_i^3 \times \boldsymbol{e}_{i+1}^3}{\sin\vartheta_\mathrm{e}} \,. \tag{14.29}$$

In equilibrium, φ_e is the angle between $\boldsymbol{e}_i^1$ and $\tilde{\boldsymbol{e}}_i^1 = \boldsymbol{e}_{i+1}^1$ and can thus be calculated from

$$\cos\varphi_\mathrm{e} = \frac{\boldsymbol{e}_{i-1}^3 \times \boldsymbol{e}_i^3}{\sin\vartheta_\mathrm{e}} \cdot \frac{\boldsymbol{e}_i^3 \times \boldsymbol{e}_{i+1}^3}{\sin\vartheta_\mathrm{e}} \,. \tag{14.30}$$

This yields

$$\varphi_\mathrm{e} = \pm \arccos\left(\frac{\cos^2\vartheta_\mathrm{e} - \boldsymbol{e}_{i-1}^3 \cdot \boldsymbol{e}_{i+1}^3}{\sin^2\vartheta_\mathrm{e}} \right) , \tag{14.31}$$

where $\varphi_\mathrm{e} > 0$ for right-handed helices and $\varphi_\mathrm{e} < 0$ for left-handed ones. For our helix geometry, $\varphi_\mathrm{e} = 37°$.

[8] We consider here only the normal vector $\boldsymbol{e}_i^1$ since the second normal vector $\boldsymbol{e}_i^2$ follows from $\boldsymbol{e}_i^2 = \boldsymbol{e}_i^3 \times \boldsymbol{e}_i^1$ for given tangential vector $\boldsymbol{e}_i^3$ and normal vector $\boldsymbol{e}_i^1$.

Note that the initial normal vector $\boldsymbol{e}_1^1$ at the beginning of the chain (between particles 0 and 1) cannot be obtained from the relation (14.29), but has to be determined from the underlying condition $\tilde{\boldsymbol{e}}_1^1 = \boldsymbol{\Phi}_1 \cdot \boldsymbol{e}_1^1 = \boldsymbol{n}_1$. The inversion of the twist transformation (14.13) corresponds to changing the sign of φ_i, and therefore (in equilibrium) $\boldsymbol{e}_1^1 = \boldsymbol{\Phi}_1^{-1} \cdot \boldsymbol{n}_1 = \cos\varphi_\mathrm{e}\,\boldsymbol{n}_1 - \sin\varphi_\mathrm{e}\,(\boldsymbol{e}_1^3 \times \boldsymbol{n}_1)$. With $\boldsymbol{n}_1 = (\boldsymbol{e}_1^3 \times \boldsymbol{e}_2^3)/\sin\vartheta_\mathrm{e}$, we finally obtain

$$\boldsymbol{e}_1^1 = \frac{1}{\sin\vartheta_\mathrm{e}}[\cos\varphi_\mathrm{e}\,(\boldsymbol{e}_1^3 \times \boldsymbol{e}_2^3) - \sin\varphi_\mathrm{e}\,(\cos\vartheta_\mathrm{e}\,\boldsymbol{e}_1^3 - \boldsymbol{e}_2^3)]\,. \tag{14.32}$$

The bending parameters Ω_e^1 and Ω_e^2 follow directly from the definition (14.20). Since, in equilibrium, the angle between $\boldsymbol{n}_i$ and $\boldsymbol{e}_i^1$ is exactly the twist angle φ_e, we have $\boldsymbol{e}_i^1 \cdot \boldsymbol{n}_i = \cos\varphi_\mathrm{e}$ and $\boldsymbol{e}_i^2 \cdot \boldsymbol{n}_i = \sin\varphi_\mathrm{e}$. Thus, in total, the generalized curvatures are given by

$$\Omega_\mathrm{e}^1 = \vartheta_\mathrm{e}\cos\varphi_\mathrm{e}\,, \tag{14.33a}$$

$$\Omega_\mathrm{e}^2 = \vartheta_\mathrm{e}\sin\varphi_\mathrm{e}\,, \tag{14.33b}$$

$$\Omega_\mathrm{e}^3 = \varphi_\mathrm{e}\,. \tag{14.33c}$$

14.1.5 Elastic forces and torques

The contributions H^curv and H^bond to the total elastic energy of the filament in a given deformed state generate two types of forces acting on the individual beads,

$$\boldsymbol{F}_i^\mathrm{curv} = -\frac{\partial}{\partial \boldsymbol{r}_i} H^\mathrm{curv}\,, \tag{14.34}$$

$$\boldsymbol{F}_i^\mathrm{bond} = -\frac{\partial}{\partial \boldsymbol{r}_i} H^\mathrm{bond}\,. \tag{14.35}$$

The "spring" force caused by the stretching or squeezing of the bonds adjacent to particle i is immediately given by

$$\boldsymbol{F}_i^\mathrm{bond} = -B(L_i - L_\mathrm{e})\boldsymbol{e}_i^3 + B(L_{i+1} - L_\mathrm{e})\boldsymbol{e}_{i+1}^3\,, \tag{14.36}$$

whereas the derivatives of H^curv are performed numerically by means of virtual displacements of the individual beads.

Consider an infinitesimally small, but arbitrarily oriented displacement $\delta\boldsymbol{r}_i$ of particle i. The components of $\delta\boldsymbol{r}_i$ that are *parallel* to the adjacent bonds with directions $\boldsymbol{e}_i^3$ and $\boldsymbol{e}_{i+1}^3$, respectively, generate the restoring forces along the bonds given by Eq. (14.36). The components *perpendicular* to the bonds, however, lead to infinitesimal rigid rotations of the adjacent triads, which changes the potential energy H^curv and thus causes the forces $\boldsymbol{F}_i^\mathrm{curv}$. As illustrated in Fig. 14.2(a), the component of the displacement $\delta\boldsymbol{r}_i$ along $\boldsymbol{e}_i^1$, given by $(\boldsymbol{e}_i^1 \cdot \delta\boldsymbol{r}_i)\boldsymbol{e}_i^1$, rotates the triad

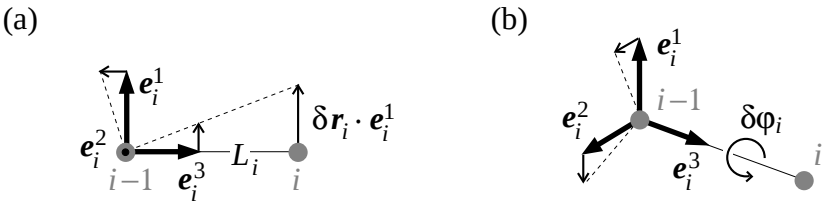

Figure 14.2 ■ (a) Infinitesimal rotation of the local triad due to a virtual displacement $\delta\boldsymbol{r}_i$ of particle i along direction $\boldsymbol{e}_i^1$ perpendicular to the bond. (Note that the proportions are exaggerated for the sake of clarity.) The tangent vector $\boldsymbol{e}_i^3$ changes its direction by $\delta\boldsymbol{e}_i^3 = (\boldsymbol{e}_i^1 \cdot \delta\boldsymbol{r}_i/L_i)\boldsymbol{e}_i^1$. The normal vector $\boldsymbol{e}_i^1$ is rotated by $\delta\boldsymbol{e}_i^1 = -(\boldsymbol{e}_i^1 \cdot \delta\boldsymbol{r}_i/L_i)\boldsymbol{e}_i^3$. (b) Infinitesimal twist deformation $\delta\varphi_i$ about the bond axis $\boldsymbol{e}_i^3$. The normal vectors change their orientations by $\delta\boldsymbol{e}_i^{1/2} = \pm\delta\varphi_i \boldsymbol{e}_i^{2/1}$.

vectors $\boldsymbol{e}_i^1$ and $\boldsymbol{e}_i^3$ by an infinitesimally small angle $(\boldsymbol{e}_i^1 \cdot \delta\boldsymbol{r}_i)/L_i$ about the axis $\boldsymbol{e}_i^2$, thus $\delta\boldsymbol{e}_i^1 = -(\boldsymbol{e}_i^1 \cdot \delta\boldsymbol{r}_i/L_i)\boldsymbol{e}_i^3$ and $\delta\boldsymbol{e}_i^3 = (\boldsymbol{e}_i^1 \cdot \delta\boldsymbol{r}_i/L_i)\boldsymbol{e}_i^1$. Analogous relations hold for the second normal vector $\boldsymbol{e}_i^2$ instead of $\boldsymbol{e}_i^1$, considering the component of $\delta\boldsymbol{r}_i$ along $\boldsymbol{e}_i^2$.

Now realize that the triad $\{\boldsymbol{e}_i^1, \boldsymbol{e}_i^2, \boldsymbol{e}_i^3\}$ is affected by displacements of both particle i and $i-1$, $\delta\boldsymbol{r}_i$ and $\delta\boldsymbol{r}_{i-1}$. Obviously, the infinitesimal rotations described above depend on the *relative* displacement $\delta\boldsymbol{r}_i - \delta\boldsymbol{r}_{i-1}$ (there is no net rotation if $\delta\boldsymbol{r}_i = \delta\boldsymbol{r}_{i-1}$). Therefore, replacing $\delta\boldsymbol{r}_i$ everywhere by $\delta\boldsymbol{r}_i - \delta\boldsymbol{r}_{i-1}$, we finally obtain the displacement relations

$$\delta\boldsymbol{e}_i^{1/2} = -\frac{1}{L_i}\,\boldsymbol{e}_i^3 \boldsymbol{e}_i^{1/2} \cdot (\delta\boldsymbol{r}_i - \delta\boldsymbol{r}_{i-1})\,, \tag{14.37a}$$

$$\delta\boldsymbol{e}_i^3 = \frac{1}{L_i}\left(\boldsymbol{e}_i^1\boldsymbol{e}_i^1 + \boldsymbol{e}_i^2\boldsymbol{e}_i^2\right) \cdot (\delta\boldsymbol{r}_i - \delta\boldsymbol{r}_{i-1})\,. \tag{14.37b}$$

Hence, a displacement $\delta\boldsymbol{r}_i$, with all other coordinates $\{\boldsymbol{r}_{j\neq i}\}$ fixed, affects the adjacent triads $\{\boldsymbol{e}_i^1, \boldsymbol{e}_i^2, \boldsymbol{e}_i^3\}$ and $\{\boldsymbol{e}_{i+1}^1, \boldsymbol{e}_{i+1}^2, \boldsymbol{e}_{i+1}^3\}$ and implies the following variations:

$$\delta\boldsymbol{e}_i^{1/2}\big|_{\{\boldsymbol{r}_{j\neq i}\}} = -\frac{1}{L_i}\,\boldsymbol{e}_i^3 \boldsymbol{e}_i^{1/2} \cdot \delta\boldsymbol{r}_i\,, \tag{14.38a}$$

$$\delta\boldsymbol{e}_{i+1}^{1/2}\big|_{\{\boldsymbol{r}_{j\neq i}\}} = +\frac{1}{L_{i+1}}\,\boldsymbol{e}_{i+1}^3 \boldsymbol{e}_{i+1}^{1/2} \cdot \delta\boldsymbol{r}_i\,, \tag{14.38b}$$

$$\delta\boldsymbol{e}_i^3\big|_{\{\boldsymbol{r}_{j\neq i}\}} = +\frac{1}{L_i}\left(\boldsymbol{e}_i^1\boldsymbol{e}_i^1 + \boldsymbol{e}_i^2\boldsymbol{e}_i^2\right) \cdot \delta\boldsymbol{r}_i\,, \tag{14.38c}$$

$$\delta\boldsymbol{e}_{i+1}^3\big|_{\{\boldsymbol{r}_{j\neq i}\}} = -\frac{1}{L_{i+1}}\left(\boldsymbol{e}_{i+1}^1\boldsymbol{e}_{i+1}^1 + \boldsymbol{e}_{i+1}^2\boldsymbol{e}_{i+1}^2\right) \cdot \delta\boldsymbol{r}_i\,. \tag{14.38d}$$

With the help of these relations, we determine the derivatives of the potential H^{curv} with respect to $\boldsymbol{r}_i$ (and thus the forces $\boldsymbol{F}_i^{\mathrm{curv}}$) by means of numerical differentiation. The variations of H^{curv} are calculated on a Cartesian grid with mesh

size $\delta x = \delta y = \delta z = \varepsilon a \ll a$ (where a is the bead radius), so that $\delta \boldsymbol{r}_i = \pm\delta\xi\, \boldsymbol{e}^\xi$ with $\xi = x, y, z$; in our simulations, $\varepsilon = 10^{-5}$. The components of the force $\boldsymbol{F}_i^{\mathrm{curv}}$ are then obtained from the central difference quotient

$$F_{i,\xi}^{\mathrm{curv}} = -\frac{H^{\mathrm{curv}}(\ldots, \xi_i + \delta\xi, \ldots) - H^{\mathrm{curv}}(\ldots, \xi_i - \delta\xi, \ldots)}{2\delta\xi} \tag{14.39}$$

that uses the elastic energy evaluated symmetrically around the current configuration to enhance the stability of the numerical differentiation.[9]

Furthermore, an infinitesimal rotational variation $\delta\varphi_i$ about the bond between particles $i-1$ and i changes the normal vectors $\boldsymbol{e}_i^1$ and $\boldsymbol{e}_i^2$, too, as can be seen in Fig. 14.2(b):

$$\delta \boldsymbol{e}_i^1 = +\boldsymbol{e}_i^2 \delta\varphi_i\,, \tag{14.40a}$$

$$\delta \boldsymbol{e}_i^2 = -\boldsymbol{e}_i^1 \delta\varphi_i\,. \tag{14.40b}$$

The corresponding change in the elastic potential H^{curv} generates a restoring twist torque about the tangent $\boldsymbol{e}_i^3$,

$$\boldsymbol{T}_i^{\mathrm{curv}} = T_i^{\mathrm{curv}} \boldsymbol{e}_i^3 \quad \text{with} \quad T_i^{\mathrm{curv}} = -\frac{\partial}{\partial\varphi_i} H^{\mathrm{curv}}\,. \tag{14.41}$$

The derivative with respect to φ_i is calculated in analogy to Eq. (14.39), with angular variation $\delta\varphi = \pm\varepsilon\pi$.

14.1.6 Motor forces

To impose a preferred reference orientation on the central axes of the helices while they rotate about the latter, we guide the first three[10] particles of each helix along circular harmonic traps (Fig. 14.3), and we drive them all with equal and constant tangential forces. This setup mimicks the flexible shaft of the flagellar filament (Fig. 12.3); it provides both a restoring torque that enforces the orientation of the filament and the constant driving torque of the flagellar motor.[11]

We express the positions of the "motor beads" in cylindrical coordinates (r_i, ϕ_i, z_i) whose origin is shifted by $\pm\frac{1}{2}d$ in y direction (for right/left helix),

[9] If we chose instead the asymmetric difference $H^{\mathrm{curv}}(\ldots, \xi_i + \delta\xi, \ldots) - H^{\mathrm{curv}}(\ldots, \xi_i, \ldots)$, a finite restoring force would exist even in equilibrium since then $H^{\mathrm{curv}}(\ldots, \xi_i + \delta\xi, \ldots) > H^{\mathrm{curv}}(\ldots, \xi_i, \ldots)$, which is unphysical.

[10] Note that it is not sufficient to guide only two particles since then the helix can still rotate freely (i.e., without deformations and thus without energy costs) about the first bond, so that the orientation of the central helix axis would not be prescribed, but could take any direction on a cone.

[11] In a more realistic setup, the first bond should be aligned with the central helix axis and "fixed" along z direction, and each helix should be driven by a torque about the first bond. This, however, requires a suitable adjustment of the equilibrium curvatures at the first few vertices.

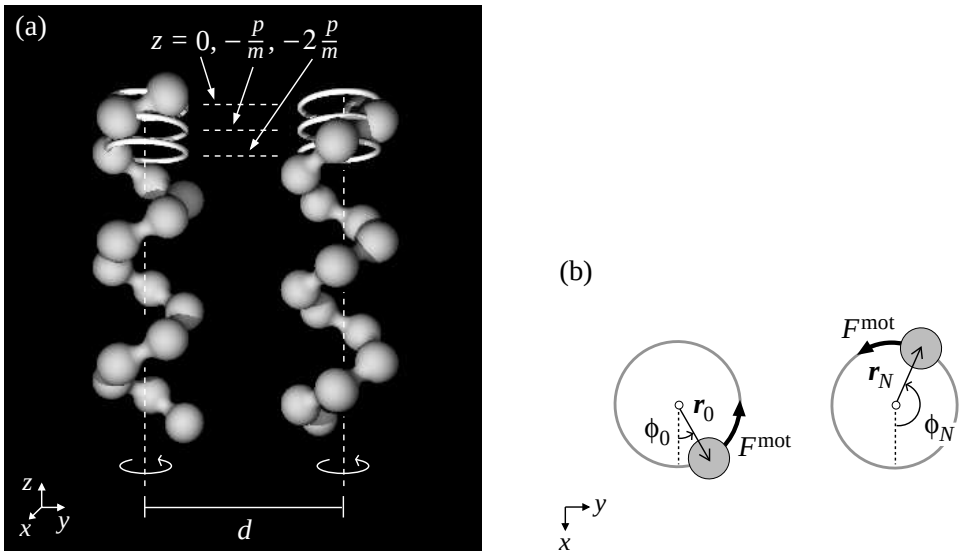

Figure 14.3 ■ (a) Model for flexible helical filaments. The bonds between adjacent beads are flexible with respect to both bending and twist deformations. The flagellar motor is mimicked by driving the first three beads of each helix with constant tangential forces on circular traps, located at $z = 0$, $-(p/m)$, and $-2(p/m)$, where p is the helix pitch and m the number of beads per winding. The separation of the central helix axes in the relaxed state is d. (b) Top view of the two helices. The phase lag ψ is defined as the difference in the phase angles of the first bead of the left and the right helix, ϕ_0 and ϕ_N.

where d is the reference distance of the two helix axes in the relaxed state (see Fig. 14.3):

$$\boldsymbol{r}_i = r_i \boldsymbol{e}_i^r + z_i \boldsymbol{e}^z \pm \frac{1}{2}\, d\, \boldsymbol{e}^y \tag{14.42}$$

with the radial unit vector $\boldsymbol{e}_i^r = [\cos\phi_i, \sin\phi_i, 0]$. The tangential driving force with constant strength F^{mot} is directed along the azimuthal unit vector $\boldsymbol{e}_i^\phi = [-\sin\phi_i, \cos\phi_i, 0]$ of the respective particle i. The toroidal harmonic trap with stiffness K^{mot} guides the particle on a circle with radius r^{mot} identical to the helix radius. Its center is located at position $[0, \pm\frac{1}{2}d, z_i^{\mathrm{mot}}]$ with $z_i^{\mathrm{mot}} = -(p/m)\, i$ [see Fig. 14.3(a)], where p is the pitch and m the number of beads per helix winding. Thus, the force generated by this motor in total reads

$$\boldsymbol{F}_i^{\mathrm{mot}} = F^{\mathrm{mot}} \boldsymbol{e}_i^\phi - K^{\mathrm{mot}} \left[(r_i - r^{\mathrm{mot}}) \boldsymbol{e}_i^r + (z_i - z_i^{\mathrm{mot}}) \boldsymbol{e}^z \right] . \tag{14.43}$$

14.1.7 Equations of motion

So far in this chapter, the bead index i referred to a single helix built of N spheres. However, as we intend to study the dynamics of *two* hydrodynamically coupled helices with $2N$ particles, we extend the range of bead indices to $i \in [0, 2N-1]$.

The bead coordinates of the first helix [on the left in Figs. 14.3(a,b)] are thus given by $\{\boldsymbol{r}_0, \ldots, \boldsymbol{r}_{N-1}\}$, those of the second (right) helix by $\{\boldsymbol{r}_N, \ldots, \boldsymbol{r}_{2N-1}\}$. In the definitions given so far, we simply have to replace i by $i \,(\mathrm{mod}\, N)$.

The total force acting on bead i is given by the internal elastic interactions $\boldsymbol{F}_i^{\mathrm{curv}} + \boldsymbol{F}_i^{\mathrm{bond}}$ and, in addition, the motor forces $\boldsymbol{F}_i^{\mathrm{mot}}$ acting only on the first three beads of each helix:

$$\boldsymbol{F}_i = \begin{cases} \boldsymbol{F}_i^{\mathrm{curv}} + \boldsymbol{F}_i^{\mathrm{bond}} + \boldsymbol{F}_i^{\mathrm{mot}} & \text{for } \; i \,(\mathrm{mod}\, N) \in \{0,1,2\} \\ \boldsymbol{F}_i^{\mathrm{curv}} + \boldsymbol{F}_i^{\mathrm{bond}} & \text{for } \; i \,(\mathrm{mod}\, N) \in [3, N-1] \end{cases} . \tag{14.44}$$

Torques are solely generated by elastic deformations of the helices, thus

$$\boldsymbol{T}_i = \boldsymbol{T}_i^{\mathrm{curv}} . \tag{14.45}$$

In our simulations, we neglect hydrodynamic interactions caused by rotational motions.[12] We consider only translational couplings, described by the mobility tensors $\boldsymbol{\mu}_{ij}^{\mathrm{tt}}$, so according to Eq. (2.21a), the particle velocities are given by

$$\boldsymbol{v}_i = \sum_j \boldsymbol{\mu}_{ij}^{\mathrm{tt}} \cdot \boldsymbol{F}_j \,, \tag{14.46}$$

and the (coupled) equations of motion for the translation of the beads read

$$\dot{\boldsymbol{r}}_i = \boldsymbol{v}_i \,. \tag{14.47}$$

Since the bond length and thus the distance of neighboring particles is about $2.6\,a$, we can apply the Rotne-Prager approximation (2.39) for the mobilities (see Fig. 2.4).[13]

The dynamics of the triads $\{\boldsymbol{e}_i^1, \boldsymbol{e}_i^2, \boldsymbol{e}_i^3\}$ is governed by two types of rotations. First of all, the (decoupled) overdamped relaxation of twist deformations is described by the rotational velocity

$$\tilde{\boldsymbol{\omega}}_i = \tilde{\omega}_i \boldsymbol{e}_i^3 \quad \text{with} \quad \tilde{\omega}_i = \mu^{\mathrm{r}} T_i^{\mathrm{curv}} , \tag{14.48}$$

[12] There are several reasons to neglect the hydrodynamic influence of rotations in detail. First of all, in the discrete model, the triads $\{\boldsymbol{e}_i^1, \boldsymbol{e}_i^2, \boldsymbol{e}_i^3\}$ are not exactly "localized", and the deformation (bending and twist) between neighboring triads is somehow "spread" along the adjacent bonds. Thus, the corresponding elastic torque is not well-localized, too. In our representation, the torque is aligned along the bond direction $\boldsymbol{e}_i^3$, it could, however, be also chosen in direction of the "mean tangent" at particle i, i.e., $\boldsymbol{e}_i^3 + \boldsymbol{e}_{i+1}^3$. Secondly, a coupling of rotation to translation can induce rotational motions of the triads that are not consistent with the condition $\boldsymbol{e}_i^3 \propto \boldsymbol{r}_i - \boldsymbol{r}_{i-1}$. Due to these ambiguities, we neglect the hydrodynamic coupling of rotational motions.

[13] The Rotne-Prager approximation, with $\boldsymbol{\mu}_{ij}^{\mathrm{tt}} = \boldsymbol{\mu}_{ij}^{\mathrm{tt}}(\boldsymbol{r}_i - \boldsymbol{r}_j)$, only takes into account two-body interactions, which substantially saves computation time (compared to calculating many-body interactions). Note, in this context, that the force $\boldsymbol{F}_i$ only depends on the nearest neighbors of particle i and hence also represents two-body interactions.

changing the twist angle by $\mathrm{d}\varphi_i = \tilde{\omega}_i \mathrm{d}t$ and thus the normal vectors $\boldsymbol{e}_i^1$ and $\boldsymbol{e}_i^2$ according to Eq. (14.40):

$$\mathrm{d}\boldsymbol{e}_i^{1/2}\big|_{\tilde{\boldsymbol{\omega}}_i} = \tilde{\boldsymbol{\omega}}_i \times \boldsymbol{e}_i^{1/2} \mathrm{d}t \tag{14.49}$$

In our model, the scalar μ^{r} is identified with the rotational mobility coefficient of a single bead with radius a, i.e., $\mu^{\mathrm{r}} = (8\pi\eta a^3)^{-1}$. In addition, the relative displacement $\mathrm{d}\boldsymbol{r}_i - \mathrm{d}\boldsymbol{r}_{i-1} = (\boldsymbol{v}_i - \boldsymbol{v}_{i-1})\mathrm{d}t$ of neighboring particles generates a rigid rotation of the ith triad. We denote the corresponding rotational velocity by $\bar{\boldsymbol{\omega}}_i$. From Eq. (14.37), we obtain

$$\mathrm{d}\boldsymbol{e}_i^{1/2}\big|_{\bar{\boldsymbol{\omega}}_i} = -\frac{1}{L_i}\, \boldsymbol{e}_i^3 \boldsymbol{e}_i^{1/2} \cdot (\boldsymbol{v}_i - \boldsymbol{v}_{i-1})\mathrm{d}t\,, \tag{14.50a}$$

$$\mathrm{d}\boldsymbol{e}_i^{3}\big|_{\bar{\boldsymbol{\omega}}_i} = \frac{1}{L_i} \left(\boldsymbol{e}_i^1 \boldsymbol{e}_i^1 + \boldsymbol{e}_i^2 \boldsymbol{e}_i^2\right) \cdot (\boldsymbol{v}_i - \boldsymbol{v}_{i-1})\mathrm{d}t\,, \tag{14.50b}$$

which can be rewritten in the form

$$\mathrm{d}\boldsymbol{e}_i^{\alpha}\big|_{\bar{\boldsymbol{\omega}}_i} = \bar{\boldsymbol{\omega}}_i \times \boldsymbol{e}_i^{\alpha}\, \mathrm{d}t \tag{14.51}$$

with angular velocity

$$\bar{\boldsymbol{\omega}}_i = \frac{1}{L_i}(-\boldsymbol{e}_i^1 \boldsymbol{e}_i^2 + \boldsymbol{e}_i^2 \boldsymbol{e}_i^1) \cdot (\boldsymbol{v}_i - \boldsymbol{v}_{i-1})\,. \tag{14.52}$$

In total, the rotational time evolution $\dot{\boldsymbol{e}}_i^{\alpha} = \mathrm{d}\boldsymbol{e}_i^{\alpha}/\mathrm{d}t\,|_{\tilde{\boldsymbol{\omega}}_i} + \mathrm{d}\boldsymbol{e}_i^{\alpha}/\mathrm{d}t\,|_{\bar{\boldsymbol{\omega}}_i}$ given by Eqs. (14.49) and (14.51) can be written in the form

$$\dot{\boldsymbol{e}}_i^{\alpha} = \boldsymbol{\omega}_i \times \boldsymbol{e}_i^{\alpha} \tag{14.53}$$

with $\boldsymbol{\omega}_i = \bar{\boldsymbol{\omega}}_i + \tilde{\boldsymbol{\omega}}_i$ or, in components with respect to the local basis $\{\boldsymbol{e}_i^1, \boldsymbol{e}_i^2, \boldsymbol{e}_i^3\}$,

$$\omega_i^1 = -\frac{1}{L_i}\, \boldsymbol{e}_i^2 \cdot (\boldsymbol{v}_i - \boldsymbol{v}_{i-1})\,, \tag{14.54a}$$

$$\omega_i^2 = +\frac{1}{L_i}\, \boldsymbol{e}_i^1 \cdot (\boldsymbol{v}_i - \boldsymbol{v}_{i-1})\,, \tag{14.54b}$$

$$\omega_i^3 = \tilde{\omega}_i\,. \tag{14.54c}$$

The equations of motion (14.47) and (14.53) are integrated numerically by means of the Heun algorithm (2.64). For a given configuration,[14] the particle velocities $\boldsymbol{v}_i$ are calculated from Eq. (14.46), and the rotational velocities $\boldsymbol{\omega}_i$ of

[14] In the compact notation used in Sect. 2.5, the complete spatial configuration at time t reads $X_t = [\{\boldsymbol{r}_{i_1}\}, \{\boldsymbol{e}_{i_1'}^{\alpha}\}, \{\boldsymbol{r}_{i_2}\}, \{\boldsymbol{e}_{i_2'}^{\alpha}\}]_t$ with $i_1 \in [0, N-1]$, $i_1' \in [1, N-1]$, $i_2 \in [N, 2N-1]$, $i_2' \in [N+1, 2N-1]$, and $\alpha \in \{1,2,3\}$. (Note that the triads $\{\boldsymbol{e}_0^1, \boldsymbol{e}_0^2, \boldsymbol{e}_0^3\}$ and $\{\boldsymbol{e}_N^1, \boldsymbol{e}_N^2, \boldsymbol{e}_N^3\}$ do not exist.)

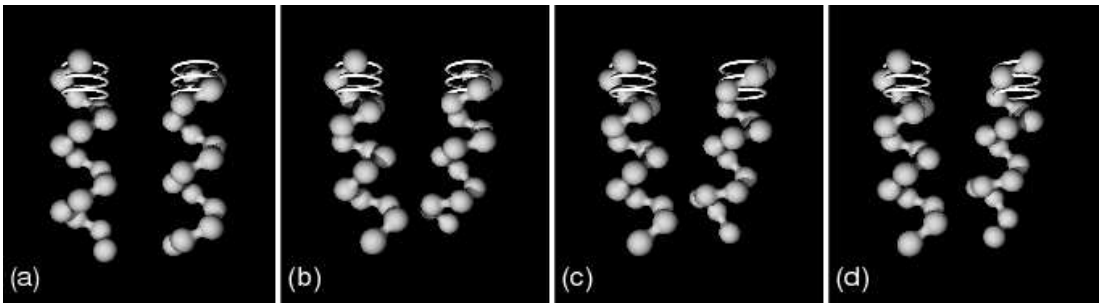

Figure 14.4 ■ Synchronization dynamics, starting from phase difference $\psi = 0.97\pi$. The snapshots show the situation after (a) 0, (b) 30, (c) 60, and (d) 90 revolutions. The helices are relatively "soft" with elastic moduli $A^1 = 20\,F^{\mathrm{mot}}a$ and $A^3 = 100\,F^{\mathrm{mot}}a$, and the motor stiffness is $K^{\mathrm{mot}} = 50\,F^{\mathrm{mot}}/a$. (If we further reduce the stiffness, the helices deform such that they touch each other.)

the triads follow from Eq. (14.54). The chosen time step corresponds to about 10^{-5} revolutions of a helix and is by two orders of magnitude shorter than the characteristic relaxation time of typical elastic deformations. We keep the driving force F^{mot} fixed since it only sets the time scale of the rotations. Thus, the relevant parameters affecting the dynamics are the bending stiffnesses $A^1 = A^2$ and the twist stiffness A^3 (all in units of $F^{\mathrm{mot}}a$). In addition, we also vary the motor stiffness K^{mot} (in units of F^{mot}/a). For the stretching stiffness, we choose the fixed value $B = 100\,F^{\mathrm{mot}}/a$, restricting the bond extensions to about $10^{-4}\,L_{\mathrm{e}}$.[15]

We perform all our simulations at helix separation $d = 10\,a$, as illustrated in Fig. 14.3(a); for smaller distances, the range where we can vary the flexibility is very small since the interacting helices deform and finally touch each other.

14.2 Synchronization dynamics

14.2.1 Dynamics and deformations of rotating helices

Figure 14.4 visualizes the dynamics of the two helices, in particular their deformations. A right-handed helix turning counterclockwise when viewed from the motor side (top view in Fig. 14.4) slightly shrinks compared to being at rest. Due to the viscous drag acting on the individual beads when the helix rotates, its radius and pitch decrease, as the comparison of Figs. 14.4(a) and (b) shows. The associated internal elastic stresses balance the external viscous drag forces. These deformations also occur if hydrodynamic interactions are not present.

[15] We explicitly checked whether a variation of B in that regime has a significant effect on the dynamics of the helices. This is not the case for the range from 50 to $200\,F^{\mathrm{mot}}/a$; the corresponding variations in the synchronization speeds are of order 2% and thus negligible compared to the influence of the elastic moduli A^α (see next section).

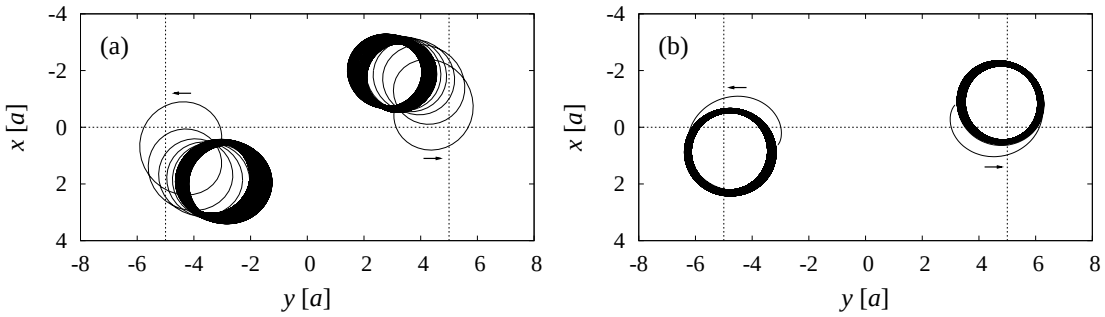

Figure 14.5 ■ Trajectories (projected onto the xy plane) of the helix tips. The arrows indicate the direction of rotation. The intersections of the dashed lines mark the position of the central axis of rotation defined by the motor. Figure (a) tracks the motion of the tip from Fig. 14.4 (viewed from the top). For comparison, we plot in (b) the motion of the tip in case of higher bending stiffness ($A^1 = 100\, F^{\mathrm{mot}} a$).

What is, however, more interesting, are the deflections that are caused by the *coupling* of the two helices via the flow field generated by their rotations [Figs. 14.4(b–d)]. The video analysis of the helix dynamics demonstrates that the helices tend to roll around each other. This can also be seen by plotting the trajectories of the helix tips (the free ends) in projection onto the xy plane (perpendicular to the axis of rotation). As Fig. 14.5(a) reveals, the helix tips each approach a fixed circular orbit after a few rotations, and the centers of these orbits are shifted relative to the projection of the respective central motor axis. Obviously, this deflection of the helices depends on their flexibility. In Fig. 14.5, we compare the dynamics of a softer and a stiffer helix (the bending stiffnesses A^1 in the two cases differ by a factor of 5, all other parameters are identical).

If the helices were much less coarse-grained with more (smaller) beads per length, corresponding to more available degrees of freedom and thus to a more "continuous" flexibility (due to a higher "density" of joints along the helix),[16] one would expect the two "filaments" to wrap around each other in a left-handed sense and form a bundle.[17]

The series of snapshots in Fig. 14.4 already indicates that there is some synchronization of the helix rotations, leading to phase locking as also observed for rigid helices. This effect will be investigated in detail in the following.

14.2.2 Phase synchronization

As in our study of rigid helices presented in the previous chapter, we consider again the dynamics of the *phase difference*, which we now define as

$$\psi(t) = \phi_N(t) - \phi_0(t)\,, \tag{14.55}$$

[16] It is not sufficient to simply apply smaller values for the elastic moduli A^α.

[17] This effect was observed in macroscopic-scale experiments with rotating helical wires in highly viscous silicone oil [131, 133, 163].

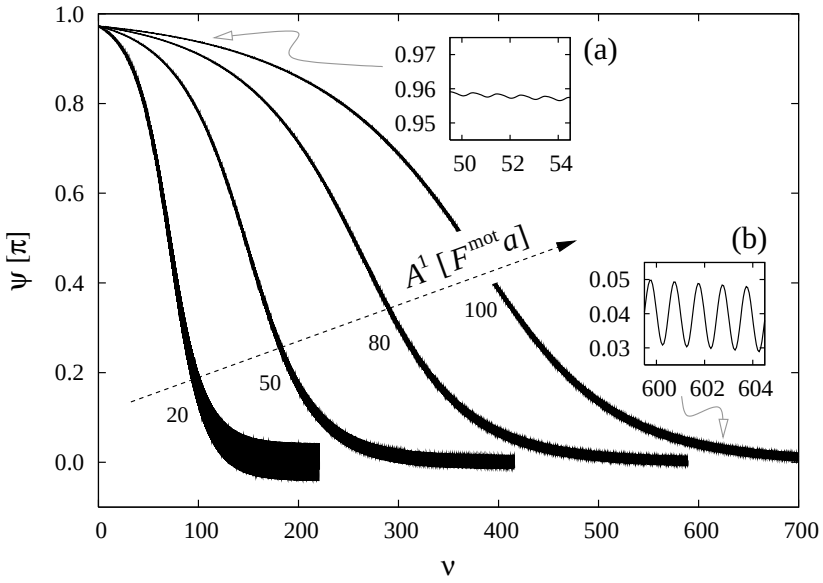

Figure 14.6 ■ Synchronization of the helix rotations. The phase difference ψ is plotted against the number of revolutions, ν. Starting from $\psi = 0.97\,\pi$, the phase difference drops down and (on average) approaches zero. The four curves show simulation data for different bending moduli: $A^1 = 20$, 50, 80, and $100\,F^{\mathrm{mot}}a$; the twist stiffness is $A^3 = 100\,F^{\mathrm{mot}}a$, and the motor stiffness is $K^{\mathrm{mot}} = 100\,F^{\mathrm{mot}}/a$. The "broadening" of the curves is due to periodic oscillations of the phase difference that are not resolved on the scale plotted here. The insets enlarge these oscillations at (a) $\langle\psi\rangle \approx \pi$ and (b) $\langle\psi\rangle \approx 0$ for the case $A^1 = 100\,F^{\mathrm{mot}}a$.

where ϕ_0 and ϕ_N are the azimuthal angles of the respective first bead of the two helices, driven along circular traps [see Fig. 14.3(b)]. In addition, we introduce with

$$\nu(t) = \frac{\phi_0(t)}{2\pi} \tag{14.56}$$

the number of rotations of the first (left) helix. Figure 14.6 shows the evolution of ψ, plotted against ν, for various bending moduli A^1 (at constant twist modulus A^3 and motor stiffness K^{mot}).

In essence, we observe the same behavior as for the rigid helices. First of all, the phase difference approaches zero (on average), when starting with ψ slightly smaller than π. Moreover, we find the expectation confirmed that the synchronization process is enhanced when flexibility is increased, i.e., when the elastic moduli are reduced and thus the helices become softer. Qualitatively, we obtain the same tendency when varying the twist modulus A^3 or the motor stiffness K^{mot}.

The "broadening" of the curves stems from oscillations in the rotational velocities $\dot{\phi}_0$ and $\dot{\phi}_N$ due to the phase dependence of the helix mobilities. Unlike the case of rigid helices (see Sect. 13.3.1), the amplitude of these oscillations

depends on the flexibility since the helices deform each other via their surrounding flow fields. Obviously, the oscillations are more pronounced for softer helices. Furthermore, their amplitude increases during the synchronization process [Figs. 14.6(a,b)], which was also observed for rigid helices [Figs. 13.3(b,c)].

Note that, although the curves in Fig. 14.6 obtained for different stiffness parameters look rather similar, they cannot be scaled (with respect to time or number of revolutions) so that they collapse on one and the same master curve (having averaged out the periodic oscillations). In particular, they are not symmetric with respect to the inflection point, so $\langle\psi\rangle(\nu)$ does not follow Eq. (13.16).

14.2.3 Dependence on flexibility

Figure 14.6 shows that the synchronization process is enhanced when flexibility is increased, i.e., when the elastic moduli are reduced and thus the helices become softer. To measure this effect quantitatively, we define the synchronization speed as the maximum slope of the curve $\langle\psi\rangle(\nu)$, i.e., after averaging out the periodic oscillations of $\psi(\nu)$ due to the rotations of the helices. The results of this analysis are presented in Fig. 14.7. The synchronization speeds, $\max_\nu |\mathrm{d}\langle\psi\rangle(\nu)/\mathrm{d}\nu|$, clearly decrease for increasing stiffness, but there is a striking qualitative difference between bending and twist stiffness. The comparison of Figs. 14.7(a) and (b) reveals that the synchronization speed is strongly reduced when we increase the bending stiffess A^1, while the variation of the twist stiffness A^3 has a smaller impact on the synchronization process. The extrapolation of the curves in Fig. 14.7(a) towards $1/A^1 = 0$ suggests that the synchronization speed tends to zero for infinitely large bending stiffness; however, based on the results of Chap. 13, we expect the speed to remain finite as long as there is still twist elasticity ($A^3 < \infty$) or flexibility of the motor ($K^{\mathrm{mot}} < \infty$).

Note that the variation of the motor stiffness (mimicking the flexible shaft of the flagellum) has the same qualitative effect as the variation of the bending stiffness. Increasing the value of K^{mot} from 20 to $100\,F^{\mathrm{mot}}/a$ (at $A^1 = A^3 = 100\,F^{\mathrm{mot}}a$), the synchronization process is slowed down by a factor of 4.

14.2.4 Flexible vs. rigid helices

In both cases, for rigid as well as for flexible helices, we observe that flexibility (the harmonic anchoring in the first case and the intrinsic elasticity in the latter) significantly enhances the synchronization process. However, if we compare numbers, we realize that the flexible helices do not synchronize by orders of magnitude faster compared to the rigid helices, as one might have expected. The synchronization of *rigid* helices (e.g., from $\psi \approx 0.99\,\pi$ to $0.01\,\pi$) takes several hundred revolutions [see Figs. 13.3(a) and 13.5], and our results for *flexible* helices yield the same order of magnitude.

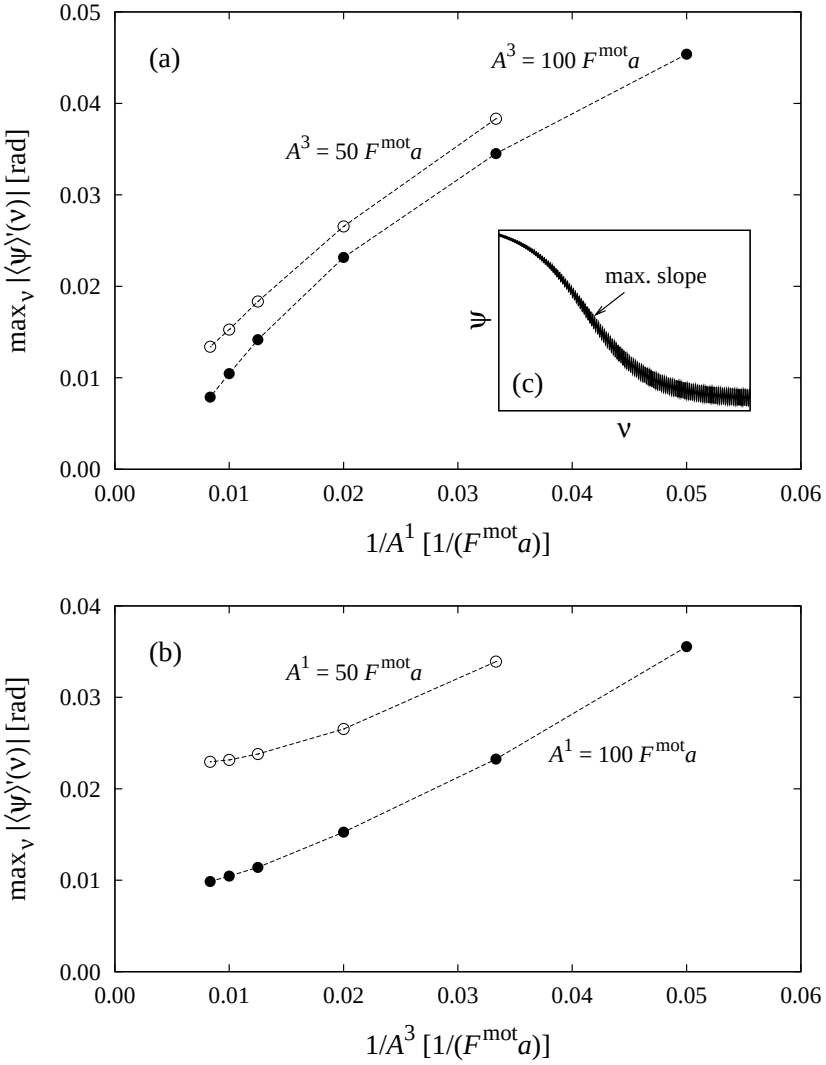

Figure 14.7 ■ Synchronization speed (in units rad per revolution) as a function of (a) the inverse bending stiffness $1/A^1$ (at constant A^3) and (b) the inverse twist stiffness $1/A^3$ (at constant A^1). The synchronization speed is determined as illustrated in the inset (c): After averaging over the oscillations, we extract the maximum slope of the curve $\langle\psi\rangle(\nu)$. For increasing bending stiffness (i.e., $1/A^1 \to 0$), the synchronization speed appears to tend to a value close to zero, while for increasing twist stiffness (i.e., $1/A^3 \to 0$), the speed seems to approach a finite value.

Note that, in the simulations with flexible helices, the distance between the central axes of rotation ($d = 10\,a$) was considerably larger than in case of the rigid helices ($d = 7\,a$),[18] which might have an effect on the efficiency of the synchronization since the flow fields decay with increasing spatial distance. Therefore, we performed a test simulation with flexible helices at distance $d = 7.5\,a$ (with

[18]The reason is simply that the flexible helices touch each other due to deformations if they are closer together.

$A^1 = A^3 = 100\,F^{\mathrm{mot}}a$, $K^{\mathrm{mot}} = 100\,F^{\mathrm{mot}}/a$) and compared the measured synchronization speed to the result at $d = 10\,a$ (with the same stiffness parameters). This, however, only gives a factor of about 2 in the synchronization speed when bringing the helices closer together.

One might argue that the overall flexibility of the discrete helical chain is not only set by the values of the elastic moduli, but also by the number of degrees of freedom, i.e., the number of joints. Thus, simulations with much more (smaller) beads per length should be performed to answer this question.

Furthermore, the length of the actually deformable part of the helix is shorter in the flexible case than in the rigid case. In the flexible case, the first two bonds are more or less "unflexible" in their relative orientation due to the tracking by the circular traps, whereas in the rigid case the helix can be tilted over its whole length.

15 Conclusions III

We reported that two rigid helices whose terminal beads are anchored in harmonic traps and which are driven by equal torques synchronize to zero phase difference. The effect is robust, i.e., if the torques are unequal, the helices synchronize to a non-zero phase lag below a critical torque difference. This agrees with the experimental observation that the helices in a macroscopic-scale model do not bundle if the motor speeds are sufficiently different [131].

Increasing the stiffness of the anchoring traps decreases the synchronization rate. We attribute this to the jiggling motion of the two helix axes which is more and more restrained. In the limit of infinite trap strength, our results are consistent with recent work based on slender-body theory for two rigid helices [132]. If the helices are prevented from translation and their axes are always kept perfectly parallel, then there is no synchronization possible. Therefore, we conclude that the additional degree of freedom due to the finite anchoring of the helix axis, i.e., the jiggling motion, is essential to enable phase synchronization in our model.

We also checked whether it is important if the helices are forced to stay at their position or if they are allowed to propel themselves. This was done by letting the helices move along the z axis but still keeping them in harmonic traps along x and y direction. However, we did not see a significant difference in the dynamics of the synchronization process compared to the results presented here.

At a first glance, the model using rigid helices might appear too artificial for describing the hydrodynamic coupling of flagellar filaments. Nevertheless, our results clearly indicate that some kind of "flexibility" is essential to allow for phase synchronization. In reality, this flexibility might have its origin in elastic deformations of the rotating flagella. Therefore, as a next step, we established a helical bead-spring model with finite bending and twist stiffness, where the motor is realized by driving the first three beads of each helix with constant and equal forces along circular harmonic traps.

As expected from the previous results, we observe a synchronization to zero phase difference in the case of flexible helices, too, and the synchronization process is enhanced if flexibility is increased. Moreover, bending elasticity seems to play the major role. Increasing the bending stiffness decreases the synchronization speed substantially, while the variation of the twist stiffness has a much smaller impact. The synchronization speeds for helices with intrinsic flexibility are by a factor of about 2 to 5 larger than those of rigid helices anchored in harmonic traps.

The synchronization process should be enhanced if we increase the number of beads. So far, the "filaments" in our model are fairly coarse-grained (each built of 15 beads, hence containing only 14 joints), so they feature too few degrees of freedom and are thus rather "unflexible". Furthermore, a better modeling of the flagellar motor, in particular the flexible hook, might increase the synchronization speed, too.

We also observe some kind of rudimentary "bundling", i.e., the free ends of the two helices slightly roll around each other. In a continuous (or, at least, less coarse-grained) model, the two helices are expected to wrap around each other, forming a bundle of interwound rotating filaments [78, 131, 133, 163].

The discrete model of a flexible helix (including hydrodynamic interactions) presented here can be also applied to study the polymorphism of bacterial flagella, i.e., changes in the helical conformation due to viscous stresses [24, 25, 46, 164, 223, 237], which is another important issue of understanding flagellar propulsion.

Bibliography

[1] L. Allen, M.W. Beijersbergen, R.J.C. Spreeuw, and J.P. Woerdman, Phys. Rev. A **45**, 8185 (1992).

[2] L. Allen, S.M. Barnett, and M.J. Padgett, *Optical Angular Momentum* (Institute of Physics Publishing, London, 2003).

[3] E. Andablo-Reyes, P. Díaz-Leyva, and J.L. Arauz-Lara, Phys. Rev. Lett. **94**, 106001 (2005).

[4] G.B. Arfken and H.J. Weber, *Mathematical Methods for Physicists* (Academic Press, San Diego, 1995).

[5] A. Ashkin, Phys. Rev. Lett. **24**, 156 (1970).

[6] A. Ashkin, J.M. Dziedzic, J.E. Bjorkholm, and S. Chu, Opt. Lett. **11**, 288 (1986).

[7] A. Ashkin and J.M. Dziedzic, Science **235**, 1517 (1987).

[8] R.D. Astumian, Science **276**, 917 (1997).

[9] R.D. Astumian, Sci. Am. **285**(1), 45 (2001).

[10] R.D. Astumian and P. Hänggi, Phys. Today **55**(11), 33 (2002).

[11] J.E. Avron, O. Gat, and O. Kenneth, Phys. Rev. Lett. **93**, 186001 (2004).

[12] J.E. Avron, O. Kenneth, and D.H. Oaknin, New J. Phys. **7**, 234 (2005). A movie showing the dynamics of the two-bead swimmer (with varying bead volume and distance) presented in this article can be found at http://www.iop.org/EJ/mmedia/1367-2630/7/1/234/swimmer.swf.

[13] R.C. Ball and J.R. Melrose, Physica A **247**, 444 (1997).

[14] A.J. Banchio, G. Nägele, and J. Bergenholtz, J. Chem. Phys. **113**, 3381 (2000).

[15] P. Bartlett, S.I. Henderson, and S.J. Mitchell, Philos. Trans. R. Soc. London, Ser. A **359**, 883 (2001).

[16] G.K. Batchelor, J. Fluid Mech. **44**, 419 (1970).

[17] G.K. Batchelor, J. Fluid Mech. **74**, 1 (1976).

[18] L.E. Becker, S.A. Koehler, and H.A. Stone, J. Fluid Mech. **490**, 15 (2003).

[19] B. Behkam and M. Sitti, in *Proceedings of the 2004 ASME International Mechanical Engineering Congress and Exposition* (Anaheim, 2004), p. 1.

[20] B. Behkam and M. Sitti, ASME J. Dynamic Systems, Measurement, Control **128**, 36 (2006).

[21] M.W. Beijersbergen, L. Allen, H.E.L.O. van der Veen, and J.P Woerdman, Opt. Commun. **96**, 123 (1993).

[22] T. Benesch and S. Yiacoumi, Phys. Rev. E **68**, 021401 (2003).

[23] H.C. Berg, Nature **245**, 380 (1973).

[24] H.C. Berg, Annu. Rev. Biochem. **72**, 19 (2003).

[25] H.C. Berg, *E. coli in Motion* (Springer, New York, 2004).

[26] J.M. Berg, J.L. Tymoczko, and L. Stryer, *Biochemistry* (W.H. Freeman, New York, 2002).

[27] R.A. Beth, Phys. Rev. **50**, 115 (1936).

[28] A.I. Bishop, T.A. Nieminen, N.R. Heckenberg, and H. Rubinsztein-Dunlop, Phys. Rev. Lett. **92**, 198104 (2004).

[29] G. Bossis, A. Meunier, and J.D. Sherwood, Phys. Fluids A **3**, 1853 (1991).

[30] G.E.P. Box and M.E. Muller, Ann. Stat. Mech. **29**, 610 (1958).

[31] J.F. Brady and G. Bossis, Ann. Rev. Fluid Mech. **20**, 111 (1988).

[32] H. Brenner, Chem. Eng. Sci. **18**, 1 (1963); **19**, 599 (1964).

[33] M.P. Brenner, Phys. Fluids **11**, 754 (1999).

[34] B.D. Brower-Toland, C.L. Smith, R.C. Yeh, J.T. Lis, C.L. Peterson, and M.D. Wang, Proc. Natl. Acad. Sci. **99**, 1960 (2002).

[35] G. Bryant, S.R. Williams, L. Qian, I.K. Snook, E. Perez, and F. Pincet, Phys. Rev. E **66**, 060501(R) (2002).

[36] R.E. Caflisch and J.H.C. Luke, Phys. Fluids **28**, 759 (1985).

[37] R.E. Caflisch, C. Lim, J.H.C. Luke, and A.S. Sangani, Phys. Fluids **31**, 3175 (1988).

[38] D.R. Cairns, M. Sibulkin, and G.P. Crawford, Appl. Phys. Lett. **78**, 2643 (2001).

[39] R. Chang and A. Yethiraj, J. Chem. Phys. **114**, 7688 (2001).

[40] J.-F. Chauwin, A. Ajdari, and J. Prost, Europhys. Lett. **32**, 373 (1995).

[41] B. Cichocki, B.U. Felderhof, K. Hinsen, E. Wajnryb, and J. Bławzdziewicz, J. Chem. Phys. **100**, 3780 (1994).

[42] B. Cichocki and K. Hinsen, Phys. Fluids **7**, 285 (1995).

[43] B. Cichocki and B.U. Felderhof, Phys. Rev. E **62**, 5383 (2000).

[44] B. Cichocki, R.B. Jones, R. Kutteh, and E. Wajnryb, J. Chem. Phys. **112**, 2548 (2000).

[45] J.W. Cooley and J.W. Tukey, Math. Comput. **19**, 297 (1965).

[46] D. Coombs, G. Huber, J.O. Kessler, and R.E. Goldstein, Phys. Rev. Lett. **89**, 118102 (2002).

[47] R.G. Cox, J. Fluid Mech. **44**, 791 (1970).

[48] J.C. Crocker and D.G. Grier, J. Colloid Interface Sci. **179**, 298 (1996).

[49] J.C. Crocker, J. Chem. Phys. **106**, 2837 (1997).

[50] J.C. Crocker, M.T. Valentine, E.R. Weeks, T. Gisler, P.D. Kaplan, A.G. Yodh, and D.A. Weitz, Phys. Rev. Lett. **85**, 888 (2000).

[51] B. Cui, H. Diamant, B. Lin, and S.A. Rice, Phys. Rev. Lett. **92**, 258301 (2004).

[52] J.E. Curtis, B.A. Koss, and D.G. Grier, Opt. Commun. **207**, 169 (2002).

[53] J.E. Curtis and D.G. Grier, Phys. Rev. Lett. **90**, 133901 (2003).

[54] J.E. Curtis and D.G. Grier, Opt. Lett. **28**, 872 (2003).

[55] N. Darnton, L. Turner, K. Breuer, and H.C. Berg, Biophys. J. **86**, 1863 (2004).

[56] V. Degiorgio, R. Piazza, and R.B. Jones, Phys. Rev. E **52**, 2707 (1995).

[57] B.V. Derjaguin and L. Landau, Acta Physicochim. (USSR) **14**, 633 (1941).

[58] J.M. Deutch and I. Oppenheim, J. Chem. Phys. **54**, 3547 (1971).

[59] K. Dholakia, G. Spalding, and M. MacDonald, Phys. World **15**(10), 31 (2002).

[60] J.K.G. Dhont, *An Introduction to Dynamics of Colloids* (Elsevier, Amsterdam, 1996).

[61] H. Diamant, B. Cui, B. Lin, and S.A. Rice, J. Phys.: Condens. Matter **17**, S2787 (2005).

[62] R. Dreyfus, J. Baudry, and H.A. Stone, Eur. Phys. J. B **47**, 161 (2005).

[63] R. Dreyfus, J. Baudry, M.L. Roper, M. Fermigier, H.A. Stone, and J. Bibette, Nature **437**, 862 (2005).

[64] E.R. Dufresne, T.M. Squires, M.P. Brenner, and D.G. Grier, Phys. Rev. Lett. **85**, 3317 (2000).

[65] E.R. Dufresne, D. Altman, and D.G. Grier, Europhys. Lett. **53**, 264 (2001).

[66] L. Durlofsky, J.F. Brady, and G. Bossis, J. Fluid Mech. **180**, 21 (1987).

[67] J. Edd, S. Payen, B. Rubinsky, M.L. Stoller, and M. Sitti, in *Proceedings of the 2003 IEEE/RSJ International Conference on Intelligent Robots and Systems* (Las Vegas, 2003), p. 2583.

[68] C. Eisenmann, U. Gasser, P. Keim, and G. Maret, Phys. Rev. Lett. **93**, 105702 (2004).

[69] C. Eisenmann, U. Gasser, P. Keim, G. Maret, and H.H. von Grünberg, Phys. Rev. Lett. **95**, 185502 (2005).

[70] D.L. Ermak and J.A. McCammon, J. Chem. Phys. **69**, 1352 (1978).

[71] J.J. Essner, K.J. Vogan, M.K. Wagner, C.J. Tabin, H.J. Yost, and M. Brueckner, Nature **418**, 38 (2002).

[72] E. Fällmann and O. Axner, Appl. Opt. **36**, 2107 (1997).

[73] L.P. Faucheux, L.S. Bourdieu, P.D. Kaplan, and A.J. Libchaber, Phys. Rev. Lett. **74**, 1504 (1995).

[74] L.P. Faucheux, G. Stolovitzky, and A. Libchaber, Phys. Rev. E **51**, 5239 (1995).

[75] B.U. Felderhof, Physica A **84**, 557 (1976); **84**, 569 (1976); **89**, 373 (1977); **151**, 1 (1988).

[76] B.A. Finlayson, *The Method of Weighted Residuals and Variational Principles* (Academic Press, New York, 1972).

[77] M. Fixman, J. Chem. Phys. **69**, 1527 (1978).

[78] H. Flores, E. Lobaton, S. Méndez-Diez, S. Tlupova, and R. Cortez, Bull. Math. Biol. **67**, 137 (2005). An animation showing the simulated bundling and tumbling of three flagella can be found at http://www.math.tulane.edu/~cortez/spiral.html.

[79] R.F. Fox and G.E. Uhlenbeck, Phys. Fluids **13**, 1893 (1970).

[80] D. Frenkel, Physica A **313**, 1 (2002).

[81] D. Frenkel and B. Smit, *Understanding Molecular Simulation* (Academic Press, San Diego, 2002).

[82] V.A. Froltsov, R. Blaak, C.N. Likos, and H. Löwen, Phys. Rev. E **68**, 061406 (2003); V.A. Froltsov, C.N. Likos, H. Löwen, C. Eisenmann, U. Gasser, P. Keim, and G. Maret, Phys. Rev. E **71**, 031404 (2005).

[83] P. Galajda and P. Ormos, Appl. Phys. Lett. **78**, 249 (2001); **80**, 4653 (2002).

[84] P. Ganatos, R. Pfeffer, and S. Weinbaum, J. Fluid Mech. **84**, 79 (1978).

[85] M.L. Gardel, M.T. Valentine, J.C. Crocker, A.R. Bausch, and D.A. Weitz, Phys. Rev. Lett. **91**, 158302 (2003).

[86] C.W. Gardiner, *Handbook of Stochastic Methods* (Springer, Berlin, 1985).

[87] U. Gasser, E.R. Weeks, A. Schofield, P.N. Pusey, and D.A. Weitz, Science **292**, 258 (2001).

[88] E. Gauger, *Hydrodynamics of Nanomachines in Biology* (diploma thesis, University of Konstanz, 2005). The electronic version is available at http://www.ub.uni-konstanz.de/kops/volltexte/2005/1691.

[89] E. Gauger and H. Stark, *Numerical Study of a Microscopic Artificial Swimmer* (preprint, 2006).

[90] P.G. de Gennes and J. Prost, *The Physics of Liquid Crystals* (Clarendon Press, Oxford, 1998).

[91] D.T. Gillespie, Am. J. Phys. **64**, 225 (1996).

[92] F. Gittes, B. Schnurr, P.D. Olmsted, F.C. MacKintosh, and C.F. Schmidt, Phys. Rev. Lett. **79**, 3286 (1997).

[93] H. Goldstein, *Classical Mechanics* (Addison-Wesley, Reading, Massachusetts, 1980).

[94] P. Grassia, E.J. Hinch, and L.C. Nitsche, J. Fluid Mech. **282**, 373 (1995).

[95] J. Gray, *Ciliary Movement* (Cambridge University Press, Cambridge, 1928).

[96] W.J. Greenleaf, M.T. Woodside, E.A. Abbondanzieri, and S.M. Block, Phys. Rev. Lett. **95**, 208102 (2005).

[97] A. Greiner, W. Strittmatter, and J. Honerkamp, J. Stat. Phys. **51**, 95 (1988).

[98] D.G. Grier, Nature **424**, 810 (2003).

[99] R.D. Groot, T.J. Madden, and D.J. Tildesley, J. Chem. Phys. **110**, 9739 (1999).

[100] H.H. von Grünberg, L. Helden, P. Leiderer, and C. Bechinger, J. Chem. Phys. **114**, 10094 (2001).

[101] B.A. Grzybowski, H.A. Stone, and G.M. Whitesides, Nature **405**, 1033 (2000); B.A. Grzybowski, X. Jiang, H.A. Stone, and G.M. Whitesides, Phys. Rev. E **64**, 011603 (2001).

[102] S. Gueron, K. Levit-Gurevich, N. Liron, and J.J. Blum, Proc. Natl. Acad. Sci. USA **94**, 6001 (1997).

[103] S. Gueron and K. Levit-Gurevich, Biophys. J. **74**, 1658 (1998).

[104] S. Gueron and K. Levit-Gurevich, Proc. Natl. Acad. Sci. USA **96**, 12240 (1999).

[105] P. Habdas and E.R. Weeks, Curr. Opin. Colloid Interface Sci. **7**, 196 (2002).

[106] J. Happel and H. Brenner, *Low Reynolds Number Hydrodynamics* (Noordhoff, Leyden, 1973).

[107] E.H. Hauge and A. Martin-Löf, J. Stat. Phys. **7**, 259 (1973).

[108] S. Henderson, S. Mitchell, and P. Bartlett, Phys. Rev. E **64**, 061403 (2001).

[109] S. Henderson, S. Mitchell, and P. Bartlett, Phys. Rev. Lett. **88**, 088302 (2002).

[110] S. Hess, Z. Naturforsch. A **23**, 1095 (1968).

[111] W. Hess and R. Klein, Physica A **94**, 71 (1978).

[112] E.L. Hill, Am. J. Phys. **22**, 211 (1954).

[113] K. Hinsen, Comput. Phys. Commun. **88**, 327 (1995). The FORTRAN source code is available at http://dirac.cnrs-orleans.fr/HYDROLIB.

[114] M.E.J. Holwill, in *Cilia and Flagella*, edited by M.A. Sleigh (Academic Press, London, 1974), p. 143.

[115] P.J. Hoogerbrugge and J.M.V.A. Koelman, Europhys. Lett. **19**, 155 (1992).

[116] A. Hosoi and B. Chan, *Propulsion in Viscous Fluids: Purcell's Three-Link Swimmer*, http://web.mit.edu/chosetec/www/robo/3link. This reference presents a video of a mechanical realization of Purcell's three-link swimmer.

[117] M. Hütter and H.C. Öttinger, J. Chem. Soc., Faraday Trans. **94**, 1403 (1998).

[118] K. Ichiki and J.F. Brady, Phys. Fluids **13**, 350 (2001).

[119] T. Ihle and D.M. Kroll, Phys. Rev. E **67**, 066705 (2003).

[120] I.M. Jánosi, T. Tél, D.E. Wolf, and J.A.C. Gallas, Phys. Rev. E **56**, 2858 (1997).

[121] K.O.L.F. Jayaweera, B.J. Mason, and G.W. Slack, J. Fluid Mech. **20**, 121 (1964); L.M. Hocking, *ibid.* **20**, 129 (1964).

[122] D.J. Jeffrey and Y. Onishi, J. Fluid Mech. **139**, 261 (1984).

[123] R.E. Johnson and C.J. Brokaw, Biophys. J. **25**, 113 (1979).

[124] R.B. Jones, Physica A **150**, 339 (1988); **157**, 752 (1989).

[125] R.B. Jones and R. Kutteh, Phys. Chem. Chem. Phys. **1**, 2131 (1999); B. Cichocki, R.B. Jones, R. Kutteh, and E. Wajnryb, J. Chem. Phys. **112**, 2548 (2000).

[126] F. Jülicher, A. Ajdari, and J. Prost, Rev. Mod. Phys. **69**, 1269 (1997).

[127] S. Juodkazis, M. Shikata, T. Takahashi, S. Matsuo, and H. Misawa, Appl. Phys. Lett. **74**, 3627 (1999).

[128] N.G. van Kampen, *Stochastic Processes in Physics and Chemistry* (North-Holland, Amsterdam, 1981).

[129] S. Khan and M.P. Sheetz, Annu. Rev. Biochem. **66**, 785 (1997).

[130] N. Kikuchi, A. Gent, and J.M. Yeomans, Eur. Phys. J. E **9**, 63 (2002).

[131] M.J. Kim, J.C. Bird, A.J. Van Parys, K.S. Breuer, and T.R. Powers, Proc. Natl. Acad. Sci. USA **100**, 15481 (2003). A movie showing the bundling of two rotating macroscopic helices can be found at http://www.pnas.org/cgi/content/full/2633596100/DC1.

[132] M.J. Kim, T.R. Powers, Phys. Rev. E **69**, 061910 (2004).

[133] M.J. Kim, M.J. Kim, J.C. Bird, J. Park, T.R. Powers, and K.S. Breuer, Exp. Fluids **37**, 782 (2004).

[134] S. Kim and S.J. Karrila, *Microhydrodynamics: Principles and Selected Applications* (Butterworth-Heinemann, Boston, 1991).

[135] Y.W. Kim and R.R. Netz, Phys. Rev. Lett. **96**, 158101 (2006).

[136] I. Klapper and H. Qian, Biophys. J. **74**, 2504 (1998).

[137] K. Klenin, H. Merlitz, and J. Langowski, Biophys. J. **74**, 780 (1998).

[138] P.E. Kloeden and E. Platen, *Numerical Solution of Stochastic Differential Equations* (Springer, Berlin, 1999).

[139] G.H. Koenderink, H. Zhang, M.P. Lettinga, G. Nägele, and A.P. Philipse, Phys. Rev. E **64**, 022401 (2001).

[140] G. Kósa and M. Shoham, in *Proceedings of the 2005 IEEE International Conference on Robotics and Automation* (Barcelona, 2005), p. 1327.

[141] C. Kural, H. Kim, S. Syed, G. Goshima, V.I. Gelfand, and P.R. Selvin, Science **308**, 1469 (2005).

[142] K. Ladavac and D.G. Grier, Opt. Express **12**, 1144 (2004). A movie showing the dynamics of colloids in an array of optical vortices can be found at http://www.opticsinfobase.org/abstract.cfm?URI=oe-12-6-1144.

[143] K. Ladavac and D.G. Grier, Europhys. Lett. **70**, 548 (2005).

[144] A.J.C. Ladd, Phys. Rev. Lett. **70**, 1339 (1993).

[145] A.J.C. Ladd, Phys. Rev. Lett. **88**, 048301 (2002).

[146] M.C. Lagomarsino, B. Bassetti, and P. Jona, Eur. Phys. J. B **26**, 81 (2002).

[147] H. Lamb, *Hydrodynamics* (Cambridge University Press, London, 1975).

[148] L.D. Landau and E.M. Lifshitz, *Fluid Mechanics* (Pergamon Press, London, 1959).

[149] A. La Porta and M.D. Wang, Phys. Rev. Lett. **92**, 190801 (2004).

[150] P. Lenz, J.-F. Joanny, F. Jülicher, and J. Prost, Phys. Rev. Lett. **91**, 108104 (2003); Eur. Phys. J. E **13**, 379 (2004).

[151] A.J. Levine and T.C. Lubensky, Phys. Rev. Lett. **85**, 1774 (2000); Phys. Rev. E **65**, 011501 (2001).

[152] D.R. Lide, *CRC Handbook of Chemistry and Physics* (CRC Press, Boca Raton, 2002).

[153] J. Lighthill, SIAM Rev. **18**, 161 (1976).

[154] J. Lighthill, J. Eng. Math. **30**, 25 (1996); **30**, 35 (1996).

[155] H. Lodish, D. Baltimore, A. Berk, S.L. Zipursky, P. Matsudaira, and J. Darnell, *Molecular Cell Biology* (W.H. Freeman, New York, 2004).

[156] H. Löwen, J. Phys.: Condens. Matter **13**, R415 (2001).

[157] W. Ludwig, Z. Vgl. Physiol. **13**, 397 (1930).

[158] J.H.C. Luke, SIAM J. Appl. Math. **49**, 1635 (1989).

[159] C. Lutz, M. Kollmann, and C. Bechinger, Phys. Rev. Lett. **93**, 026001 (2004).

[160] C. Lutz, *Structure and Dynamics of Equilibrium and Non-Equilibrium Systems: Colloidal Suspensions in Confining Light Fields* (doctoral thesis, University of Konstanz, 2005). The electronic version is available at http://www.ub.uni-konstanz.de/kops/volltexte/2006/1728.

[161] H. Machemer, J. Exp. Biol. **57**, 239 (1972).

[162] F.C. MacKintosh and C.F. Schmidt, Curr. Opin. Colloid Interface Sci. **4**, 300 (1999).

[163] R.M. Macnab, Proc. Natl. Acad. Sci. USA **74**, 221 (1977).

[164] R.M. Macnab, M.K. Ornston, J. Mol. Biol. **112**, 1 (1977).

[165] R.M. Macnab, in *Escherichia coli and Salmonella typhimurium*, edited by F.C. Neidhardt (Am. Soc. Microbiol., Washington DC, 1987), p. 70.

[166] A.C. Maggs, Phys. Rev. E **57**, 2091 (1998).

[167] M.O. Magnasco, Phys. Rev. Lett. **71**, 1477 (1993).

[168] A. Malevanets and R. Kapral, J. Chem. Phys. **110**, 8605 (1999).

[169] M. Manghi, X. Schlagberger, and R.R. Netz, Phys. Rev. Lett. **96**, 068101 (2006).

[170] M.D. Manson, P.M. Tedesco, and H.C. Berg, J. Mol. Biol. **138**, 541 (1980).

[171] MAPLE is a registred trademark of Waterloo Maple Inc.

[172] S. Martin and T. Gisler (private communication).

[173] T.G. Mason and D.A. Weitz, Phys. Rev. Lett. **74**, 1250 (1995).

[174] T.G. Mason, K. Ganesan, J.H. van Zanten, D. Wirtz, and S.C. Kuo, Phys. Rev. Lett. **79**, 3282 (1997).

[175] P. Mazur, Physica A **110**, 128 (1982).

[176] P. Mazur and W. van Saarloos, Physica A **115**, 21 (1982).

[177] M.J. McHenry, E. Azizi, and J.A. Strother, J. Exp. Biol. **206**, 327 (2003).

[178] A.D. Mehta, M. Rief, J.A. Spudich, D.A. Smith, and R.M. Simmons, Science **283**, 1689 (1999).

[179] J.-C. Meiners and S.R. Quake, Phys. Rev. Lett. **82**, 2211 (1999).

[180] A. Mertelj, J.L. Arauz-Lara, G. Maret, T. Gisler, and H. Stark, Europhys. Lett. **59**, 337 (2002).

[181] J.E. Molloy, K. Dholakia, and M.J. Padgett, J. Mod. Opt. **50**, 1501 (2003).

[182] T.J. Murphy and J.L. Aguirre, J. Chem. Phys. **57**, 2098 (1972).

[183] G. Nägele, Phys. Rep. **272**, 215 (1996).

[184] A. Najafi and R. Golestanian, Phys. Rev. E **69**, 062901 (2004). A movie showing the dynamics of the linear three-bead swimmer (with varying bond lengths) presented in this article can be found at http://focus.aps.org/stories/v13/st27/vid-v13-st27-1.gif.

[185] P. Nelson, *Biological Physics: Energy, Information, Life* (W.H. Freeman, New York, 2003).

[186] M.E.J. Newman and G.T. Barkema, *Monte Carlo Methods in Statistical Physics* (Oxford University Press, New York, 1999).

[187] B. Noetinger, Physica A **163**, 545 (1990).

[188] S. Nonaka, Y. Tanaka, Y. Okada, S. Takeda, A. Harada, Y. Kanai, M. Kido, and N. Hirokawa, Cell **95**, 829 (1998).

[189] S. Nonaka, H. Shiratori, Y. Saijoh, and H. Hamada, Nature **418**, 96 (2002).

[190] H.C. Öttinger, *Stochastic Processes in Polymeric Fluids* (Springer, Berlin, 1996).

[191] J.T. Padding and A.A. Louis, Phys. Rev. Lett. **93**, 220601 (2004).

[192] M. Padgett, J. Courtial, and L. Allen, Phys. Today **57**(5), 35 (2004).

[193] S. Panyukov and Y. Rabin, Phys. Rev. E **62**, 7135 (2000).

[194] W. Paul and J. Baschnagel, *Stochastic Processes: From Physiscs to Finance* (Springer, Berlin, 1999).

[195] G.S. Perkins and R.B. Jones, Physica A **171**, 575 (1991); **189**, 447 (1992).

[196] T.N. Phung, J.F. Brady, and G. Bossis, J. Fluid Mech. **313**, 181 (1996).

[197] W. Poon, P. Pusey, and H. Lekkerkerker, Phys. World **9**(4), 27 (1996).

[198] W.H. Press, B.P. Flannery, S.A. Teukolsky, and W.T. Vetterling, *Numerical Recipes in C: The Art of Scientific Computing* (Cambridge University Press, Cambridge, 1992).

[199] E.M. Purcell, Am. J. Phys. **45**, 3 (1977).

[200] P.N. Pusey, in *Liquids, Freezing, and Glass Transition*, proceedings of the Les Houches Summer School of Theoretical Physics 1989, Part II, edited by J.P. Hansen, D. Levesque, and J. Zinn-Justin (North-Holland, Amsterdam, 1991), p. 763.

[201] D.C. Rapaport, *The Art of Molecular Dynamics Simulation* (Cambridge University Press, Cambridge, 2004).

[202] P. Reimann, Phys. Rep. **361**, 57 (2002).

[203] P. Reimann and P. Hänggi, Appl. Phys. A **75**, 169 (2002).

[204] I.H. Riedel, K. Kruse, and J. Howard, Science **309**, 300 (2005).

[205] H. Risken, *The Fokker-Planck Equation* (Springer, Berlin, 1989).

[206] A. Rohrbach, Phys. Rev. Lett. **95**, 168102 (2005).

[207] Lord Rothschild, Nature **163**, 358 (1949).

[208] J. Rotne and S. Prager, J. Chem. Phys. **50**, 4831 (1969).

[209] S.I. Rubinow and J.B. Keller, J. Fluid Mech. **11**, 447 (1961).

[210] D. Rudhardt, C. Bechinger, and P. Leiderer, Phys. Rev. Lett. **81**, 1330 (1998).

[211] D. Ryter and U. Deker, J. Math. Phys. **21**, 2662 (1980).

[212] F.A. Samatey, H. Matsunami, K. Imada, S. Nagashima, T.R. Shaikh, D.R. Thomas, J.Z. Chen, D.J. DeRosier, A. Kitao, and K. Namba, Nature **431**, 1062 (2004).

[213] K. Sandomirski, S. Martin, G. Maret, H. Stark, and T. Gisler, J. Phys.: Condens. Matter **16**, S4137 (2004).

[214] M. Schmiedeberg and H. Stark, Europhys. Lett. **69**, 629 (2005).

[215] F.G. Schmidt, B. Hinner, and E. Sackmann, Phys. Rev. E **61**, 5646 (2000).

[216] R. Schmitz and B.U. Felderhof, Physica A **116**, 163 (1982).

[217] P.N. Segrè, E. Herbolzheimer, and P.M. Chaikin, Phys. Rev. Lett. **79**, 2574 (1997).

[218] G. Sewell, *The Numerical Solution of Ordinary and Partial Differential Equations* (Academic Press, San Diego, 1988).

[219] J.W. Shaevitz, J.Y. Lee, and D.A. Fletcher, Cell **122**, 941 (2005).

[220] M.P. Sheetz, *Laser Tweezers in Cell Biology* (Academic Press, San Diego, 1998).

[221] M.A. Sleigh, in *Cilia and Flagella*, edited by M.A. Sleigh (Academic Press, London, 1974), p. 79.

[222] I.K. Snook, K.M. Briggs, and E.R. Smith, Physica A **240**, 547 (1997).

[223] S.V. Srigiriraju and T.R. Powers, Phys. Rev. Lett. **94**, 248101 (2005); Phys. Rev. E **73**, 011902 (2006).

[224] H. Stark (private communication).

[225] J.F. Staropoli and U. Alon, Biophys. J. **78**, 513 (2000).

[226] L. Starrs and P. Bartlett, J. Phys.: Condens. Matter **15**, S251 (2003); Faraday Discuss. **123**, 323 (2003).

[227] C.D. Stern, Nature **418**, 29 (2002).

[228] J.J. Stoker, *Differential Geometry* (Wiley-Interscience, New York, 1969).

[229] A.D. Stroock, S.K.W. Dertinger, A. Ajdari, I. Mezić, H.A. Stone, and G.M. Whitesides, Science **295**, 647 (2002).

[230] D.J. Struik, *Lectures on Classical Differential Geometry* (Addison-Wesley, Reading, Massachusetts, 1961).

[231] H. Tanaka and T. Araki, Phys. Rev. Lett. **85**, 1338 (2000).

[232] H. Tanaka, J. Phys.: Condens. Matter **17**, S2795 (2005).

[233] G.I. Taylor, Proc. R. Soc. Lond. A **209**, 447 (1951).

[234] G.I. Taylor, *Low Reynolds Number Flows* (Video no. 21617, Encyclopædia Britannica Educational Corp., Chicago, 1967). This movie (streaming metafile) can be viewed at http://modular.mit.edu:8080/ramgen/ifluids/Low_Reynolds_Number_Flow.rm.

[235] S.-Y. Tee, P.J. Mucha, L. Cipelletti, S. Manley, M.P. Brenner, P.N. Segrè, and D.A. Weitz, Phys. Rev. Lett. **89**, 054501 (2002).

[236] T. Tlusty, A. Meller, and R. Bar-Ziv, Phys. Rev. Lett. **81**, 1738 (1998).

[237] L. Turner, W.S. Ryu, and H.C. Berg, J. Bacteriol. **182**, 2793 (2000). Movies of swimming *E. coli* can be found at http://webmac.rowland.org/labs/bacteria/movies_ecoli.html.

[238] E.J. Verwey and J.T.G. Overbeek, *Theory of the Stability of Lyophobic Colloids* (Elsevier, Amsterdam, 1948).

[239] A. Vilfan and F. Jülicher, Phys. Rev. Lett. **96**, 058102 (2006).

[240] H.-Y. Wang and J.-D. Bao, Physica A **337**, 13 (2004).

[241] M.D. Wang, M.J. Schnitzer, H. Yin, R. Landick, J. Gelles, and S.M. Block, Science **282**, 902 (1998).

[242] E.R. Weeks, J.C. Crocker, A.C. Levitt, A. Schofield, and D.A. Weitz, Science **287**, 627 (2000).

[243] Q.-H. Wei, C. Bechinger, D. Rudhardt, and P. Leiderer, Phys. Rev. Lett. **81**, 2606 (1998).

[244] Q.-H. Wei, C. Bechinger, and P. Leiderer, Science **287**, 625 (2000).

[245] P. Weiss, Science News **169**, 107 (2006).

[246] J. Wilkie, Phys. Rev. E **70**, 017701 (2004).

[247] H. Yamakawa, J. Chem. Phys. **53**, 436 (1970).

[248] H. Yamakawa and M. Fujii, J. Chem. Phys. **64**, 5222 (1976).

[249] H. Yamakawa, *Helical Wormlike Chains in Polymer Solutions* (Springer, Berlin, 1997).

[250] K. Yonekura, S. Maki-Yonekura, and K. Namba, Nature **424**, 643 (2003).

[251] K. Zahn, J.M. Méndez-Alcaraz, and G. Maret, Phys. Rev. Lett. **79**, 175 (1997).

[252] R. Zwanzig, J. Stat. Phys. **9**, 215 (1973).

List of publications

This thesis is partly based on the following articles:

B Two-point microrheology –
Hydrodynamic coupling of rotating beads in optical traps

▷ *Hydrodynamic coupling of two rotating spheres trapped in harmonic potentials*
M. Reichert and H. Stark, Phys. Rev. E **69**, 031407 (2004).

▷ *Direct observation of hydrodynamic rotation-translation coupling between two colloidal spheres*
S. Martin, M. Reichert, H. Stark, and T. Gisler (submitted).

C Drafting of colloids –
The benefits of hydrodynamic interactions

▷ *Circling particles and drafting in optical vortices*
M. Reichert and H. Stark, J. Phys.: Condens. Matter **16**, S4085 (2004).

▷ *Surmounting barriers: The benefit of hydrodynamic interactions*
C. Lutz, M. Reichert, H. Stark, and C. Bechinger, Europhys. Lett. **74**, 719 (2006).

D Swimming of microorganisms –
Synchronization of rotating helical flagella

▷ *Synchronization of rotating helices by hydrodynamic interactions*
M. Reichert and H. Stark, Eur. Phys. J. E **17**, 493 (2005).

Further papers by the author related to this work:

▷ *Rotational diffusion in a chain of particles*
H. Stark, M. Reichert, and J. Bibette, J. Phys.: Condens. Matter **17**, S3631 (2005).

Zusammenfassung

Hydrodynamische Wechselwirkungen in kolloidalen und biologischen Systemen

Kolloidale Suspensionen haben viele Eigenschaften mit atomaren Systemen gemeinsam; insbesondere beobachtet man mit zunehmender Teilchenzahldichte flüssige, kristalline und glasartige Phasen [197, 200]. Kolloide können gewissermaßen als „Analogcomputer“ angesehen werden, die „Rechnungen“ in Echtzeit erlauben für komplexe Situationen wie z. B. Keimbildung und Wachstum von Kristallen [87], Teilchendynamik nahe am Glasübergang [242], die Wechselwirkung von Versetzungen [69] etc. Der herausragende Vorteil von Kolloiden als Modellsysteme ist die Möglichkeit, deren Wechselwirkungen nach Wunsch maßzuschneidern [60, 80]. Außerdem können sie verhältnismäßig einfach durch äußere Felder kontrolliert und manipuliert werden [156], z. B. mit sogenannten „optischen Pinzetten“. Aus diesem Grund werden Kolloide oft als vielseitige Modellsysteme angesehen, um fundamentale Prozesse in atomaren Systemen näher zu beleuchten und neuartige Konzepte der statistischen Physik aufzugreifen; Beispiele hierfür sind entropische Kräfte [210], lichtinduzierte Phasenübergänge [243] oder zweidimensionales Schmelzen [68].

Allerdings gibt es neben Potentialkräften wie z. B. der elektrostatischen Wechselwirkung, die in gewisser Weise den Wechselwirkungen in atomaren Systemen entsprechen, auch Wechselwirkungen, die nur in kolloidalen Systemen auftreten. Wenn sich Teilchen in einer viskosen Flüssigkeit bewegen, erzeugen sie ein Strömungsfeld, welches alle anderen Teilchen in ihrer Bewegung beeinflusst. Diese Wechselwirkungen, die durch die umgebende Flüssigkeit zu Stande kommen und die nur vorhanden sind, wenn sich Teilchen bewegen, werden *hydrodynamische Wechselwirkungen* genannt [60, 106, 134]. Die Dynamik von Kolloiden spielt sich typischerweise bei sehr kleinen Reynolds-Zahlen ab. Da in diesem Regime die viskosen Kräfte gegenüber Trägheitseffekten dominieren, wird die Bewegung der suspendierten Teilchen maßgeblich durch hydrodynamische Wechselwirkungen bestimmt. Ihre Auswirkungen auf die Dynamik kolloidaler und biologischer Systeme (mit charakteristischen Längenskalen im Mikrometerbereich) sind das zentrale Thema der vorliegenden Arbeit.

In den vergangenen Jahrzehnten beschäftigten sich experimentelle und theoretische Studien hauptsächlich mit makroskopischen rheologischen Eigenschaften und dem Transportverhalten von kolloidalen Suspensionen (wie z. B. effektive Viskositäten oder Diffusionskoeffizienten) [14, 183, 200, 251]. In diesen Fällen treten hydrodynamische Effekte nur in Form von Ensemblemittelwerten über den gesamten Konfigurationsraum auf. Doch trotz ihrer wissenschaftlichen und

technologischen Bedeutung ist unser Verständnis der hydrodynamischen Wechselwirkungen bei Weitem noch nicht vollständig.

Neuere Untersuchungen verfolgen daher einen anderen Zugang. Sie konzentrieren sich auf wenige Teilchen mit dem Ziel, die Rolle der hydrodynamischen Wechselwirkungen systematisch zu analysieren, angefangen bei der freien Diffusion eines einzelnen Teilchenpaares [49]. In einem anderen Experiment betrachtet man zwei Kolloidkügelchen, die mit Hilfe von optischen Pinzetten in einem festen Abstand gehalten werden und deren thermische Fluktuationen über die umgebende Flüssigkeit miteinander korreliert sind [15, 179].

Auf Grund ihrer langen Reichweite und ihrem Vielteilchencharakter erzeugen hydrodynamische Wechselwirkungen eine Vielzahl faszinierender kollektiver Phänomene, insbesondere in Systemen, in denen Teilchen fern vom Gleichgewicht angetrieben werden. Beispielsweise führen sie zu zeitlich periodischen Bewegungsmustern [37, 121, 222] oder zu vorübergehend chaotischer Dynamik in der Sedimentation von Clustern, die aus einigen wenigen kugelförmigen Teilchen bestehen [84, 120].

Experimente mit magnetischen runden Scheibchen, die auf einer Flüssigkeit-Luft-Grenzschicht schwimmen und durch ein rotierendes Magnetfeld in Drehung versetzt werden, zeigen spontane Musterbildung durch dynamische Selbstorganisation [101]. Theoretische Arbeiten deuten an, dass die hydrodynamische Kopplung von Rotationsbewegungen abstoßende Kräfte zwischen rotierenden Teilchen verursachen kann [150]. Diese könnten eine räumliche Anordnung von Mikrowirbeln erzeugen, die an einen Wigner-Kristall erinnert und möglicherweise zweidimensionales Schmelzen aufweist. Ein solches Szenario soll in aktiven Membranen auftreten, in die biologische Motoren (z. B. ATP-Synthase) eingebettet sind.

Schwimmbewegungen von Mikroorganismen finden ebenfalls bei sehr kleinen Reynolds-Zahlen statt [199]. Sie sind daher ebenfalls hydrodynamischen Wechselwirkungen unterworfen. Es gibt sowohl experimentelle als auch theoretische Hinweise darauf, dass z. B. die schlagenden Geißeln von nebeneinander schwimmenden Spermien sich auf Grund der hydrodynamischen Kopplung in Phase bewegen [23, 233]. Neuere Experimente mit Spermien, die an ebenen Grenzflächen schwimmen, zeigen ein durch Selbstorganisation gebildetes hexagonales Gitter. Es besteht aus dynamischen Wirbeln, welche durch zirkulierende Zellen geformt werden [204]. Außerdem wird vermutet, dass hydrodynamische Effekte auch eine führende Rolle spielen könnten bei der Fortbewegung von Bakterien, die vorwärts schwimmen, indem sie ein Bündel aus schraubenartigen Flagellen in Drehung versetzen [23]. Dies bedeutet, dass die Rotationen der einzelnen Flagellen synchonisiert sein müssen. Es stellt sich die Frage, ob der zu Grunde liegende Mechanismus auf hydrodynamischen Wechselwirkungen beruht. Der Effekt der Bündelbildung wurde auch in makroskopischen Experimenten nachgewiesen, in denen starre spiralförmige Drähte in hochviskosem Silikonöl gedreht wurden [131, 163].

Alle diese Beispiele zeigen deutlich, dass hydrodynamische Wechselwirkungen zu vielen interessanten Phänomenen führen, die sowohl für die Grundlagen- als

auch für die angewandte Forschung von Bedeutung sind, von den Materialwissenschaften bis hin zur Biologie.

Die vorliegende Dissertation präsentiert analytische Arbeiten und Simulationsergebnisse für verschiedene kolloidale und biologische Systeme auf der Mikrometerskala, deren Dynamik maßgeblich durch hydrodynamische Wechselwirkungen bestimmt wird. In Teil A stellen wir zunächst die theoretischen Konzepte zur Beschreibung und Simulation hydrodynamischer Wechselwirkungen vor, gefolgt von einer fundierten Beschreibung Brown'scher Dynamik. Die Teile B–D präsentieren die Ergebnisse dreier unterschiedlicher Projekte, die in sich abgeschlossen sind und daher unabhängig voneinander gelesen werden können. Jeder Teil beginnt mit einer ausführlichen Einführung in das jeweilige Thema und endet mit einer kurzen Zusammenfassung und Diskussion der Ergebnisse.

Teil B behandelt hydrodynamische Wechselwirkungen in der Mikrorheologie, einer Methode zur Bestimmung des viskoelastischen Verhaltens weicher Materie (wie z. B. biologischem Gewebe) auf der Mikrometerskala. Wir betrachten die überdämpfte Bewegung zweier kugelförmiger Kolloidteilchen in einer Newton'schen Flüssigkeit. Die Teilchen sind in optischen Pinzetten gefangen, sowohl bezüglich ihrer Position als auch ihrer Orientierung. Ausgehend von einer Langevin-Beschreibung der Dynamik, untersuchen wir die thermische Bewegung dieses Systems und erhalten ein umfangreiches Spektrum an Korrelationsfunktionen. Unser Hauptaugenmerk gilt den Rotationsfreiheitsgraden und ihrer Kopplung an die Translationen der Teilchen. Wir erweitern damit frühere Untersuchungen, die sich ausschließlich auf die translatorischen Korrelationen beschränkten [15, 179]. Eine wichtige Eigenschaft unseres Systems ist die Selbstkopplung von Translation und Rotation eines Teilchens, die durch das benachbarte Teilchen vermittelt wird. In der dazugehörigen Korrelationsfunktion ist daher eine charakteristische Zeitverzögerung deutlich zu erkennen. Unsere analytischen Ergebnisse stimmen gut mit Korrelationsfunktionen überein, die aus eigenen Simulationen der Brown'schen Dynamik und auch aus verfügbaren experimentellen Daten [172] bestimmt wurden.

In Teil C untersuchen wir die Dynamik von Kolloidkügelchen, die in einer ringförmigen harmonischen Falle umlaufen. Dabei führen hydrodynamische Wechselwirkungen in diesem System zu charakteristischen kollektiven Phänomenen. Zunächst werden die Teilchen mit konstanter Kraft angetrieben. Mit Hilfe einer linearen Analyse untersuchen wir die Stabilität von regelmäßigen Clustern von zirkulierenden Teilchen, und wir erläutern den periodischen Grenzzyklus, in den das System hineinläuft. Wir verdeutlichen, dass „Windschatten"effekte von Teilchenpaaren für die Interpretation dieses Grenzzyklus' entscheidend sind. Ein zusätzlich zur konstanten Kraft entlang der Ringfalle angelegtes periodisches Sägezahnpotential bewirkt eine neuartige kollektive Bewegungsmode, die an eine Raupe erinnert. Sie wird maßgeblich durch die weitreichenden hydrodynamischen Wechselwirkungen bestimmt, die es den Teilchen ermöglichen, Potentialbarrieren zu überwinden. Unsere numerischen Ergebnisse sind in guter Übereinstimmung

mit experimentellen Daten [160]. Die beobachteten kollektiven Effekte könnten auch in thermischen Ratschen von Bedeutung sein, also Modellen, die üblicherweise zur Beschreibung von biologischen Motoren herangezogen werden [9, 126, 185].

Das Thema von Teil D ist die Schwimmbewegung von Mikroorganismen. Wie bereits erwähnt, verwenden viele Arten von Bakterien als Antrieb mehrere rotierende schraubenförmige Flagellen, welche typischerweise Bündel bilden. Dazu müssen ihre Rotationen aber synchronisiert sein. Die zentrale Frage unserer Untersuchung ist, ob hydrodynamische Wechselwirkungen eine solche Synchronisation bewirken können. Als einfachstes Modell betrachten wir zwei starre Spiralen, die aus fest miteinander verbundenen Kugeln modelliert werden; wir vernachlässigen also zunächst elastische Deformationen. Die beiden Spiralen werden durch konstante und gleiche Drehmomente angetrieben. Außerdem sind sie räumlich fixiert, indem wir ihre Enden in harmonischen Fallen verankern. Bei endlicher Stärke dieser Fallen beobachten wir tatsächlich eine Phasensynchronisation der Rotationen der beiden Spiralen. Die Synchronisationsgeschwindigkeit nimmt allerdings mit zunehmender Fallenstärke ab; im Grenzfall unendlich starker Fallen findet keine Synchronisation mehr statt. Daraus folgern wir, dass ein gewisses Maß an Flexibilität notwendig ist. Deshalb verfeinern wir unser Modell in einem zweiten Schritt und berücksichtigen nun elastische Deformationen der Spiralen im Rahmen der nichttrivialen Elastizitätstheorie von spiralförmigen dünnen Stäben. Auch in diesem Modell beobachten wir, dass die Rotationen synchronisiert sind. Insbesondere wird durch die zusätzliche Flexibilität der Spiralen die Synchronisationsgeschwindigkeit weiter erhöht. Außerdem beobachten wir eine Tendenz der beiden Spiralen, sich zu bündeln.

Danksagung

Es gibt zahlreiche Menschen, die mich während meiner Promotionszeit unterstützt und auch geprägt haben. Sie haben damit einen wesentlichen Anteil am Erfolg der vorliegenden Arbeit. Darüber hinaus hätte es ohne die wertvollen Begegnungen mit all diesen Menschen wohl kaum einen so großen Spaß gemacht. Dafür möchte ich allen von ganzem Herzen danken.

Mein ganz besonderer Dank gilt PD Holger Stark für die interessante Themenstellung und die Betreuung dieser Arbeit. Seine stete Diskussionsbereitschaft und auch sein kritisches Hinterfragen haben viel zum Fortschritt meiner Forschung beigetragen. Durch immer wieder neue Ideen hat er meine Motivation aufrechterhalten und entscheidende Impulse gegeben. Eine vertrauensvolle Zusammenarbeit war der Grundstein für das Gelingen dieser Arbeit.

Ich weiß es sehr zu schätzen, dass Prof. em. Rudolf Klein sich bereit erklärt hat, als zweiter Gutachter dieser Arbeit zur Verfügung zu stehen. Insbesondere aber möchte ich mich bei ihm auch für diverse Diskussionen, Gespräche und Ratschläge sowohl hinsichtlich meiner wissenschaftlichen Arbeit als auch zu anderen Themen bedanken.

Bei Prof. Georg Maret bedanke ich mich für die freundliche Aufnahme an seinem Lehrstuhl und für viele hilfreiche Anregungen. Auf keinen Fall unerwähnt lassen möchte ich auch die Workshops des von ihm mit viel Engagement vorangetriebenen Internationalen Graduiertenkollegs „Soft Condensed Matter“ der Universitäten Konstanz, Strasbourg und Grenoble; diese Veranstaltungen – ungezwungen und doch auf sehr hohem wissenschaftlichen Niveau – gaben mir immer wieder Gelegenheit, meine eigenen Arbeiten einem breiten Publikum zu präsentieren, woraus sich viele anregende Diskussionen ergaben.

Der Erfolg des Projekts C „Drafting of colloids“ ist maßgeblich von der Zusammenarbeit mit Prof. Clemens Bechinger und Dr. Christoph Lutz von der Universität Stuttgart geprägt. Ich kann mir keine bessere Art der Zusammenarbeit zwischen Theorie und Experiment vorstellen. Ich danke Dr. Christoph Lutz für die Durchführung der Experimente und die geduldige Erklärung experimenteller Details. Und der spürbare Enthusiasmus, den Prof. Clemens Bechinger dem Projekt entgegenbrachte, sorgte für den nötigen Schwung, um in relativ kurzer Zeit zu spannenden Ergebnissen zu kommen.

Die experimentellen Arbeiten im Rahmen des Projekts B „Two-point microrheology“ wurden von Dr. Stephen Martin durchgeführt. Insbesondere durch die Diskussionen mit PD Thomas Gisler bin ich selbst zu einem tieferen Verständnis meiner eigenen Ergebnisse gekommen.

Großer Dank gebührt auch all jenen, die die vorliegende Schrift mit großer Sorgfalt Korrektur gelesen und viele hilfreiche Hinweise gegeben haben, als da

wären: PD Holger Stark, PD Thomas Gisler, Peter Henseler, Erik Gauger, Andrej Grimm und Christine Kircher.

Ganz herzlich möchte ich mich bei allen meinen Kollegen der Nachwuchsgruppe um PD Holger Stark für ein sehr angenehmes Arbeitsklima bedanken. Dies sind (in „chronologischer“ Reihenfolge): Dr. Faez Miri, Matthias Huber, Michael Schmiedeberg, Erik Gauger und Andrej Grimm.

Ich erinnere mich immer wieder gerne an die vielen Gespräche und Diskussionen mit Dr. Faez Miri. Mit seiner Art, über die verschiedensten Fragen der Physik zu diskutieren, hat er während seiner Zeit in Konstanz für eine ungemein stimulierende Atmosphäre in unserem damaligen „Multikulti“-Büro gesorgt. Außerdem hat er mir in vielen Gesprächen ein absolut ideologiefreies Bild von seinem Heimatland Iran vermittelt.

Mit Matthias Huber verbinden mich zahlreiche freundschaftliche Gespräche über – im wahrsten Sinne des Wortes – Gott und die Welt. Unsere offenen Diskussionen haben mir immer wieder geholfen, die Welt auch aus einem ganz anderen Blickwinkel wahrzunehmen.

Bedanken möchte ich mich insbesondere auch bei Erik Gauger und Andrej Grimm. Es hat mir großen Spaß bereitet, ihre Diplomarbeiten mitzubetreuen, und ich habe dabei selbst sehr viel gelernt. Und dann wären da noch all die guten Gespräche – sei es in der Kaffeeecke auf Z10 oder auch zu manch morgendlicher Stunde in Eriks Küche –, die ich nicht missen möchte und die mich immer wieder aufgemuntert haben, wenn es mal wieder nicht ganz so lief wie geplant. Unvergessen sind auch die kreativen und lustigen Versuche in „experimenteller Fotografie“ zusammen mit Andrej.

An dieser Stelle darf natürlich Markus Müller nicht fehlen, der während seiner Zeit als „Asyl-Diplomand“ auf Z10 und auch danach immer wieder für gute Laune und Abwechslung gesorgt hat.

Ich bedanke mich bei allen Kolleginnen und Kollegen am Lehrstuhl von Prof. Georg Maret. Ich habe mich in dieser Gruppe sehr wohl gefühlt als „Theoretiker unter Experimentatoren“, und ich erinnere mich sehr gerne an die vielen gemeinsamen Aktivitäten wie Lehrstuhlausflüge oder Tagungsreisen zurück. Den beiden Sekretärinnen des Lehrstuhls, Sabine Lucas und Doris Drexler, danke ich vielmals für die schnelle und reibungslose Abwicklung zahlreicher Verwaltungsangelegenheiten.

Den Mitgliedern des Lehrstuhls von Prof. Peter Nielaba danke ich für die Gastfreundschaft beim „Rahmenprogramm“ diverser Tagungsbesuche und auch bei anderen Gelegenheiten. Peter Henseler und Wolfram Quester danke ich für ihre selbstlose Hilfe bei so manchem Computerproblem.

Die erholsamen Ausflüge und Wanderungen gemeinsam mit Peter Henseler haben mir immer wieder geholfen, den Kopf vom Forschungsalltag freizubekommen. Auch dafür bin ich von ganzem Herzen dankbar. Die Gespräche mit ihm über die unterschiedlichsten Themen haben mir stets sehr viel bedeutet und meinen geistigen Horizont erweitert.

Ein ganz besonderes Dankeschön geht an Markus Hager für die ungezählten Stunden bei dem ein oder anderen gemütlichen Bierchen oder beim Beachvolleyball, um wieder aus den Sphären der Physik auf den Boden zu kommen. Ich werde die vielen lustigen Erlebnisse nie vergessen, allen voran unsere legendäre „Kühlschrank"-Aktion.

An dieser Stelle darf ich natürlich auch meine zweite „geistige Heimat" (neben der Universität Konstanz) nicht unerwähnt lassen: das „Café Zeitlos". Ich bedanke mich beim ganzen „Zeitlos"-Team für die nette Atmosphäre, die so oft für die nötige Entspannung und Abwechslung gesorgt hat.

* * * * *

Diese Arbeit wurde von der Deutschen Forschungsgemeinschaft im Rahmen des Sonderforschungsbereichs Transregio 6 „Physics of colloidal dispersions in external fields" (Teilprojekt C5 „Hydrodynamically coupled colloidal motors") und des Internationalen Graduiertenkollegs „Soft Condensed Matter" finanziell unterstützt.